LUND UNIVERSITY

Sources and Diagnostics for Attosecond Science

Miranda, Miguel

2012

Link to publication

Citation for published version (APA):
Miranda, M. (2012). *Sources and Diagnostics for Attosecond Science*. [Doctoral Thesis (compilation), Atomic Physics].

Total number of authors:
1

General rights
Unless other specific re-use rights are stated the following general rights apply:
Copyright and moral rights for the publications made accessible in the public portal are retained by the authors and/or other copyright owners and it is a condition of accessing publications that users recognise and abide by the legal requirements associated with these rights.
- Users may download and print one copy of any publication from the public portal for the purpose of private study or research.
- You may not further distribute the material or use it for any profit-making activity or commercial gain
- You may freely distribute the URL identifying the publication in the public portal

Read more about Creative commons licenses: https://creativecommons.org/licenses/

Take down policy
If you believe that this document breaches copyright please contact us providing details, and we will remove access to the work immediately and investigate your claim.

LUND UNIVERSITY

PO Box 117
221 00 Lund
+46 46-222 00 00

SOURCES AND DIAGNOSTICS FOR ATTOSECOND SCIENCE

Miguel Nicolau da Costa Ribeiro de Miranda

Doctoral Thesis
2012

LUND UNIVERSITY

U. PORTO
FC FACULDADE DE CIÊNCIAS
UNIVERSIDADE DO PORTO

Sources and Diagnostics for Attosecond Science

© 2012 Miguel Miranda
All rights reserved
Printed in Sweden by Media-Tryck, Lund, 2012

Division of Atomic Physics
Department of Physics
Faculty of Engineering, LTH
Lund University
P.O. Box 118
SE–221 00 Lund
Sweden

Department of Physics and Astronomy
Faculty of Sciences
University of Porto
Rua do Campo Alegre 687
4169–007 Porto
Portugal

www.atomic.physics.lu.se
dfa.fc.up.pt

ISSN 0281-2762
Lund Reports on Atomic Physics, LRAP-466

ISBN: 978-91-7473-392-1

“Sou um convalescente do Momento. [...] E ver passar a Vida faz-me tédio.”
Álvaro de Campos

Opiário

ABSTRACT

Ultrafast science refers to physical events that happen on the femtosecond (1 fs=10^{-15}s) and attosecond (1 as= 10^{-18}s) timescales. Generation of attosecond pulses is usually achieved by interacting high-intensity femtosecond pulses with matter (typically gases), in a process called high-order harmonic generation (HHG). Under the correct conditions, this process leads to the creation of sub-fs pulses in the extreme ultraviolet (XUV) region.

The work presented in this thesis focuses around generating, characterizing, and applying ultrashort light pulses, both in the femtosecond and attosecond domain.

The first part describes the effort on the femtosecond laser sources, with emphasis on carrier-envelope phase (CEP) stability and control, and temporal and spatial characterization. An existing high-power (30 fs, 6 mJ) laser system was successfully CEP-stabilized, using an acousto-optic programmable dispersive filter (AOPDF) for CEP control. CEP detection at kilohertz rates is also demonstrated. A method for the characterization of ultrashort laser pulses, based on a glass wedges and chirped mirror compressor, has been developed and demonstrated on pulses in the few-cycle regime. This technique, together with spectral interferometry, has been used to characterize in space and time femtosecond laser pulses, in the optical / near-infrared domain.

The second part deals with the HHG sources and applications. The spatial coherence of one of the HHG sources, together with its high photon flux, has allowed us to perform single-shot holography in the extreme ultraviolet (XUV) domain. Another HHG source, with lower power but higher repetition rate, was used for the characterization of properties of argon and helium atoms. For this, a technique typically used for the temporal characterization of attosecond pulse trains, RABBITT (reconstruction of attosecond beating by interfering two-photon transitions) was used, allowing us to study the phase of a resonant two-photon ionization in helium, and to measure photoemission delays in argon.

SUMÁRIO

Ciência ultra-rápida refere-se a eventos físicos que se desenvolvem em escalas de tempo de femtosegundos (1 fs=10^{-15}s) e attosegundos (1 as= 10^{-18}s). A geração de impulsos com durações de attosegundos é tipicamente conseguida através da interacção de impulsos de femtosegundos de alta intensidade com matéria (tipicamente gases), num processo chamado geração de harmónicos de ordem elevada (HHG). Em condições apropriadas, este processo pode levar à criação de impulsos com durações inferiores a um femtosegundo, com comprimentos de onda na região do extremo ultra-violeta (XUV).

Nesta tese é descrito o trabalho efectuado na geração, caracterização e aplicação de impulsos ultra-curtos, tanto no regime de femtosegundos como de attosegundos.

A primeira parte descreve o trabalho efectuado nas fontes laser de femtosegundos, com destaque na medida e controlo da fase absoluta do campo eléctrico, e na caracterização espacial e temporal. Um sistema laser anteriormente existente (30 fs, 6 mJ) foi modificado de modo a ter a sua fase absoluta estabilizada, utilizando um filtro acusto-óptico de dispersão programável (AOPDF). Medida de fase absoluta a taxas de kilohertz é também demonstrada. Um novo método para caracterizar temporalmente impulsos ultra-curtos foi desenvolvido, baseado num compressor temporal de espelhos chirpados, e foi demonstrado em impulsos ultra-curtos no regime de poucos ciclos. Esta técnica, em conjunto com interferometria espectral, foi utilizada para caracterizar no espaço e no tempo impulsos ultra-curtos.

A segunda parte do trabalho está relacionada com fontes e aplicações de HHG. A coerência espacial de uma fonte, em conjunto com o seu elevado fluxo de energia, permitiu a realização de holografia no domínio dos ultra-violeta extremos (XUV). Outra fonte de HHG, com menor energia por impulso mas com maior taxa de repetição, foi usada para estudar propriedades atómicas de argon e hélio. A técnica normalmente ulilizada para caracterização de trens de impulsos de attosegundos, RABBIIT (reconstrução de impulsos de attosegundos por interferência de transições a dois fotões) foi utilizada para estudar uma ionização ressonante por dois fotões em hélio, e para medir atrasos relativos na foto-emissão em árgon.

POPULAR SCIENCE SUMMARY

What is a photographic camera flash good for? The easy answer is "to illuminate". There is more to it though: the duration of a camera flash is usually much shorter than the shutter speed of the camera. This allows us to take sharp pictures of fast objects with an inexpensive camera. Ultrafast science is based on a similar principle: no shutter is capable of opening and closing fast enough to "freeze" the motion of molecules breaking up and forming new ones on a chemical reaction; or, much faster, electrons "spinning" around the nucleus of an atom. The trick is to use very short light pulses (our flashes). Events like the ones described take place in times as short as *femtoseconds* and *attoseconds*, respectively. If we want to see what happens, for example, during a chemical reaction, and not only the before and after, we need a flash shorter than the time it takes to occur.

But how short is a femtosecond? And an attosecond? A femtosecond is 0.000000000000001 seconds (or 10^{-15} s), and an attosecond is one thousand times smaller. To put it in perspective, suppose you have a clock and that, at each second, your clock would fall behind one femtosecond. How long would it take for it to be one second off? It would take longer than thirty million years.

There is a fundamental limitation to how short a light pulse can be. Light is an oscillation, or vibration, of the electric and the magnetic fields, that propagate as waves. Visible light, that our eyes can perceive, has oscillations periods of about two femtoseconds, and a light pulse cannot be shorter than that. To create even shorter pulses, we have to go higher in the frequency spectrum, towards X-rays. Light pulses with durations of some femtoseconds are nowadays generated directly from lasers. These laser pulses can then be used to interact with matter and generate light at higher frequencies, and even shorter pulses can be created, with durations of around one hundred attoseconds.

This thesis describes the work undertaken on creating, taming, measuring and using such short light pulses, both in the femtosecond and attosecond regime. Creating such short light pulses poses a considerable technical challenge. Interestingly, it is as difficult to keep them short as it is to create them, and the same goes for characterizing them: since these are the shortest events artificially created, we do not have an even shorter light pulse to measure them, so we have to use these pulses to measure themselves.

POPULÄRVETENSKAPLIG SAMMANFATTNING

Vad är en fotografisk kamerablixt bra för? Det enkla svaret är “att belysa”. Det är dock inte hela svaret: en kamerablixt är i regel mycket kortare än slutartiden på kameran. Det gör det möjligt att ta skarpa bilder av snabba objekt med en billig kamera. Ultrasnabb vetenskap bygger på en liknande princip: ingen slutare kan öppnas och stängas tillräckligt snabbt för att “frysa” rörelsen hos molekyler då de bryts upp i beståndsdelar som sedan bildar nya molekyler i en kemisk reaktion, eller någonting ännu mycket snabbare, elektroner som “snurrar” runt kärnan av en atom. Tricket är att använda mycket korta ljuspulser (våra blixtar). Händelser som de som beskrivs ovan äger rum på tidsskalor så korta som *femtosekunder* respektive *attosekunder*. Om vi vill se vad som händer exempelvis under en kemisk reaktion, och inte bara före och efter, behöver vi en blixt kortare än den tid det tar att för reaktionen att ske.

Men hur kort är en femtosekund? Och en attosekund? En femtosekund är 0.000000000000001 sekunder (eller 10^{-15} s) och en attosekund är tusen gånger mindre. För att sätta det i perspektiv, antag att du har en klocka och att din klocka varje sekund halkar efter med en femtosekund. Hur lång tid skulle det ta innan klockan gick en sekund fel? Den skulle ta längre än 30 miljoner år.

Det finns en grundläggande begränsning för hur kort en ljuspuls kan vara. Ljus är en svängning eller vibration av elektriska och magnetiska fält som propagerar som vågor. Synligt ljus, som våra ögon kan uppfatta, har svängningsperioder på ca. två femtosekunder, och en ljuspuls kan inte vara kortare än så. För att skapa ännu kortare pulser måste vi gå högre upp i frekvensspektrat, mot röntgenstrålar. Ljuspulser som är några femtosekunder långa kan idag genereras direkt från lasrar. Dessa laserpulser kan sedan användas för att interagera med materia och generera ljus vid högre frekvenser, och ännu kortare pulser kan skapas, som är omkring hundra attosekunder långa.

Denna avhandling beskriver arbetet med att skapa, tämja, mäta och använda sådana korta ljuspulser, både i femtosekund- och attosekundregimen. Att skapa så korta ljuspulser är en stor teknisk utmaning. Intressant nog är det lika svårt att hålla dem korta som det är att skapa dem, och detsamma gäller för att karakterisera dem: eftersom dessa är de kortaste händelser som har skapats artificiellt så har vi ingen ännu kortare ljuspuls att mäta dem med, utan vi måste använda samma pulser och låta dem mäta sig själva.

LIST OF PUBLICATIONS

This thesis is based on the following papers, which will be referred to by their roman numerals in the text.

I **Carrier-envelope phase stabilization of a multi-millijoule, regenerative-amplifier-based chirped-pulse amplifier system**
T. Fordell, M. Miranda, A. Persson, and A. L'Huillier.
Opt. Express **17**, 21091–21097 (2009).

II **High-speed carrier-envelope phase drift detection of amplified laser pulses**
T. Fordell, M. Miranda, C. L. Arnold, and A. L'Huillier.
Opt. Express **19**, 23652–23657 (2011).

III **Simultaneous compression and characterization of ultrashort laser pulses using chirped mirrors and glass wedges**
Miguel Miranda, Thomas Fordell, Cord Arnold, Anne L'Huillier, and Helder Crespo.
Opt. Express **20**, 688–697 (2012).

IV **Characterization of broadband few-cycle laser pulses with the d-scan technique**
Miguel Miranda, Cord L. Arnold, Thomas Fordell, Francisco Silva, Benjamín Alonso, Rosa Weigand, Anne L'Huillier, and Helder Crespo.
Opt. Express **20**, 18732–18743 (2012).

V **Spatiotemporal characterization of few-cycle laser pulses**
Benjamín Alonso, Miguel Miranda, Íñigo J. Sola, and Helder Crespo.
Opt. Express **20**, 17880–17893 (2012).

VI **Generation and spatiotemporal characterization of 4.5-fs pulses from a hollow-core fiber compressor**
Benjamín Alonso, Miguel Miranda, Francisco Silva, Vladimir Pervak,
Jens Rauschenberger, Julio San Román, Íñigo J. Sola, and Helder Crespo.
(2012) *Manuscript in preparation.*

VII **Space-time focusing of phase-stabilized nanojoule-level 2.5-cycle pulses to peak intensities $> 3 \times 10^{13}$W/cm^2 at 80 MHz**
Miguel N. Miranda, Pedro B. Oliveira, L. M. Bernardo, Franz X. Kärtner, and Helder M. Crespo.
CLEO/Europe and EQEC 2009 Conference Digest **CF1 2**, (2009).

VIII **Spatial and spectral properties of the high-order harmonic emission in argon for seeding applications**
X. He, M. Miranda, J. Schwenke, O. Guilbaud, T. Ruchon, C. Heyl,
E. Georgadiou, R. Rakowski, A. Persson, M. B. Gaarde, and A. L'Huillier.
Phys. Rev. A **79**, 063829 (2009).

IX **Single-shot holography using high-order harmonics**
J. Schwenke, A. Mai, M. Miranda, X. He, G. Genoud, A. Mikkelsen,
S.-G. Pettersson, A. Persson, and A. L'Huillier.
J. Mod. Opt. **106**, 2723–2730 (2008).

X **Phase Measurement of Resonant Two-Photon Ionization in Helium**
M. Swoboda, T. Fordell, K. Klünder, J. M. Dahlström, M. Miranda, C. Buth,
K. J. Schafer, J. Mauritsson, A. L'Huillier, and M. Gisselbrecht.
Phys. Rev. Lett. **104**, 103003 (2010).

XI **Photoemission-time-delay measurements and calculations close to the 3s-ionization-cross-section minimum in Ar**
D. Guénot, K. Klünder, C. L. Arnold, D. Kroon, J. M. Dahlström,
M. Miranda, T. Fordell, M. Gisselbrecht, P. Johnsson, J. Mauritsson,
E. Lindroth, A. Maquet, R. Taïeb, A. L'Huillier, and A. S. Kheifets.
Phys. Rev. A **85**, 053424 (2012).

ABBREVIATIONS

APT	Attosecond Pulse Train
ATI	Above-Threshold Ionization
CEO	Carrier–Envelope Offset
CEP	Carrier–Envelope Phase
CPA	Chirped Pulse Amplification
CRAB	Complete Reconstruction of Attosecond Burst
CW	Continuous Wave
DOG	Double Optical Gate
FEL	Free-Electron Laser
FWHM	Full-Width at Half-Maximum
FROG	Frequency-Resolved Optical Gating
GD	Group Delay
GDD	Group Delay Dispersion
HHG	High-order Harmonic Generation
IR	Infrared
KLM	Kerr-Lens Modelocking
MBES	Magnetic Bottle Electron Spectrometer
MCP	Microchannel Plate
ML	Mode Locking
RABBITT	Reconstruction of Attosecond Beating By Interfering Two-photon Transitions
SAP	Single Attosecond Pulse
SFA	Strong-Field approximation
TDSE	Time-Dependent Schrödinger Equation
TOF	Time Of Flight
XUV	Extreme Ultraviolet ($10 < \hbar\omega < 124$ eV)

CONTENTS

1 Introduction **1**
1.1 Aim and Outline . . . 1

2 Ultrashort Pulses **3**
2.1 Introduction . . . 3
2.2 Description . . . 4
2.2.1 Spectral phase . . . 6
2.2.2 Wavelength/Frequency Representation . . . 8
2.3 Dispersion . . . 8
2.3.1 Propagation in Dispersive Media . . . 8
2.3.2 Dispersion Compensation . . . 10
2.4 Generation . . . 14
2.4.1 Mode-locked Lasers . . . 14
2.4.2 Chirped-Pulse Amplification . . . 16
2.4.3 Spectral Broadening in a Hollow-Core Fiber . . . 16
2.5 Second harmonic generation . . . 19
2.6 Experimental Laser Setups . . . 21
2.6.1 Laser System in Lund . . . 22
2.6.2 Laser System in Porto . . . 23

3 Characterization **25**
3.1 Introduction . . . 25
3.2 Spectral Interferometry . . . 26
3.3 Spatiotemporal Characterization . . . 27
3.4 Autocorrelation . . . 28
3.4.1 Interferometric Autocorrelation . . . 30
3.4.2 Intensity Autocorrelation . . . 30
3.5 Frequency-Resolved Optical Gating (FROG) . . . 30
3.6 Spectral Phase Interferometry for Direct Electric-field Reconstruction (SPIDER) . . . 32
3.7 Multiphoton Intrapulse Interference Phase Scan (MIIPS) . . . 34
3.8 d-scan . . . 36
3.9 Carrier-Envelope Phase . . . 39

4 High-Harmonic Generation, Attosecond Pulses and Applications **43**
4.1 Introduction . . . 43
4.2 High-Harmonic Generation . . . 43
4.2.1 Experiments . . . 47
4.3 Attosecond Pulses . . . 47
4.3.1 Attosecond Pulse Shaping . . . 47
4.3.2 Isolated Attosecond Pulses . . . 49
4.3.3 Experimental Setup . . . 49
4.4 Characterization . . . 51
4.4.1 Photoionization . . . 52
4.4.2 RABBITT . . . 53

4.4.3 Streaking and FROG-CRAB . . . 54
4.4.4 Experimental Detection . . . 56
4.5 Applications . . . 58
4.5.1 XUV Holography . . . 58
4.5.2 Resonant Two-Photon Ionization . . . 60
4.5.3 Time Delay Measurements . . . 61

5 Summary and Outlook 63

Comments on the papers 65

Acknowledgements 67

References 69

Papers

I Carrier-envelope phase stabilization of a multi-millijoule, regenerative-amplifier-based chirped-pulse amplifier system 83

II High-speed carrier-envelope phase drift detection of amplified laser pulses 92

III Simultaneous compression and characterization of ultrashort laser pulses using chirped mirrors and glass wedges 101

IV Characterization of broadband few-cycle laser pulses with the d-scan technique 113

V Spatiotemporal characterization of few-cycle laser pulses 127

VI Generation and spatiotemporal characterization of 4.5-fs pulses from a hollow-core fiber compressor 143

VII Space-time focusing of phase-stabilized nanojoule-level 2.5-cycle pulses to peak intensities $> 3 \times 10^{13} \mathrm{W/cm^2}$ at 80 MHz 158

VIII Spatial and spectral properties of the high-order harmonic emission in argon for seeding applications 162

IX Single-shot holography using high-order harmonics 172

X Phase Measurement of Resonant Two-Photon Ionization in Helium 183

XI Photoemission-time-delay measurements and calculations close to the $3s$-ionization-cross-section minimum in Ar 189

CHAPTER 1

INTRODUCTION

When the laser was invented in 1960 [1], it was often seen as “a solution looking for a problem” [2]. More than 50 years later, and even if many problems have indeed been found and solved, this description is still true. Not only has the laser helped to solve problems, it “created” new problems of its own. As laser technology progressed, the boundaries of known physics have also been pushed, either by confirming theoretical predictions or by surprising scientists with unexpected results.

The work performed in this thesis was based on, and motivated by, two things: laser technology in itself (more specifically ultrafast lasers - or ultrashort light pulses), and on the other hand, a relatively recent topic in physics which was built around unexpected results from light matter interaction at high intensities: high-order harmonic generation (HHG) [3, 4].

Recent advances in laser technology allow scientists to reach light pulses whose duration is comparable to the duration of the electric field cycle. In the optical domain, this corresponds to around 2 fs (1 fs=10^{-15} s). This has made possible the study of physical phenomena on unprecedentedly short time scales: as with photography, to “freeze” an object motion in time, a short exposure time can be used. Another way is to use a short *flash* instead: this would be a direct analogy to ultrafast techniques. On the other hand, short pulses have also allowed to reach high optical intensities while keeping average powers low. This has made possible to probe matter at high intensities with reduced thermal and other cumulative effects.

An example of high intensity phenomena is HHG: since its discovery, it has become a tool for producing coherent light in the extreme ultra-violet (XUV) region (wavelengths of around 10 to 100 nm) as well as for the generation of even shorter pulses, shorter than 100 as (1 as=10^{-18} s), which can be used to probe matter on an unprecedentedly short time-scale.

1.1 Aim and Outline

This thesis is the result of a joint doctoral program between Lund University in Sweden, and Porto University in Portugal. The aim was to study HHG with ultrashort light pulses, towards the generation of isolated attosecond light pulses. The ultrafast optics laboratory at Porto University had the experience with the generation of ultrashort femtosecond light pulses, while Lund had the expertise regarding HHG and attosecond pulses.

The work presented in this thesis has been performed both in Porto and in Lund, and is based on eleven papers (referred to in the text as Papers **I** to **XI**). Most of it was of experimental nature, and it was realized in three different laboratories: the HHG setup based on a 10 Hz high-energy beamline in Lund (∼35 fs, ∼100 mJ), the HHG and attosecond setup based on the 1 kHz beamline, also in Lund (∼30 fs, ∼3 mJ), and the ultrafast optics laboratory in Porto (∼30 fs, ∼1 mJ).

Papers **I** and **II** describe the efforts and results taken to CEP-stabilize and control the kHz laser system in Lund. This is a necessary step to obtain controlled and reproducible ultrashort pulses. Demonstration of CEP stabilization and control was achieved for both the amplifier and after a hollow-core gas-filled compressor. Papers **III** and **IV** deal with pulse characterization in the time domain. This work was motivated by the difficulty of time characterization of the hollow-core fiber compressor in Lund, and was experimentally realized in Porto. A new characterization technique was demonstrated, first on an ultrafast oscillator, and then on a hollow-core gas-filled fiber compressor.

This technique was successfully applied as a part of a complete spatiotemporal characterization method based on spectral interferometry, in Papers **V** and **VI**. This successfully characterized in time and space ultrashort laser pulses.

In Paper **VII**, space and time compression of ultrashort laser pulses is presented. A tradeoff between spatial and temporal compression is achieved, using chirped mirrors and microscope objectives. The results obtained suggest that HHG from low-power, high repetition rate ultrashort lasers might be feasible.

In Paper **VIII**, the spectral and spatial characteristics of one of the HHG sources in Lund (the high-energy 10 Hz beamline) are studied. This same HHG setup was used as a source for single-shot inline holography in the XUV region, which is described in Paper **IX**.

In parallel to the research towards better control of the short laser pulses for HHG and attosecond pulse generation, work has been performed on the applications of the existing attosecond sources. This was done using the kilohertz source in Lund, where properties of simple atomic systems were studied with the same experimental technique (RABBITT) that is used for the characterization of attosecond pulse trains. Phase properties of resonant two-color two-photon ionization in helium were studied in Paper **X**, and attosecond photoemission delays in argon were measured in Paper **XI**.

In Chapter 2 an introduction is presented on the fundamental concepts about ultrashort light pulses, namely generation and propagation. The issues encountered when dealing with ultrashort pulses are discussed. Even if the concepts and techniques are introduced from a “femtosecond” point of view, the mathematical framework applies as well to the attosecond regime. Chapter 3 introduces some basic concepts about the characterization of ultrashort pulses, and some of the most commonly used techniques are presented. Some of the concepts here introduced are also applicable to the attosecond regime. Chapter 4 introduces some of the physical principles behind HHG, discusses the properties of the radiation produced, and presents some applications. Finally, Chapter 5 summarizes the obtained results and conclusions, and an outlook is presented.

Chapter 2

Ultrashort Pulses

2.1 Introduction

The term “ultrashort” is obviously subjective. The ultrashort light pulse “race” took a whole new step with the invention of the laser [1, 5]. Soon after the laser was invented, Q-switch techniques [6] allowed for the production of pulses in the nanosecond (1 ns=10^{-9}s) regime. It was however with the advent of mode-locked lasers [7–11], and especially the titanium-sapphire (Ti:Al_2O_3) laser [12], that pulses in the femtosecond (1 fs=10^{-15}s) regime became routinely possible.

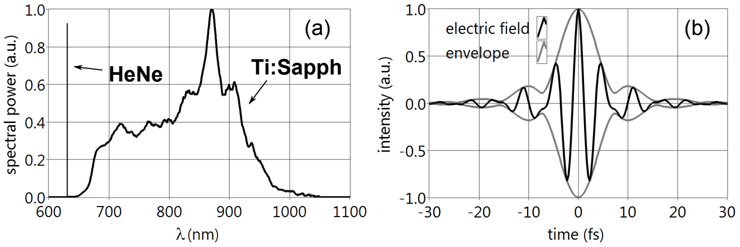

Figure 2.1: Comparison between a typical broadband spectrum from an ultrafast Ti:sapphire laser used during the work presented in this thesis, and a common HeNe laser. The typical HeNe spectral bandwidth is typically of around 0.002 nm. With such a broadband spectrum, the Ti:sapphire laser can produce pulses as the one simulated on the right: its duration is of just a few optical cycles.

The work presented in this thesis deals with ultrashort light pulses, in two different regimes: in the femtosecond and in the attosecond timescales. A common aspect between them is that their durations are comparable to the duration of their carrier cycle. Or, equivalently, their spectral width is comparable to their central frequency. Figure 2.1 shows the spectrum from the ultrafast laser used in Porto, and the shortest pulse that can be obtained from it. The laser in Lund has similar properties, and these are representative of state-of-the-art ultrafast lasers. For a comparison, the spectrum of a HeNe laser is also shown, but not to scale: the actual HeNe spectral width is much shorter than the drawn line. Even broader spectra than the one shown in Fig. 2.1 were obtained with the goal of reaching even shorter pulses.

The broad bandwidth of such sources, which is necessary to obtain such short pulses, poses considerable technical challenges: different spectral components "travel" at different speeds through glasses and other materials, effectively stretching ultrashort pulses in time. The shortest the pulse, the broader its spectrum, and the harder it is to keep the pulse short.

This chapter discusses the issues around ultrashort pulse generation and propagation. Some of the concepts and basic mathematical tools often used on the subject are presented, as well as some practical techniques commonly employed to keep ultrashort pulses, well, ultrashort.

A very good and detailed description of ultrashort laser pulses can be found for example in Diels' and Rudolph's book [13]. The text that follows introduces some of the most important concepts of ultrashort pulses for this thesis, and applies to both the femtosecond and attosecond regimes.

2.2 Description

An ultrashort pulse can be represented either in the time or spectral domain, and these representations are related through the Fourier transform relations

$$\begin{aligned} \tilde{U}(\omega) &= \mathcal{F}\left\{U(t)\right\} = \int U(t)e^{-i\omega t}dt \\ U(t) &= \mathcal{F}^{-1}\left\{\tilde{U}(\omega)\right\} = \frac{1}{2\pi}\int \tilde{U}(\omega)e^{i\omega t}d\omega \end{aligned} \tag{2.1}$$

Since $U(t)$ is a real quantity,

$$\tilde{U}(\omega) = \tilde{U}^*(-\omega). \tag{2.2}$$

One can always represent a real quantity by a sum of two complex quantities, being that one is the complex conjugate of the other. It is rather common (and it will be often the case during this thesis) to omit the complex conjugate. This is valid because there is redundancy in the spectral representation: since one knows that the electric field is a real quantity, half of the complex spectrum contains enough information about the pulse (Fig. 2.2). To find the actual electric field it is simply enough to take the real part of this complex quantity. Further, a pulse can be conveniently described by an envelope multiplied by a monochromatic field (and now $U(t)$ denotes a complex representation)

$$U(t) = |U(t)|e^{i\phi(t)} = A(t)e^{i\omega t} \tag{2.3}$$

so a pulse can be even more simply described by a complex quantity, $A(t)$, whose phase varies (usually) much slower than the carrier frequency. This allows a precise representation of the pulse with a lower numerical effort (a lower resolution is needed to properly sample it, compared to using the full real representation) as long as one keeps in mind there is a carrier frequency associated with it. Figure 2.3 shows an example of taking a sinusoidal carrier and applying an envelope. As the envelope width becomes comparable to, or even shorter than, the carrier period, the envelope itself will have a higher spectral content than the original carrier.

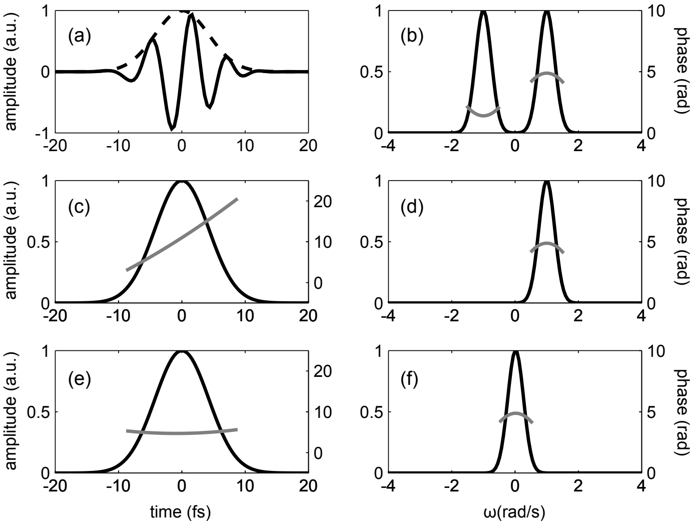

Figure 2.2: Real and complex representations, in the time and frequency domains, of an ultrashort pulse. (a) An oscillating field has its amplitude modulated by an envelope (dashed line). (b) The corresponding spectral representation has two lobes, with opposite phases. (c) By keeping only the positive frequencies in (d), and Fourier transforming back to the time domain, we get a complex representation of the pulse in time. The envelope in (c) is the same as in (a), and the underlying electric field can be recovered by taking the real part of the complex field. (e) The phase variation can be minimized by a spectral shift (f).

The intensity is usually defined as [1]

$$I(t) = \frac{cn\epsilon_0}{2}|U(t)|^2 \tag{2.4}$$

This definition is commonly used even in the context of ultrashort laser pulses: the actual energy flow from an electromagnetic wave follows the *field* and not the (slower) envelope; however, the definition above is commonly used in the literature.

Similarly, the spectral representation can also be decomposed as a spectral envelope and a phase

$$\tilde{U}(\omega) = |\tilde{U}(\omega)|e^{i\phi(\omega)} \tag{2.5}$$

The spectral representation is rather useful when dealing with linear optics: most propagation effects are easily described in the spectral domain. The electric field as a function of time can easily be obtained by Fourier transforming the complex spectrum (Eq. 2.1).

---

[1] Even if against S.I. standards, the word *intensity* will be used to represent power per area unit, i.e., W/cm^2 .

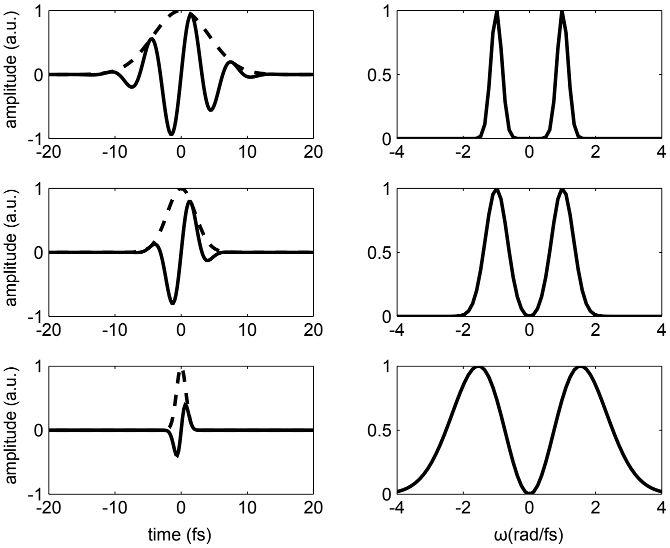

Figure 2.3: Effect of applying an envelope to a sinusoidal carrier. As the envelope time width decreases, the spectral width increases. As the envelope becomes so short as not to fit a single cycle of the original carrier, its own spectral content dominates and not only the spectral width, but also the effective carrier frequency, increase.

2.2.1 Spectral phase

It is common to express the spectral phase as a Taylor series. So, taking a (somewhat arbitrary) central frequency ω_0

$$\phi(\omega) = \phi_0 + \phi_0'(\omega - \omega_0) + \frac{1}{2!}\phi_0''(\omega - \omega_0)^2 + \frac{1}{3!}\phi_0'''(\omega - \omega_0)^3 + \cdots \tag{2.6}$$

where

$$\phi_0 = \phi(\omega_0), \phi_0' = \left.\frac{\partial\phi(\omega)}{\partial\omega}\right|_{\omega=\omega_0}, \phi_0'' = \left.\frac{\partial^2\phi(\omega)}{\partial\omega^2}\right|_{\omega=\omega_0}, \phi_0''' = \left.\frac{\partial^3\phi(\omega)}{\partial\omega^3}\right|_{\omega=\omega_0} \tag{2.7}$$

etc. The first term, ϕ_0 is the absolute phase. In most situations it is (or was) discarded: historically, when the shortest pulses available were still very long compared to the electric field cycle duration, this phase was usually meaningless. With the advent of few-cycle pulses, and highly nonlinear effects, this phase can be extremely important (see Chapter 4 and Section 3.9).

The second term, ϕ_0', is the *group delay.* The effect of applying a linear phase in the spectral domain is a *translation* in time. So, if one has a given spectrum $\tilde{U}(\omega)$, corresponding to a pulse in time $U(t)$, applying a linear phase term $\exp(i\omega\tau)$ shifts the pulse in time

$$\begin{aligned} \tilde{U}(\omega) &\to U(t) \\ \tilde{U}(\omega)e^{i\omega\tau} &\to U(t-\tau) \end{aligned} \tag{2.8}$$

This term is also often ignored, since usually an external reference is not available, and therefore the pulse arrival time is not important.

The quadratic term of the expansion is the first that leads to a deformation of the pulse envelope. It is usually called *group delay dispersion* (GDD). If a spectral phase is quadratic the pulse has "pure" GDD. Figure 2.4 shows some examples of how GDD and higher order phase terms affect the temporal shape of a pulse.

The phase introduced by glasses and other linear elements is usually well described by a few terms of the Taylor expansion of the spectral phase (see Fig. 2.6), so it is often very convenient to use the above defined terms.

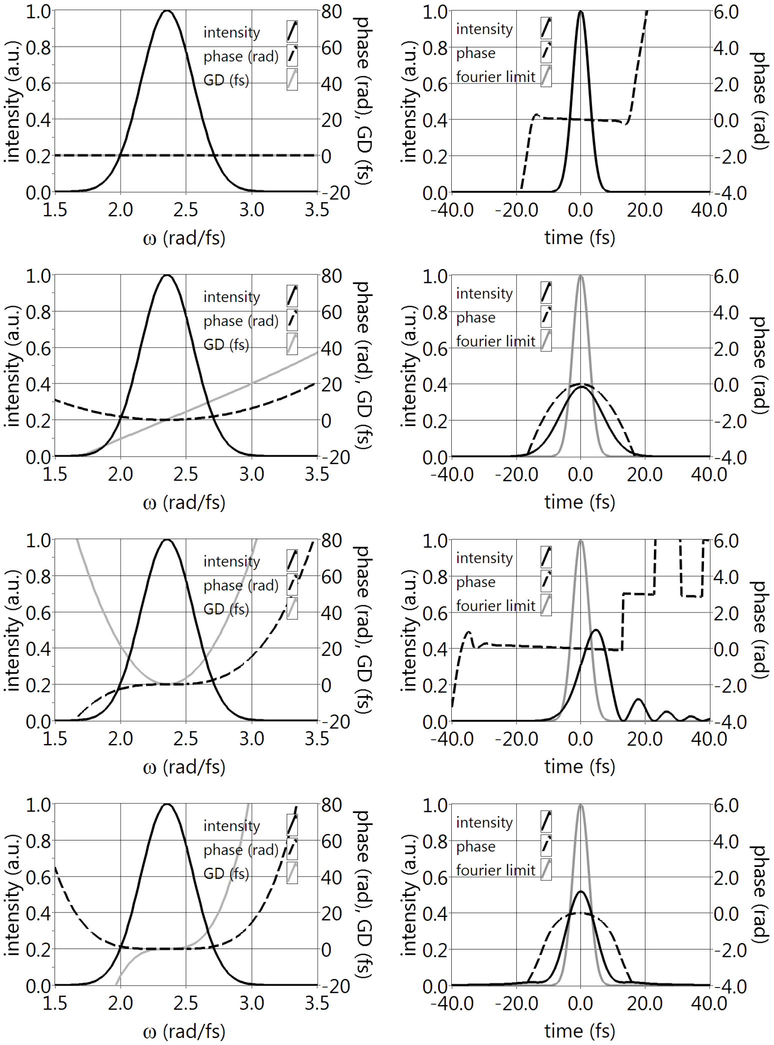

Figure 2.4: Effect of applying different phases in the spectral domain. A flat phase gives the shortest possible pulse (top row). Quadratic and higher order phase terms distort the pulse's shape and its instantaneous frequency as a function of time.

2.2.2 Wavelength/Frequency Representation

From a numerical point of view, a frequency representation is more advantageous, since it is easy to go from the time domain to a spectral representation via Fourier transform. However, it is more common to have a spectrum represented as a function of wavelength. Even if the conversion is straightforward, there are some issues that should be taken into account, especially for broadband spectra.

Consider a spectrum measured in the laboratory. Virtually all spectrometers give as output a curve (that we will denote by $S_\lambda(\lambda)$), which is a function of wavelength.

$$S_\lambda(\lambda) = \left.\frac{dE}{d\lambda}\right|_\lambda . \tag{2.9}$$

For a single pulse (or for a defined integration time), this is the spectral energy density. To convert it to a frequency representation one has to take into account that this is an energy distribution. The function we want is

$$S_\omega(\omega) = \left.\frac{dE}{d\omega}\right|_\omega , \tag{2.10}$$

and it relates to the measured spectrum as

$$\frac{dE}{d\omega} = \frac{dE}{d\lambda}\left|\frac{d\lambda}{d\omega}\right| . \tag{2.11}$$

A conversion between the two representations is given by

$$S_\omega(\omega) = S_\lambda(\lambda)\left|\frac{d\lambda}{d\omega}\right| = S_\lambda(\lambda)\frac{2\pi c}{\omega^2} = S_\lambda(\lambda)\frac{\lambda^2}{2\pi c} . \tag{2.12}$$

This is in contrast with, say, converting phase between different representations. If the phase curve $\phi(\lambda)$ is known, then the phase as a function of frequency is obtained by just evaluating $\phi(\lambda)$ at the corresponding frequency

$$\phi(\omega) = \phi(\lambda)|_{\lambda=\frac{2\pi c}{\omega}} . \tag{2.13}$$

2.3 Dispersion

2.3.1 Propagation in Dispersive Media

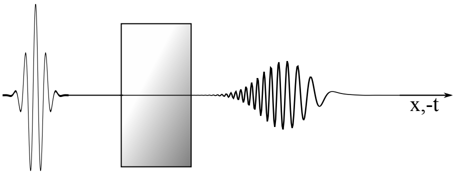

Figure 2.5: As an ultrashort pulse goes through a piece of glass, it is stretched in time, and the instantaneous frequency varies in time. Usually, the longer wavelengths will travel faster.

Special considerations have to be taken into account when dealing with an ultrashort pulse, due to its broad bandwidth. In general, during propagation in a material, the carrier and the envelope do not travel at the same speed, and different frequencies (or wavelengths) have different phase velocities. This leads to a reshaping in time of the electric field of the pulse. As seen before, two quantities are usually introduced, the group delay (GD) and the group-delay dispersion (GDD). These can be expressed not only as a value referring to a central frequency, but also as a function of frequency. This is often needed when a phase is not conveniently described by a few terms of the Taylor expansion of the phase. The new quantities are then

$$GD(\omega) = \frac{d\phi(\omega)}{d\omega} \tag{2.14}$$

and the group delay dispersion (GDD)

$$GDD(\omega) = \frac{d^2\phi(\omega)}{d\omega^2} \tag{2.15}$$

other higher order phase terms can be described similarly, i.e., third-order dispersion (TOD), fourth-order dispersion, etc

$$TOD(\omega) = \frac{d^3\phi(\omega)}{d\omega^3} \tag{2.16}$$

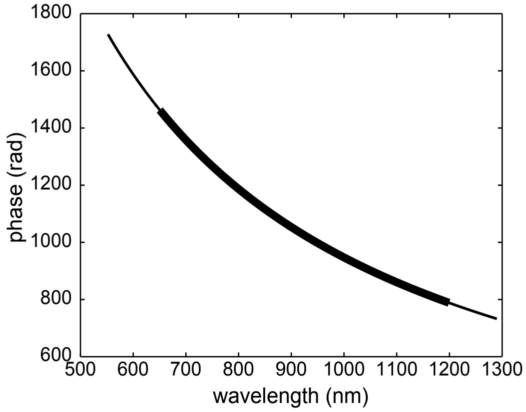

Figure 2.6: Comparison between the phase introduced by 1 mm of BK7 glass calculated from Sellmeier formulas (thin line) and a fit (thick line) using an expansion up to third-order dispersion (TOD). Even for such a broad bandwidth, specifying GDD and TOD is enough for a very accurate phase representation.

The most common situation of propagation in dispersive media one encounters in practical situations is simply that of glasses and/or gases (i.e., air). For transparent media, the propagation can be easily described as a spectral phase filter. Consider a transparent medium with a wavelength-dependent refractive index $n(\omega)$. The phase acquired as function of frequency, after propagating through a thickness L is

$$\phi(\omega) = k(\omega)L = \frac{\omega}{c}n(\omega)L \tag{2.17}$$

so, given a pulse with a spectrum $\tilde{U}(\omega)$, after propagation the spectrum will be

$$\tilde{U}'(\omega) = \tilde{U}(\omega)\exp\left\{i\frac{\omega}{c}n(\omega)L\right\}. \tag{2.18}$$

Convenient ways of fitting refraction index curves to measured data are the use of Sellmeier equations, which take the form

$$n^2(\lambda) = 1 + \frac{B_1\lambda^2}{\lambda^2 - C_1} + \frac{B_2\lambda^2}{\lambda^2 - C_2} + \cdots, \tag{2.19}$$

or, a little less common, the Cauchy equation

$$n(\lambda) = A + \frac{B}{\lambda^2} + \frac{C}{\lambda^4} + \cdots \tag{2.20}$$

An extensive list of Sellmeier formulas for many glasses and crystals can be found in Ref. [14], and Sellmeier formulas have been adapted to gases, with pressure and temperature dependence included, as shown in Ref. [15]. The effects of linear propagation in glasses in this thesis were simulated from these formulas (Papers **III**, **IV**, and **V**).

2.3.2 Dispersion Compensation

An obvious solution to compensate for the pulse stretching due to dispersion would be to use a glass whose dispersion would lead to the contrary effect, that is, where longer wavelengths would travel slower than shorter ones. Unfortunately, such materials are not available in the near infra-red (NIR) region where Ti-Sapphire lasers usually operate, so other methods have been employed.

Gratings and Prisms Compressors

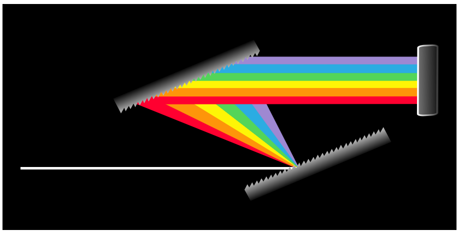

Figure 2.7: Grating compressor. The different wavelengths are dispersed in space and made to travel different paths. A double pass setup allows the spatial recombination of the different frequency components.

The first technique designed to introduce negative dispersion used reflection gratings [16] to spatially separate different spectral components, make them travel different lengths, and recombine them later. This technique led to compression of pulses down to 30 fs [17] and is still extensively used due to the high amount of negative dispersion obtainable this way.

Positive dispersion can be obtained by introducing a -1 magnification telescope between gratings [18]. This is extensively used in chirped pulse amplification (CPA) chains since often the material dispersion alone is not enough to stretch the pulses enough to prevent damage (see Section 2.4.2). A common solution is to use an all-reflective system, like an Öffner triplet [19].

In a similar way to gratings, prisms can also be used [20] (Fig. 2.8). The advantage is that the losses are usually much lower (especially if they can be used at Brewster's angle), at the expense of reduced compactness. Prisms are almost always less diffractive than gratings, so that larger distances between prisms are needed to provide enough spatial separation between the different spectral components. Furthermore, because the light has to traverse glass, there is intrinsic material dispersion that limits the amount of total negative dispersion achievable [21]. Several schemes exist that are more suited for amplifiers [21, 22] and combinations of prisms and gratings are also commonly used (and even *grisms*, prisms where one of the surfaces is a grating [23]).

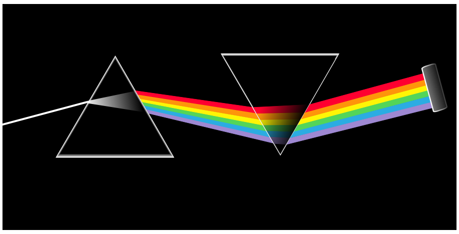

Figure 2.8: Prisms compressor. The different wavelengths are dispersed in space and made to travel different paths. A double pass setup allows the spatial recombination of the different frequency components (adapted from [24]).

It is interesting to note that refraction *always* leads to dispersion [25]. While this effect is often negligible, it might not be the case for extremely broadband pulses.

Chirped mirrors

More recently, dielectric mirrors have been specifically designed in such a way that the reflection phase compensates for material dispersion [26]. By varying the layers thicknesses, different wavelengths penetrate different depths into the multilayer structure (Fig. 2.9). The advantage of such approach is that a mirror can be specifically designed to have a phase curve that matches a given target, e.g., a glass (Fig. 2.10), and the reflectivity is usually very high (typically over 99%). While the analysis of the phase introduced by a multilayer stack (both in amplitude and phase) is reasonably straightforward (see e.g. [27, 28]), the reverse engineering problem, i.e., to design the multilayer stack for getting a certain phase at reflection, is not [29, 30]. A lot of research is currently performed on the design of chirped mirrors.

Double-chirped mirrors employ an anti-reflection coating and an extra layer structure [27, 31] that act as an impedance matching from air to the chirped structure itself. This type of mirrors was used in Papers **III**, **IV**, **V**, **VI** and **VII** to compress ultrashort pulses.

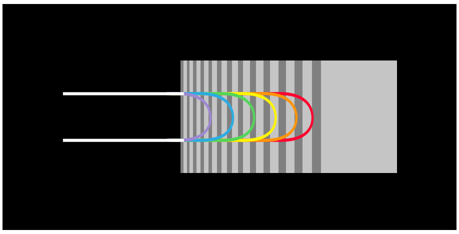

Figure 2.9: Simplified schematic of a chirped mirror. By varying the layers' thicknesses, different wavelengths penetrate different depths into the multilayer stack. An anti-reflection coating (not shown) is used between the air-chirped structure interface to minimize impedance mismatch.

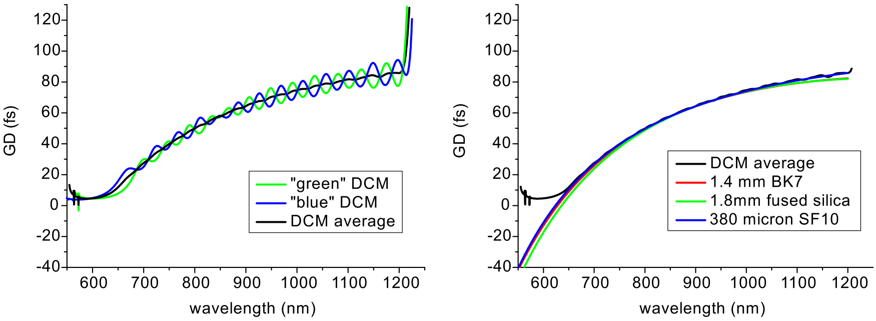

Figure 2.10: Dispersion curves for the double chirped mirrors (DCM) used in Paper **VII**. The mirrors are fabricated in matched pairs (here named "green" and "blue") in such way that the phase ringing is minimized when used together. The chirped mirrors were designed for intra-cavity dispersion compensation of a Ti:Sapphire oscillator, but other materials are still well compensated. The glasses' curves are inverted to facilitate visualization.

Pulse Shapers

A pulse shaper is a device that allows for arbitrary spectral phase manipulation. The most common approach consists in separating different optical frequencies in space, and applying some spatial filter in order to shape the different spectral components [32–34]. Figure 2.11 shows the basic principle of such device: the grating separates the different wavelengths to different directions, and a lens focuses each of these frequency components to some element which is capable of manipulating either the phase or amplitude (for example, a spatial-light modulator). A symmetric arrangement recombines the pulse. There are many variants for such devices, using different dispersion methods (e.g., prisms instead of gratings), focussing elements (e.g., mirrors instead of lenses) and modulators (e.g., acousto-optic modulators instead of spatial-light modulators) [35–37].

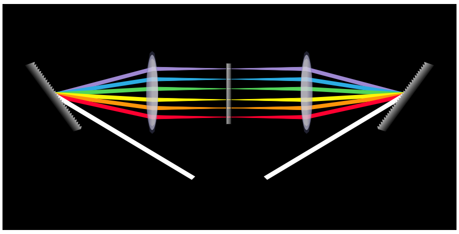

Figure 2.11: Working principle of a pulse shaper. The incoming beam is dispersed on a grating (left) and separated in its different spectral components. An imaging optical element (in this case, a lens) focuses each spectral component in space. Active (e.g. spatial light modulators) or passive (e.g. wedges) elements are used to modulate the spectral amplitude and/or phase. The different spectral components are then recombined.

A different kind of pulse shaper was extensively used in the experiments carried out in Lund. It is based on an Acousto-Optic Programmable Dispersive Filter (AOPDF) [38], usually named DAZZLER (commercial name). An acoustic wave co-propagates with a given pulse, and the acoustic wave's phase can be "imprinted" to the optical field. This is accomplished by controlling the coupling between two crystal axes (see Fig. 2.12).

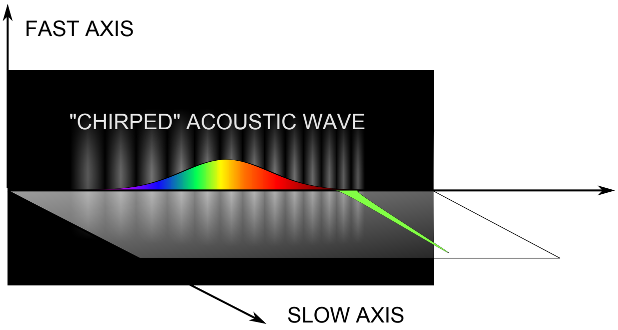

Figure 2.12: Principle of an Acousto-Optic Programmable Dispersive Filter (AOPDF). An acoustic wave is sent to the optical crystal, creating a refraction index grating. As the light is much faster than the sound, the incoming pulse "sees" a stationary grating. This couples the light from one crystal axis to the other. Since the two crystal axes have different propagation speeds, different frequency components can be made to have an effective transit time shorter or longer, depending on the shape of the acoustic wave.

This approach has the advantage of a collinear arrangement, which makes alignment easy, and the whole system is very compact.

2.4 Generation

2.4.1 Mode-locked Lasers

The generation of ultrashort pulses is usually done using *mode-locked* lasers. The main idea behind it is to have laser emission on as many cavity modes as possible: if their phases are synchronized, this leads to a pulse buildup in the time domain. State-of-the-art lasers deliver pulses with a duration very close to a single cycle [39–42].

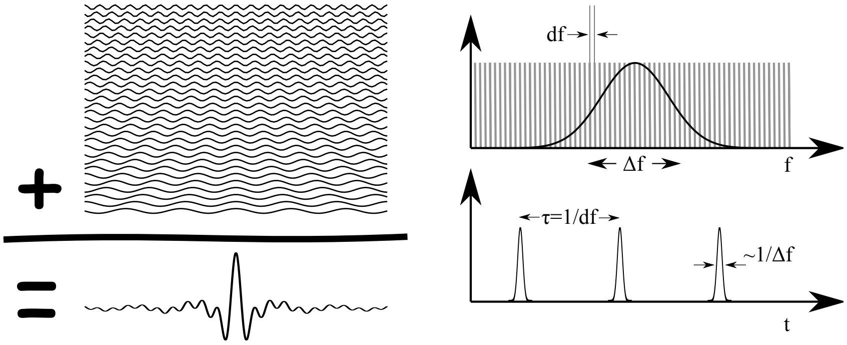

Figure 2.13: Coherent addition of 30 consecutive modes of a cavity (left), leading to the creation of a pulse. The cavity frequency spacing, determined by the cavity length, determines the distance in time between consecutive pulses. The gain bandwidth determines the shortest duration obtainable for the pulses.

The basic difference between a “common” laser and a mode-locked laser is that in the former the operation is mostly monochromatic whereas in the latter a large bandwidth is desired.

Moulton [12] first studied Titanium-doped Sapphire as a laser medium, and its broad gain bandwidth makes it the material of choice for current state-of-the-art ultrashort laser systems. Other characteristics, such as a good thermal conductivity, high quantum efficiency, and mechanical strength make Ti:sapphire the most used gain medium for ultrashort lasers.

While a broad gain bandwidth is necessary to produce short pulses, it is not enough. Even if a gain medium has a large gain bandwidth, typically a laser based on such medium will not emit on a large bandwidth, but only on a narrow one: mode competition will usually lead to single frequency operation for the mode with the highest gain. Besides, the phase between different spectral components needs to be synchronized to achieve short pulses. Some mechanism to induce a broad bandwidth operation, as well as modelocking, is necessary.

Most modern ultrashort lasers based on Ti:sapphire work on the Kerr-lens modelocking (KLM) method: the basic idea is to make the laser cavity more stable when higher intensities are present, to favor mode-locked operation compared to CW operation. This can be achieved by carefully designing the laser cavity.

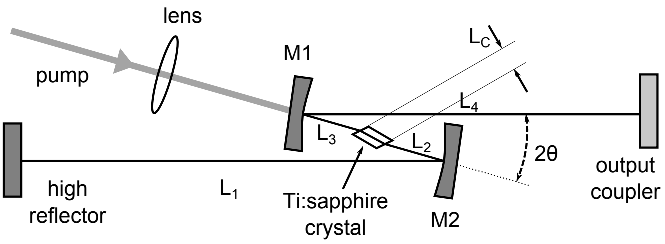

Figure 2.14: Schematic of an ultrafast oscillator. Typical configurations are *Z-shaped* (as shown) or *X-shaped* (when the curved mirrors are oriented such that the beam crosses). Real oscillators will include dispersion management components (not shown) such as glass wedges, chirped mirrors and/or prisms (adapted from [43]).

Cavity Stability

Many textbooks on lasers have detailed analysis about cavity stability (e.g. [44–46]) using the ABCD matrix formalism for Gaussian beams. Here, we will mainly take a closer look at specific details concerning ultrashort pulse mode-locked lasers. A good analysis of ultrashort-specific issues can be found in [47].

To avoid losses, the gain medium is often used at Brewster's angle. This introduces an asymmetry between the tangential and sagittal planes, leading to an astigmatic cavity. This can be compensated for by using off-axis focusing mirrors [48]. Off-axis optical elements can also be represented using an ABCD matrix formalism [49], but now the sagittal and tangential planes have to be considered separately.

A typical design criteria for KLM oscillators is to somehow favor the mode-locking operation compared to the CW operation. This can be done by designing the cavity to be more stable for the ML mode, to have a higher gain on the ML mode, or both.

The cavity stability can be studied by considering the round-trip propagation: if the cavity is stable, the beam will not diverge as the number of round-trips grows. This can be expressed as [44, 46]

$$-1 < S' < 1 \tag{2.21}$$

$$S' = \frac{A+D}{2}. \tag{2.22}$$

Defining

$$S = 1 - S'^2, \tag{2.23}$$

the stability condition can be written as

$$S > 0. \tag{2.24}$$

For a given cavity, the beam characteristics of the fundamental Gaussian mode can be determined by noting that, after a round-trip, the beam becomes the same. It follows from this that the wavefronts at both the back-mirror and the output coupler are flat ($R = \infty$). These conditions fully determine the cavity modes, and it is then straightforward to calculate the beam size and curvature at any given point inside the cavity.

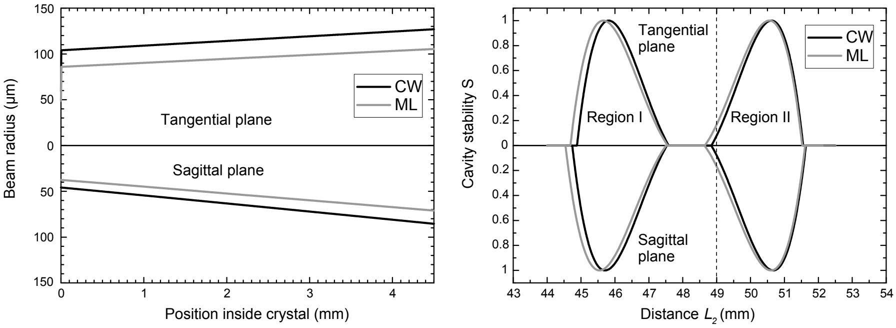

Figure 2.15: Mode size inside the crystal (left) and cavity stability as a function of distance L_2 (adapted from [43]).

Mode-locked operation can be simulated by introducing a *lens* in the gain medium. This is a simple way to take into account Kerr lensing which will occur if there is enough intensity in the crystal. It is then possible to design a cavity that will privilege mode-locking operation compared to CW operation. This can be achieved by choosing the cavity parameters in such a way that cavity is more stable for ML operation (Fig. 2.15), and the pump laser's mode can be optimized to match the ML mode better than the CW mode (Fig. 2.15). This is usually called *soft aperturing*, in contrast to actually using a (real) *hard aperture* to introduce losses on the CW mode.

2.4.2 Chirped-Pulse Amplification

Chirped-Pulse Amplification (CPA) was first introduced by Strickland and coworkers [50] and became a standard tool for high-energy, short pulse production.

Optical amplification of ultrashort pulses is problematic due to the high instantaneous intensities achieved. The solution around this consists in *chirping* the pulse (thus making it longer in time), amplifying it, and later compressing it (Fig. 2.16).[2] This avoids the high intensities in the gain medium, while allowing energy transfer to the pulse. Afterwards, the pulse can be spatially expanded and temporally compressed, keeping the intensity at safe levels. Chirped pulse amplifiers were extensively used both in Porto and in Lund, each having different characteristics (see Section 2.6).

2.4.3 Spectral Broadening in a Hollow-Core Fiber

Spectral broadening and posterior pulse compression with a hollow-core gas-filled fiber was first introduced by Nisoli [53] and has become a workhorse for the generation of high-energy, ultra-short pulses [54–58]. Nonlinear propagation of pulses leads to

---

[2] A different scheme that consists in splitting the pulse in many replicas and later recombining them [51, 52] has also been used, but is not very popular, as it is not suited for pulses in the femtosecond regime.

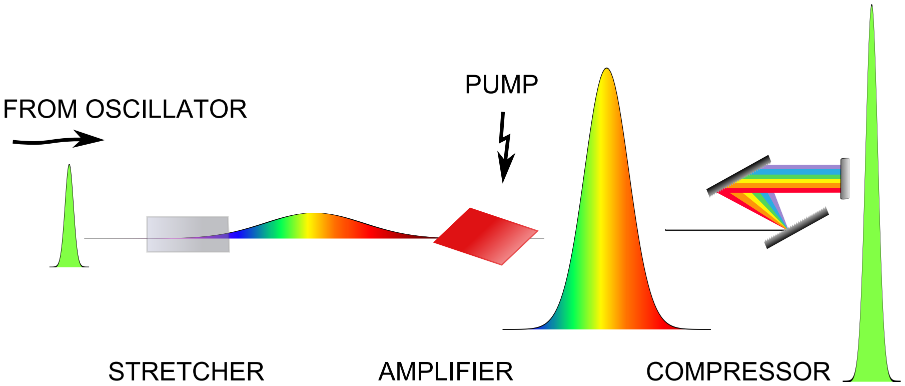
FROM OSCILLATOR
PUMP
STRETCHER
AMPLIFIER
COMPRESSOR

Figure 2.16: Schematic of a CPA chain. A dispersive element is used to make the pulse longer (sometimes, as shown, a glass element, or some other dispersive element, as a grating stretcher), typically to durations of a few picoseconds to hundreds of picoseconds. The pulse can then be safely amplified while keeping instantaneous intensities below damage threshold. After amplification, the pulse generally has a smaller bandwidth due to gain-narrowing in the amplification process. Negative dispersion is then introduced to compress the pulse in time, typically to approximately 30 fs.

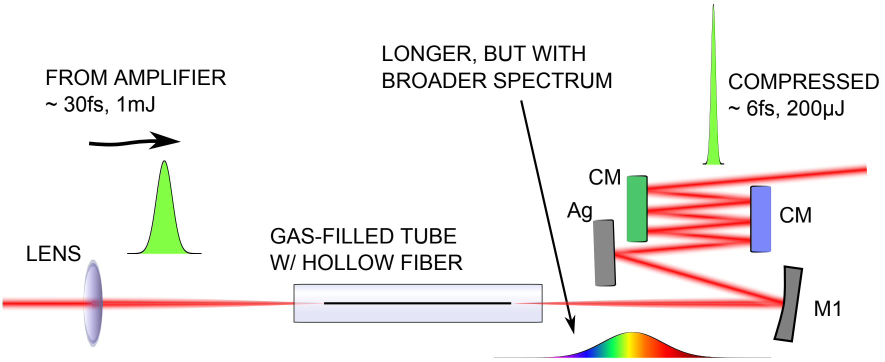
FROM AMPLIFIER
~ 30fs, 1mJ
LONGER, BUT WITH
BROADER SPECTRUM
COMPRESSED
~ 6fs, 200µJ
CM
Ag
CM
LENS
GAS-FILLED TUBE
W/ HOLLOW FIBER
M1

Figure 2.17: Simplified schematic of a hollow-core fiber compressor. The pulse is contained inside the hollow fibre, allowing for a larger interaction distance. Nonlinear effects lead to spectral broadening, and, together with the gas dispersion, to a *chirping* of the pulse. Chirped mirrors are used to flatten the spectral phase and produce shorter pulses.

spectral broadening, which in turn allows one to create shorter pulses, since more spectral content is now available.

Contrary to normal waveguides, where the light is in principle completely confined, in a hollow-core fiber the transmission is intrinsically lossy. This happens because, while in a typical fiber (like the ones used for communications) the refractive index is higher in the center, the opposite occurs in a hollow-core fiber (which is usually filled with a gas). Still, solutions exist with acceptable losses for small propagation distances, which are of interest since it allows one to maintain the propagation of a relatively small sized mode for a longer distance than would be possible in free-space, due to diffraction. Keeping a small mode size is necessary to induce nonlinear effects.

The mode of interest is the EH_{11} [59] which is fortunately also the easiest to couple into. A typical CPA-based system produces a beam with a spatial mode which can usually be approximated by a Gaussian beam. It is then useful to study the best coupling between a Gaussian beam and the EH_{11} mode of a hollow-fiber. For a fiber with a radius a, and in the approximation $a \gg \lambda$, the intensity profile of such mode is [59]

$$I_{EH_{11}}(r) = I_0 J_0^2 \left(\frac{2.405r}{a} \right), r < a, \tag{2.25}$$

where J_0 is the zeroth-order Bessel function of the first kind. We want to couple a Gaussian beam into it:

$$I_{Gauss}(r) = I_0 \exp \left(-\frac{2r^2}{w_0^2} \right). \tag{2.26}$$

The maximum coupling between modes can be found by maximizing

$$\eta = \int_0^\infty U_{EH_{11}}(r) \cdot U_{Gauss}(r) dr, \tag{2.27}$$

where $U_{EH_{11}}(r)$ and $U_{Gauss}(r)$ are the corresponding modes' amplitudes, and both fields have been normalized to unity energy. The best matching is obtained for $w_0 \simeq 0.65a$, giving an efficiency of $\sim 98\%$ (see Fig. 2.18).

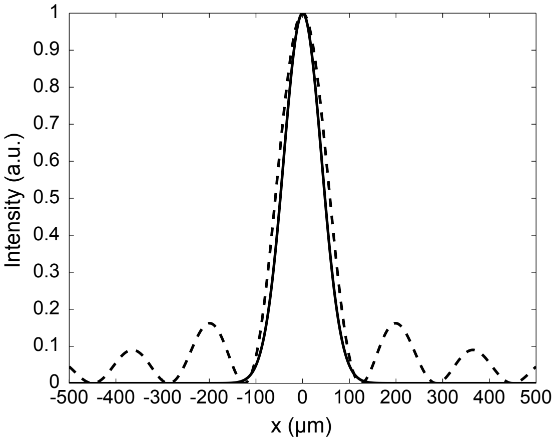

Figure 2.18: Comparison between the EH_{11} mode of a hollow fiber and the best-matching Gaussian. The dashed line is a zeroth order Bessel function of the first kind, which is the EH_{11} mode in the central lobe.

To couple the laser beam into the fiber a lens or a focusing mirror is used. For Gaussian beam propagation the spot size w_0 at the focus is related to the beam radius before focusing w_L by

$$w_0 = \frac{\lambda f}{\pi w_L}, \tag{2.28}$$

so we can easily find which focusing distance should be used

$$f = \frac{0.65\pi a w_L}{\lambda}. \tag{2.29}$$

The dynamics of spectral broadening in hollow-core fibers are very complex, and the output of such systems is very sensitive to the input parameters. The main broadening mechanism is usually self-phase modulation (SPM) due to Kerr effect, but other effects must be taken into account, such as plasma effects from the gas ionization and the linear dispersion.

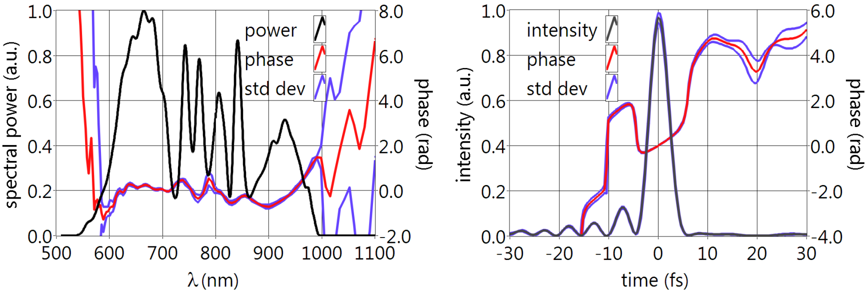

Figure 2.19: Example of a spectrum obtained by broadening in a hollow-core fiber (from Paper **VI**). The spectral phase and the time-domain reconstruction were obtained using the *d-scan* technique (Papers **III** and **IV**). The pulse duration is 4.5 fs FWHM.

Hollow-fiber setups were built in Porto and in Lund. Figure 2.19 shows some experimental results obtained with the Porto setup. Due to the strong nonlinearities inherent to the spectral broadening process, the spectral phase from such pulses usually exhibit strong and fast phase variations. This, together with the broad bandwidth, makes the characterization of pulses from hollow-core fibers challenging, and was the main reason for the development of the "*d-scan*" technique (see Section 3.8 and Papers **III** and **IV**).

Different ways of spectral broadening are often used, like filamentation [60], where no hollow fiber is used to guide the light, but instead the nonlinear Kerr lensing and diffraction compensate each other to keep a small mode. All these techniques are hard to scale for higher energies while keeping a compact setup. Alternatives exist, such as broadening with planar waveguides [61, 62].

2.5 Second harmonic generation

In this section we will take a closer look at second harmonic generation (SHG) for the special case of ultrashort laser pulses. In most nonlinear optics books the SHG signal is derived for the specific case of a monochromatic wave, or, in some cases, for the sum of a few monochromatic waves. For the case of SHG a typical expression would be

$$I(2\omega, L) = \frac{2\omega^2 d_{eff}^2 L^2}{n_{2\omega} n_\omega^2 c^3 \epsilon_0} \left(\frac{\sin(\Delta k L/2)}{\Delta k L/2} \right)^2 I(\omega)^2, \tag{2.30}$$

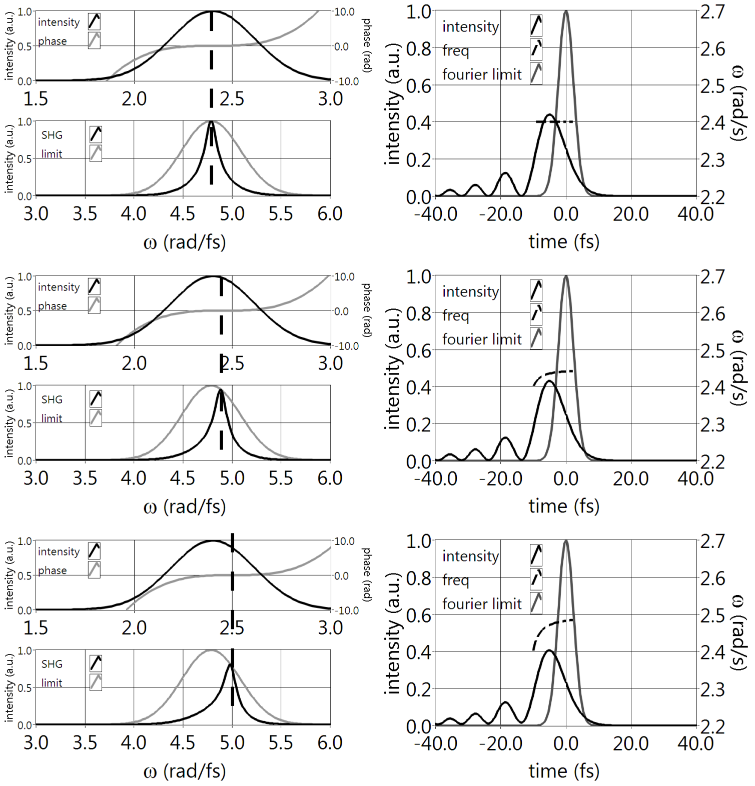

Figure 2.20: Second harmonic generation spectra for different dispersion curves. Left column shows the fundamental spectra and corresponding SHG spectra (notice the doubled frequency axis on the SHG spectra) and the right column shows the pulse in the time domain. As the phase inflection point is shifted to higher frequencies (left column, top plots), the main pulse instantaneous frequency increases (left column) leading to a peak SHG signal at the corresponding doubled frequencies (left column, bottom plots).

where L is the medium (SHG crystal) length, d_{eff} is the effective nonlinear susceptibility for the considered wavelengths, and $\Delta k = k(2\omega) - 2k(\omega)$ is the phase mismatch.

Since this is not a linear process, to find the response from a polychromatic pulse we cannot simply decompose the input in monochromatic waves (i.e. Fourier transform it), calculate the signal as a function of frequency and add it all up together. Instead, we would have to go back to the nonlinear coupled equation. Fortunately, there is a simple model that gives very good results, with the condition that the conversion efficiency is low, and it is very commonly used in the context of ultrashort pulse characterization. It consists in simply taking the pulse *in time*, squaring it, and taking the Fourier transform again to find the spectral amplitude:

$$\tilde{U}(\omega) \xrightarrow{\mathcal{F}\{\}} U(t) \xrightarrow{\wedge 2} U(t)^2 \xrightarrow{\mathcal{F}\{\}^{-1}} \tilde{U}_{SHG}(\omega) \tag{2.31}$$

so

$$\begin{aligned} S_{ideal}(\omega) &= \left|\tilde{U}_{SHG}(\omega)\right|^2 && (2.32)\\ &= \left|\int\left(\int\tilde{U}(\Omega)\exp(i\Omega t)d\Omega\right)^2\exp(-i\omega t)dt\right|^2 && (2.33)\\ &= \left|\int\tilde{U}(\Omega)\tilde{U}(\omega-\Omega)d\Omega\right|^2. && (2.34)\end{aligned}$$

Deviations from this simple model to more complex models can be taken into account by adding a spectral filter $R(\omega)$ to the measured SHG spectrum [13, 63]

$$S_{meas}(\omega) = S_{ideal}(\omega)\cdot R(\omega). \tag{2.35}$$

This is a good approximation even near the single-cycle regime, and for non-collinear SHG geometries [63, 64]. This model is assumed correct for many characterization methods (like autocorrelations and FROG, see Chapter 3), but care must be taken to ensure that it is legitimate to do so, in particular including the nonlinearity bandwidth.

This simple model can give some insight into how the SHG spectrum shape looks like for different kinds of spectral phases. Figure 2.20 shows some examples of typical spectral phases and corresponding time profiles and SHG spectra: a rule of thumb is that, when the phase has an inflection point at a given frequency ω_0 (which means that $GDD(\omega_0) = 0$), then the neighboring frequencies will constructively interfere in time. This leads to a main pulse whose frequency content mostly originates from that spectral region (Fig. 2.20, right column). Since the SHG process is nonlinear, the conversion efficiency from this main pulse will dominate, and the SHG spectrum will have a higher content from this main pulse, with the corresponding frequency of $2\omega_0$.

This analysis is the basis for determining the phase of a pulse using the MIIPS technique (see Section 3.7) and the *d-scan* technique in Papers **III** and **IV**.

2.6 Experimental Laser Setups

Three laser setups were mainly used during the work performed for this thesis: two CPA laser systems in Lund and one in Porto.

One of them is part of the Lund Laser Center high power facility, and the low-energy part (around 100 mJ, 35 fs, 10 Hz repetition rate) of this beam was available for the HHG source described in Papers **VIII** and used in Paper **IX**. This laser system was used purely as a tool, and no work on the laser itself was performed during the work presented on this thesis.

The other two systems were lower energy, and active work was carried out on optimizing them.

Both are based on similar CEP-stabilized ultrafast oscillators (FemtoLasers Rainbow). It is a chirped-mirror based Kerr-lens modelocking system, which can deliver a spectrum with a bandwidth around 800 nm, supporting 6 fs pulses. The repetition rate is of about 80 MHz and the energy per pulse is of about 2 nJ. Both systems are schematically depicted on Fig. 2.21.

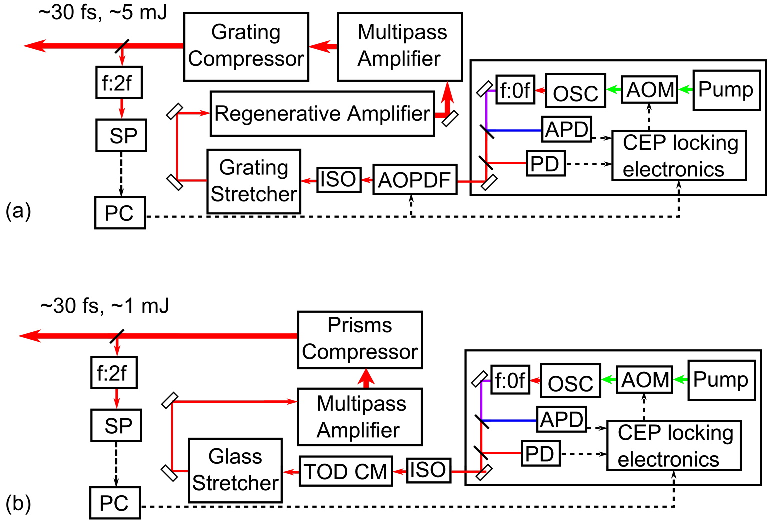
~30 fs, ~5 mJ
Grating Compressor
Multipass Amplifier
f:2f
SP
PC
Regenerative Amplifier
Grating Stretcher
ISO
AOPDF
f:0f
OSC
AOM
Pump
APD
PD
CEP locking electronics
(a)
~30 fs, ~1 mJ
Prisms Compressor
Multipass Amplifier
Glass Stretcher
TOD CM
ISO
f:2f
SP
PC
f:0f
OSC
AOM
Pump
APD
PD
CEP locking electronics
(b)

Figure 2.21: Schematic representation of the laser system in (a) Lund and (b) Porto. A detailed description is given in the text. OSC - oscillator; AOM - acousto-optic modulator; APD - avalanche photodiode; PD - photodiode; AOPDF - acousto-optic programmable dispersion filter; ISO - optical isolator (Faraday rotator); TOD CM - third-order dispersion chirped mirrors; SP - spectrometer; PC - personal computer.

2.6.1 Laser System in Lund

The Lund CPA chain has two amplification stages: the first one is a *regenerative* amplifier and the second one is a *multipass* amplifier. Before the first amplifier the pulses are sent through an AOPDF (Fastlite Dazzler), which allows to fine-tune the compression (since dispersion is linear, higher-order dispersion terms can be pre-compensated) and also allows for spectral shaping. A Faraday rotator is used as an isolator to prevent unwanted reflections or leakages from the high power pulses to couple into the oscillator. A grating stretcher, based on an Õffner triplet is used to stretch the pulses to a duration of around 200 ps. In the regenerative amplifier, the pulses are amplified to an energy of about 0.4 mJ after around 12 passes, and the repetition rate is reduced to 1 kHz.

The second amplification stage uses a multipass (five passes) bow-tie configuration, without focusing. The amplifying crystal is kept in vacuum, and it is cryogenically cooled to -80º C. At this stage the beam has a diameter of about 1 mm. Depending on the desired output power, it can be pumped by one or two Q-switched Nd:Ylf lasers, with 30 W and 20 W of average power. At maximum power, up to 10 W can be extracted, corresponding to 10 mJ per pulse. This pulse is then spatially expanded to a diameter of about 2 cm, and compressed with a grating compressor. Most of the experiments were done using pulses energy lower than the maximum. A typical used value was of 3 mJ per pulse.

Papers **I** and **II** describe this system in detail, as well as the work carried out on its CEP stabilization, and it was the source for the HHG and attosecond setup used in Papers **X** and **XI**.

2.6.2 Laser System in Porto

The other used laser system is a commercially available amplifier (Femtolasers FemtoPower Compact PRO CEP), which includes the above-mentioned ultrafast oscillator. The pulses are also sent through a Faraday rotator for optical isolation, and through a glass stretcher, which stretches the pulses to about 20 ps. Specially designed chirped mirrors are used to pre-compensate for the dispersion mismatch between the total amplifier dispersion and the prisms compressor. The beam is then sent to a multipass amplifier. It is a nine pass amplifier, and the beam is focused in the gain medium at each pass (focusing length of 50 cm) with spherical mirrors. After four passes, a Pockels cell pulse-picker selects pulses at 1 kHz repetition rate, and they are sent back into the amplifier. After five more passes the pulses are extracted and compressed with a Proctor-Wise prism compressor [21, 22]. The final compressed pulses have 1 mJ energy per pulse, with a duration of less than 30 fs.

The oscillator in Porto was used in Papers **III**, **V** and **VII**. The amplified output was used for hollow-core fiber compression, which was used in Papers **IV** and **VI**.

Chapter 3

Characterization

3.1 Introduction

So we have ultrashort pulses. How do we know we really have them?

Suppose that we are doing some time measurement, like, for example, reading some voltage as a function of time on an oscilloscope. The measurement device can be characterized by its spectral response $H(\omega)$ or, equivalently, by its *impulse response function* $h(t)$. So let us suppose that we are trying to measure a voltage $v(t)$ with such system. The signal that we will actually read, $s(t)$ is given by[1]

$$s(t) = v(t) \otimes h(t), \tag{3.1}$$

where $\otimes$ denotes convolution. In the limiting case where $h(t)$ is much shorter than any feature of $v(t)$, it can be approximated by a Dirac delta function, and the measured quantity faithfully represents the physical quantity $v(t)$. This can also be represented in the spectral domain by

$$S(\omega) = V(\omega) \cdot H(\omega) \tag{3.2}$$

and the problem can be seen as a *bandwidth* one: if $h(t)$ is short, then its bandwidth is large. If $H(\omega)$ is flat (or at least larger than the noise level) in the region containing $V(\omega)$, then $S(\omega)$ will contain the necessary information about $V(\omega)$.

Unfortunately, this kind of measurement is usually not realizable with ultrashort pulses. Since we do not have an oscilloscope fast enough to measure the intensity variations on such a short time scale (~fs), and much less to actually resolve the underlying electric field (or, equivalently, to measure the phase as well), other type of approaches are needed.

A lot of work has been devoted to the problem of characterizing ultrashort events in the last decades. A good review on characterization can be found in Ref. [65]. Below a short introduction is given to techniques and principles used during this work.

---

[1] This assumes the system is linear.

3.2 Spectral Interferometry

If a broadband, well-characterized reference pulse is available, then it is straightforward to characterize another pulse. For that, one can use spectral interferometry. Usually that isn't the case though, so it will still be necessary to characterize a reference pulse. It is also an extremely useful technique to characterize linear elements (for example, glasses and chirped mirrors) and the fundamentals of spectral interferometry will be useful for later discussing a complete technique (SPIDER).

Spectral interferometry was first used in the 1970's [66, 67] to characterize dispersion characteristics of optical fibers. The concept is similar to holography [67, 68] but in the time domain instead of spatial domain.

Consider two ultrahort laser pulses, again described in the spectral domain

$$\tilde{U}_1(\omega) = |\tilde{U}_1(\omega)| \exp(i\phi_1(\omega)) \tag{3.3}$$

$$\tilde{U}_2(\omega) = |\tilde{U}_2(\omega)| exp(i\phi_2(\omega)). \tag{3.4}$$

If they are combined, then the resulting field is simply the sum of the spectra, added coherently. A typical case is when a pulse is split in two (like, for example, with the Mach-Zender interferometer in Fig. 3.3), each replica goes through different glasses, for example, and the replicas are delayed with respect to each other. Then

$$\tilde{U}(\omega) = |\tilde{U}(\omega)| exp(i\phi(\omega)) \tag{3.5}$$

$$\tilde{U}_2(\omega) = \tilde{U}(\omega) e^{i\varphi(\omega)} e^{i\omega\tau}, \tag{3.6}$$

where $\varphi(\omega)$ is the phase introduced by the glass (or some other thing) and τ is the delay. $\varphi(\omega)$ could of course include the delay term but we'll keep it as it is for clarity.

The measured power spectrum is then

$$S(\omega) = |\tilde{U}_T(\omega)|^2 = |\tilde{U}(\omega) + \tilde{U}(\omega) e^{i\varphi(\omega)} e^{i\omega\tau}|^2 \tag{3.7}$$

$$= 2|\tilde{U}(\omega)|^2 + |\tilde{U}(\omega)|^2 e^{i\varphi(\omega)} e^{i\omega\tau} + |\tilde{U}(\omega)|^2 e^{-i\varphi(\omega)} e^{-i\omega\tau} \tag{3.8}$$

$$= 2|\tilde{U}(\omega)|^2 \left(1 + \cos\{\varphi(\omega) + \omega\tau\}\right) \tag{3.9}$$

and will be, in general, a fringe pattern[2]. The spacing between fringes will depend on the time delay and phase difference between the replicas. If done correctly, it is possible to extract the spectral phase difference $\varphi(\omega)$ between them. The delay τ leads to the spectral phase $\omega\tau$, which effectively translates the phase information $\varphi(\omega)$, similarly to what happens with off-axis holography. If the carrier frequency is high enough, the different terms in Eq. 3.8 can be separated by Fourier transforming them.

---

[2] It might seem counter-intuitive that two pulses well separated in time interfere. In order to properly resolve the spectral fringes they *must* actually be well separated, otherwise the fringes will not properly sample the spectral envelope. It just happens that a spectrometer stretches the pulses (see, e.g. [69]): if a spectrometer (for example, a CCD spectrometer) has a resolution of $d\omega$, with each pixel taking the whole corresponding area, then a light field reaching a given pixel must be at least $\sim 1/d\omega$ long. The spectrometer resolution thus defines how well separated two pulses can be while still being possible to have interference fringes.

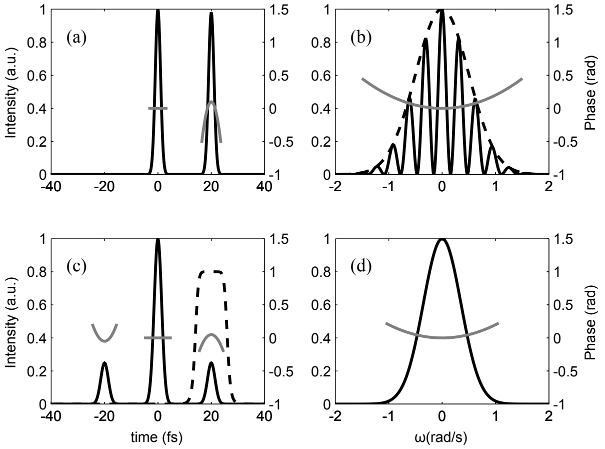

Figure 3.1: Retrieving phase information from a spectral interference pattern. In this example, a pulse with a flat phase (a *reference pulse*) and a chirped pulse are sent to a spectrometer. Both pulses have the same spectral power (dashed line in (b)) but the test pulse has a quadratic phase (gray line in (b)), and they interfere to give the spectral interference pattern (b). Fourier transforming this interference pattern yields the result in (c), which consists on a cross-term (at 'zero' delay) and two terms which contain the phase difference between the test and the reference pulse. Isolating the term with positive delay and Fourier-transforming back to the spectral domain we obtain the test pulse's spectral phase (gray line in (d)).

$$\begin{aligned}\mathcal{F}\{S(\omega)\} = {} & 2\mathcal{F}\left\{|\tilde{U}(\omega)|^2\right\} + \\ & + \mathcal{F}\left\{|\tilde{U}(\omega)|^2 e^{i\varphi(\omega)} e^{i\omega\tau}\right\} + \\ & + \mathcal{F}\left\{|\tilde{U}(\omega)|^2 e^{-i\varphi(\omega)} e^{-i\omega\tau}\right\}\end{aligned} \tag{3.10}$$

$$\begin{aligned}\mathcal{F}\{S(\omega)\} = {} & 2\mathcal{F}\left\{|\tilde{U}(\omega)|^2\right\} + \\ & + \mathcal{F}\left\{|\tilde{U}(\omega)|^2 e^{i\varphi(\omega)}\right\} \otimes \delta(t-\tau) + \\ & + \mathcal{F}\left\{|\tilde{U}(\omega)|^2 e^{-i\varphi(\omega)}\right\} \otimes \delta(t+\tau)\end{aligned} \tag{3.11}$$

If the terms are displaced enough (i.e., τ is large enough) then the "sidebands" are well separated from the DC term, and can be filtered. Fourier transforming back to the spectral domain gives us the original spectral phase (Fig. 3.1).

3.3 Spatiotemporal Characterization

A particularly simple implementation of spectral interferometry can be done using optical fibers [70, 71]. The implementation schematically shown in Fig. 3.2 has been

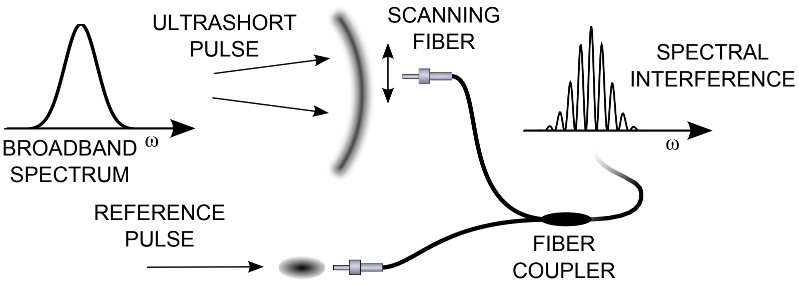

Figure 3.2: Spatiotemporal characterization with spectral interferometry. Optical fibers are used to probe light on different small portions of a beam.

used in Papers **V** and **VI** to characterize, in space and time, ultrashort light pulses. This arrangement has the advantage that the recombination of the beams is done with a fiber coupler, making it alignment-free. The two different light paths are balanced such that the dispersion introduced by the two different fibers are the same (or as close as possible). Since spectral interferometry depends only on the phase differences, the spectral pattern measured does not depend on the fiber length. If a reference pulse, whose temporal characteristics are known, is available, then one of the fibers can be used as a reference. Another fiber can be used to scan the spatial extent of another beam. This is specially useful to measure a pulse whose spectral characteristics vary across its profile, and can also measure spatial deformations of a beam. A high spatial resolution can be achieved by using fibers with small-sized cores. Since the detection is *linear*, the sensitivity is quite high, so small amounts of energy are enough. This technique was used together with the *d-scan* technique (see Section 3.8) to characterize in space and time ultrashort laser pulses.

Spectral interferometry is a powerful (and often overlooked) technique, and was used often during the context of this work. It is very useful for finding the time overlap between pulses, for the characterization of linear elements (for example, glasses and dielectric mirrors), and ultrashort pulses, when a reference is available.

3.4 Autocorrelation

An autocorrelation uses the pulse itself as a gate. The fundamental idea of an autocorrelation is to create two replicas, and delay one with respect to the other. By scanning this delay, insight into the pulse duration can be obtained by using some nonlinear detection [72].

The most basic autocorrelation is the *field autocorrelation*, and it can be realized with a collinear interferometer and a linear detector (Fig. 3.3). Unfortunately, it contains no phase information about the pulse: the Fourier transform of the field autocorrelation is simply the spectrum of the pulse. If, however, there is a phase difference between the two pulses, this phase can be measured, just as in spectral interferometry. In principle it can yield the same information as spectral interferometry, and it has some advantages and some disadvantages.

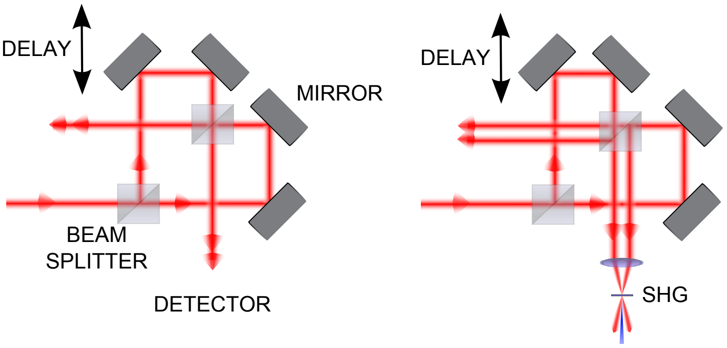
DELAY
MIRROR
BEAM SPLITTER
DETECTOR
DELAY
SHG

Figure 3.3: Mach-Zehnder interferometer. Collinear (left) and noncollinear (right) versions.

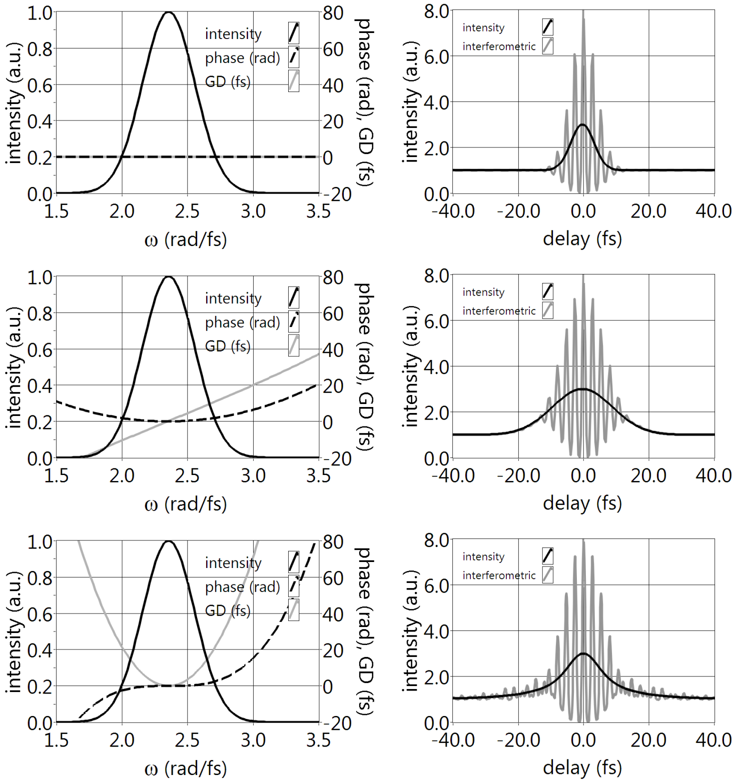

Figure 3.4: Intensity and interferometric autocorrelations for three typical cases: pulse with a Fourier limited Gaussian spectrum, and the same spectrum with pure GDD and pure TOD. The intensity correlation can be directly measured or be obtained numerically from the interferometric autocorrelation.

3.4.1 Interferometric Autocorrelation

Much more useful is the nonlinear interferometric autocorrelation (IAC). It can be realized optically with a collinear interferometer having, instead of a linear detector, a nonlinear process. The most commonly used one is the second-order autocorrelation, and it can be done using a SHG crystal, or using a nonlinear detector [73, 74]. Its form is

$$IAC(\tau) = \int \left\{ [E(t-\tau) + E(t)]^2 \right\}^2 dt \tag{3.12}$$

and it gives more insight into the phase of the pulse (see Fig.3.4). Because the interference fringes depend on the spectral content of the pulse compared to its replica, the presence of chirp can be inferred from the fringes' washout. The optical realization of an IAC is done with a collinear interferometer, and the signal is not background-free. This has advantages and disadvantages: The theoretical contrast between the peak value of an IAC and its background is 8:1, so this is a good check for the quality of a measurement. On the other hand, the interferometric nature of the measurement increases the necessary sampling to properly resolve the fringes.

3.4.2 Intensity Autocorrelation

The intensity autocorrelation

$$A_I(\tau) = \int I(t)I(t-\tau)dt \tag{3.13}$$

is widely used, and it can be realized experimentally with the noncollinear setup shown in Fig. 3.3. Since the SHG signal is spatially separated from the fundamental field, the measurement can be done *background-free*. Because it is not interferometric, the delay sampling is less demanding than in the interferometric case.

Intensity autocorrelations can also be obtained by *low-pass filtering* an interferometric autocorrelation (see Fig. 3.4). This is especially useful when a noncollinear geometry is not possible.

Equations 3.12 and 3.13 assume a flat spectral SHG response (see Section 2.5). Care must be taken to ensure that this is indeed the case: in some cases, a smaller SHG bandwidth can lead to an autocorrelation whose width is *smaller* than it should [64], therefore the real pulse duration will be underestimated.

Autocorrelations have been extensively used for ultrashort pulse measurements. More complex analysis can be done to extract further information: iterative methods to get phase information from correlations and spectra [63, 75, 76] are often used. In Paper **VII** autocorrelations were used to estimate the pulse width and peak intensity of ultrashort pulses from an ultrafast oscillator achievable at the focus of a microscope objective, using chirped mirrors for compression.

3.5 Frequency-Resolved Optical Gating (FROG)

A lot more information about a pulse can be obtained by spectrally resolving the autocorrelation signal. That is, instead of simply measuring the SHG power as a function of delay, one measures the spectrum. The resulting 2D trace yields phase information about the pulse. Instead of SHG generation, other nonlinearities can be used, yielding

nonlinearity	$E_{sig}(t,\tau)$
SHG	$E(t)E(t-\tau)$
PG	$E(t)\|E(t-\tau)\|^2$
SD	$E(t)^2E^*(t-\tau)$
THG	$E(t)^2E(t-\tau)$

Table 3.1: FROG signal for different nonlinear processes. SHG: second harmonic generation, PG: polarization gating, SD: self-diffraction, THG: third harmonic generation

even more information. The concept of frequency resolved autocorrelations had been introduced before (for example [77]) and it was known that the signal depended on the spectral phase of the pulse. Later, iterative algorithms were used to extract the pulse's phase from these traces, with the generic name of FROG (Frequency Resolved Optical Gating) [78–80].

A FROG trace can give an intuitive representation in the *time-frequency* domain of an ultrashort pulse, being formally equivalent to a *spectrogram*[3][64, 80, 82].

The generic form for a FROG trace is:

$$S(\omega,\tau)=\left|\int E(t)G(t-\tau)e^{-i\omega t}dt\right|^2 \tag{3.14}$$

also often written as

$$S(\omega,\tau)=\left|\int E_{sig}(t,\tau)e^{-i\omega t}dt\right|^2 \tag{3.15}$$

where $G(t)$ is usually called the *gate*. $E_{sig}(t,\tau)$ is indicated for different nonlinear processes in Table 3.1. Even if most commonly the gate is related to the electric field $E(t)$ it is not necessarily so. For the most simple case of SHG FROG,

$$S(\omega,\tau)=\left|\int E(t)E(t-\tau)e^{-i\omega t}dt\right|^2, \tag{3.16}$$

the gate is simply the field itself. This form of FROG can be experimentally realized with a noncollinear autocorrelator (Fig. 3.3). Numerical iterative algorithms are used to extract the pulse information from the measured FROG traces. These are usually based on generalized projection algorithms [23, 83, 84] and are robust and mature methods.

There are many variants of FROG available, each with different strengths and weaknesses. For example, single-shot versions [85], and interferometric versions of FROG [86, 87] are often used. Single-shot measurements are obviously attractive (but require higher pulse energy than multi-shot). Collinear [86, 87] versions have the advantage of increased bandwidth, and extra information is obtained which allows further cross-checking and validation of the data. The disadvantage of such scheme is the increased resolution needed to resolve the FROG trace.

---

[3] Other ways of representing ultra-short pulses are sometimes used, for example, the chronocyclic representation [81] which is the ultrashort pulse analog of the Wigner distribution. These representations are powerful tools for the analysis of ultrashort pulse.

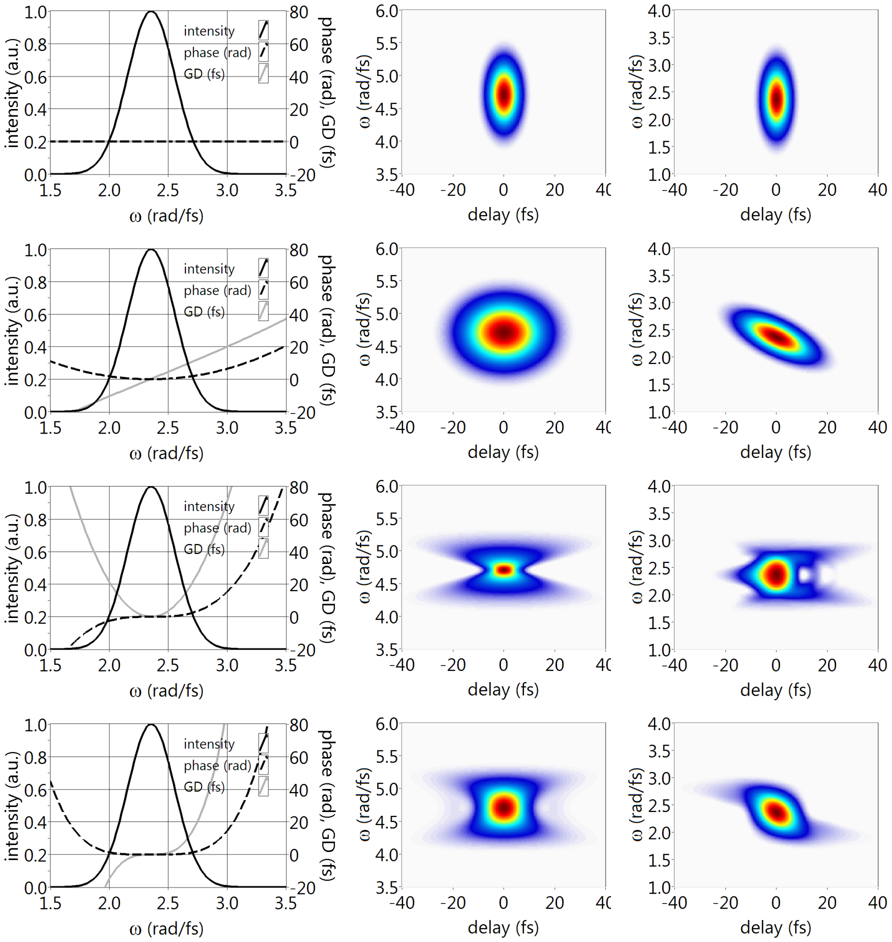

Figure 3.5: Simulated FROG traces for SHG FROG (cental column) and PG (right column). Top to bottom: Fourier-limited pulse (6 fs FWHM), same spectrum but with pure GDD (30 fs^2), pure TOD (340 fs^3), and pure FOD (2000 fs^4).

It turns out that if the gate $G(t)$ is independent of the field to be recovered $E(t)$, then both can in principle be recovered [23, 88]. The FROG retrieval method is also used for attosecond pulse characterization (see Section 4.4.3).

3.6 Spectral Phase Interferometry for Direct Electric-field Reconstruction (SPIDER)

A different approach to ultrashort pulse measurement relies on spectral interferometry. We have previously discussed how linear interferometry can only give us relative phase information (3.2), so it needs a reference. A different approach, while still using spectral interferometry, was devised by Iaconis and Walmsley [89]. It relies on *spectral* *shearing.* The basic idea is, if one can take a spectrum, shift it (phase included), and interfere it with the original one, then the spectral interference fringes do depend on the original spectrum's phase.

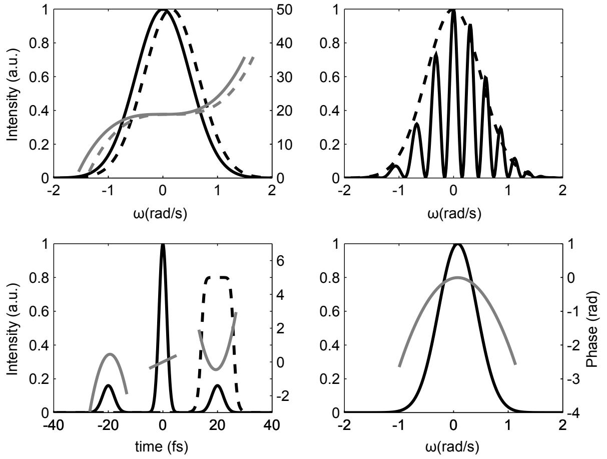

Figure 3.6: Spider retrieving algorithm. A pulse and its sheared replica are combined to produce interference fringes. A Fourier analysis of this fringe pattern allows its phase to be retrieved. The phase which is directly retrieved from this interference pattern is not the original pulse's phase, but instead related to the original pulse's *group delay*.

Consider a complex spectrum and its sheared and delayed replica

$$\tilde{U}(\omega) = |\tilde{U}(\omega)|e^{i\phi(\omega)} \tag{3.17}$$

$$\tilde{U}_s(\omega) = \tilde{U}(\omega-\Omega)e^{i\omega\tau} = |\tilde{U}(\omega-\Omega)|e^{i\phi(\omega-\Omega)}e^{i\omega\tau}. \tag{3.18}$$

The measured spectral intensity of the two pulses combined is then

$$\begin{aligned} S(\omega) &= |\tilde{U}(\omega)+\tilde{U}_s(\omega)|^2 \\ &= |\tilde{U}(\omega)|^2 + |\tilde{U}(\omega-\Omega)|^2 + \\ &+ |\tilde{U}(\omega)||\tilde{U}(\omega-\Omega)|e^{i\{\phi(\omega)-\phi(\omega-\Omega)\}}e^{-i\omega\tau} \\ &+ |\tilde{U}(\omega)||\tilde{U}(\omega-\Omega)|e^{i\{-\phi(\omega)+\phi(\omega-\Omega)\}}e^{i\omega\tau}. \end{aligned} \tag{3.19}$$

Proceeding as before (Section 3.2), the term around $-\tau$ can be isolated, thus retrieving $\phi(\omega)-\phi(\omega-\Omega)$. For a small shear Ω

$$GD(\omega) \simeq \frac{\phi(\omega)-\phi(\omega-\Omega)}{\Omega}, \tag{3.20}$$

and the phase $\phi(\omega)$ can be obtained by integration.

In practical SPIDER implementations (Fig. 3.7), instead of spectrally shearing one of the replicas, both are sheared, but by slightly different amounts, using sum-frequency generation. Mixing the fundamental pulse with a quasi-monochromatic field in a sum frequency generation (SFG) crystal yields a spectral shift. To achieve

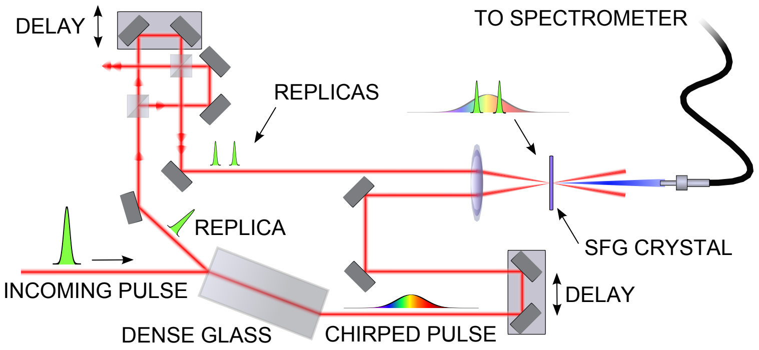

Figure 3.7: Schematic of a typical SPIDER setup. The pulse to be measured is split into a replica and a chirped pulse. The replica is further divided into two replicas, which are later mixed with the chirped pulse in a sum frequency generation (SFG) crystal. If the chirped pulse is stretched enough, then each replica will only "see" a monochromatic part of the field.

different spectral shifts for the two replicas, a *chirped* beam is usually employed as the quasi-monochromatic beam, which is obtained from the pulse to be measured itself. Then, the time delay between the replicas determines not only the carrier $\omega\tau$ but also the shear Ω.

There are several SPIDER-related techniques designed to increase the robustness and to deal with spectral "holes" [90, 91], as well as variants that decrease the high spectrometer resolution which is often necessary (for example, Spatially-Encoded Arrangement SPIDER (SEA-SPIDER) [92] and two-dimensional spectral shearing interferometry (2DSI) [93]).

3.7 Multiphoton Intrapulse Interference Phase Scan (MIIPS)

Another approach has been taken to the characterization of ultrashort laser pulses. It is based on applying a set of different spectral phase curves to an unknown spectral pulse, combined with nonlinear detection [94–97]. It is a convenient technique to be used with pulse shapers and/or compressors in general, as it is often the case that most of the experimental setup needed to measure the pulse is already present (either in the form of a pulse shaper or a compressor).

The typical implementation of MIIPS uses a pulse shaper, but it can be done with passive elements as well, like gratings or prisms compressors [96]. Let us again consider an ultrashort laser pulse in the spectral domain, with an intrinsic spectral phase $\phi(\omega)$

$$\tilde{U}(\omega) = |\tilde{U}(\omega)| \exp\{i\phi(\omega)\} \tag{3.21}$$

If a spectral phase $\varphi(\omega)$ is applied, (with a passive element or with a pulse shaper), and the pulse is sent to a SHG crystal, the SHG signal will depend on the intrinsic $\phi(\omega)$ and the applied $\varphi(\omega)$ phases (see section 2.5).

Applying a phase function as suggested in Ref. [95]

$$\varphi(\delta, \omega) = \alpha \sin(\gamma\omega - \delta) \tag{3.22}$$

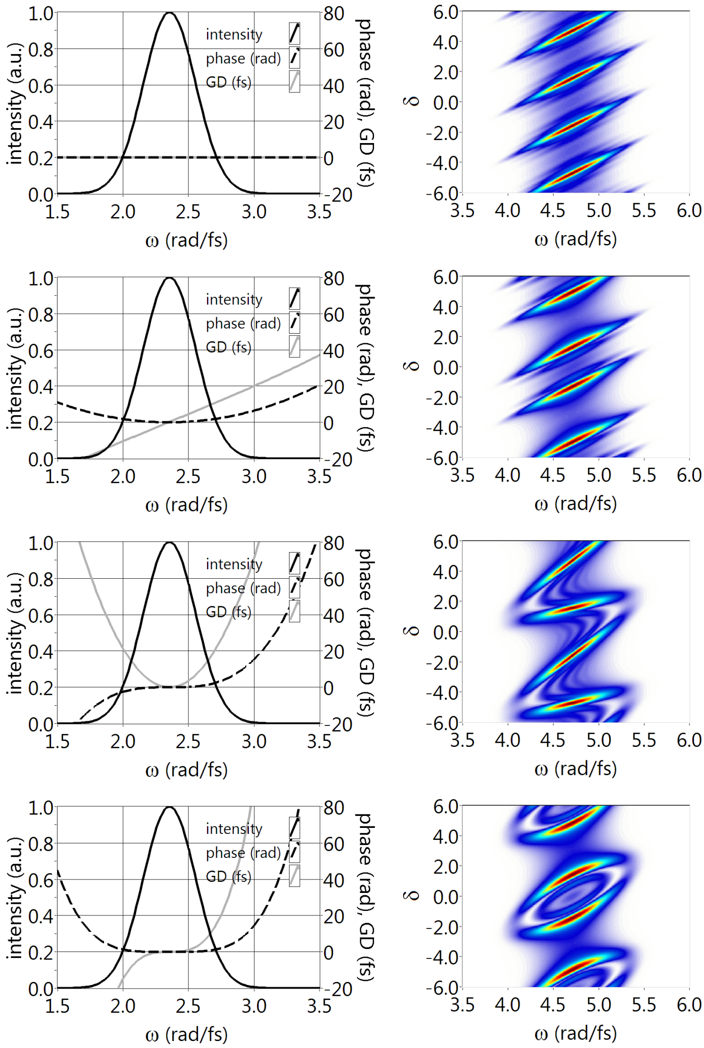

Figure 3.8: Examples of MIIPS traces for some representative spectra. FWHM for the Fourier limited spectrum is $6fs$.

the SHG signal becomes

$$S(\omega,\delta) = \left| \int \left(\int \tilde{U}(\Omega) \exp\{i\varphi(\Omega,\delta)\} \exp(i\Omega t) d\Omega \right)^2 \exp(-i\omega t) dt \right|^2 \tag{3.23}$$

which can also be expressed as a convolution

$$S(\omega,\delta) = \left| \int \tilde{U}(\Omega) \exp\{i\varphi(\Omega,\delta)\} \tilde{U}(\omega-\Omega) \exp\{i\varphi(\omega-\Omega,\delta)\} d\Omega \right|^2 \tag{3.24}$$

Figure 3.8 shows some examples of MIIPS traces, with $\alpha = 1.5\pi$, and $\gamma = 6\text{fs}$ (which is approximately the FWHM for the Fourier limit of the spectrum).

The pulse is characterized by determining which phase locally compresses each frequency (see section 2.5). If the spectral phase varies slowly, whatever GDD locally *flattens* a given spectral phase will lead to a maximal SHG signal at the corresponding (doubled) frequency. Experimentally one would find what GDD had to be introduced at a given frequency ω to maximize the SHG signal at the frequency 2ω. This approach will not completely determine the phase (typically it works well up to TOD) but as a pulse shaper is used, the phase can be partially corrected, and iteratively becomes flat.

3.8 d-scan

During this thesis a technique called *d-scan* (for dispersion scan) was developed that allowed us to characterize ultrashort laser pulses from an oscillator or from a hollow-core fiber compressor. It is based on the MIIPS concept of applying spectral phases, but an iterative numerical algorithm was used allowing us to retrieve the spectral phase, and it was experimentally realized with a chirped mirror and glass wedges compressor (see Fig. 3.10). The spectral phase function is simply that introduced by linear propagation through a glass, $\varphi(\omega, z) = zk(\omega)$, where $k(\omega)$ is the glass' wavenumber, which can be easily calculated from Sellmeier formulas (see Section 2.3.1). The SHG spectrum as a function of the glass thickness z is then

$$S(\omega, z) = \left| \int \left(\int \tilde{U}(\Omega) \exp\{izk(\Omega)\} \exp(i\Omega t) d\Omega \right)^2 \exp(-i\omega t) dt \right|^2 . \tag{3.25}$$

The question is now how to find the phase from the 2D scans, which consist on SHG spectra vs glass insertion (Fig. 3.9). A MIIPS analysis could be used here, as the glass dispersion is well known. Since a pulse shaper is not available, an iterative phase correction (that would lead to a better phase measurement) isn't possible.

Our approach was to use an iterative algorithm that uses the measured fundamental spectrum, and tries to find which spectral phase best recreates the measured scan. We found this approach to have some advantages from a bandwidth point of view: since all the generated wavelength components depend, to some degree, on the generating wavelength components, the phase could be retrieved even when some wavelengths were not phase-matched, or purely absent.

One of the striking advantages of this technique is that most of the setup was already there, as a pulse compressor (Fig. 3.10), i.e., the glass wedges and the chirped mirrors. The only necessary modifications from the present chirped mirror compressor were adding a SHG crystal and an encoder for the wedges' position. A simple solution was found using an optical encoder with a transparent strip (Fig. 3.11). This way, the wedge's position was scanned by hand, and a trigger signal was sent to a personal computer to acquire SHG spectra.

The technique is described in detail in Papers **III** and **IV**, and was used in Papers **V** and **VI**. It was utilized in Porto to characterize an ultrafast oscillator and the output of a hollow-core fiber compressor. Figure 3.12 shows the experimental and retrieved scans of the output from the ultrafast oscillator in Porto, with the corresponding spectral phase and time domain reconstructions.

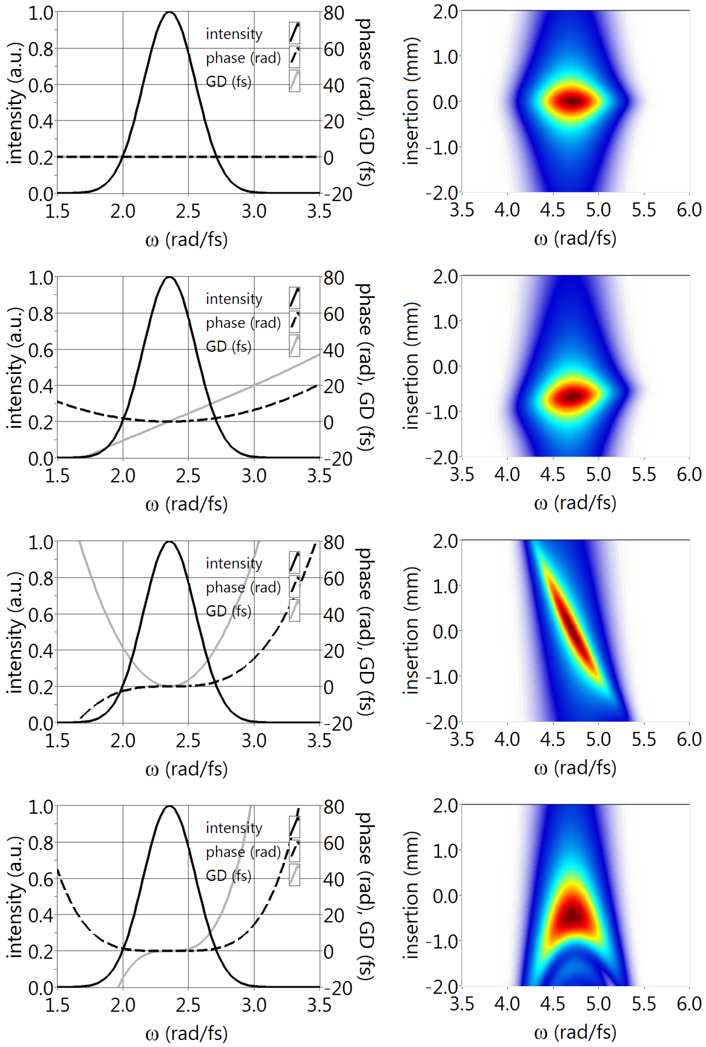

Figure 3.9: Examples of d-scan traces for some representative spectra. FWHM for the Fourier limited spectrum is 6 fs.

In all previous techniques, one of the main problems is the bandwidth of the nonlinear process conversion. Broadband SHG generation requires the use of thinner crystals, sacrificing efficiency. For the case of autocorrelations, the SHG response should be flat within the whole region of interest to ensure a correct estimation of the pulse duration. In the case of FROG, since the measurement is frequency-resolved, the spectral response can in principle be corrected [64, 98] as long as it is above the noise levels in the region of interest. In the case of SPIDER and related techniques, a calibrated SHG response is not necessary since the information is encoded in the fringes. The same is true for MIIPS, but for a different reason: as long as there is

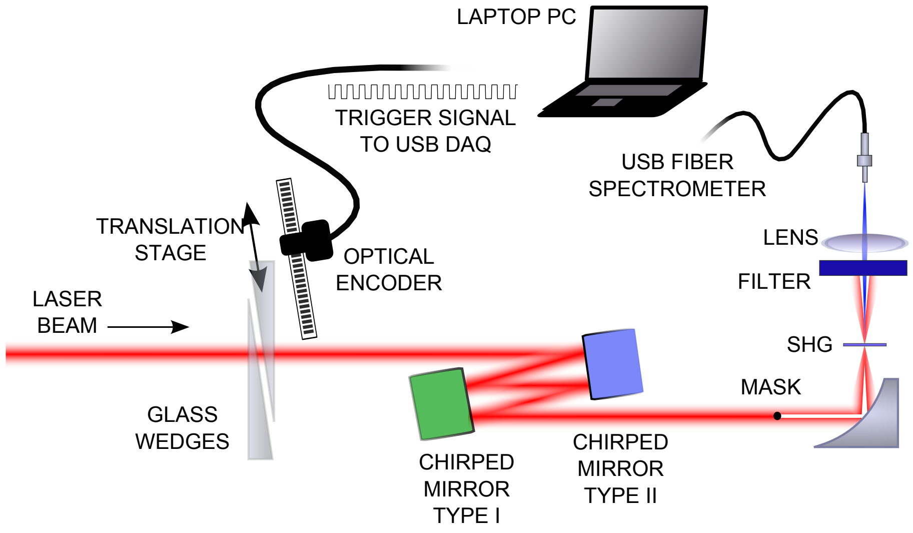
LAPTOP PC
TRIGGER SIGNAL
TO USB DAQ
USB FIBER
SPECTROMETER
TRANSLATION
STAGE
OPTICAL
ENCODER
LENS
FILTER
LASER
BEAM
SHG
MASK
GLASS
WEDGES
CHIRPED
MIRROR
TYPE I
CHIRPED
MIRROR
TYPE II

Figure 3.10: Simplified schematic of the experimental setup used. The encoder is a simple linear strip printed on a normal laser printer transparency.

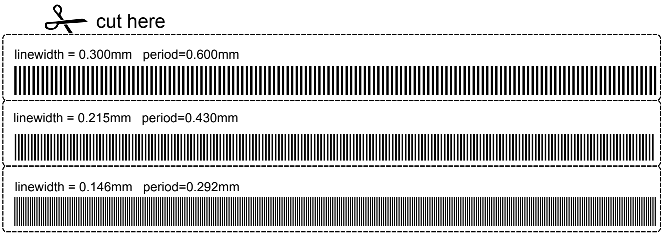
cut here
linewidth = 0.300mm period=0.600mm
linewidth = 0.215mm period=0.430mm
linewidth = 0.146mm period=0.292mm

Figure 3.11: As a courtesy to the reader, we provide the same strips that were used for the encoder. Feel free to cut it out of the thesis.

enough SHG signal at a given frequency, it is not necessary that it follows the *ideal* model for SHG. In the case of the *d-scan* retrieval technique, we found that even in the absence of signal at some frequencies, the algorithm still worked well in some cases (Papers **III**, Paper **IV** and Paper **VI**). A mathematically strict criterium for when the bandwidth is enough or not is however not easy to formulate.

Effective bandwidth increase can also be accomplished by dithering the crystal [99], at the expense of added complexity. For higher energy pulses, where higher-order nonlinearities are achievable, Kerr-effect can be used as a nonlinearity, with larger bandwidths.

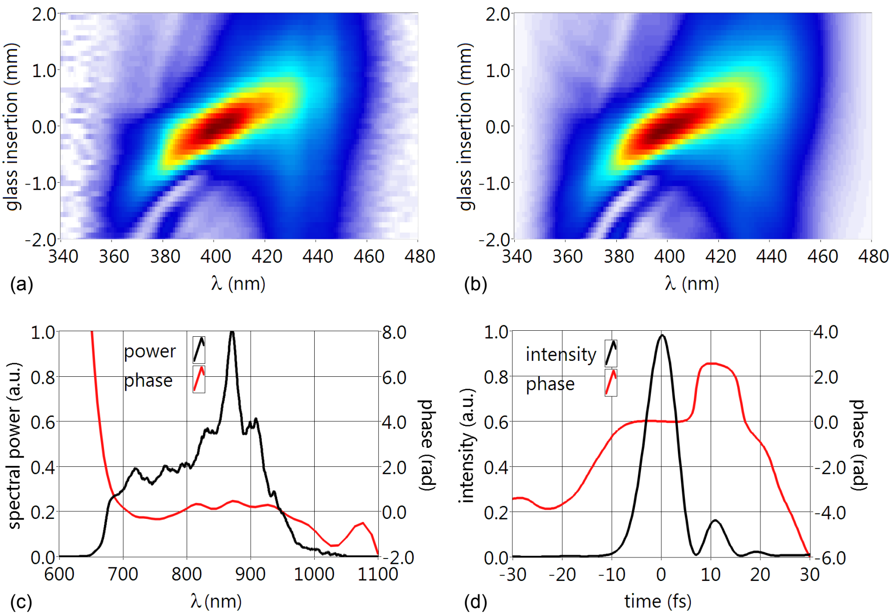

Figure 3.12: Temporal characterization of an ultrafast oscillator with the *d-scan* technique (from Paper **III**). The fundamental spectrum (c) and the SHG spectra as a function of glass insertion (a) were measured. An iterative algorithm applies phases to the fundamental spectrum and simulates the SHG process to recreate (b) the measured trace. From this retrieved phase (c) the pulse can be reconstructed in the time domain (d).

3.9 Carrier-Envelope Phase

All the self-referenced methods described so far have (at least) one limitation: they are not capable of measuring a pulse's absolute phase. This is normally called *Carrier-Envelope Phase (CEP)* or *Carrier-Envelope Offset (CEO)*. Methods to measure the CEP *drift* of oscillators were proposed and demonstrated [100], and stabilization of the drift was accomplished [101–103]. Consider an ultrashort pulse oscillator: in general, the *phase* and *group* velocity are different which leads to a dephasing between the carrier and the envelope (Fig. 3.13). Let us assume for simplicity that the pulse's spectrum is octave spanning: it is possible then to generate SHG from a given spectral line on the red side of the spectrum and produce one with the approximate frequency of an existing one from the blue side of the spectrum. If the first one has a frequency

$$f_n = nf_{rep} + \delta \tag{3.26}$$

its second harmonic will have a frequency of

$$2f_n = 2nf_{rep} + 2\delta. \tag{3.27}$$

Since there is already an existing frequency component at around $2nf_{rep}$, the addition of these two will lead to a field at the average frequency, but *beating* at the frequency difference between the fields, δ, which can be detected by fast electronics.

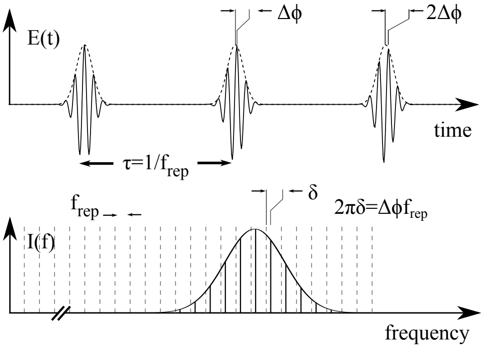

Figure 3.13: CEP drift on a mode-locked laser on the time and frequency representations (adapted from [101]).

Since most spectra are not octave-spanning (although some state-of-the-art oscillators do indeed deliver octave spanning spectra, e.g. [40–42]), spectral broadening from nonlinear interactions is necessary before SHG. Monolithic schemes [104] take advantage of spectral broadening in nonlinear crystals to achieve directly both effects, with added simplicity. It should be stressed that the signal obtained from these methods are not directly related to the CEP, but to its drift.

A spectral interference approach allows single shot CEP measurements [105]. It requires more energy so it is only done on higher energy pulses, like typically obtained with ultrafast amplifiers.

Consider first an octave-spanning pulse: if we perform SHG with full bandwidth, the fundamental and SHG will overlap at the wings (see Fig 3.14). This interference pattern depends on the fundamental field CEP phase.

Using the simple model for SHG presented in section 2.5, it is easy to see that a constant phase applied to a fundamental field is doubled in the corresponding second harmonic

$$\begin{aligned} U'(\omega) &= U(\omega)e^{i\phi_0} \\ U'_{SHG}(\omega) &= U_{SHG}(\omega)e^{i2\phi_0}. \end{aligned} \tag{3.28}$$

Delaying one with respect to the other by τ, the resulting total field will be

$$U_T(\omega) = e^{i\phi_0}\left(U(\omega) + U_{SHG}(\omega)e^{i\phi_0}e^{i\omega\tau}\right). \tag{3.29}$$

Proceeding as shown in Section 3.2, the term around the carrier $\omega\tau$ can be isolated (if the delay τ is suitable) and ϕ_0 can be extracted.

In practice, SHG results in a signal with a polarization normal to the fundamental pulse's polarization, so no interference will occur. This can be easily solved by using a polarizer at a convenient angle, which will project both spectra's polarization in a common axis.

Unfortunately, most pulses do not have an octave-spanning spectrum. Typically, spectral broadening is achieved by some nonlinear effect, e.g. Kerr effect in a glass. A problem is that the spectral phase of a pulse undergoing such a nonlinearity depends

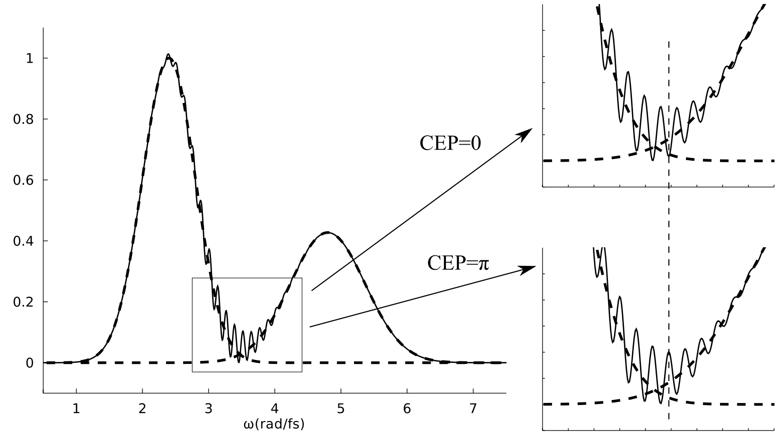

Figure 3.14: Interference fringes between an octave-spanning spectrum and its corresponding SHG spectrum (fundamental and SHG spectra shown in dashed lines, centered at around $\omega = 2.4\ rad/fs$ and $\omega = 4.8\ rad/fs$ respectively). The interference pattern depends on the absolute phase of the fundamental spectrum.

on the intensity of the pulse: a variation in the pulse intensity will lead to a variation of the phase measurement, even if the CEP itself doesn't change [106, 107]. This is, however, very difficult to avoid, and a laser system has to be stable in power if it is to be stabilized in CEP.

The CEP stabilization can be achieved in different ways. A common technique is to act directly on the laser oscillator: a slow signal is sent to the oscillator CEP controller, effectively changing its CEP to stabilize the CEP at the amplifier output (or somewhere else). Other techniques consist on using external elements, often part of the stretcher or compressor, or active modulators.

Papers **I** and **II** describe the work that took place in Lund to make the system CEP stable. Stabilization was achieved by controlling the oscillator's CEP, or by using the AOPDF to introduce a correction phase. Figure 3.15 shows long-term stability of the CEP phase with a standard deviation of around 400 mrad. For this measurement, the slow feedback loop was achieved by adjusting the oscillator's CEP.

Other methods exist to measure CEP, relying for example on above threshold ionization (ATI) [108, 109] and terahertz-emission spectroscopy [110]. These are usually much more complex to realize. A different approach for CEP-dependent experiments is to, instead of controlling it, measuring it at the laser repetition rate. If the outcome of the laser interaction can also be measured at the same rate, it can simply be *tagged* to the corresponding CEP.

An alternative approach is to use parametric amplification: in some situations, it is possible to directly generate radiation which is inherently CEP stable [111, 112].

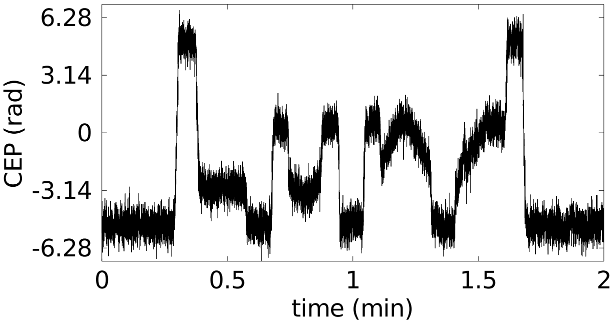

Figure 3.15: CEP-stability measurement and control of the Lund laser system.

CHAPTER 4

HIGH-HARMONIC GENERATION, ATTOSECOND PULSES AND APPLICATIONS

4.1 Introduction

This chapter introduces some basic concepts to the generation, propagation, characterization and applications of HHG radiation. An introduction to HHG and attosecond physics can be found for example, in [113, 114]. Some applications of the HHG sources in Lund are presented.

4.2 High-Harmonic Generation

High Harmonic Generation (HHG) was first observed in 1987 [3, 4] from the interaction of gases with high-intensity laser pulses. Nonlinear optics was well understood using perturbation theory, and from this point of view, it was natural that the efficiency of a nonlinear process would decrease exponentially with the order of the process. The observed harmonics followed this behavior up to a certain order and for low intensities, but strangely, for very high intensities, the efficiency as a function of harmonic order stops falling exponentially, and instead a *plateau* was observed (Fig. 4.1). This could not be understood from a perturbative process point of view.

At light intensities of about $10^{13} W/cm^2$, the magnitude of the electric field of light approaches that of the Coulomb potential of valence electrons in rare gases. At such extreme light fields, the electron might simply "tunnel out" of the atom Coulomb potential: if this happens, the interaction of the electron with the core is rather small, and the laser-electron interaction dominates.

High Harmonic Generation can be intuitively understood by a simple model, the Three Step Model [115, 116] (Fig. 4.2). In this simple model, as soon as the electron is released from the nucleus, its trajectory can be calculated from classical mechanics.

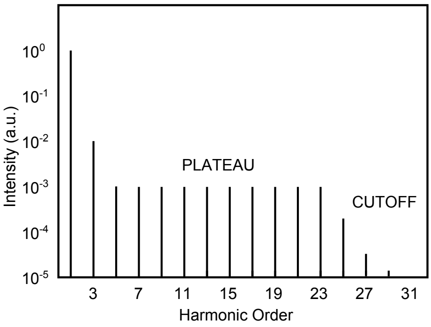

Figure 4.1: Simplified schematic of a typical High-Harmonic Generation spectrum. For the first few orders, the emission efficiency drops very fast, and is then followed by an efficiency *plateau*. It then drops abruptly again at the *cutoff*.

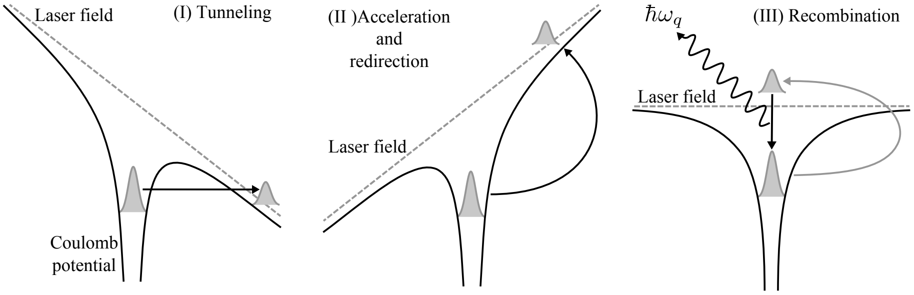

Figure 4.2: Three step model. If the laser intensity is enough that the light electric field is comparable to the Coulomb potential, an outer electron might be able to tunnel out (I). The electron trajectory is then mostly dominated by the laser driving field (II) and its trajectory is well described by Newtonian mechanincs. When (and if) the electron collides with the nucleus, a photon is emitted (III). Its energy depends on the energy the electron acquired while accelerated in the continuum (adapted from [117]).

The only force acting on it is the driving laser field. Consider a driving electric field

$$E(t) = E_0 \sin(\omega t). \tag{4.1}$$

The position of the electron relative to the nucleus can be obtained by integrating the acceleration twice:

$$x(t) = \frac{eE_0}{m\omega^2}\left[sin(\omega t) - sin(\omega t_i) - \omega(t - t_i)cos(\omega t_i)\right], \tag{4.2}$$

so the only parameter that determines the trajectory (besides the field amplitude) is t_i, the electron's tunneling time relative to the laser field. This tunneling time determines when (and if, at all) the electron returns to the nucleus. From this simple model, the energy the electron acquires from the driving field while in the continuum can be calculated (Fig. 4.3). For a given wavelength and intensity of the driving field, the maximum energy an electron can acquire while accelerated in the continuum, and brought back to the nucleus, is 3.17 U_p, where

$$U_p = \frac{e^2 I}{2 m_e \omega^2 \epsilon_0 c} \tag{4.3}$$

is the *ponderomotive* energy. It follows from energy conservation that, after recombination, the maximum photon energy that can be emitted is

$$\hbar\omega_m = I_p + 3.17 U_p \tag{4.4}$$

which agrees rather well with the experimental results [116].

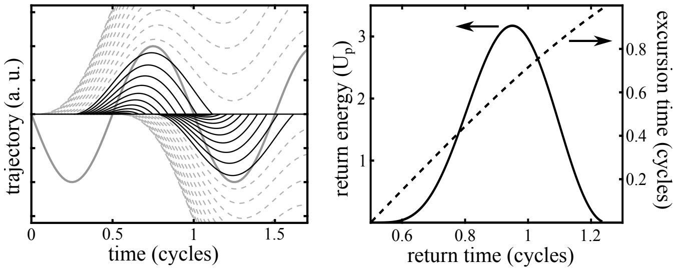

Figure 4.3: Examples of electron trajectories in the continuum for different tunneling times (left), and return energy acquired by the electron as a function of time spent in the continuum (right) (adapted from [117]).

As can be seen in Fig. 4.3, there are two different trajectories that lead to the same final energy. These are called the *short* and *long* trajectories, and the contributions from these trajectories have different properties. The time delay with respect to the fundamental driving field varies from a few hundred attoseconds to more than a cycle, and that leads to different characteristics for the emitted radiation, as the accumulated phase of the electronic wave is much larger for the long than for the short trajectory.

The phase of the emitted harmonics depend on the intensity of the driving field approximately with [118]

$$d\phi_q^j = \alpha_q^j dI, \tag{4.5}$$

where q refers to the harmonic order and j to the quantum path (i.e., short or long trajectory). For each given harmonic q, the parameter α is much larger for the long than for the short trajectory. This has important consequences: since the driving field varies both in time and space, the term dI/dt will lead to a *frequency modulation* of the emitted harmonic, which produces a broadening of the harmonics width (or even splitting) and the term $dI/d\mathbf{r}$ will lead to a spatial phase modulation of the emitted harmonics as a function of the radial coordinate, similarly to Kerr lensing (Fig. 4.4). Because the α's parameters are different for the short and long trajectories, this leads to the shorter trajectories' emission having different divergence than the long trajectories' emission. These effects shape the harmonics emission in the spectral and spatial domain.

As with other nonlinear processes, *phase-matching* (Fig. 4.5) plays an important role on the efficiency of the HHG process, as well as on the spectral and temporal

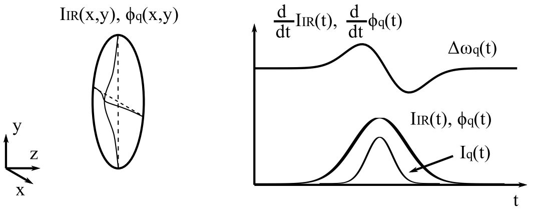
$I_{IR}(x,y)$, $\phi_q(x,y)$
y
z
x
$\frac{d}{dt}I_{IR}(t)$, $\frac{d}{dt}\phi_q(t)$
$\Delta\omega_q(t)$
$I_{IR}(t)$, $\phi_q(t)$
$I_q(t)$
t

Figure 4.4: Spatial and spectral shaping of the harmonics field due to spatial and temporal variations of the driving IR field, for a given harmonic q. Similarly to the Kerr effect, a spatial variation of the intensity beam profile leads to a space-varying phase front of the generated harmonics, which has a similar effect to a lens. The time-varying intensity of the IR driving field leads to variation of the instantaneous frequency of the generated harmonics.

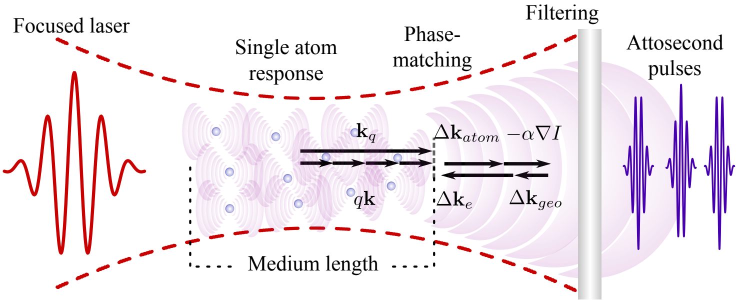
Focused laser
Single atom response
Phase-matching
Filtering
Attosecond pulses
$\mathbf{k}_q$
$q\mathbf{k}$
$\Delta\mathbf{k}_{atom}$ $-\alpha\nabla I$
$\Delta\mathbf{k}_e$
$\Delta\mathbf{k}_{geo}$
Medium length

Figure 4.5: Single-atom response and collective (macroscopic) response. The efficiency of the process, as well as the spectral and temporal characteristics of the output HHG radiation depend on a number of microscopic and macroscopic factors (adapted from [117]).

characteristics of the resulting radiation. In general, the phase matching condition for the q-th harmonic is [119]

$$\mathbf{k}_q = q\mathbf{k} + \nabla\Phi_q \tag{4.6}$$

where $\mathbf{k}_q$ is the wave vector of the q'th harmonic, $\mathbf{k}$ is the wave vector of the fundamental driving field, and Φ_q is the intensity-dependent harmonic phase.

A centrosymmetric medium cannot lead to even-order harmonics: since the HHG process repeats itself every half-cycle of the driving field, but with a different sign, the end result in the time-domain is that, for each IR cycle, two consecutively emitted burst are “flipped” relative to each other. The emission of odd-order harmonics is dependent on several phase-matching parameters. These depend on the intrinsic HHG phase itself, geometric effects (Gouy phase shift), the harmonics’ phase dependence with the driving laser intensity, which in turn varies temporally and spatially, and dispersion effects of the generation gas, both on the driving field as on the generated harmonics. As HHG is inevitably accompanied by ionization, plasma formation induces strong phase modulations into both the driving IR and generated XUV fields, which also influence phase-matching.

4.2.1 Experiments

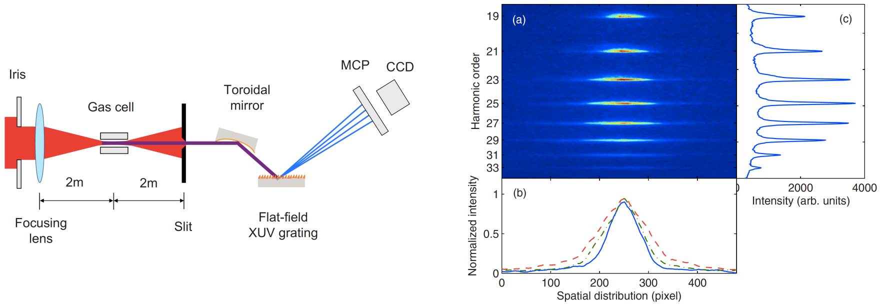

Figure 4.6: Schematic of the setup used in Paper **VIII**, and an example of spatial and spectral measurement.

In this thesis, HHG experiments have been performed using the low-energy arm of a 10 Hz 40 TW laser, as well as a 1 kHz 3 mJ laser. In Paper **VIII** the spatial and spectral properties of the 10Hz HHG beamline in Lund are characterized. The HHG source is schematically shown in Fig. 4.6, together with an example of a spectral and spatial measurement. The driving beam has up to 100 mJ of energy, with a duration of about 35 fs. From this, typically only 10 mJ were used. Optimization of HHG generation in the laboratory involves finding experimental conditions that minimize the phase mismatch between the IR and the generated harmonics. A set of tradeoffs has to be taken: for example, higher IR intensities are necessary to reach higher harmonics; this can be done by using tighter focusing of the fundamental IR beam, but this also reduces the interaction volume, increases ionization, and changes the Gouy phase shift parameters, and all these factors will change the phase-matching conditions.

4.3 Attosecond Pulses

Since its observation, HHG was proposed as a process to create short pulses [120]. It follows from the temporal coherence of the HHG emission that it should be possible to obtain extremely short pulses if the harmonics' phases are locked. Figure 4.7 schematically depicts how the harmonics' spectral phase translate to in the time domain. The width of the individual harmonics roughly determines the length of the pulse train, and the width of the spectral envelope roughly determines the length of the individual pulses. A similar argument holds for the spectral and temporal phases.

4.3.1 Attosecond Pulse Shaping

The attosecond pulses generated by HHG have an intrinsic phase due to the generation process itself and therefore are not, in general, temporally compressed. A way of doing so is to use transmission through transmission filters [121, 122]: some materials exhibit negative dispersion in certain XUV spectral regions, and can then compensate the

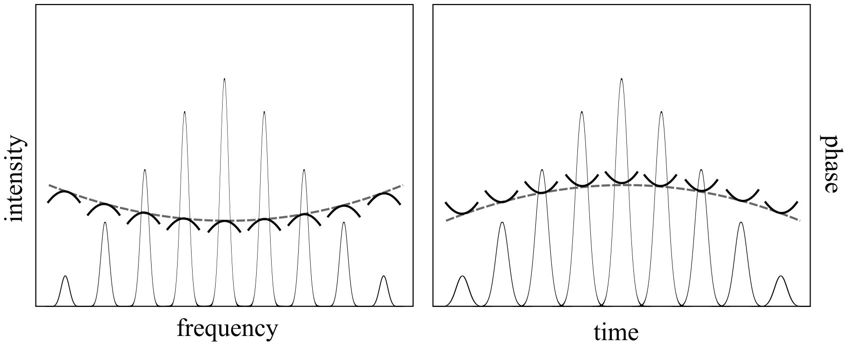

Figure 4.7: Inter-harmonic chirp (dashed line) and intra-harmonic chirp (continuous lines). The inter-harmonic chirp mostly determines the average pulse width and characteristics on the time domain (right side) while the intra-harmonic chirp determines the pulse train width and chirp.

intrinsic positive chirp of the generation process. A commonly used material during the work presented here was aluminum. It is useful also because it efficiently blocks the generating IR radiation, so aluminum filters were used even when the attosecond pulses did not need to be short for some particular application. Figure 4.8 shows a simulated example of transmission through 200 nm of aluminum of a typical XUV spectrum generated with our attosecond setup. The optical properties of numerous materials in the XUV region can be found for example in Refs. [123, 124]. In this spectral region, aluminum exhibits negative dispersion (Fig. 4.8a), but it is not the case for higher energies. Other materials, e.g. zirconium or semiconductors have different absorption and phase properties, and might be used for different generation conditions.

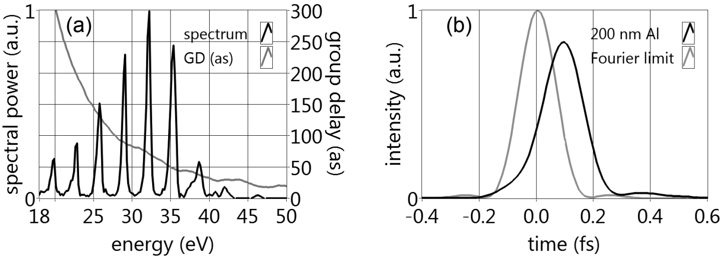

Figure 4.8: (a) A typical measured harmonic spectrum, and calculated group delay curve for transmission through 200 nm of aluminum. (b) The corresponding temporal reconstruction of one of the attosecond pulses from the train, assuming it was Fourier limited before transmission. The FWHM duration for the Fourier limited case is of about 150 as.

Another approach is to use multilayer mirrors [125–128]. As in the optical domain, multilayer mirrors can be designed to match desired spectral characteristics, both in amplitude and phase. It is more difficult though to fabricate mirrors for the XUV spectral domain due to the shorter wavelengths.

4.3.2 Isolated Attosecond Pulses

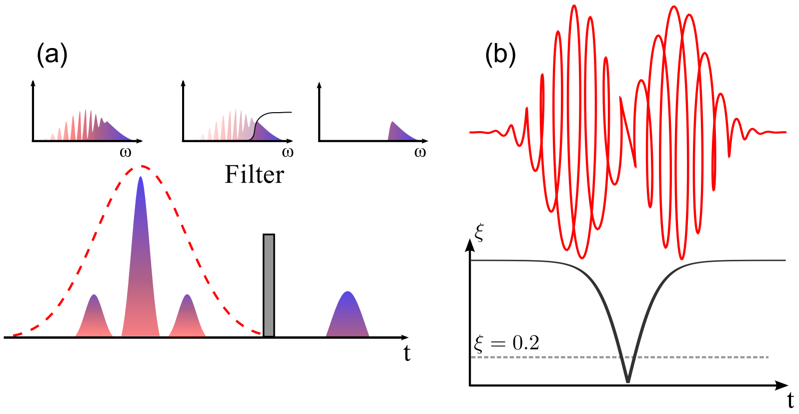

Figure 4.9: Isolated attosecond pulses generation by (a) spectral filtering on the cutoff region and (b) polarization gating.

A spectrum made up of well-separated harmonics will lead to a train of pulses but not to an isolated one: for that, a spectral continuum is needed.

A first proposed and demonstrated technique consisted in spectral filtering the cutoff region [125, 129] using thin metallic filters. Since the spectral content varies from pulse to pulse in the train, with a larger bandwidth for the shortest pulses, then selecting a given bandwidth continuum would translate, in the time domain, to an isolated attosecond pulse. The recent approaches to generate isolated pulses consist in some form of temporal gating, either by "simply" reducing the fundamental driving field to the single-cycle regime, or by employing some time-domain gating to confine the HHG emission to an interval shorter than the pulse itself. *Polarization gating* [58, 130, 131] is one such method, where the ellipticity of the generating pulse is made to vary throughout the pulse: since the HHG emission strongly depends on the ellipticity, the emission can be confined to an interval shorter than the pulse itself. Other routes, as using two-colour fields [132], or combining the two approaches (double optical gating - DOG) [133], and ionization gating [134] have been proposed or/and demonstrated.

4.3.3 Experimental Setup

Figure 4.10 shows a schematic representation of the attosecond setup in Lund. It is based on a Mach-Zehnder type pump-probe setup: part of the fundamental IR field is used to generate XUV radiation, while a small portion of IR is combined with the generated XUV, with a variable time delay. For the experiments presented in Papers **X** and **XI**, the laser beam was taken directly from the compressor of the ultrafast amplifier (about 3 mJ, 30 fs, 1 kHz).

The main part of the beam is focused in a pulsed gas cell synchronized with the laser beam at 1 kHz. This allows generation at the full laser repetition rate while keeping a good vacuum in the generation chamber. The chambers are connected through small

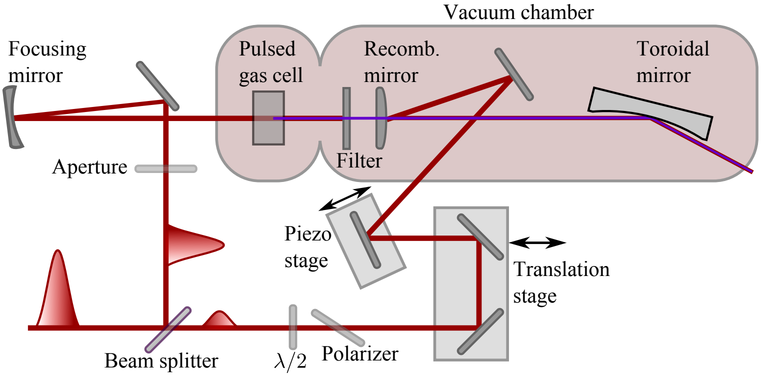

Figure 4.10: Attosecond setup used in Lund. The driving field was either the beam directly from the ultra-short amplifier (about 3 mJ, 30 fs, 1 kHz) or from the hollow-fiber compressor (about 300 μJ, 7 fs, 1 kHz). Most of the pulse's energy (the "pump" arm) is used to generate XUV radiation in argon, and a small part (the "probe" arm) is collinearly recombined with the XUV with a variable delay, and with a controllable energy (using the half-wavelength plate and a polarizer). The recombination mirror is a convex metallic mirror with a central hole, with a curvature designed to match the reflected IR (the probe) wavefront with the XUV wavefront. A toroidal mirror at a grazing incidence focusses both XUV and probe IR beams in a detection chamber (not shown).

holes ($\sim$ 3 mm) to minimize gas flow from the generation to the other chambers. The beam focussing is done with a spherical mirror, with focussing lengths of typically 50 cm, and small angles were used to minimize astigmatism. The XUV radiation is separated from the driving IR radiation using free-standing thin metallic filters (typically 200 nm of aluminum, depending on the desired spectral characteristics), and the recombination mirror clips the outer region of the XUV beam: this increases the ratio between short/long trajectory radiation in the final beam, since the long trajectory radiation has a higher divergence.

The probe arm is split from the main one using a broadband ultrafast beamsplitter, and its energy is controlled with a typical half-wave plate and polarizer combination. It is then sent into the recombination chamber. A curved mirror with a central hole is used for combining the XUV with the IR probe. Its hole size allows for most of the XUV radiation to go through, but the IR probe is large enough that enough is reflected off of it. Since the XUV beam is divergent and the IR probe is collimated, the recombination mirror is curved to match the reflected IR's curvature to the XUV's. Two delay stages are used: a *rough* motorized stage and a *fine* piezo mount. Later, a feedback loop was implemented to stabilize the pump-probe delay (Fig. 4.11). Because of the long length of the Mach-Zehnder arms, the delay between pump and probe arms would drift due to thermal effects. To compensate for this, an active stabilization system was implemented, which uses the IR beam itself for stabilization. This active stabilization was used in Paper **XI** and the related experiment is discussed in Section 4.5.3.

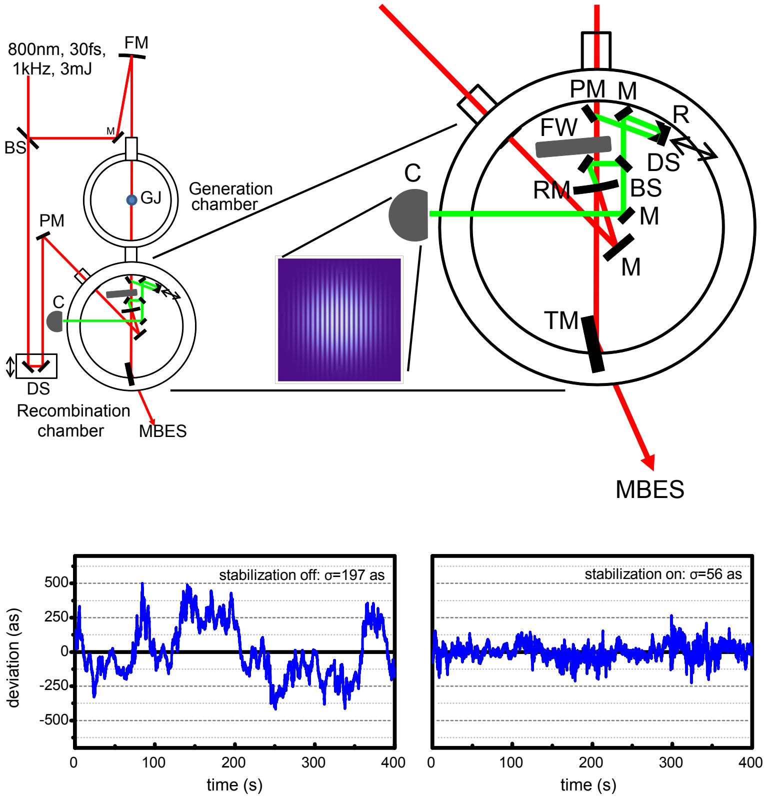
800nm, 30fs,
1kHz, 3mJ
FM
M
BS
GJ
Generation
chamber
PM
C
DS
Recombination
chamber
MBES
PM
M
R
FW
DS
C
RM
BS
M
M
TM
MBES
stabilization off: σ=197 as
stabilization on: σ=56 as
deviation (as)
500
250
0
-250
-500
0
100
200
300
400
time (s)
time (s)

Figure 4.11: HHG generation and detection setup with active stabilization. The existing setup was modified to improve the timing stability between the XUV and the IR probe beam. The secondary Mach-Zehnder interferometer is shown in green. A small portion of the generating beam is removed with a pickup mirror (PM) before the aluminum filter (FW) and sent to a delay line (R, DS). A part of the probe IR beam leaks through the "holey" mirror (RM) and is combined with the previous leaked beam in a beam-splitter (BS) with a small displacement. The resulting beam is sent to a webcam where a fringe pattern (due to the noncollinear arrangement) is recorded (inset, showing a simulated interference pattern). A bandpass filter (not shown) before the camera decreases the spectral bandwidth, increasing the temporal coherence and allowing for delays much longer than the pulse temporal width without loosing fringe visibility. A software tracks the interference fringe displacement and sends a feedback signal to the piezo translator (PM).

4.4 Characterization

As discussed before (see Chapter 3), linear detection is not sufficient for a temporal characterization of ultrashort pulses, and this holds in the attosecond domain. Unfortunately, the reachable intensities on the XUV region are usually too low to directly achieve nonlinear effects (although it is possible, see e.g. [135–137]). A solution for this is to use the IR field together with the XUV, since photoionization processes in the presence of an external IR field depend on the time characteristics of both fields.

4.4.1 Photoionization

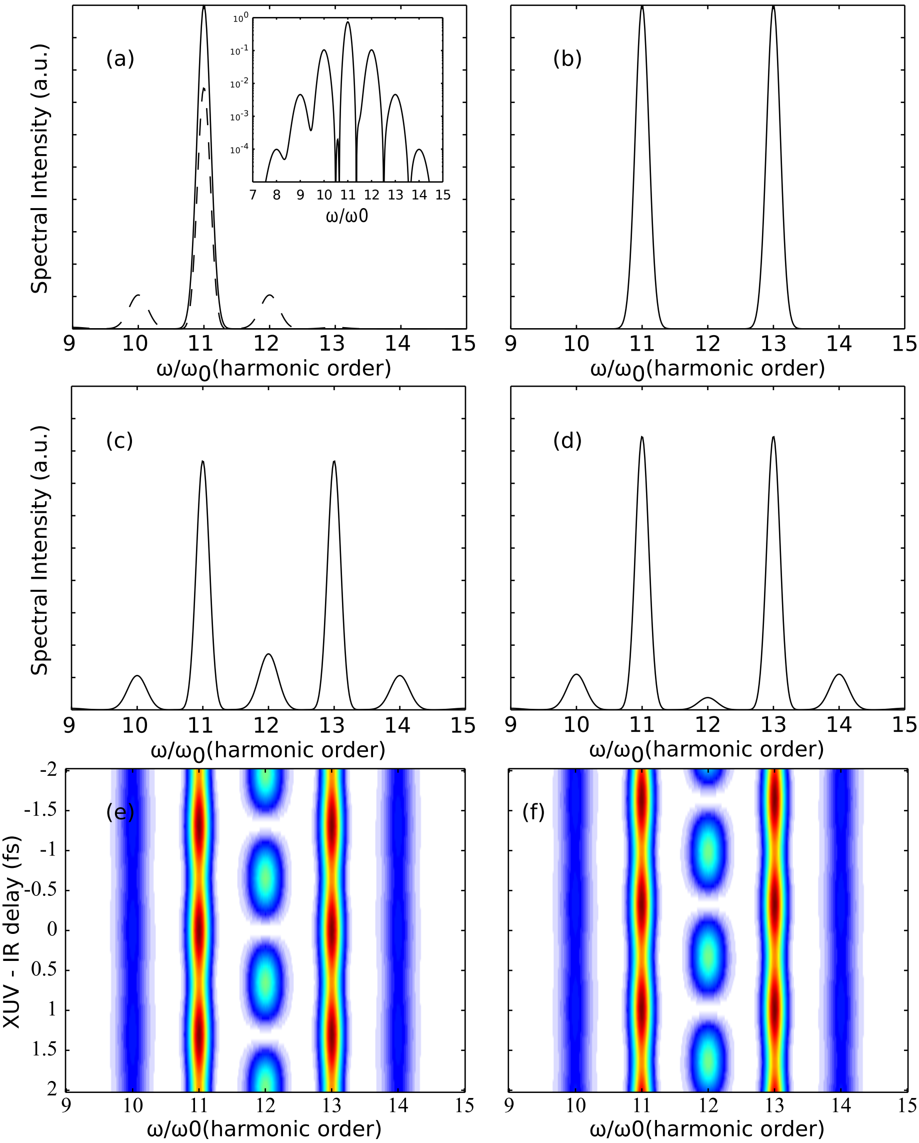

Figure 4.12: (a) An isolated photoelectron harmonic (continuous line) and the same spectrum after applying an IR field (dashed line). Sidebands are created with rapidly falling amplitudes (inset shows same plot in logaritmic scale). (b) A different spectrum, with two well separated harmonics. When an IR field is applied, the sidebands from each harmonic will interfere, with an amplitude depending on their relative phases (c) and (d). As the delay between the harmonics and the IR is scanned (e) and (f), the sidebands intensity also varies. The maxima and minima positions depend on the relative phase between the harmonics.

When a light field (here $\mathbf{E}_{XUV}(t)$) interacts with an atom, ionization might occur. The probability of getting an electron with momentum $\mathbf{p}_f$, is $P(\mathbf{p}_f) \propto |a(\mathbf{p}_f)|^2$, with [138]

$$a(\mathbf{p}_f) = -i \int \mathbf{d}(\mathbf{p}_f)\mathbf{E}_{XUV}(t) \exp\left[\frac{i}{\hbar}\left(I_p + \frac{\mathbf{p}_f^2}{2m}\right)t\right] dt, \tag{4.7}$$

where $a(\mathbf{p}_f)$ is the amplitude of the electronic wave as a function of momentum $\mathbf{p}_f$, $\mathbf{d}(\mathbf{p}_f)$ is the dipole transition matrix element (whose magnitude can be measured experimentally [139–141]), m is the electron mass, and I_p is the ionization potential. The above expression is simply the Fourier transform of the field $\mathbf{E}_{XUV}(t)$, with a response curve $\mathbf{d}(\mathbf{p}_f)$, at the frequency $\hbar\omega = \mathbf{p}_f^2/(2m)$, so the photoelectron spectrum maps the electric field spectrum of the incident light. As with an optical spectrometer, this carries no information about the time properties of the XUV field. As seen before, a nonlinear process is needed for temporal characterization: this nonlinear response is provided by the presence of the IR field. Its effect can described under the strong field approximation (SFA), and the previous momentum distribution becomes [138]

$$\begin{aligned} a(\mathbf{p}_f, \tau) = -i \int & \mathbf{d}[\mathbf{p}_f + e\mathbf{A}(t)]\mathbf{E}_{XUV}(t-\tau) \\ & \times \exp\left[\frac{i}{\hbar}\left(I_p + \frac{\mathbf{p}_f^2}{2m}\right)t\right] \exp\{i\phi_{IR}(\mathbf{p}_f, t)\}dt, \end{aligned} \tag{4.8}$$

where

$$\phi_{IR}(\mathbf{p}_f, t) = \frac{1}{2m\hbar}\int_t^{+\infty} \left[2e\mathbf{p}_f \cdot \mathbf{A}(t') + e^2\mathbf{A}^2(t')\right] dt'. \tag{4.9}$$

The IR field acts as a *phase modulator* of the electronic wave packets. This is formally the same as frequency modulation (FM). A simple case occurs for low IR intensities: in this scenario, $\mathbf{A}^2(t)$ can be neglected compared to $\mathbf{A}(t)$, and the modulation is a sinusoidal wave. This will produce sidebands on the electron spectrum, with the amplitude of the sidebands decreasing as a Bessel function (Fig. 4.12). These sidebands do not carry any information about the harmonics phase, but if the photoelectron spectrum consists of several harmonics, and the sidebands of different harmonics overlap, this will lead to an interference (or *beating*) of the sideband signal. This interference depends on the phase difference between the harmonics and on the applied IR field (Fig. 4.12). This is the basic idea behind the RABBITT (Reconstruction of Attosecond Beating By Interference of Two-photon Transitions) [142, 143] method, as will be discussed below.

4.4.2 RABBITT

Figure 4.13 shows the quantum paths[1] used in RABBITT. The interference can be used to characterize attosecond pulses, provided their properties do not change from one pulse to another in the train. The phase difference between adjacent harmonics causes a beating of the sidebands [142]

$$S_q(\tau) \propto 1 + \cos(2\omega\tau - \Delta\phi_q - \Delta\phi_q^{at}) \tag{4.10}$$

---

[1] There are actually more paths, if one considers higher-order processes, but these will usually be much weaker.

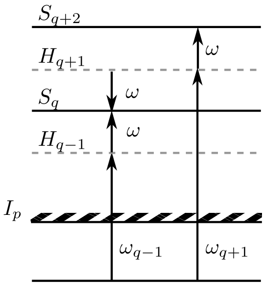

Figure 4.13: Photon-picture of different photon energy combinations leading to interference (sidebands).

where τ is the time delay between the XUV and the IR field, ω is the driving field frequency, $\Delta\phi_q = \phi_{q+1} - \phi_{q-1}$ is the phase difference between adjacent odd harmonics, and $\Delta\phi_q^{at}$ is the *intrinsic* phase difference due to the ionization process itself.

The characterization of the harmonics' relative phase assumes that this $\Delta\phi_q^{at}$ is negligible or well known. In this case, from the sidebands' beating positions (Fig. 4.15, right column) the phase between harmonics can be measured. The XUV spectrum can be measured separately (by simply switching off the IR field) and the time profile can be reconstructed from the spectrum and the retrieved inter-harmonic phases. The RABBITT technique is limited in the sense that only an average pulse is reconstructed, i.e., the pulse to pulse variations in the attosecond pulse train are not detected. Furthermore, the *absolute* phase is not measurable either. Therefore, one of the measured harmonics' phase is assumed to be zero, and the other phases are obtained by recursively concatenating the measured phase differences

$$\phi_{q+1} = \phi_{q-1} + \Delta\phi_q \tag{4.11}$$

and the pulses are then reconstructed as

$$U(t) = \sum_{odd\ q} A_q \exp\left\{-i(\omega_q t + \phi_q)\right\}, \tag{4.12}$$

where A_q are the harmonics' amplitudes.

The capability to measure not only the harmonic phase but also the intrinsic atomic phases is very interesting, and has been exploited to study the phase of resonant two-photon ionization in helium in Paper **X** (see Section 4.5.2) and the photoemission time-delays between different electronic shells in argon in Paper **XI** (see Section 4.5.3).

4.4.3 Streaking and FROG-CRAB

A different approach has to be taken for the characterization of isolated pulses, since there are no harmonics to start with. It still uses a cross-correlation technique, and photoionization in the presence of an IR field, but a stronger IR field is employed to strongly distort the photo-electron spectrum, and a perturbative analysis is not valid anymore. This regime is called *streaking*, and can be described with a simple, semi-classical two-step picture. An electron from the outer shell of an atom is ionized by interaction with an attosecond pulse. Depending on the ionization time, it is then accelerated or decelerated (it gains or loses energy) by the IR field (as in a streaking camera). If the photo-electron wavepackets are *chirped* they might get "compressed" or "stretched" by the IR field (see Fig. 4.14).

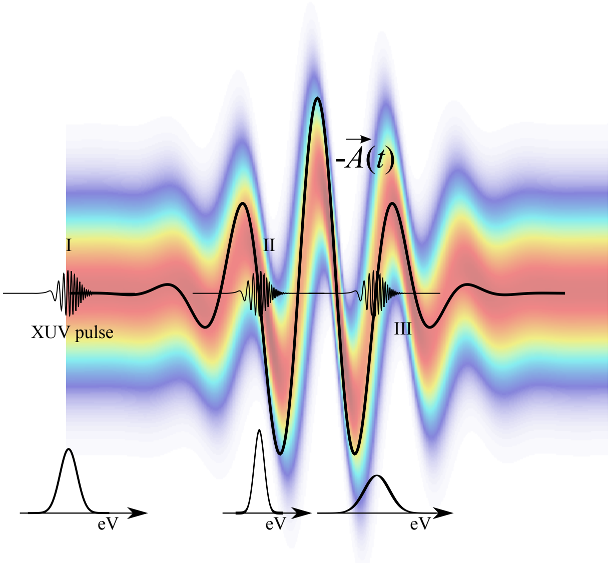

Figure 4.14: *Naive* picture of what is going on during a streaking experiment. In the absence of interaction between the XUV pulse and the fundamental pulse (case I) the photoelectron energy spectrum maps the XUV optical spectrum. In the presence of a varying $\mathbf{A}(t)$ field, the electron bunch is either compressed, if the early part of the wave packet will be decelerated (case II) or stretched (case III) depending on the XUV chirp.

Mairesse and Quéré noted that the Strong Field Approximation expression for the final electron momentum (Eq. 4.8) can, under some approximations, be written as a FROG trace [144]. $d(\mathbf{p})$ is assumed constant within the spectral region of interest, so that Eq. 4.8 can be rewritten as Eq. 3.14 in Section 3.5 [144, 145], with

$$E(t) = E_{XUV}(t) \tag{4.13}$$

and

$$G(t) = \exp\left\{i\phi_{IR}(t)\right\}. \tag{4.14}$$

Then, similar algorithms as for a blind-FROG (see Section 3.5) can be used to extract *both* the XUV field and the gate (which is related to the IR field).

Figure 4.15 shows a comparison between simulated FROG-CRAB and RABBITT scans, for Fourier limit, pure GDD, and pure TOD cases, respectively. In the FROG-CRAB case, an isolated pulse is assumed, as well as an ultrashort IR field, with around 4 fs duration FWHM. For the RABBITT case, a train of pulses is assumed (and hence the harmonics structure), and the IR field is much longer than the scan length. The phase retrieval from the RABBITT scans is straightforward: the sidebands positions directly give us the phase between adjacent harmonics. In the FROG-CRAB case, the

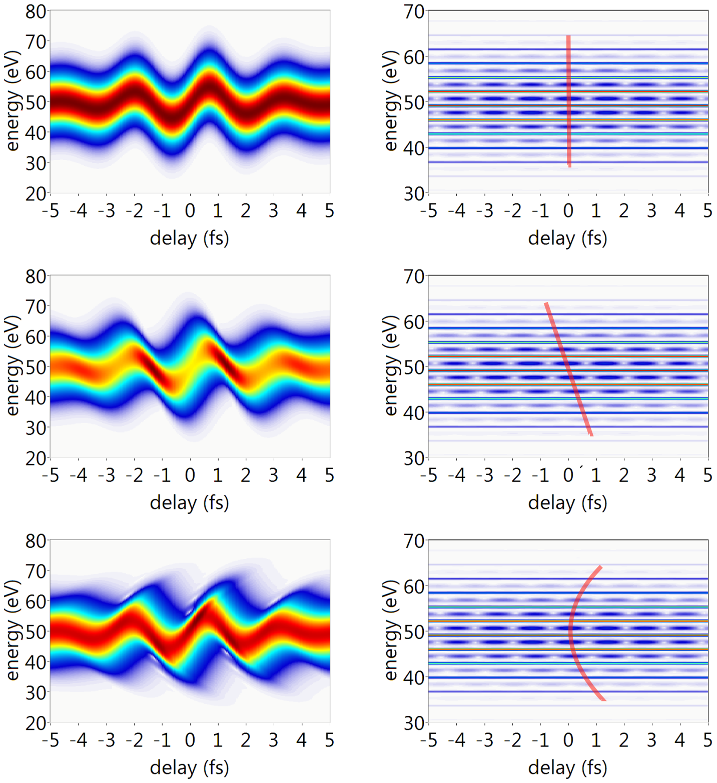

Figure 4.15: Comparison between a measurement using the FROG-CRAB technique (left column) and a measurement using the RABBITT technique (right column). On the former case, an isolated pulse is being characterized while in the latter we have a train of pulses. Top row corresponds to a flat phase (Fourier-limited) XUV pulse, middle row to pure GDD, and bottom row to pure TOD.

FROG algorithm can be used to find the XUV and the IR pulses that better fit the measured (or simulated, in this case) data.

4.4.4 Experimental Detection

In the experiments carried out in Lund, the photoelectron detection was done with a Magnetic Bottle Electron Spectrometer (MBES) [146, 147]. Its operation is depicted in Fig. 4.16, and it is based on time-of-flight (TOF) spectroscopy. As the radiation ionizes a gas (typically argon was used in the experiments), free electrons are created, whose kinetic energy (and therefore, speed) depends on the radiation photon energy. A strong magnetic field, parallel to the flight tube, is applied in the ionization region, decreasing in strength toward the detector. The electrons ejected from ionization spiral around the magnetic field lines, and as the field strength decreases, their velocities are slowly converted into velocity in the flight tube direction. In this way, electrons emitted within a solid angle of 2π sr are collected.

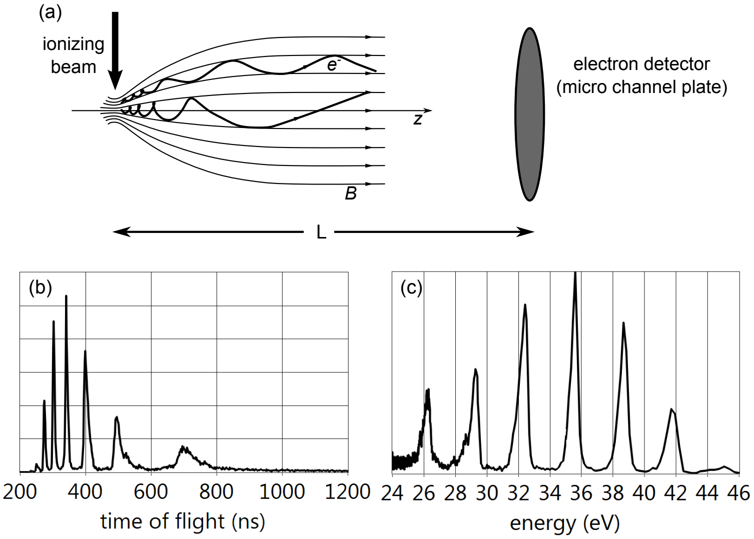

Figure 4.16: Photoelectron detection with a Magnetic Bottle Electron Spectrometer (MBES). (a) A magnetic field collects electrons emitted in a 2π steradian angle towards the detector, in this case a Micro-Channel Plate (MCP). The electrons are counted as a function of arrival time (b), which can then be converted to an electron count as a function of kinetic energy (c).

The electrons are detected as a function of arrival time (Fig. 4.16b), and from this their kinetic energy can be derived, as well as the associated photon energy

$$\hbar\omega = I_p + \frac{\alpha}{(t - t_0)^2}, \tag{4.15}$$

where I_p is the ionization potential, t_0 is a time-delay introduced to take into account the system synchronization, and α is a constant that depends on the MBES length. In practice, to calibrate the system we use a long pulse to generate harmonics, and the parameters are adjusted to match the expected harmonics frequencies (Fig. 4.16b).

Typical measurements with long and short IR pulses are presented in Fig. 4.17, where a RABBITT scan and a streaking scan are shown. The RABBITT scan (Fig. 4.17b) was made using the long IR pulses as a source for XUV generation, leading to a harmonic signal (Fig. 4.17a) and the IR intensity levels at the probe arm are kept low enough as to not deplete the fundamental harmonics signal, while giving enough signal at the sidebands frequencies (where the even-numbered harmonics would be). Figure 4.17d shows an example of a streaking experiment done in Lund using the a hollow-core fiber compressor as a HHG source. The generated IR pulses were not short enough to produce isolated attosecond pulses (as can be seen from the harmonics structure). The interference structure visible at delays beyond the estimated pulse width indicate the presence of strong satellite pulses: in these conditions, a longer scan would have been necessary to perform a FROG-CRAB retrieval.

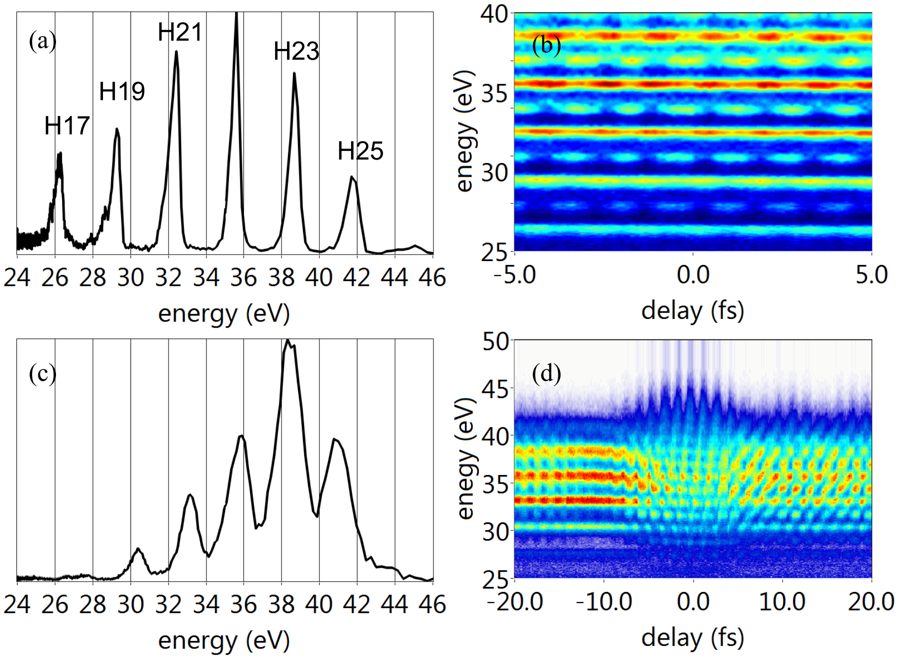

Figure 4.17: (a) A typical photoelectron spectrum from HHG in argon with a relatively long ($\sim 30\ fs$) IR pulse, and the corresponding RABBITT trace (b). (c) Same as (a), but with a short ($\sim 7\ fs$) IR pulse, obtained from a hollow-core fiber compressor.(d) A streaking measurement, where the probe IR intensity is much higher than the one used in (b).

4.5 Applications

Finally, we present some applications of harmonic pulses and attosecond pulse trains carried out in this thesis work.

4.5.1 XUV Holography

The temporal and spatial coherence of the HHG radiation makes it suitable for holography. The basic concept behind holography is to record an interference pattern, which contains information about the (spatial) phase of a wave.

The concept is similar to that presented in the section about spectral interferometry (Section 3.2) and it consists in adding two coherent fields so as to obtain an interference pattern. Suppose we have an *object* wave $O = o(x, y)$ and a *reference* wave $R = r(x, y)$. At a given plane their interference pattern is given by

$$\begin{aligned} I(x, y) &= |o(x, y) + r(x, y)|^2 \\ &= |o(x, y)|^2 + |r(x, y)|^2 + o^*(x, y)r(x, y) + o(x, y)r^*(x, y) \end{aligned} \tag{4.16}$$

If the reference wave is a plane wave, then the last term, $o(x, y)r^*(x, y)$ is simply the object wave that we want. As with spectral interferometry, if the above terms have different carrier frequencies, it is possible to separate them. The “simple” solution to reconstruct the object wave is to use a tilted plane wave as a reference [148]. This is called *off-axis* holography. Since this is hard to realize in the XUV domain, a setup similar to the original one by Gabor [149] (inline) is employed. The object is simply placed in front of a reference wave (partially obstructing it) and diffracts it. An observation screen detects the interference between the reference and the diffracted waves.

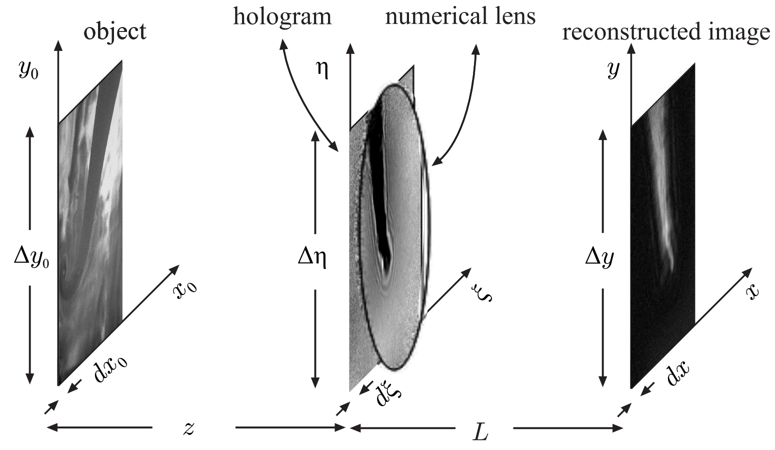

Figure 4.18: Numerical reconstruction of a digital hologram. A numerical lens is applied to the measured hologram, and Fresnel propagation is used to simulate propagation to the observation plane.

The problem now is how to extract information about the object from the recorded interference pattern. In an all-optical hologram, this is accomplished by developing the recorded pattern as a transparency, illuminating it, and using a lens (which in some cases could simply be the observer’s eye) to bring the object to focus.

In the case of digital holography, the imaging operation is done numerically: a numerical lens is applied to the hologram (Fig. 4.18), and the Fresnel approximation is used to simulate the propagation between planes. Unfortunately, in the case of inline holography, more information will be contained in the formed image (namely the infamous twin-image) but since it will not be brought to focus it is still possible to discern an image of the original object, but with added noise.

In Paper **IX**, the high photon flux of the 10 Hz HHG source (described in Paper **VIII**) has been used to perform single-shot XUV holography (Fig. 4.19). An XUV Schwarzschild objective was used slightly tilted to focus the XUV radiation before the object (Fig. 4.19b), giving a magnified interference pattern at the observation plane of the MCP (Fig. 4.19c). The Schwarzschild objective has a reflective coating that decreases the spectral width of the XUV radiation, increasing the coherence length.

A more robust algorithm [150] was used to iteratively retrieve the object’s amplitude. The basic principle is the same as described before, but the field is iteratively propagated back and forth from the object to the hologram plane and vice-versa. At each iteration, constraints are applied (in the hologram plane the intensity pattern is

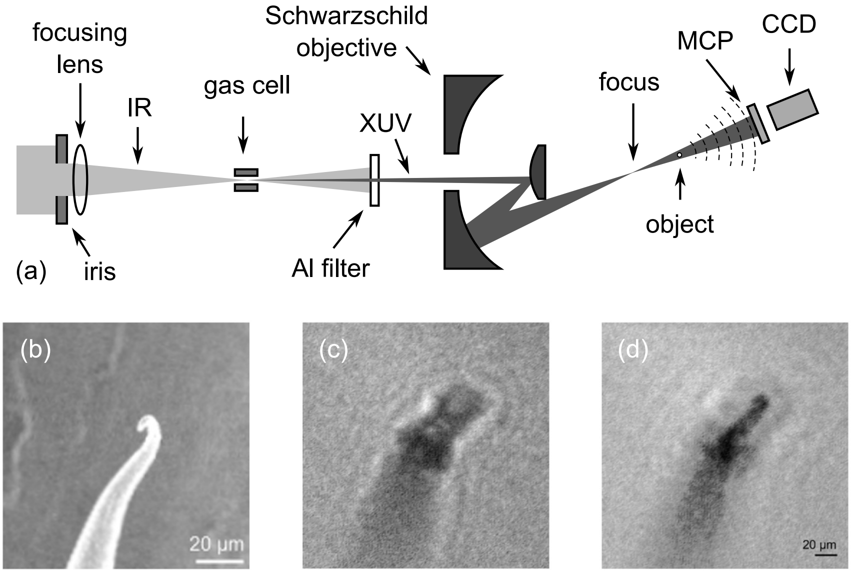

Figure 4.19: (a) XUV holography setup based on the 10 Hz HHG source. (b) Scanning tunneling microscope (STM) image of a deformed STM tip, its single-shot hologram (c) and corresponding reconstruction (d) using an iterative algorithm. From Paper **IX**.

known, whereas it is also known that the object cannot have a transmission higher than 1), leading to an increased signal-to-noise ration of the retrieved object (Fig. 4.19d).

4.5.2 Resonant Two-Photon Ionization

The RABBITT technique can be used to characterize the Group-Delay between adjacent harmonics. This assumes, however, that there is no *intrinsic* phase of the photoelectrons due to the photoemission process itself. Recalling again the RABBITT beating

$$S_q(\tau) \propto 1 + \cos(2\omega\tau - \Delta\phi_q - \Delta\phi_q^{at}) \tag{4.17}$$

By comparing RABBITT measurements done in different conditions, $\Delta\phi_q^{at}$ can be measured, and insight into atomic processes can be obtained. In Paper **X** the RABBITT technique is used to study the phase of photoelectron in a two-photon ionization in helium.

Figure 4.20 shows a schematic description of the principle of the experiment: the transition energy from $1s^2$ to $1s3p$ in helium (23.09 eV) roughly matches the energy of the 15th harmonic (23.25 eV) of the IR field (1.55 eV, for a central wavelength of 800 nm). This level offers a path to reach the continuum through a resonance. The ionization potential of He (24.59 eV) corresponds to an energy slightly below that of the 16th harmonic (24.80 eV) of the IR field. There is no HHG field at that frequency (since it is an even harmonic) but it can be reached through multi-photon processes, by using the IR field. The difference to a “normal” RABBITT measurement is that one of the quantum paths to the 16th sideband involves a resonant state.

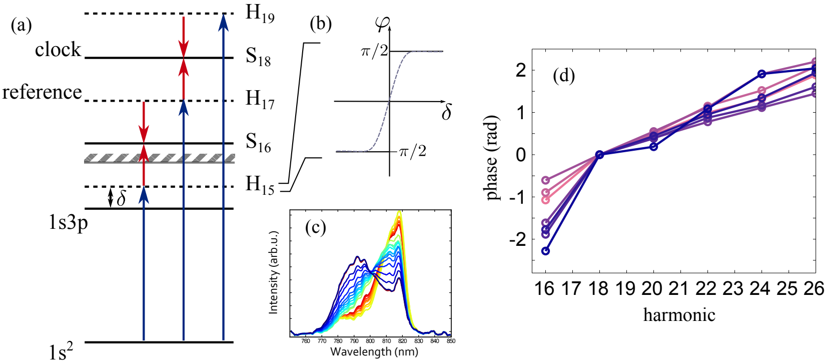

Figure 4.20: (a) Energy levels in helium and the considered transitions. The energy of harmonic 15 roughly matches the $1s^2 \rightarrow 1s3p$ transition energy in He. (b) Typical phase behavior for transitions around a resonance. (c) Spectral shaping of the laser spectrum to scan energy transitions around the 1s3p transition. (d) Phase measurements at different central laser wavelengths.

Changing the fundamental wavelength of the generating IR field, all the harmonics have their frequency changed as well. The 15th harmonic frequency can then be swept across the resonant transition. For this, an AOPDF (a DAZZLER, see Section 2.3.2) was used to shape the fundamental IR spectrum (see Fig. 4.20c). A phase shift of the 16th sideband relative to the others is observed as the detuning δ is swept across the resonance.

Another way of observing this phase shift is by *inducing* a change of the $1s^2 \rightarrow 1s3p$ transition energy. Instead of sweeping the 15th harmonic energy, the IR field can induce a Stark shift on the energy levels. By changing the IR intensity, the transition energy is made to move across the 15th harmonic energy with a similar effect. Comparing both measurements allowed us to determine the AC Stark shift of the $1s^2 \rightarrow 1s3p$ transition energy.

The details about this experiment and the theory underlying it can be found in Paper **X**.

4.5.3 Time Delay Measurements

When an XUV pulse interacts with an atom, if the photon energy is high enough, ionization might occur. In the quantum picture, this means that the associated electronic wave packet (EWP) expands and is no longer confined to the vicinity of the nucleus. As the EWP spreads away from the nucleus, its group delay depends on the interaction with the remaining core potential. By comparing streaking or RABBITT traces from different electronic shells, information about the ionization process can be obtained.

Time delay between the formation of electron wave packets originating from different atomic orbitals were first observed by Schulze *et al* [152] using isolated attosecond pulses and streaking. Previously, Cavalieri *et al* [153] had performed similar experiments in solids.

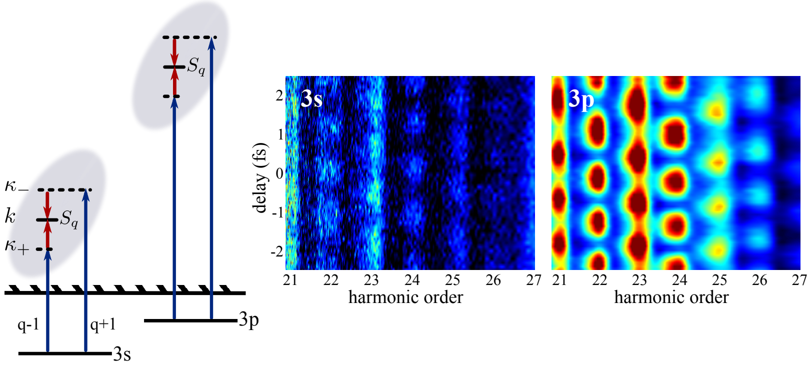

Figure 4.21: Photoionization from 3s and $3p$ shells, and a RABBITT trace containing both channels. Even if the energy scales are the same, the different ionization potential leads to different final photo-electron energies, which do not overlap (adapted from [151]).

The work described in Paper **XI** follows the work previously done in Lund by Klünder *et al* [151] on time-delay emission in argon using not isolated attosecond pulses and streaking measurements, but trains of pulses (and a spectrum made of harmonics) and the RABBITT technique. An improvement was made to the setup, by adding an active stabilization of the Mach-Zehnder interferometer (see Section 4.3.3 and Fig. 4.11).

CHAPTER 5

SUMMARY AND OUTLOOK

This thesis describes the work undertaken in Porto and Lund, with the idea of optimizing the sources and diagnostics for generating well-controlled attosecond pulses. The emphasis was on the laser side of the problem, with most of the work on generation and characterization of ultrashort laser pulses. Papers **I** and **II** describe and discuss the CEP stabilization of a multi-milijoule laser system. CEP detection at kHz repetition rates is also demonstrated. Papers **III**, **IV**, **V**, and **VI** introduce techniques for the characterization, both temporal and spatial, of ultrashort laser pulses.

The *d-scan* technique (Papers **III** and **IV**) shows promising possibilities for ultrashort laser pulse characterization beyond the usual bandwidth limitations. Even if experimental simplicity was the main motivation behind its development, it turned out to be extremely robust and relaxed with respect to bandwidth. It is not clear though, at this point, which are the real limitations. Research into faster, more robust and generic retrieval methods could make easier the characterization of ultrashort pulses in the single-cycle regime. Attosecond pulse characterization might also benefit from developments on femtosecond pulse characterization techniques. Papers **V** and **VI** demonstrate a simple technique for spatiotemporal characterization of ultrashort laser pulses. Especially for the case of ultra broadband pulses, spatiotemporal effects can be of extreme importance when used for highly nonlinear effects (e.g., HHG).

Paper **VII** describes a simple setup based on chirped mirrors and microscope objectives to achieve high intensities with low-average power oscillators. The estimated achieved intensities, even if below the necessary to induce HHG, give some hope for future development of compact and inexpensive table-top HHG sources.

Papers **VIII** and **IX** report respectively on the characterization and application of the 10 Hz HHG source in Lund. The spatial and spectral properties were studied in Paper **VIII**, and absolute energy measurements were also performed. In Paper **IX** this source was used for single-shot holography in the XUV region. This kind of setup has the potential for femtosecond time-resolved pump-probe imaging experiments in the XUV region.

Finally, in Papers **X** and **XI** the 1 kHz HHG source in Lund was used to study atomic properties in Helium and Argon. The same technique used to characterize trains of attosecond pulses (RABBITT) can be used to extract phase information from the ionized electrons. These in turn carry information about atomic properties.

In Paper **X** the RABBITT technique was used to characterize the phase properties of two-photon two-color ionization through a resonant level in Helium. In Paper **XI**, the same technique was used to study the photoemission delay from different valence shells in Argon.

Since the beginning of this thesis, a lot of changes have happened in both laboratories, in Porto and in Lund. The kilohertz CPA system in Lund has recently been upgraded to deliver shorter and even more energetic pulses. Emphasis is currently being placed on improving its stability: proper CEP detection and control relies on a high pulse-to-pulse source stability, and the same goes for spectral broadening and pulse compression with hollow-core fibers. A new HHG setup is also planned, more compact and stable. These will be key factors for producing isolated attosecond pulses. The larger bandwidth of the new system means it will also have a higher tunability range. In parallel, a new laser systems have been installed in Lund, a high repetition rate (200 kHz) optical parametric chirped pulse amplifier (OPCPA) capable of delivering 6 fs pulses with energies of around 10 μJ.

The CPA system in Porto has also been modified several times during the course of this thesis. The work on its stability, and on the hollow-core fiber compressor, made it recently capable of reliably producing sub-5 fs pulses, with a CEP stability of less than 100 mrad. An HHG setup is expected to be built in the near future.

COMMENTS ON THE PAPERS

I **Carrier-envelope phase stabilization of a multi-millijoule, regenerative-amplifier-based chirped-pulse amplifier system**
In this paper we perform the CEP stabilization and control of the laser system in Lund. I worked on the laser and the f-2f setup, and on the system optimization for CEP-stable operation. I also took part in writing the manuscript.

II **High-speed carrier-envelope phase drift detection of amplified laser pulses**
In this paper we show a fast CEP phase detector, based on a CCD array and FPGA electronics, capable of single-shot operation at the laser repetition rate. I worked on the experimental setup (amplifier, hollow fiber compressor and f-2f detection).

III **Simultaneous compression and characterization of ultrashort laser pulses using chirped mirrors and glass wedges**
In this paper we show a simple method of characterizing ultrashort laser pulses. I had the original idea, developed the algorithm and performed most of the experimental work and experimental analysis, and wrote the article.

IV **Characterization of broadband few-cycle laser pulses with the d-scan technique**
In this paper we study and show the capabilities and limitations of the d-scan technique for ultrashort laser pulse characterization. Its applicability is experimentally demonstrated on demanding situations. I made the simulations and improved the phase-retrieval algorithm to deal with the more complex sources. I took a major role on the experimental setup and wrote the paper.

V **Spatiotemporal characterization of few-cycle laser pulses**
In this paper we study the spatio-temporal characteristics of ultra-short pulses, specifically issues on focusing. I took part in the temporal compression and characterization.

VI **Generation and spatiotemporal characterization of 4.5-fs pulses from a hollow-core fiber compressor**
In this paper we study the spatio-temporal characteristics of ultra-short pulses from a hollow-core gas-filled fiber. I took part on building the experimental setup, and on the temporal compression and characterization.

VII **Space-time focusing of phase-stabilized nanojoule-level 2.5-cycle pulses to peak intensities $> 3 \times 10^{13}$W/cm^2 at 80 MHz**
In this paper we show the relative high intensities achievable directly from a laser oscillator, using microscope objectives and chirped mirrors. I took part on building the experimental setup, processing and analyzing the data, and writing the manuscript.

VIII **Spatial and spectral properties of the high-order harmonic emission in argon for seeding applications**
In this paper we study the spectral and spatial properties of radiation from high-harmonic generation in argon. I took part in building and optimizing the HHG setup and in the absolute energy measurements, and wrote the acquisition and data processing software. I also took part in the interpretation of the data and in the writing of the manuscript.

IX **Single-shot holography using high-order harmonics**
In this paper we demonstrate single-shot holography from an HHG source. I took part in building the HHG source and the holography setup, and wrote the signal acquisition code and real-time reconstruction of the XUV holograms.

X **Phase Measurement of Resonant Two-Photon Ionization in Helium**
In this paper we study the phase properties of two-photon resonant ionization of He. The phase information is gained by cross-correlating an IR field with a high-order harmonic comb, where the lowest harmonic is resonant with the bound $1s3p$ state in He. I took part in preparing the HHG and RABBITT setup and data acquisition, and on the spectral shaping of the driving field for the wavelength-dependence study.

XI **Photoemission-time-delay measurements and calculations close to the 3s-ionization-cross-section minimum in Ar**
In this paper we study the photoemission time delay in argon. I took part on the HHG setup, the RABBITT setup, and on the active stabilization of the interferometer.

ACKNOWLEDGEMENTS

During the years spent commuting between Porto and Lund i had the opportunity to meet and work with many and very interesting people. This work would not have been possible without their help and support.

I was fortunate enough to have had not only one, but two amazing supervisors. I thank Anne L'Huillier and Helder Crespo for all they taught me and for their enthusiasm, but mostly for their support and patience.

I was also fortunate to work in two very different places. I would like to thank the guys from my group in Lund: my co-supervisor Cord Louis Arnold for telling me so much about axicons, Filippo Campi, Stefanos Carlström, Diego Guénot, Christoph Heyl, David Kroon, Eleonora Lorek (kompisen!), Linnea Rading, Piotr Rudawski, Esben Larsen, Fernando Brizuela, Byunghoon Kim, Marija Kotur, Chen Guo, Per Johnsson, Johan Mauritsson, and past members (but always in my heart...) Michele Giunta, Xinkui He, Jörg Schwenke, Marcus Dahlström (sorry about the office decoration), Thierry Ruchon (valeu, cara), Thomas "*laser aligner extraordinaire*" Fordell, Marko Swoboda, Dr. Erik Mansten, Thomas Remetter, and Rafal Rakowski. Hiermit druecke ich meine tiefste Dankbarkeit an Kathrin Klünder aus. Du warst meine beste Mitbewohnerin, Kollegin und Freundin die man sich nur vorstellen kann. I managed to interact with some other people at the Atomic physics department as well. I would like to thank Jenny Karlsson for (almost) never saying "no" to a coffee, Guillaume Genoud, Pontus Svenmarker, Erik Mårsell, and Aboma Merdasa.

It was also a pleasure to learn all about lasers from Anders Persson, some stuff about atoms with Mathieu Gisselbrecht, and to get "roof" with Franck Lépine. Finally i would also like to thank some of those who made, or make, Atomfysik such a great place to work at. In particular Sune Svanberg, Claes-Göran Wahlström, Minna Ramkull, Camilla Nilsson, Harriett Lindahl, and Bertil Hermansson.

Other people i met in Lund didn't contribute *at all* to this work. For this i'm indebted to them. I would like to thank the Portuguese crew, the very same i tried to avoid when coming to Sweden (more or less in order of appearance): Sofia Olim (trenga), Telmo Santos, Luís Pegado, Salomé Santos, Tânia Silva, Bruno Silva, Bruno Medronho, Tiago Matos, Sara Costa, José Teles, Irene Pala, and Ana Abreu. Um muito obrigado para o Tiago Ferreira, o Eusébio do NMR cá de Lund. I had the opportunity to meet non-Portuguese as well: i would like to thank Nina Reichhardt for always lending me different kitchen appliances, Charlotte Gustavsson, Çelen Cenker and Irem Nasir (respectively my 2nd and 3rd favorite Turks), Mariano Massa, Stefano Macrelli, Susana Ribeiro, Sandra Lemos, David Schwarzelmüller, Séverine Cozzi, Kathrin Fingerle, Vera Chudnikova (you google it), and Edouard Berrocal.

I had the opportunity to share a house with some “different” and “special” friends. I especially thank Iris Dumas (and Neva), Jessica Reed, Thomas Heissat, Caroline Blondel, Camille Borella, Silvio Scuderi, Cecile Rousseau, Sophie, Janina Sprenger, Natalia Avaliani (wait for me to watch the next episode, ok?), Mike Kondrashov, Sebastian Ramisch, and Juan Diego.

It was also a pleasure to share the laboratory in Porto with Alexandra Amorim, António “Toni” do Aido, Francisco Silva, Cledson Santana, Ana Sofia, José Miguel Teixeira and Pedro Oliveira. A special “grazie mille!” goes to Fabio Giambruno, who taught me (among other things) very specific Italian safety techniques. I’m also eternally grateful to Francisco Carpinteiro for his eternal patience and over-engineering late at night in the workshop and to Florbela Teixeira for telling me all about Lund. It was also great to be able to have someone available for a coffee break when not working. João Maria Barbosa de Noronha Freire de Andrade (uf...), Juliana Oliveira, Susana Oliveira, and João Penedones (ainda estou à espera que me resolvas o integral) did a great job with the almost scientific discussions. And i acknowledge FCT’s support (grant FCT SFRH/BD/37100/2007). A word of gratitude goes to Profs. Luís Bernardo, António Pereira Leite, João Bessa Sousa, João Lopes dos Santos, Paulo Marques, David Schmool, Carla Rosa, João Pedro Araújo, and Joaquim Agostinho Moreira.

I also worked with some of *nuestros hermanos*: muchas gracias a Benjamín Alonso, Íñigo Sola, e Rosa Weigand.

Uma palavra final de agradecimento ao Carlos França e ao Tiago Dias, por terem a paciência que têm (menos o Carlos quando bebe uns copos). Um agradecimento *ainda mais* especial à minha família: às Dulces, aos Manueis, à Isabel, e aos novos membros João e Mariana.

REFERENCES

1. T. H. Maiman. *Stimulated optical radiation in Ruby.* Nature **187**, 493 (1960).

2. Laura Garwin, Tim Lincoln and Steven Weinberg. *A Century of Nature: Twenty-One Discoveries that Changed Science and the World.* University Of Chicago Press 1 edition (2003). ISBN 0226284158.

3. A. McPherson, G. Gibson, H. Jara, U. Johann, T. S. Luk, I. A. McIntyre, K. Boyer and C. K. Rhodes. *Studies of multiphoton production of vacuum-ultraviolet radiation in the rare gases.* J. Opt. Soc. Am. B **4**, 595 (1987).

4. M. Ferray, A. L'Huillier, X. F. Li, G. Mainfray and C. Manus. *Multiple-harmonic conversion of 1064 nm radiation in rare gases.* J. Phys. B **21**, L31 (1988).

5. T. H. Maiman. *Stimulated optical emission in Ruby.* J. Opt. Soc. Am. **50**, 1134 (1960).

6. F. J. McClung and R. W. Hellwarth. *Giant Optical Pulsations from Ruby.* Appl. Opt. **1**, 103–105 (1962).

7. Willis E. Lamb. *Theory of an Optical Maser.* Phys. Rev. **134**, A1429–A1450 (1964).

8. L. E. Hargrove, R. L. Fork and M. A. Pollack. *Locking of HeNe laser modes induced by synchronous intracavity modulation.* Applied Physics Letters **5**, 4–5 (1964).

9. A.J. DeMaria, W.H. Glenn Jr., M.J. Brienza and M.E. Mack. *Picosecond laser pulses.* Proceedings of the IEEE **57**, 2 – 25 (1969).

10. E.P. Ippen, C.V. Shank and A. Dienes. *Passive mode locking of the cw dye laser.* Applied Physics Letters **21**, 348–350 (1972).

11. C. V. Shank and E. P. Ippen. *Subpicosecond kilowatt pulses from a mode-locked cw dye laser.* Applied Physics Letters **24**, 373–375 (1974).

12. P. F. Moulton. *Spectroscopic and laser characteristics of $Ti{:}Al_2O_3$.* J. Opt. Soc. Am. B **3**, 125–133 (1986).

13. J.-C. Diels and W. Rudolph. *Ultrashort laser pulse phenomena.* Academic Press (1996).

14. Optical Society Of America. *Handbook of Optics, Vol. 2: Devices, Measurements, and Properties, Second Edition.* McGraw-Hill Professional 2 edition (1994). ISBN 0070479747.

15. A. Börzsönyi, Z. Heiner, M. P. Kalashnikov, A. P. Kovács and K. Osvay. *Dispersion measurement of inert gases and gas mixtures at 800 nm.* Appl. Opt. **47**, 4856–4863 (2008).

16. E. Treacy. *Optical pulse compression with diffraction gratings.* Quantum Electronics, IEEE Journal of **5**, 454 – 458 (1969).

17. C. V. Shank, R. L. Fork, R. Yen, R. H. Stolen and W. J. Tomlinson. *Compression of femtosecond optical pulses.* Applied Physics Letters **40**, 761–763 (1982).

18. O. Martinez. *3000 times grating compressor with positive group velocity dispersion: Application to fiber compensation in 1.3-1.6 μm region.* Quantum Electronics, IEEE Journal of **23**, 59 – 64 (1987).

19. G. Cheriaux, P. Rousseau, F. Salin, J. P. Chambaret, Barry Walker and L. F. Dimauro. *Aberration-free stretcher design for ultrashort-pulse amplification.* Opt. Lett. **21**, 414–416 (1996).

20. R. L. Fork, O. E. Martinez and J. P. Gordon. *Negative dispersion using pairs of prisms.* Opt. Lett. **9**, 150 (1984).

21. Z. Cheng, F. Krausz and Ch. Spielmann. *Compression of 2 mJ kilohertz laser pulses to 17.5 fs by pairing double-prism compressor: analysis and performance.* Optics Communications **201**, 145 – 155 (2002).

22. Bob Proctor and Frank Wise. *Quartz prism sequence for reduction of cubic phase in a mode-locked Ti:Al2O3 laser.* Opt. Lett. **17**, 1295–1297 (1992).

23. S. Kane and J. Squier. *Grism-pair stretcher-compressor system for simultaneous second- and third-order dispersion compensation in chirped-pulse amplification.* Journal of the Optical Society of America B-Optical Physics **14**, 661–665 (1997).

24. Pink Floyd. Dark Side of the Moon (1990).

25. O. E. Martinez, J. P. Gordon and R. L. Fork. *Negative group-velocity dispersion using refraction.* J. Opt. Soc. Am. B **1**, 1003 (1984).

26. R. Szipöcs, K. Ferencz, Ch. Spielmann and F. Krausz. *Chirped multilayer coatings for broadband dispersion control in femtosecond lasers.* Opt. Lett. **19**, 201 (1994).

27. F. X. Kärtner, N. Matuschek, T. Schibli, U. Keller, H. A. Haus, C. Heine, R. Morf, V. Scheuer, M. Tilsch and T. Tschudi. *Design and fabrication of double-chirped mirrors.* Opt. Lett. **22**, 831 (1997).

28. Nicolai Matuschek, Franz X. Kärtner and Ursula Keller. *Exact Coupled-Mode Theories for Multilayer Interference Coatings with Arbitrary Strong Index Modulations.* IEEE JOURNAL OF QUANTUM ELECTRONICS **33**, 295 (1997).

29. R. Szipöcs and A. Köházi-Kis. *Theory and design of chirped dielectric laser mirrors.* Appl. Phys. B **65**, 115 (1997).

30. Nicolai Matuschek ad Franz X. Kärtner and Ursula Keller. *Analytical Design of Double-Chirped Mirrors with Custom-Tailored Dispersion Characteristics.* IEEE JOURNAL OF QUANTUM ELECTRONICS **35**, 129 (1999).

31. Nicolai Matuschek, Franz X. Kärtner and Ursula Keller. *Theory of Double-Chirped Mirrors.* IEEE JOURNAL OF SELECTED TOPICS IN QUANTUM ELECTRONICS **4**, 197 (1998).

32. C. Froehly, B. Colombeau and M. Vampouille. *II Shaping and Analysis of Picosecond Light Pulses.* volume 20 of *Progress in Optics* pages 63 – 153. Elsevier (1983).

33. R. Thurston, J. Heritage, A. Weiner and W. Tomlinson. *Analysis of picosecond pulse shape synthesis by spectral masking in a grating pulse compressor.* Quantum Electronics, IEEE Journal of **22**, 682 – 696 (1986).

34. A. M. Weiner. *Femtosecond pulse shaping using spatial light modulators.* Review of Scientific Instruments **71**, 1929–1960 (2000).

35. Marc M. Wefers and Keith A. Nelson. *Programmable phase and amplitude femtosecond pulse shaping.* Opt. Lett. **18**, 2032–2034 (1993).

36. C. W. Hillegas, J. X. Tull, D. Goswami, D. Strickland and W. S. Warren. *Femtosecond laser pulse shaping by use of microsecond radio-frequency pulses.* Opt. Lett. **19**, 737–739 (1994).

37. Stefan Rausch, Thomas Binhammer, Anne Harth, Franz X. Kärtner and Uwe Morgner. *Few-cycle femtosecond field synthesizer.* Opt. Express **16**, 17410–17419 (2008).

38. F. Verluise, V. Laude, Z. Cheng, C. Spielmann and P. Tournois. *Amplitude and Phase Control of Ultrashort Pulses by Use of an Acousto-Optic Programmable Dispersive Filter: Pulse Compression and Shaping.* Opt. Lett. **25**, 575–577 (2000).

39. U. Morgner, F. X. Kärtner, S. H. Cho, Y. Chen, H. A. Haus, J. G. Fujimoto, E. P. Ippen, V. Scheuer, G. Angelow and T. Tschudi. *Sub-two-cycle pulses from a Kerr-lens mode-locked Ti:sapphire laser.* Opt. Lett. **24**, 411 (1999).

40. T. Fuji, A. Unterhuber, V.S. Yakovlev, G. Tempea, A. Stingl, F. Krausz and W. Drexler. *Generation of smooth, ultra-broadband spectra directly from a prismless Ti:sapphire laser.* Applied Physics B: Lasers and Optics **77**, 125–128 (2003). 10.1007/s00340-003-1254-z.

41. Stefan Rausch, Thomas Binhammer, Anne Harth, Jungwon Kim, Richard Ell, Franz X. Kärtner and Uwe Morgner. *Controlled waveforms on the single-cycle scale from a femtosecond oscillator.* Opt. Express **16**, 9739–9745 (2008).

42. H. M. Crespo, J. R. Birge, E. L. Falcão-Filho, M. Y. Sander, A. Benedick and F. X. Kärtner. *Nonintrusive phase stabilization of sub-two-cycle pulses from a prismless octave-spanning Ti:sapphire laser.* Opt. Lett. **33**, 833–835 (2008).

43. Helder Crespo. *Cascaded four-wave mixing processes and laser pulse generation in ultrafast nonlinear optics.* PhD thesis Instituto Superior Técnico, Lisbon, Portugal (2006).

44. A. E. Siegman. *Lasers.* University Science Books, Sausalito (1986).

45. O. Svelto. *Principles of Lasers.* Plenum Press, New York (1998).

46. Peter W. Milonni and Joseph H. Eberly. *Lasers.* Wiley New York, NY (1988).

47. G. Cerullo, S. De Silvestri, V. Magni and L. Pallaro. *Resonators for Kerr-lens mode-locked femtosecond Ti:sapphire lasers.* Opt. Lett. **19**, 807–809 (1994).

48. H. Kogelnik, E. Ippen, A. Dienes and C. Shank. *Astigmatically compensated cavities for CW dye lasers.* Quantum Electronics, IEEE Journal of **8**, 373 – 379 (1972).

49. J.-P. Taché. *Ray matrices for tilted interfaces in laser resonators.* Appl. Opt. **26**, 427–429 (1987).

50. D. Strickland and G. Mourou. *Compression of amplified chirped optical pulses.* Opt. Commun. **56**, 219 (1985).

51. Harry E. Bates, Robert R. Alfano and Norman Schiller. *Picosecond pulse stacking in calcite.* Appl. Opt. **18**, 947–949 (1979).

52. Shian Zhou, Frank W. Wise and Dimitre G. Ouzounov. *Divided-pulse amplification of ultrashort pulses.* Opt. Lett. **32**, 871–873 (2007).

53. M. Nisoli, S. De Silvestri and O. Svelto. *Generation of high energy 10 fs pulses by a new pulse compression technique.* Appl. Phys. Lett. **68**, 2793 (1996).

54. M. Nisoli, S. De Silvestri, O. Svelto, R. Szipöcs, K. Ferencz, Ch. Spielmann, S. Sartania and F. Krausz. *Compression of high-energy laser pulses below 5 fs.* Opt. Lett. **22**, 522 (1997).

55. B. Schenkel, J. Biegert, U. Keller C. Vozzi, M. Nisoli, G. Sansone, S. Stagira, S. De Silvestri and O. Svelto. *Generation of 3.8-fs pulses from adaptive compression of a cascaded hollow fiber supercontinuum.* Opt. Lett. **28**, 1987 (2003).

56. A. Baltuška, Th. Udem, M. Uiberacker, M. Hentschel, E. Goulielmakis, Ch. Gohle, R. Holzwarth, V. S. Yakovlev, A. Scrinzi, T. W. Hänsch and F. Krausz. *Attosecond control of electronic processes by intense light fields.* Nature **421**, 611 (2003).

57. E. Goulielmakis, M. Uiberacker, R. Kienberger, A. Baltuska, V. Yakovlev, A. Scrinzi, Th. Westerwalbesloh, U. Kleineberg, U. Heinzmann, M. Drescher and F. Krausz. *Direct Measurement of Light Waves.* Science **305**, 1267 (2004).

58. I. J. Sola, E. Mével, L. Elouga, E. Constant, V. Strelkov, L. Poletto, P. Villoresi, E. Benedetti, J.-P. Caumes, S. Stagira, C. Vozzi, G. Sansone and M. Nisoli. *Controlling attosecond electron dynamics by phase-stabilized polarization gating.* Nature Phys. **2**, 319 (2006).

59. E. A. J. Marcatili and R. A. Sctimeltzer. *Hollow Metallic aildl Dielec-tric Waveguides for Long Distance Optical Transmission and Lasers.* BELL SYSTEM TECHNICAL JOURNAL 43 (4P2): 1783-+ 1964 **43**, 1783 (1964).

60. C.P. Hauri, W. Kornelis, F.W. Helbing, A. Heinrich, A. Couairon, A. Mysyrowicz, J. Biegert and U. Keller. *Generation of intense, carrier-envelope phase-locked few-cycle laser pulses through filamentation.* Appl. Phys. B **79**, 673 (2004).

61. Selcuk Akturk, Cord L. Arnold, Bing Zhou and Andre Mysyrowicz. *High-energy ultrashort laser pulse compression in hollow planar waveguides.* Opt. Lett. **34**, 1462–1464 (2009).

62. C L Arnold, B Zhou, S Akturk, S Chen, A Couairon and A Mysyrowicz. *Pulse compression with planar hollow waveguides: a pathway towards relativistic intensity with table-top lasers.* New Journal of Physics **12**, 073015 (2010).

63. A. Baltuška, Z. Wei, M. S. Pshenichnikov, D. A. Wiersma and R. Szipöcs. *All-solid-state cavity-dumped sub-5-fs laser.* Appl. Phys. B **65**, 175 (1997).

64. Rick Trebino. *Frequency-resolved optical gating: the measurement of ultrashort laser pulses.* Kluwer Academic Publishers (2000).

65. Ian A. Walmsley and Christophe Dorrer. *Characterization of ultrashort electromagnetic pulses.* Adv. Opt. Photon. **1**, 308–437 (2009).

66. Cl Froehly, A Lacourt and J Ch Viénot. *Time impulse response and time frequency response of optical pupils.:Experimental confirmations and applications.* Nouvelle Revue d'Optique **4**, 183 (1973).

67. J. Piasecki, B. Colombeau, M. Vampouille, C. Froehly and J. A. Arnaud. *Nouvelle méthode de mesure de la réponse impulsionnelle des fibres optiques.* Appl. Opt. **19**, 3749–3755 (1980).

68. Jean-Charles Viénot, Jean-Pierre Goedgebuer and Alain Lacourt. *Space and time variables in optics and holography: recent experimental aspects.* Appl. Opt. **16**, 454–461 (1977).

69. B. Rubin and R. M. Herman. *Monochromators as light stretchers.* American Journal of Physics **49**, 868–871 (1981).

70. Jacob Cohen, Pamela Bowlan, Vikrant Chauhan and Rick Trebino. *Measuring temporally complex ultrashort pulses using multiple-delay crossed-beam spectral interferometry.* Opt. Express **18**, 6583–6597 (2010).

71. Benjamín Alonso, Íñigo J. Sola, Óscar Varela, Juan Hernández-Toro, Cruz Méndez, Julio San Román, Amelle Zaïr and Luis Roso. *Spatiotemporal amplitude-and-phase reconstruction by Fourier-transform of interference spectra of high-complex-beams.* J. Opt. Soc. Am. B **27**, 933–940 (2010).

72. Jean-Claude M. Diels, Joel J. Fontaine, Ian C. McMichael and Francesco Simoni. *Control and measurement of ultrashort pulse shapes (in amplitude and phase) with femtosecond accuracy.* Appl. Opt. **24**, 1270–1282 (1985).

73. Yoshihiro Takagi, Tohru Kobayashi, Keitaro Yoshihara and Shunji Imamura. *Multiple- and single-shot autocorrelator based on two-photon conductivity in semiconductors.* Opt. Lett. **17**, 658–660 (1992).

74. D.T. Reid, W. Sibbett, J.M. Dudley, L.P. Barry, B. Thomsen and J.D. Harvey. *Commercial Semiconductor Devices for Two Photon Absorption Autocorrelation of Ultrashort Light Pulses.* Appl. Opt. **37**, 8142–8144 (1998).

75. K. Naganuma, K. Mogi and H. Yamada. *General method for ultrashort light pulse chirp measurement.* Quantum Electronics, IEEE Journal of **25**, 1225 – 1233 (1989).

76. Wenlong Yang, Matthew Springer, James Strohaber, Alexandre Kolomenski, Hans Schuessler, George Kattawar and Alexei Sokolov. *Spectral phase retrieval from interferometric autocorrelation by a combination of graduated optimization and genetic algorithms.* Opt. Express **18**, 15028–15038 (2010).

77. Akira Watanabe, Hiroshi Saito, Yuzo Ishida and Tatsuo Yajima. *Computer-assisted spectrum-resolved SHG autocorrelator for monitoring phase characteristics of femtosecond pulses.* Optics Communications **63**, 320 – 324 (1987).

78. D. J. Kane and R. Trebino. *Characterization of Arbitrary Femtosecond Pulses Using Frequency-Resolved Optical Gating.* IEEE J. Quantum Electron. **29**, 571 (1993).

79. R. Trebino and D. J. Kane. *Using phase retrieval to measure the intensity and phase of ultrashort pulses: frequency-resolved optical gating.* J. Opt. Soc. Am. A **10**, 1101 (1993).

80. R. Trebino, K. W. DeLong, D. N. Fittinghoff, J. Sweetser, M. A. Krumbügel and B. Richman. *Measuring ultrashort laser pulses in the time-frequency domain using frequency-resolved optical gating.* Rev. Sci. Instrum. **68**, 1 (1997).

81. J. Paye. *The chronocyclic representation of ultrashort light pulses.* Quantum Electronics, IEEE Journal of **28**, 2262 –2273 (1992).

82. W. Koenig, H. K. Dunn and L. Y. Lacy. *The Sound Spectrograph.* The Journal of the Acoustical Society of America **18**, 19–49 (1946).

83. Kenneth W. DeLong, David N. Fittinghoff, Rick Trebino, Bern Kohler and Kent Wilson. *Pulse retrieval in frequency-resolved optical gating based on the method of generalized projections.* Opt. Lett. **19**, 2152–2154 (1994).

84. Daniel J Kane. *Real-Time Measurement of Ultrashort Laser Pulses Using Principal Component Generalized Projections.* IEEE Journal of selected topics in quantum electronics **4**, 278–284 (1998).

85. Patrick O'Shea, Mark Kimmel, Xun Gu and Rick Trebino. *Highly Simplified Device for Ultrashort-Pulse Measurement.* Opt. Lett. **26**, 932–934 (2001).

86. Ivan Amat-Roldán, Iain Cormack, Pablo Loza-Alvarez, Emilio Gualda and David Artigas. *Ultrashort pulse characterisation with SHG collinear-FROG.* Opt. Express **12**, 1169–1178 (2004).

87. Gero Stibenz and Günter Steinmeyer. *Interferometric frequency-resolved optical gating.* Opt. Express **13**, 2617–2626 (2005).

88. Kenneth W. DeLong, Rick Trebino and William E. White. *Simultaneous recovery of two ultrashort laser pulses from a single spectrogram.* J. Opt. Soc. Am. B **12**, 2463–2466 (1995).

89. C. Iaconis and I. A. Walmsley. *Spectral phase interferometry for direct electric field reconstruction of ultrashort optical pulses.* Opt. Lett. **23**, 792 (1998).

90. Dane R. Austin, Tobias Witting and Ian A. Walmsley. *Resolution of the relative phase ambiguity in spectral shearing interferometry of ultrashort pulses.* Opt. Lett. **35**, 1971–1973 (2010).

91. Adam S. Wyatt, Alexander Grün, Philip K. Bates, Olivier Chalus, Jens Biegert and Ian A. Walmsley. *Accuracy measurements and improvement for complete characterization of optical pulses from nonlinear processes via multiple spectral-shearing interferometry.* Opt. Express **19**, 25355–25366 (2011).

92. Adam S. Wyatt, Ian A. Walmsley, Gero Stibenz and Günter Steinmeyer. *Sub-10 fs pulse characterization using spatially encoded arrangement for spectral phase interferometry for direct electric field reconstruction.* Opt. Lett. **31**, 1914–1916 (2006).

93. Jonathan R. Birge, Richard Ell and Franz X. Kärtner. *Two-dimensional spectral shearing interferometry for few-cycle pulse characterization.* Opt. Lett. **31**, 2063–2065 (2006).

94. Vadim V. Lozovoy, Igor Pastirk and Marcos Dantus. *Multiphoton intrapulse interference. IV. Ultrashort laserpulse spectral phase characterization and compensation.* Opt. Lett. **29**, 775–777 (2004).

95. Bingwei Xu, Jess M. Gunn, Johanna M. Dela Cruz, Vadim V. Lozovoy and Marcos Dantus. *Quantitative investigation of the multiphoton intrapulse interference phase scan method for simultaneous phase measurement and compensation of femtosecond laser pulses.* J. Opt. Soc. Am. B **23**, 750–759 (2006).

96. Yves Coello, Vadim V. Lozovoy, Tissa C. Gunaratne, Bingwei Xu, Ian Borukhovich, Chien hung Tseng, Thomas Weinacht and Marcos Dantus. *Interference without an interferometer: a different approach to measuring, compressing, and shaping ultrashort laser pulses.* J. Opt. Soc. Am. B **25**, A140–A150 (2008).

97. Vadim V. Lozovoy, Bingwei Xu, Yves Coello and Marcos Dantus. *Direct measurement of spectral phase for ultrashort laser pulses.* Opt. Express **16**, 592–597 (2008).

98. Selcuk Akturk, Ciro D'Amico and Andre Mysyrowicz. *Measuring ultrashort pulses in the single-cycle regime using frequency-resolved optical gating.* J. Opt. Soc. Am. B **25**, A63–A69 (2008).

99. Patrick O'Shea, Mark Kimmel, Xun Gu and Rick Trebino. *Increased-bandwidth in ultrashort-pulse measurement using an angle-dithered nonlinear-optical crystal.* Opt. Express **7**, 342–349 (2000).

100. H. R. Telle, G. Steinmeyer, A. E. Dunlop, J. Stenger, D. H. Sutter and U. Keller. *Carrier-envelope offset phase control: A novel concept for absolute optical frequency measurement and ultrashort pulse generation.* Appl. Phys. B **69**, 327 (1999).

101. D. J. Jones, S. A. Diddams, J. K. Ranka, A. Stentz, R. S. Windeler, J. L. Hall and S. T. Cundiff. *Carrier-envelope phase control of femtosecond mode-locked lasers and direct optical frequency synthesis.* Science **288**, 635 (2000).

102. A. Apolonski, A. Poppe, G. Tempea, Ch. Spielmann, Th. Udem, R. Holzwarth, T. W. Hänsch and F. Krausz. *Controlling the phase evolution of few-cycle light pulses.* Phys. Rev. Lett. **85**, 740 (2000).

103. U. Morgner, R. Ell, G. Metzler, T. R. Schibli, F. X. Kärtner, J. G. Fujimoto, H. A. Haus and E. P. Ippen. *Nonlinear Optics with Phase-Controlled Pulses in the Sub-Two-Cycle Regime.* Phys. Rev. Lett. **86**, 5462–5465 (2001).

104. Takao Fuji, Jens Rauschenberger, Alexander Apolonski, Vladislav S. Yakovlev, Gabriel Tempea, Thomas Udem, Christoph Gohle, Theodor W. Hänsch, Walter Lehnert, Michael Scherer and Ferenc Krausz. *Monolithic carrier-envelope phase-stabilization scheme.* Opt. Lett. **30**, 332–334 (2005).

105. Masayuki Kakehata, Hideyuki Takada, Yohei Kobayash, Kenji Torizuka, Yoshihiko Fujihira, Tetsuya Homma and Hideo Takahashi. *Single-shot measurement of carrier-envelope phase changes by spectral interferometry.* Opt. Lett. **26**, 1436 (2001).

106. Chengquan Li, Eric Moon, He Wang, Hiroki Mashiko, Christopher M. Nakamura, Jason Tackett and Zenghu Chang. *Determining the phase-energy coupling coefficient in carrier-envelope phase measurements.* Opt. Lett. **32**, 796–798 (2007).

107. He Wang, Michael Chini, Eric Moon, Hiroki Mashiko, Chengquan Li and Zenghu Chang. *Coupling between energy and phase in hollow-core fiber based f-to-2f interferometers.* Opt. Express **17**, 12082–12089 (2009).

108. T. Wittmann, B. Horvath, W. Helml, M. G. Schätzel, X. Gu, A. L. Cavalieri, G. G. Paulus and R. Kienberger. *Single-shot carrier-envelope phase measurement of few-cycle laser pulses.* Nat. Phys. **5**, 357 (2009).

109. A. M. Sayler, Tim Rathje, Walter Müller, Klaus Rühle, R. Kienberger and G. G. Paulus. *Precise, real-time, every-single-shot, carrier-envelope phase measurement of ultrashort laser pulses.* Opt. Lett. **36**, 1–3 (2011).

110. Markus Kreß, Torsten Löffler, Mark D. Thomson, Reinhard Dörner, Hartmut Gimpel, Karl Zrost, Thorsten Ergler, Robert Moshammer, Uwe Morgner, Joachim Ullrich and Hartmut G. Roskos. *Determination of the carrier-envelope phase of few-cycle laser pulses with terahertz-emission spectroscopy.* Nature Physics **2**, 327–331 (2006).

111. Andrius Baltuška, Takao Fuji and Takayoshi Kobayashi. *Controlling the Carrier-Envelope Phase of Ultrashort Light Pulses with Optical Parametric Amplifiers.* Phys. Rev. Lett. **88**, 133901 (2002).

112. C. Vozzi, G. Cirmi, C. Manzoni, E. Benedetti, F. Calegari, G. Sansone, S. Stagira, O. Svelto, S. De Silvestri, M. Nisoli and G. Cerullo. *High-energy, few-optical-cycle pulses at 1.5 μm with passive carrier-envelope phase stabilization.* Opt. Express **14**, 10109–10116 (2006).

113. T. Brabec and F. Krausz. *Intense few-cycle laser fields: Frontiers of nonlinear optics.* Rev. Mod. Phys. **72**, 545 (2000).

114. F. Krausz and M. Ivanov. *Attosecond physics.* Reviews of Modern Physics **81**, 163–234 (2009).

115. P. B. Corkum. *Plasma perspective on strong-field multiphoton ionization.* Phys. Rev. Lett. **71**, 1994 (1993).

116. K. J. Schafer, B. Yang, L. F. DiMauro and K. C. Kulander. *Above threshold ionization beyond the high harmonic cutoff.* Phys. Rev. Lett. **70**, 1599 (1993).

117. Kathrin Klünder. *Electron Wave Packet Dynamics on the Attosecond Time Scale.* PhD thesis Lund University (2012).

118. K. Varjú, Y. Mairesse, B. Carre, M. B. Gaarde, P. Johnsson, S. Kazamias, R. Lopez-Martens, J. Mauritsson, K. J. Schafer, Ph. Balcou, A. L'Huillier and P. Salières. *Frequency chirp of harmonic and attosecond pulses.* J. Mod. Opt. **52**, 379 (2005).

119. P. Balcou, P. Salières, A. L'Huillier and M. Lewenstein. *Generalized phase-matching conditions for high harmonics: The role of field-gradient forces.* Phys. Rev. A **55**, 3204–3210 (1997).

120. G. Farkas and C. Tóth. *Proposal for attosecond light pulse generation using laser induced multiple-harmonic conversion processes in rare gases.* Phys. Lett. A **168**, 447 (1992).

121. K. T. Kim, C. M. Kim, M.-G. Baik, G. Umesh and C. H. Nam. *Single sub-50-attosecond pulse generation from chirp-compensated harmonic radiation using material dispersion.* Phys. Rev. A **69**, 051805 (2004).

122. R. López-Martens, K. Varjú, P. Johnsson, J. Mauritsson, Y. Mairesse, P. Salières, M. B. Gaarde, K. J. Schafer, A. Persson, S. Svanberg, C.-G. Wahlström and A. L'Huillier. *Amplitude and phase control of attosecond light pulses.* Phys. Rev. Lett. **94**, 033001 (2005).

123. Center for X-ray Optics, Lawrence Berkley National Laboratory (2009).

124. E. D. Palik, editor. *Handbook of optical constants of solids, vol. 1.* Academic Press San Diego (1985).

125. M. Hentschel, R. Kienberger, Ch. Spielmann, G. A. Reider, N. Milosevic, T. Brabec, P. Corkum, U. Heinzmannß, M. Drescher and F. Krausz. *Attosecond metrology.* Nature **414**, 509 (2001).

126. R. Kienberger, E. Goulielmakis, M. Uiberacker, A. Baltuška, V. Yakovlev, F. Bammer, A. Scrinzi, Th. Westerwalbesloh, U. Kleineberg, U. Heinzmann, M. Drescher and F. Krausz. *Atomic transient recorder.* Nature **427**, 817 (2004).

127. A. Wonisch, U. Neuhäusler, N. M. Kabachnik, T. Uphues, M. Uiberacker, V. Yakovlev, F. Krausz, M. Drescher, U. Kleineberg and U. Heinzmann. *Design, fabrication, and analysis of chirped multilayer mirrors for reflection of extreme-ultraviolet attosecond pulses.* Appl. Opt. **45**, 4147–4156 (2006).

128. Michael Hofstetter, Martin Schultze, Markus Fieß, Benjamin Dennhardt, Alexander Guggenmos, Justin Gagnon, Vladislav S. Yakovlev, Eleftherios Goulielmakis, Reinhard Kienberger, Eric M. Gullikson, Ferenc Krausz and Ulf Kleineberg. *Attosecond dispersion control by extreme ultraviolet multilayer mirrors.* Opt. Express **19**, 1767–1776 (2011).

129. M. Drescher, M. Hentschel, R. Kienberger, G. Tempea, Ch. Spielmann, G. Reider, P.B. Corkum and F. Krausz. *X-Ray Pulses Approaching the Attosecond Frontier.* Science **291**, 1923 (2001).

130. P. B. Corkum, N. H. Burnett and M. Y. Ivanov. *Subfemtosecond pulses.* Opt. Lett. **19**, 1870 (1994).

131. Bing Shan, Shambhu Ghimire and Zenghu Chang. *Generation of the attosecond extreme ultraviolet supercontinuum by a polarization gating.* Journal of Modern Optics **52**, 277–283 (2005).

132. Yu Oishi, Masanori Kaku, Akira Suda, Fumihiko Kannari and Katsumi Midorikawa. *Generation of extreme ultraviolet continuum radiation driven by a sub-10-fs two-color field.* Opt. Express **14**, 7230–7237 (2006).

133. H. Mashiko, S. Gilbertson, C. Li, S. D. Khan, M. M. Shakya, E. Moon and Z. Chang. *Double optical gating of high-order harmonic generation with carrier-envelope phase stabilized lasers.* Phys. Rev. Lett. **100**, 103906 (2008).

134. Thomas Pfeifer, Aurélie Jullien, Mark J. Abel, Phillip M. Nagel, Lukas Gallmann, Daniel M. Neumark and Stephen R. Leone. *Generating coherent broadband continuum soft-x-ray radiation by attosecond ionization gating.* Opt. Express **15**, 17120–17128 (2007).

135. D. Descamps, L. Roos, C. Delfin, A. L'Huillier and C.-G. Wahlström. *Two and three-photon ionization of rare gases using femtosecond harmonic pulses generated in a gas medium.* Phys. Rev. A **64**, 031401 (2001).

136. P. Tzallas, D. Charalambidis, N. A. Papadogiannis, K. Witte and G. D. Tsakiris. *Direct observation of attosecond light bunching.* Nature **426**, 267 (2003).

137. P. Tzallas, J. Kruse, E. Skantzakis, L.A.A. Nikolopoulos, G.D. Tsakiris and D. Charalambidis. *Two-XUV-Photon Processes: A Key Instrument in Attosecond Pulse Metrology and Time Domain Applications.* In Kaoru Yamanouchi, Mauro Nisoli and Wendell T. Hill, III, editors, *Progress in Ultrafast Intense Laser Science VIII* volume 103 of *Springer Series in Chemical Physics* pages 97–119. Springer Berlin Heidelberg (2012). ISBN 978-3-642-28725-1.

138. J. Itatani, F. Quéré, G. L. Yudin, M. Yu. Ivanov, F. Krausz and P. B. Corkum. *Attosecond Streak Camera.* Phys. Rev. Lett. **88**, 173903 (2002).

139. J. B. West and G. V. Marr. *The Absolute Photoionization Cross Sections of Helium, Neon, Argon and Krypton in the Extreme Vacuum Ultraviolet Region of the Spectrum.* Proceedings of the Royal Society of London. Series A, Mathematical and Physical Sciences **349**, pp. 397–421 (1976).

140. M. Gisselbrecht, D. Descamps, C. Lynga, A. L'Huillier, C.-G. Wahlström and M. Meyer. *Absolute photoionization cross sections of excited He states in the near-threshold region.* Phys. Rev. Lett. **82**, 4607 (1999).

141. J.A. Samson and Wayne Stolte. *Precision measurements of the total photoionization cross sections of He, Ne, Ar, Kr, and Xe.* Journal of Electron Spectroscopy and Related Phenomena pages 265–276 (2002).

142. P. M. Paul, E. S. Toma, P. Breger, G. Mullot, F. Augé, Ph. Balcou, H. G. Muller and P. Agostini. *Observation of a train of attosecond pulses from high harmonic generation.* Science **292**, 1689 (2001).

143. H. G. Muller. *Reconstruction of attosecond harmonic beating by interference of two-photon transitions.* Appl. Phys. B **74**, 17 (2002).

144. Y. Mairesse and F. Quéré. *Frequency-resolved optical gating for complete reconstruction of attosecond bursts.* Phys. Rev. A **71**, 011401(R) (2005).

145. F. Quéré, Y. Mairesse and J. Itatani. *Temporal characterization of attosecond XUV fields.* J. Mod. Opt. **52**, 339 (2005).

146. P. Kruit and F. H. Read. *Magnetic field paralleliser for 2π electron-spectrometer and electron-image magnifier.* J. Phys. E **16**, 313 (1983).

147. A.M Rijs, E.H.G Backus, C.A de Lange, N.P.C Westwood and M.H.M Janssen. *'Magnetic bottle' spectrometer as a versatile tool for laser photoelectron spectroscopy.* Journal of Electron Spectroscopy and Related Phenomena **112**, 151 – 162 (2000).

148. Emmett N. Leith and Juris Upatnieks. *Reconstructed Wavefronts and Communication Theory.* J. Opt. Soc. Am. **52**, 1123–1128 (1962).

149. D. Gabor. *A New Microscopic Principle.* Nature **161**, 777–778 (1948).

150. Tatiana Latychevskaia and Hans-Werner Fink. *Solution to the Twin Image Problem in Holography.* Phys. Rev. Lett. **98**, 233901 (2007).

151. K. Klünder, J. M. Dahlström, M. Gisselbrecht, T. Fordell, M. Swoboda, D. Guénot, P. Johnsson, J. Caillat, J. Mauritsson, A. Maquet, R. Taïeb and A. L'Huillier. *Probing Single-Photon Ionization on the Attosecond Time Scale.* Phys. Rev. Lett. **106**, 143002 (2011).

152. M. Schultze, M. Fieß, N. Karpowicz, J. Gagnon, M. Korbman, M. Hofstetter, S. Neppl, A. L. Cavalieri, Y. Komninos, Th. Mercouris, C. A. Nicolaides, R. Pazourek, S. Nagele, J. Feist, J. Burgdörfer, A. M. Azzeer, R. Ernstorfer, R. Kienberger, U. Kleineberg, E. Goulielmakis, F. Krausz and V. S. Yakovlev. *Delay in Photoemission.* Science **328**, 1658–1662 (2010).

153. A. L. Cavalieri, N. Müller, Th. Uphues, V. S. Yakovlev, A. Baltuška, B. Horvath, B. Schmidt, L. Blümel, R. Holzwarth, S. Hendel, M. Drescher, U. Kleineberg, P. M. Echenique, R. Kienberger, F. Krausz and U. Heinzmann. *Attosecond spectroscopy in condensed matter.* Nature **449**, 1029 (2007).

PAPERS

PAPER I

Carrier-envelope phase stabilization of a multi-millijoule, regenerative-amplifier-based chirped-pulse amplifier system

T. Fordell, M. Miranda, A. Persson, and A. L'Huillier.

Opt. Express **17**, 21091–21097 (2009).

Carrier-envelope phase stabilization of a multi-millijoule, regenerative-amplifier-based chirped-pulse amplifier system

T. Fordell[1], **M. Miranda**[1,2], **A. Persson**[1] **and A. L'Huillier**[1]

[1] *Department of Physics, Lund University, P.O. Box 118,*
SE-221 00 Lund, Sweden
[2] *IFIMUP-IN Departamento de Física da Faculdade de Ciências da Universidade do Porto*
Rua do Campo Alegre, 687, 4169-007 Porto
thomas.fordell@fysik.lth.se

Abstract: This article reports on the successful stabilization of the carrier-envelope phase of a 1-kHz laser system that includes a large grating stretcher, a regenerative amplifier, a multipass amplifier and a grating compressor. Phase stability for pulse energies up to 6 mJ is demonstrated using electronic feedback to the oscillator locking electronics as well as feedback via an acousto-optic programmable dispersive filter.

© 2009 Optical Society of America

OCIS codes: (140.3425) Laser stabilization; (320.7090) Ultrafast lasers; (120.5050) Phase measurement

---

References and links

1. D. J. Jones, S. A. Diddams, J. K. Ranka, A. Stentz, R. S. Windeler, J. L. Hall, S. T. Cundiff, "Carrier-envelope phase control of femtosecond mode-locked lasers and direct optical frequency synthesis," Science **288**, 635-639 (2000).
2. A. Polonski, A. Poppe, G. Tempea, Ch. Spielmann, Th. Udem, R. Holzwarth, T. W. Hänsch, F. Krausz, "Controlling the phase evolution of few-cycle light pulses," Phys. Rev. Lett. **85**, 740 (2000).
3. R. Holzwarth, Th. Udem, T. W. Hänsch, J. C. Knight, W. J. Wadsworth, P. St.J. Russell, "Optical frequency synthesizer for precision spectroscopy," Phys. Rev. Lett. **85**, 2264 (2000).
4. G. Sansone, E. Benedetti, F. Calegari, C. Vozzi, L. Avaldi, R. Flammini, L. Poletto, P. Villoresi, C. Altucci, R. Velotta, S. Stagira, S. De Silvestri, M. Nisoli, "Isolated single-cycle attosecond pulses," Science **20**, 443-446 (2006).
5. E. Goulielmakis, M. Schultze, M. Hofstetter, V.S. Yakovlev, J. Gagnon, M. Uiberacker, A. L. Aquila, E. M. Gullikson, D. T. Attwood, R. Kienberger, F. Krausz, U. Kleineberg, "Single-cycle nonlinear optics," Science **20**, 1614-1617 (2008).
6. H. Mashiko, S. Gilbertson, C. Li, S. D. Khan, M. M. Shakya, E. Moon, Z. Chang, "Double optical gating of high-order harmonic generation with carrier-envelope phase stabilized lasers," Phys. Rev. Lett. **100**, 103906 (2008).
7. A. Baltuška, Th. Udem, M. Uiberacker, M. Hentschel, E. Goulielmakis, Ch. Gohle, R. Holzwarth, V. S. Yakovlev, A. Scrinzi. T. W. Hänsch, F. Krausz, "Attosecond control of electronic processes by intense light fields," Nature **421**, 611-615 (2003).
8. A. Assion, G. Tempea, E. Goulielmakis, M. Uiberacker, " Attosecond sources: Few-cycle laser amplifiers bridge the gap between femto- and attosecond ranges," Laser Focus World, April, 75 (2008).
9. L. Canova, X. Chen, A. Trisorio, A. Jullien, A. Assion, G. Tempea, N. Forget, T. Oksenhelder, R. Lopez-Martens, "Carrier-envelope phase stabilization and control using a transmission grating compressor and an AOPDF," Opt. Lett. **34**, 1333 (2009).
10. M. Kakehata, H. Takada, Y. Kobayashi, K. Torizuka, H. Takamiya, K. Nishijima, T. Homma, H. Takahashi, K. Okubo, S. Nakamura, Y. Koyama,"Carrier-envelope-phase stabilized chirped-pulse amplification system scalable to higher pulse energies," Opt. Express **12**, 2070-2074 (2004).

#116024 - $15.00 USD Received 21 Aug 2009; revised 13 Oct 2009; accepted 2 Nov 2009; published 4 Nov 2009

11. E. Gagnon, I. Thomann, A. Paul, A.L. Lytle, S. Backus, M. M. Murnane, H. C. Kapteyn, A. S. Sandhu, “Long term carrier-envelope phase stability from a grating-based, chirped pulse amplifier,” Opt. Lett. **31**, 1866-1868 (2006).
12. K.-H. Hong, J. Lee, B. Hou, J.A. Nees, E. Power, G.A. Morou, “Carrier-envelope phase stabilization of high-contrast femtosecond laser pulses with relativistic intensity,” Appl. Phys. Lett. **89**, 031113 (2006).
13. T. Imran, Y. S. Lee, C. H. Nam, K.-H. Hong, T. J. Yu, J. H. Sung, “Stabilization and control of the carrier-envelope phase of high-power femtosecond laser pulses using the direct locking technique,” Opt. Express **15**, 104-112 (2007).
14. C. Li, E. Moon, H. Mashiko, C. M. Nakamura, P. Ranitovic, C.M. Maharjan, C. Lewis Cocke, Z. Chang, and G. G. Paulus, “Precision control of carrier-envelope phase in grating based chirped pulse amplifiers,” Opt. Express **14**, 11468-11476 (2006).
15. C. Li, H. Mashiko, H. Wang, E. Moon, S. Gilbertson, Z. Chang, “Carrier-envelope phase stabilization by controlling compressor grating separation,” Appl. Phys. Lett. **92**, 191114 (2008).
16. A. Cotel, A. Soujeff, R. Czarny, L. Heng, V. Moro, ”CEP stabilization of a 3.5mJ, 5 kHz femtosecond laser based on gratings stretcher/compressor and regenerative amplifier”, *ATTO-09 conference abstract*, Manhattan, KS USA (2009).
17. T. Fuji, J. Rauschenberger, C. Gohle, A. Apolinski, Th. Udem, V. S. Yakovlev, G. Tempea, T. W. Hänsch, and F. Krausz, “Attosecond control of optical waveforms,” New J. Phys. **7**, 116 (2005).
18. M. Swoboda, T. Fordell, K. Klünder, M. Miranda, J. M. Dahlström, J. Mauritsson, A. L’Huillier, and M. Gisselbrecht,” Resonantly Enhanced Two-Photon Ionization of Helium Studied by an Attosecond Pulse Train’, *UFO VII/HFSW XIII conference abstract*, Arcachon, France (2009).
19. N. Forget, L. Canova, X. Chen, A. Jullien, R. López-Martens, ”Closed loop carrier-envelope phase stabilization with an acousto-optic programmable dispersive filter,” Opt. Lett. , *in press*
20. H. Wang, C. Li, J. Tackett, H. Mashiko, C. M. Nakamura, E. Moon, Z. Chang, “Power locking of high-repetition-rate chirped pulse amplifiers,” Appl. Phys. B **89**, 275 (2009).

1. Introduction

Ever since their first demonstration at the turn of the century, carrier-envelope phase (CEP) stable femtosecond oscillators have brought on a revolution in metrology [1-3]. Phase-stable amplification of these pulses has, in turn, become a very important tool in attosecond science, especially in the production of single attosecond pulses [4-6]. By now, phase-stable amplification has been demonstrated in several types of laser systems based on chirped-pulse amplification (CPA), from systems having material, prism or transmission grating stretchers and compressors [7-9] to grating based systems that can be scaled to very high energies [10-16]. CEP stable multi-millijoule CPA systems have also recently become commercially available. These systems have been built with CEP stability in mind, contrary to equipment often present in many laboratories. Therefore, practical, uncomplicated modifications that can add CEP stability to existing systems are of great interest to a large scientific community.

This article reports on the successful CEP stabilization of a relatively large 1-kHz Ti:Sapphire-based CPA laser system consisting of a commercial CEP-stable seed oscillator, a large Öffner triplet grating stretcher, a regenerative amplifier, a cryogenically-cooled multipass amplifier and a grating compressor. CEP stability for pulse energies up to 6 mJ is demonstrated. This upgrade has been done non-invasively, that is, without causing long interruptions to scientific experiments conducted with the laser.

2. Description of the laser system

The original CPA system (35 fs, 1.5 mJ) was delivered in 1998 (B.M. Industries / Thales). Prior to this work, a considerable overhaul was performed in 2006 when the amplifiers were upgraded to give 10 mJ per pulse before compression (Amplitude technologies). The present system layout is shown in Fig. 1(a). The seed oscillator is a CEP-stable Femtosource Rainbow, which provides very stable operation due to its rigid construction and collinear f-to-0 setup. The oscillator uses its broad bandwidth together with self-phase modulation in a periodically-poled lithium-niobate crystal to achieve the octave spanning spectrum required in the self-referencing

#116024 - $15.00 USD Received 21 Aug 2009; revised 13 Oct 2009; accepted 2 Nov 2009; published 4 Nov 2009
(C) 2009 OSA

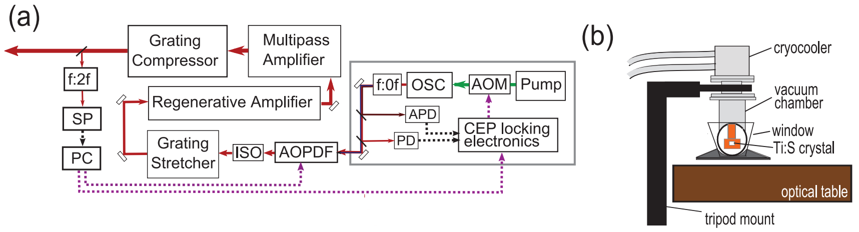

Fig. 1. (a) Simplified laser setup: AOM: acousto-optic modulator; OSC: oscillator; APD: avalanche photodiode; PD: photodiode; AOPDF: acousto-optic programmable dispersive filter; ISO: optical isolator; SP: spectrometer; PC: personal computer. Electrical connections are indicated with dashed lines and slow loop feedback paths in purple. (b) Cryocooler setup in the multipass amplifier. The vibrating cryocooler is mounted on a separate tripod completely isolated from the optical table.

f-to-0 interferometer without the need for a photonic crystal fibre [17]. Phase stabilization electronics (XPS800-E, Menlosystems) stabilizes the oscillator pulse-to-pulse phase slip to $\pi/2$ with a resulting in-loop phase jitter well below 100 mrad root-mean-square (RMS).

For fine control of system dispersion, an acousto-optic programmable dispersive filter (AOPDF, Fastlite Dazzler) is used after the oscillator. With the low-jitter option installed, factory timing jitter measurements on this particular unit point to an added optical CEP jitter of 50 mrad RMS. Besides being useful for dispersion management, the AOPDF can also be used to fine tune the carrier frequency of amplified pulses simply by changing the spectral shape of the seed pulses [18]. The stretcher is a large, folded, triplet Öffner grating stretcher with a 5-ps/nm stretch factor. The size of this stretcher is considerable compared to stretchers in commercial CEP stable systems. The diameter of the concave mirror is 30 cm, the grating is 14 cm x 12 cm, the beam height is 20 cm above the table surface, the footprint is 120 cm x 60 cm, and the total beam path is 11 meters. Needless to say, this device is extremely sensitive to vibrations.

The first of the two amplifiers is regenerative with three KD*P Pockels cells (pulse picker, switch in/out, and cleaner). Saturation at an output energy of 0.5 mJ is obtained after roughly 13 cavity roundtrips. The second amplifier is a standard cryogenically-cooled five-pass bow-tie amplifier that is designed to boost the pulse energy up to 10 mJ. Both amplifiers are pumped by light from a 30-W diode-pumped solid-state laser (DM30, Photonics Industries). For pulse energies above 5 mJ or so, a second flashlamp-pumped 20-W laser (YLF20W, B.M. Industries) is used for the multipass amplifier. Finally, the beam is sent over to the adjacent optical table and into a standard double pass grating compressor. With large dielectric gratings (14 cm x 12 cm) optimized for 800 nm the throughput is approximately 74%. In order not to damage the gratings, the beam is expanded to 1.6 cm full width at half maximum (FWHM) in a telescope before entering the compressor. Frequency-resolved optical gating measurements indicate a minimum pulse length of 34 fs FWHM after compression. By tuning the AOPDF this can be reduced to 30 fs if minor satellites to the main pulse are allowed. For reference, the autocorrelation trace assuming a sech^2 pulse shape yields 30 fs and 26 fs, respectively.

A self-referencing f-to-2f interferometer (APS800, MenloSystems) is used as a CEP detector for the amplified pulses. During amplification a slow drift of the CEP usually occurs, and this must be compensated by another feedback loop, the so called slow loop [7]. Several different implementations of the slow loop have been demonstrated, including feedback to the oscillator locking electronics [7], grating position [14] or prism position [8] in the stretcher, and grating separation in the compressor [15]. CEP control using an AOPDF has also very recently been

#116024 - $15.00 USD Received 21 Aug 2009; revised 13 Oct 2009; accepted 2 Nov 2009; published 4 Nov 2009
(C) 2009 OSA

demonstrated [9, 19]. In this work the slow loop has been implemented in two different ways: voltage feedback to the oscillator locking electronics and phase control of the acoustic wave in the AOPDF. Feedback paths are indicated in purple in Fig. 1(a).

3. Route to carrier-envelope-phase stability

Early on it was clear that the first problem to be encountered on a route to a stable CEP would be the cryogenic cooler assembly in the multipass amplifier. Gas pressure fluctuations in the cryocooler (ARS DE-104) generate a considerable amount of vibrations, and these must not propagate to the optical table. For this reason the cryocooler assembly was mounted on a separate tripod and is hovering a few millimeters above the optical table surface completely isolated from the rest of the setup (Fig. 1(b)). Later, during first tests after installation of the CEP-stable oscillator and the phase detector for the amplified pulses, no CEP stability was observed even with the noisy cryocooler turned off. What follows in this section is a short summary of the path to a stable and controllable phase: the encountered problems and their solutions.

The second problem encountered was electromagnetic interference in the oscillator fast loop and in the pulse picking caused by the high-voltage switching of the three Pockels cells. In the fast loop this interference manifested itself as clear and regular spikes in the error signal, whereas the interference in the pulse picking was more subtle. These interference problems where removed by re-routing cables, putting aluminum foil for added shielding, using a band-pass filter in front of the pulse counter input and by using separate pulse pick-up photodiodes for different parts of the system in order to remove potential ground loops and noise propagation. As a result a total of four separate photodiodes are used in timing and control.With these modifications CEP stability on the few second time scale was observed with short stable periods interrupted by long periods of very turbulent behavior.

By inspection, i.e., by tapping on different parts while monitoring the CEP, it became clear that the stretcher seemed by far the most sensitive part with respect to vibrations. To investigate the role of table vibrations further, a piezo-electric transducer was mounted on the optical tables, and it turned out that even very weak floor vibrations could cause severe turbulence of the phase. Thus it seemed that vibrations in the floor were exciting resonances in the table, in the rigid table legs, and in the optomechanical components themselves. Since the system stretches over two separate optical tables, floating the tables did not seem like a quick and easy solution. Instead, special anti-vibration rubber sheets (Novibra) were placed under the table legs as well as under the cryocooler tripod in order to isolate the optical tables from floor vibrations with excellent results. Even though the anti-vibration sheets are not designed for demanding applications, they do remove efficiently the part of the noise spectrum that can induce resonances in the table and the table legs (50-100 Hz or so). Note also that the laboratory is located in the basement of the building and that there is no heavy traffic nearby, which makes the environment already quiet by default.

At this point the system could be regarded as phase stable; however, to further reduce the phase jitter and to be able to operate the flashlamp-pumped Nd:YLF laser, vibration isolating sheets (Sorbothane) were placed under the pump lasers. Also, rotary pumps, cooling water and cryocooler pumps, and pump laser drivers are all located in separate rooms away from the laser setup. Vibrating cooling water hoses have also been clamped down by a large concrete block before going onto the optical table.

4. Results

Fig. 2(a) shows single-shot, in-loop phase jitter measured at an output energy of 6 mJ with slow loop feedback applied to the AOPDF (red dots in the background) and the oscillator locking

#116024 - $15.00 USD Received 21 Aug 2009; revised 13 Oct 2009; accepted 2 Nov 2009; published 4 Nov 2009

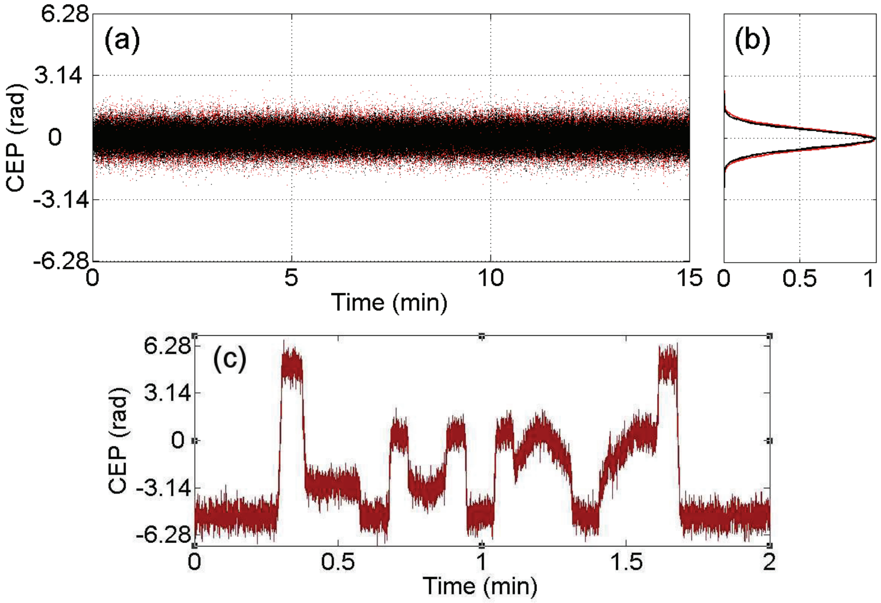

Fig. 2. (a) In-loop, single shot CEP jitter at a pulse energy of 6 mJ with slow loop feedback applied to the AOPDF (red dots in the background) and to the oscillator locking electronics (black dots). (b) Histograms of the data in (a) show gaussian distributions with a standard deviation of 510 mrad and 470 mrad. (c) CEP control using the AOPDF at an output energy of 4.2 mJ is demonstrated by spelling ”Lund”.

electronics (black dots). Here, approximately every fourth pulse has been recorded. In both cases the resulting noise has a gaussian distribution with a standard deviation of 510 mrad and 470 mrad, respectively (Fig. 2(b)). The electronic feedback has the advantage of providing a tight lock. There are, however, a number of disadvantages, including feedback range limitations and, especially, added noise to the oscillator locking electronics.

The Dazzler feedback scheme, on the other hand, will never run out of range due to its cyclic nature, the feedback being just the phase of the acoustic wave that ranges from 0 to 2π. Furthermore, this technique will not disturb the oscillator in any way. In this work, the disadvantage was the slow update rate of the acoustic waveform (around 6 Hz or so), and the fact that only 32 different waveforms could be preloaded into the memory of the driver electronics, which resulted in a feedback step size of $2\pi/32 = 200$ mrad. Therefore, the feedback value could differ from the correct one by up to 100 mrad. These disadvantages do not exist in newer models with much higher update rates and in which several hundred waveforms can be preloaded into memory. Nevertheless, suprisingly good results were obtained also with our device as can be seen in Fig. 2(c), where CEP control at an output energy of 4.2 mJ is demonstrated by spelling ”Lund”.

Other possible implementations of the slow loop include control of various grating, prism or wedge positions in the beam path. While all of these would probably work, they are based on mechanically moving parts and will sooner or later run out of range forcing a reset of the feedback and momentary instabilities in the phase; therefore, an AOPDF based approach that will neither disturb the oscillator nor will it ever run out of range is probably the method of choice for large laser systems such as the one discussed here where the slow loop needs to correct large drifts. A summary of CEP noise measured at different pumping conditions is given in Table 1. Again, the data is single-shot with approximately every fourth pulse recorded over a time span of 15 minutes, which is the typical time scale of an attosecond experiment.

Energy (mJ)	AOPDF	Electronic
3.1	390	390
5.2	490	460
6.0	510	470

Table 1. Measured in-loop phase jitter (mrad) for different feedback schemes and at different pumping conditions. The data is single-shot with approximately every fourth pulse recorder over a time span of 15 minutes.

5. Discussion

The results presented in the previous section are encouraging and would presumably result in observable CEP dependent effects in many experiments, but for certain applications, such as the production of single attosecond pulses using high-order harmonic generation, reduced CEP jitter would be desirable. One big contributor to CEP noise in the present system is the cryogenic cooler setup in the multipass amplifier (Fig. 1(b)). Even though it is hovering above the optical table surface, vibrations propagate via the tripod to the floor and to the table. But more importantly, the entire vacuum chamber vibrates, including the Ti:sapphire crystal and the windows. This has two consequences: first, the overall beam pointing stability is reduced and second, since the windows are tilted, the movement of the vacuum chamber results in a changing path length in vacuum (and air), and hence a change in phase. By turning off the cryocooler for a few seconds, a clear reduction in CEP jitter can be seen: the RMS jitter drops from the 400 mrad regime to the 300 mrad range. Thus, in order to increase the stability of the laser, a new design incorporating vibration dampers for the cryocooler is needed.

To further reduce the CEP jitter, additional layers of vibration damping material might be put under the pump lasers, the stretcher assembly, and also under the table legs. Active stabilization of pulse energy fluctuations [20] and an update of the AOPDF drive circuitry are other minimally invasive steps that can be taken for additional noise reduction.

6. Conclusions

In conclusion, it was shown that CEP stability can be added to a relatively large, and partly old, CPA based laser system consisting of a large grating stretcher, a regenerative amplifier, a cryogenically-cooled multipass amplifier and a grating compressor. The necessary steps needed to achieve CEP stable operation at an output energy of 6 mJ were described and additional steps to further reduce the CEP jitter were proposed. Clearly, by progressing step by step CEP stability can be added to existing CPA laser systems without causing long interruptions to scientific experiments.

Acknowledgements

The authors acknowledge discussions with P. Johnsson and technical support from R. Herzog (Fastlite). Furthermore, contributions in the early stages of this work by C.-G. Wahlström, E. Mansten and E. Pourtal are acknowledged. This research was supported by the Marie Curie Intra-European Fellowship ATTOCO, the Fundação para a Ciência e a Tecnologia

#116024 - $15.00 USD Received 21 Aug 2009; revised 13 Oct 2009; accepted 2 Nov 2009; published 4 Nov 2009

(grant SFRH/BD/37100/2007), the European Research Council (ALMA), the Swedish Research Council, and the Knut and Alice Wallenberg Foundation.

#116024 - $15.00 USD Received 21 Aug 2009; revised 13 Oct 2009; accepted 2 Nov 2009; published 4 Nov 2009

Paper II

High-speed carrier-envelope phase drift detection of amplified laser pulses

T. Fordell, M. Miranda, C. L. Arnold, and A. L'Huillier.

Opt. Express **19**, 23652–23657 (2011).

High-speed carrier-envelope phase drift detection of amplified laser pulses

T. Fordell,* M. Miranda, C. L. Arnold, and A. L'Huillier

Department of Physics, Lund University,
P.O. Box 118, 22100 Lund, Sweden
**thomas.fordell@fysik.lth.se*

Abstract: An instrument for measuring carrier-envelope phase (CEP) drift of amplified femtosecond laser pulses at repetition rates up to the 100-kHz regime is presented. The device can be used for real-time pulse labeling and it could also enable single-loop CEP control of future high-repetition rate laser amplifiers. The scheme is demonstrated by measuring the CEP drift of a 1-kHz source.

© 2011 Optical Society of America

OCIS codes: (320.7090) Ultrafast lasers; (140.3425) Laser stabilization; (120.5050) Phase measurement.

References and links

1. D. J. Jones, S. A. Diddams, J. K. Ranka, A. Stentz, R. S. Windeler, J. L. Hall, and S. T. Cundiff, "Carrier-envelope phase control of femtosecond modelocked lasers and direct optical frequency synthesis," Science **288**, 635–639 (2000).
2. A. Polonski, A. Poppe, G. Tempea, Ch. Spielmann, Th. Udem, R. Holzwarth, T. W. Hänsch, and F. Krausz, "Controlling the phase evolution of few-cycle light pulses," Phys. Rev. Lett. **85**, 740–743 (2000).
3. G. Sansone, E. Benedetti, F. Calegari, C. Vozzi, L. Avaldi, R. Flammini, L. Poletto, P. Villoresi, C. Altucci, R. Velotta, S. Stagira, S. De Silvestri, and M. Nisoli, "Isolated single-cycle attosecond pulses," Science **20**, 443–446 (2006).
4. E. Goulielmakis, M. Schultze, M. Hofstetter, V. S. Yakovlev, J. Gagnon, M. Uiberacker, A. L. Aquila, E. M. Gullikson, D. T. Attwood, R. Kienberger, F. Krausz, and U. Kleineberg, "Single-cycle nonlinear optics," Science **20**, 1614–1617 (2008).
5. O. D. Mücke, O. Kuzucu, F. N. C. Wong, E. P. Ippen, F. X. Kärtner, S. M. Foreman, D. J. Jones, L.-S. Ma, J. L. Hall, and J. Ye, "Experimental implementation of optical clockwork without carrier-envelope phase control," Opt. Lett. **29**, 2806–2808 (2004).
6. S. Gilbertson, S. D. Khan, Y. Wu, M. Chini, and Z. Chang, "Isolated attosecond pulse generation without the need to stabilize the carrier-envelope phase of driving lasers," Phys. Rev. Lett. **105**, 093902 (2004).
7. S. T. Cundiff, "Phase stabilization of ultrashort optical pulses," J. Phys. D: Appl. Phys. **35**, R43–R59 (2002).
8. Y. S. Lee, J. H. Sung, C. H. Nam, T. J. Yu, and K.-H. Hong, "Novel method for carrier-envelope phase stabilization of femtosecond laser pulses," Opt. Express **13**, 2969–2976 (2005).
9. S. Koke, C. Grebing, H. Frei, A. Anderson, A. Assion, and G. Steinmeyer, "Direct frequency comb synthesis with arbitrary offset and shot-noise limited phase noise," Nat. Photonics **4**, 462–465 (2005).
10. P. A. Roos, L. Xiaoqin, R. P. Smith, J. A. Pipis, T. M. Fortier, and S. T. Cundiff, "Solid-state carrier-envelope phase stabilization via quantum interference control of injected photocurrents," Opt. Lett. **30**, 735–737 (2005).
11. K. Osvay, M. Görbe, C. Grebing, and G. Steinmeyer, "Bandwidth-independent linear method for detection of the carrier-envelope offset phase," Opt. Lett. **32**, 3095–3097 (2007).
12. A. Baltuška, Th. Udem, M. Uiberacker, M. Hentschel, E. Goulielmakis, Ch. Gohle, R. Holzwarth, V. S. Yakovlev, A. Scrinzi, T. W. Hänsch, and F. Krausz, "Attosecond control of electronic processes by intense light fields," Nature **421**, 611–615 (2003).
13. M. Kakehata, H. Takada, Y. Kobayashi, K. Torizuka, Y. Fujihira, T. Homma, and H. Takahashi, "Single-shot measurement of carrier-envelope phase changes by spectral interferometry," Opt. Lett. **26**, 1436–1438 (2001).
14. S. Koke, C. Grebing, B. Manschwetus, and G. Steinmeyer, "Fast f-to-2f interferometer for a direct measurement of the carrier-envelope phase drift of ultrashort amplified laser pulses," Opt. Lett. **33**, 2545–2547 (2008).

#150427 - $15.00 USD Received 5 Jul 2011; revised 22 Aug 2011; accepted 24 Aug 2011; published 7 Nov 2011

15. K. Kress, T. Löffler, M. D. Thomson, R. Dörner, H. Gimpel, K. Zrost, T. Ergler, R. Moshammer, U. Morgner, J. Ullrich, and H. G. Roskos, "Determination of the carrier-envelope phase of few-cycle laser pulses with terahertz-emission spectroscopy," Nat. Phys. **2**, 327–331 (2006).
16. C. A. Haworth, L. E. Chipperfield, P. L. Knight, J. P. Marangos, and J. W. G. Tisch, "Half-cycle cutoffs in harmonic spectra and robust carrier-envelope phase retrieval," Nat. Phys. **3**, 52–57 (2007).
17. T. Wittmann, B. Horvath, W. Helmi, M. G. Schätzel, X. Gu, A. L. Cavalieri, and G. G. Paulus, "Single-shot carrier-envelope phase measurement of few-cycle laser pulses," Nat. Phys. **5**, 357–362 (2009).
18. A. M. Sayler, T. Rathje, W. Müller, K. Rühle, R. Kienberger, and G. G. Paulus, "Precise, real-time, every-single-shot, carrier-envelope phase measurement of ultrashort laser pulses," Opt. Lett. **36**, 1–3 (2011).
19. T. Fordell, M. Miranda, A. Persson, and A. L'Huillier, "Carrier-envelope phase stabilization of a multi-millijoule, regenerative-amplifier-based chirped-pulse amplifier system," Opt. Express **17**, 21091–21097 (2009).
20. C. Li, E. Moon, H. Wang, H. Mashiko, C. M. Nakamura, J. Tackett, and Z. Zhang, "Determining the phase-energy coupling coefficient in carrier-envelope phase measurements," Opt. Lett. **32**, 796–798 (2007).
21. H. Wang, M. Chini, E. Moon, H. Mashiko, C. Li, and Z. Chang, "Coupling between energy and phase in hollow-core fiber based f-to2f interferometers," Opt. Express **17**, 12082–12089 (2009).
22. H. Wang, C. Li, J. Tackett, H. Mashiko, C. M. Nakamura, E. Moon, and Z. Zhang, "Power-locking of high-repetition rate chirped-pulse amplifiers," Appl. Phys. B **89**, 275–279 (2007).
23. A. Guandalini, P. Eckle, M. Anscombe, P. Schlup, J. Biegert, and U. Keller, "5.1 fs pulses generated by filamentation and carrier envelope phase stability analysis," J. Phys. B: At. Mol. Opt. Phys. **39**, S257–S264 (2006).

---

1. Introduction

The ability to stabilize and control the phase slip of the carrier wave under the pulse envelope in femtosecond oscillators has become a crucial part of time and frequency metrology since it provides a straightforward, and elegant, way to link the radio frequency domain coherently to the optical frequency domain, and vice versa [1, 2]. Moreover, phase stable amplification of these carrier-envelope-phase-stable pulses has revolutionized ultrafast science by enabling the production of isolated attosecond XUV pulses [3, 4]. While optical clockwork as well as single attosecond XUV pulses without the need to control the carrier-envelope phase (CEP) have both been recently demonstrated [5, 6], CEP stabilization and control has become, and will remain, a fundamental feature of modern femtosecond laser systems.

Different techniques have been developed to detect CEP drift and even its absolute value. The standard way to detect CEP drift is to first generate an octave spanning spectrum via supercontinuum generation and then to monitor the interference between the fundamental spectrum and its second harmonic in a so called f-to-2f interferometer. In laser oscillators, a narrow spectral region is filtered out and detected with a photodiode. Typically, a phase-locked loop is then used to lock the signal from the photodiode (the 'beat note') to one quarter of the pulse repetition rate by modulating the pump power or by tilting a mirror in a prism based intra-cavity dispersion compensator. Such a scheme locks the phase slip from pulse to pulse to $\pi/4$ [7]. The photodiode signal can also be used to directly modulate the pump power [8] or to drive an acousto-optic modulator external to the laser cavity [9]. In addition to the f-to-2f scheme, semiconductor-based solutions also exist for generating the beat note [10]. CEP detection at low power levels and narrow bandwidths can be done using linear interferometry [11].

Once the oscillator has been stabilized, high-power CEP-stable pulses can be produced by properly selecting the pulses to be amplified. During amplification, a slow drift of the CEP usually occurs, and this needs to be corrected by a second feedback loop, the slow loop [12]. Here again, an f-to-2f interferometer is usually employed but with a spectrometer instead of a photodiode [13]. A computer then monitors the interference fringes in the spectrum and computes a correction to be fed back into the laser system. Such a measurement with data transfer from a spectrometer to a computer is slow and plagued with high latencies, but this is normally not a problem since only a few hertz of bandwidth is needed for the slow loop to perform well; however, this means that the phase of only a fraction of the pulses can be recorded for high-repetition-rate laser systems. In [14], the spectrometer in such an f-to-2f interferometer was

#150427 - $15.00 USD Received 5 Jul 2011; revised 22 Aug 2011; accepted 24 Aug 2011; published 7 Nov 2011

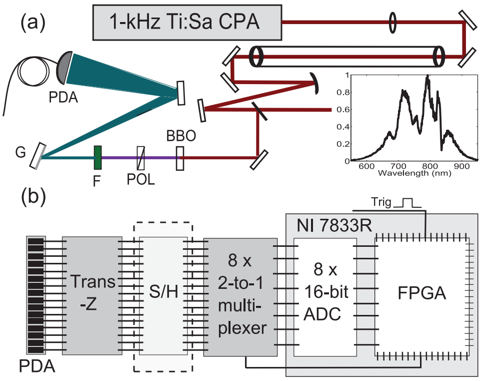

Fig. 1. (a) Experimental setup. POL: polarizer; F: short pass filter; G: grating; PDA: photodiode array. A spectrum of the hollow fiber output is also shown. (b) Electronics for signal processing. Trans-Z: transimpedance amplifier; ADC: analog to digital converter.

replaced by two photomultiplier tubes in quadrature, which meant that the relative CEP could be determined unambiguously in a $]-\pi/2,\pi/2[$ interval at multi-kHz repetition rates.

The absolute CEP can be measured with techniques based on, e.g., THz emission [15], half-cycle cutoffs in high-harmonic spectra [16] and above-threshold ionization [17]. Recently, using above-threshold ionization, single-shot CEP measurements with very low latency (20 µs) was demonstrated [18].

This letter presents a scheme for measuring the relative CEP at high pulse repetition rates and with latencies in the µs regime. The method is especially designed to be used with hollow-fiber pulse compressors and it is based on the traditional f-to-2f technique, which is simple to implement, robust and offers a visually clear picture of the phase stability (the jitter of the spectral fringe pattern). Here, the spectrometer normally used is replaced by a grating that disperses an octave spanning spectrum onto a photodiode array. A field-programmable gate-array (FPGA, NI PCI-7833R) is then used to calculate, in real time, the CEP from the measured interference pattern. An FPGA based approach for fringe pattern analysis has several advantages compared to other solutions, including straightforward graphical programming (NI Labview) that results in high-speed task-dedicated electronic hardware, fast data transfer to the host computer as well as a (built-in) graphical user interface.

2. Experimental setup and results

The test setup is illustrated in Fig. 1a. CEP-stable pulses from a 30-fs, 1-kHz chirped-pulse amplifier (CPA) system [19] are spectrally broadened in a hollow fiber. After collimation of the beam but before dispersion compensation by double chirped mirrors, a reflection off an uncoated glass plate is used to pick off a sample of the beam for CEP measurement (<10 µJ). The octave spanning spectrum (about 5 fs transform limit) is then doubled in a nonlinear crystal (0.5-mm BBO), spectrally filtered (short pass), and angularly dispersed by a grating (1800 grooves/mm, 500-nm blaze) before hitting a 16-element photodiode array (PDA, Hamamatsu S4111-16R). Optical alignment of the detector is very easy since the interference fringes used to detect CEP drift are even visible to the naked eye. The photocurrents from the PDA (Fig. 1b) are then amplified by a transimpedance amplifier (16 channels) and multiplexed down to 8 parallel lines before being digitized (ADC, 8x200 kS/s) and processed by the FPGA. A sample-and-

Received 5 Jul 2011; revised 22 Aug 2011; accepted 24 Aug 2011; published 7 Nov 2011
(C) 2011 OSA

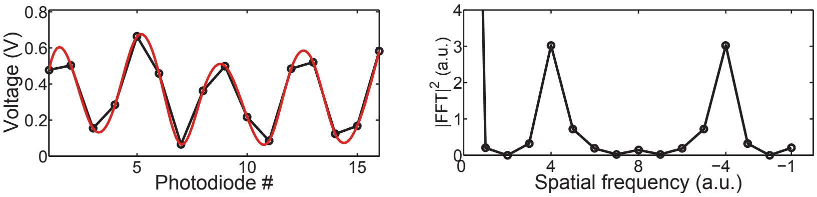

Fig. 2. (a) Raw data of the interference pattern on the PDA (circles) with piecewise linear (black) and spline (red) interpolations. (b) Double-sided complex Fourier transform of the raw data in (a). The CEP is given by the phase of the Fourier component at position 4.

hold (S/H) circuit can be inserted before the analog multiplexer to make sure that the signal does not change during digitization. In this work, for simplicity, a S/H circuit was not used; instead, the first 8 channels were digitized on the rising slope while the rest were digitized on the descending slope (at equal magnitudes). In the FPGA, a 16-point fast-Fourier-transform (FFT) is computed and the phase of the relevant Fourier component is extracted, unwrapped and transferred via a buffer to the PC for storage. The time required for this process, excluding the rise time of the PDA and the amplifier, is around 14 μs and is mostly limited by the analog to digital conversion (ADC) (2x4 μs) and multiplexing (3 μs). Interference patterns can be continuously read, analyzed and the data saved at pulse repetition rates up to 70 kHz. If only the first 8 channels are used, the latency drops to around 7 μs and the maximum trigger rate goes up to 200 kHz.

The current proof-of-principle setup is limited to about 50 kHz by the response of the transimpedance amplifier; however, the rise time of the PDA is well below 1 μs and permits, with an improved amplifier, very high pulse rates. A proportional-integral-derivative (PID) controller is also programmed into the FPGA and can be run in parallel to the above signal processing in order to provide rapid feedback to a (future) high-repetition-rate laser system. Fig. 2a shows a typical interference pattern measured at 460 nm with the setup in Fig. 1; the open circles are the actual data points and the black and red lines are piecewise linear and spline interpolations, respectively. The corresponding spectrum from which the CEP is extracted is shown in Fig. 2b. The interference signal at 460 nm is surprisingly good considering the relatively narrow spectrum shown in the inset in Fig. 1. Clearly, the spectrum from the fiber has broad wings.

Some care has to be taken when extracting the phase from such a short data set. Computer simulations show that the relation between the computed phase and the actual phase is slightly nonlinear due to the low number of points used for the FFT. This nonlinearity can go up to 100 mrad, but it can be reduced by windowing the data. Window functions that go to zero at the edges should be avoided since they cut away much of the interesting signal; hence, e.g. a Hamming window, or variations thereof, is recommended. A Hamming window will reduce the nonlinearity to approximately 10 mrad, which is negligible in most cases. Furthermore, a short data set means that the extracted phase becomes more sensitive to noise in the signal. Again, simulations show that this level of sensitivity is acceptable: for example, a noisy signal with 20% noise in each data point and with a randomly varying background level (random offset and random slope, both varying in an interval equal in amplitude to the amplitude of the signal) will together produce a jitter of around 60 mrad and 100 mrad for 16 and 8 channels, respectively. If a more noise resilient detection is required, the number of data points must be increased. For example, a 32 cell PDA with 4-to-1 multiplexers and S/H circuits would still yield latencies of only a few tens of μs. Sub-10 μs latencies could be obtained by updating to the latest multifunction FPGA modules that require only 1 μs for the ADC.

To check the noise level of the detector, the phase of an artificial, static pattern was measured (flash lamp + transmission grating). With a signal level comparable to that in Fig. 2a, a root-mean-square (RMS) phase jitter of a few mrad was measured even when the FPGA was triggered at 200 kHz. The dominant source of this phase noise is the analog-to-digital converter, which produces an RMS noise level of nearly 2 mV per sample per channel. The photon shot noise is an order of magnitude smaller due to the large amounts of photons available from the hollow fiber ($>10^6$/pulse/photodiode). Adding a low-noise amplifier in front of the ADC and/or increasing the beam intensity can be used to reduce the relative contribution of the ADC quantization noise and to push the detector noise level into the sub-mrad regime.

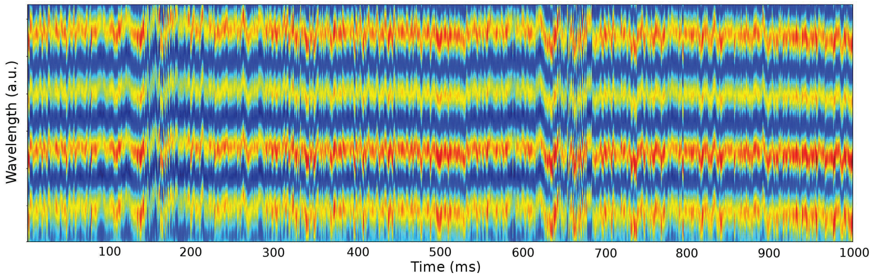

Fig. 3. A short excerpt of 1000 consecutive interference patterns recorded at 1 kHz with only the oscillator being locked. For visual clarity, a spline interpolation as in Fig. 2a has been done for each pulse.

Fig. 3 shows a traditional view of the fringe pattern around 460 nm of 1000 consecutive laser pulses recorded at 1 kHz with only the oscillator being locked (no slow loop). The data is a short excerpt from a much longer data set. At such a low repetition rate, the computed CEP as well as all of the raw data can easily be transferred and saved continuously to the host computer. If triggered above 30 kHz or so, only the CEP can be continuously transferred and saved. Three distinct features from this short excerpt can be seen: the pulse-to-pulse jitter, the slow drift due to only the oscillator being locked, and the large disturbances at 150 ms and 650 ms caused by vibrations of the cryogenic cooler unit that operates at 2 Hz and cools the Ti:Sa crystal in the multipass amplifier. The RMS CEP jitter in Fig. 3 is around 600 mrad. This value should only be used to get an idea of the scale of the CEP fluctuations. With also the slow feedback loop running, the phase jitter in front of the fiber as measured with a commercial f:2f interferometer (APS800) was around 450 mrad [19]. It must be emphasized that these numbers should not be compared to each other for several reasons, one obvious reason being the slow loop. More importantly, it is still unclear exactly how, e.g., beam pointing and pulse energy fluctuations, are coupled to measured and true CEP fluctuations in different setups. The method proposed here measures the pulses as they exit the hollow fiber and are sent to the experiment, which means that a considerable part of the measured CEP jitter arising from such effects should reflect true changes of the CEP in the hollow fiber and not just artifacts of the measurement, which is the case when the measurement is done in front of the fiber.

The f:2f technique is well known to interpret pulse energy fluctuations as CEP fluctuations. This coupling has been estimated in [20] to be around 160 mrad for every 1 per cent change in pulse energy for traditional f:2f interferometers based on white light generation in sapphire. A value of 120 mrad has been measured for a hollow fiber setup [21]. In this work, the energy fluctuations in front of the fiber were below 1 per cent. Consequently, energy fluctuations are of minor importance for the results presented here; however, for a laser with better CEP stability, pulse energy fluctuations can become an issue. In a feedback loop, the detrimental effect of energy fluctuations can be reduced by averaging over a few pulses. If the CEP of the laser is not stabilized, that is, if the pulses are only labeled by their CEP, then the averaging must be done during data analysis. But this only means that more shots must be recorded than what would otherwise be necessary. Active stabilization of the pulse energy can also be employed [22]. Another approach would be to measure the pulse energy simultaneously with the CEP. After a calibration of the coupling strength has been performed, real-time compensation of this effect can easily be performed by the FGPA. Finally, the coupling can probably also be reduced by having a broader white light continuum [23].

Up to a few tens of kHz the signal level from the photodiode array should not be a problem, after all, a 45^o s-polarized reflection off an uncoated glass surface (R$\approx$ 1.5%) provided sufficient signal in this work; however, when going towards 100 kHz and possibly above, a broader spectrum combined with an improved transimpedance amplifier will be needed in addition to an increase of the beam split-off ratio.

3. Conclusion

In conclusion, an instrument for fast CEP measurement of amplified femtosecond pulses has been presented. Spectral broadening of the input pulses was done in a hollow-core fiber, which is, along with CEP measurement and stabilization, a crucial component in many laboratories at the forefront of ultrafast science where single attosecond XUV pulses are produced via high-harmonic generation. The device presented can be used for real-time pulse labeling and rapid feedback for single-loop CEP stabilization at pulse repetition rates up to the 100-kHz regime.

#150427 - $15.00 USD Received 5 Jul 2011; revised 22 Aug 2011; accepted 24 Aug 2011; published 7 Nov 2011

PAPER III

Simultaneous compression and characterization of ultrashort laser pulses using chirped mirrors and glass wedges

Miguel Miranda, Thomas Fordell, Cord Arnold, Anne L'Huillier, and Helder Crespo.

Opt. Express **20**, 688–697 (2012).

Simultaneous compression and characterization of ultrashort laser pulses using chirped mirrors and glass wedges

Miguel Miranda,[1,2,*] Thomas Fordell,[2] Cord Arnold,[2] Anne L'Huillier,[2] and Helder Crespo[1]

[1] *IFIMUP-IN and Departamento de Física e Astronomia, Universidade do Porto, Rua do Campo Alegre 687, 4169-007 Porto, Portugal*
[2] *Department of Physics, Lund University, P.O. Box 118, SE-221 00 Lund, Sweden*
[*] *mmiranda@fc.up.pt*

Abstract: We present a simple and robust technique to retrieve the phase of ultrashort laser pulses, based on a chirped mirror and glass wedges compressor. It uses the compression system itself as a diagnostic tool, thereby making unnecessary the use of complementary diagnostic tools. We used this technique to compress and characterize 7.1 fs laser pulses from an ultrafast laser oscillator.

©2011 Optical Society of America

OCIS codes: (320.2250) Femtosecond phenomena; (320.5520) Pulse compression; (320.7090) Ultrafast lasers; (320.7100) Ultrafast measurements.

References and links

1. J. C. M. Diels, J. J. Fontaine, I. C. McMichael, and F. Simoni, "Control and measurement of ultrashort pulse shapes (in amplitude and phase) with femtosecond accuracy," Appl. Opt. **24**(9), 1270–1282 (1985).
2. K. Naganuma, K. Mogi, and H. Yamada, "General method for ultrashort light pulse chirp measurement," IEEE J. Quantum Electron. **25**(6), 1225–1233 (1989).
3. A. Baltuška, Z. Wei, M. S. Pshenichnikov, D. A. Wiersma, and R. Szipöcs, "All-solid-state cavity-dumped sub-5-fs laser," Appl. Phys. B **65**(2), 175–188 (1997).
4. J. W. Nicholson, J. Jasapara, W. Rudolph, F. G. Omenetto, and A. J. Taylor, "Full-field characterization of femtosecond pulses by spectrum and cross-correlation measurements," Opt. Lett. **24**(23), 1774–1776 (1999).
5. D. J. Kane and R. Trebino, "Characterization of arbitrary femtosecond pulses using frequency-resolved optical gating," IEEE J. Quantum Electron. **29**(2), 571–579 (1993).
6. R. Trebino and D. J. Kane, "Using phase retrieval to measure the intensity and phase of ultrashort pulses: frequency-resolved optical gating," J. Opt. Soc. Am. A **10**(5), 1101–1111 (1993).
7. C. Iaconis and I. A. Walmsley, "Spectral phase interferometry for direct electric-field reconstruction of ultrashort optical pulses," Opt. Lett. **23**(10), 792–794 (1998).
8. A. S. Wyatt, I. A. Walmsley, G. Stibenz, and G. Steinmeyer, "Sub-10 fs pulse characterization using spatially encoded arrangement for spectral phase interferometry for direct electric field reconstruction," Opt. Lett. **31**(12), 1914–1916 (2006).
9. J. R. Birge, H. M. Crespo, and F. X. Kärtner, "Theory and design of two-dimensional spectral shearing interferometry for few-cycle pulse measurement," J. Opt. Soc. Am. B **27**(6), 1165–1173 (2010).
10. V. V. Lozovoy, I. Pastirk, and M. Dantus, "Multiphoton intrapulse interference. IV. Ultrashort laser pulse spectral phase characterization and compensation," Opt. Lett. **29**(7), 775–777 (2004).
11. B. Xu, J. M. Gunn, J. M. D. Cruz, V. V. Lozovoy, and M. Dantus, "Quantitative investigation of the multiphoton intrapulse interference phase scan method for simultaneous phase measurement and compensation of femtosecond laser pulses," J. Opt. Soc. Am. B **23**(4), 750–759 (2006).
12. Y. Coello, V. V. Lozovoy, T. C. Gunaratne, B. Xu, I. Borukhovich, C.-H. Tseng, T. Weinacht, and M. Dantus, "Interference without an interferometer: a different approach to measuring, compressing, and shaping ultrashort laser pulses," J. Opt. Soc. Am. B **25**(6), A140–A150 (2008).
13. V. V. Lozovoy, B. Xu, Y. Coello, and M. Dantus, "Direct measurement of spectral phase for ultrashort laser pulses," Opt. Express **16**(2), 592–597 (2008).
14. J. A. Nelder and R. Mead, "A simplex method for function minimization," Comput. J. **7**, 308–313 (1965).
15. J. W. Nicholson, F. G. Omenetto, D. J. Funk, and A. J. Taylor, "Evolving FROGS: phase retrieval from frequency-resolved optical gating measurements by use of genetic algorithms," Opt. Lett. **24**(7), 490–492 (1999).
16. A. Baltuška, M. S. Pshenichnikov, and D. A. Wiersma, "Amplitude and phase characterization of 4.5-fs pulses by frequency-resolved optical gating," Opt. Lett. **23**(18), 1474–1476 (1998).
17. A. Baltuška, M. S. Pshenichnikov, and D. A. Wiersma, "Second-harmonic generation frequency-resolved optical gating in the single-cycle regime," IEEE J. Quantum Electron. **35**(4), 459–478 (1999).

#156410 - $15.00 USD Received 14 Oct 2011; revised 18 Nov 2011; accepted 18 Nov 2011; published 23 Dec 2011

1. Introduction

The characterization of ultrashort laser pulses is often as important as the generation process itself. Since no methods exist for the direct measurement of such short events, self-referencing techniques are usually employed.

Traditionally, ultrashort pulses have been characterized by nonlinear autocorrelation diagnostics (see, e.g., [1]), which are still widely used in many laboratories. Although relatively simple to implement, these fail to provide complete information about the pulses. Still, several methods have been devised allowing for the reconstruction of the amplitude and phase of the pulses by combination of autocorrelation and spectral measurements (see, e.g [2–4].). An important improvement over these techniques came in 1993 with the introduction of frequency resolved optical gating (FROG) [5, 6]: by spectrally resolving an autocorrelation (or cross-correlation) signal, a sonogram-like trace is created from which complete characterization of a given pulse can be performed using an iterative algorithm. The quality of the retrieval is reflected by the corresponding FROG error, and the time and frequency marginals of the trace also provide a means to cross-check the results. There are many variants of FROG today, which all rely on spectrally resolving some time-gated signal. Other methods widely used today are related to the technique of spectral phase interferometry for direct electric-field reconstruction (SPIDER), first introduced in 1998 [7]. These methods do not rely on temporal gating, but instead on interferometry in the spectral domain: the spectrum of a given pulse is made to interfere with a frequency-shifted (sheared) replica of itself, and the resulting spectral interferogram is recorded. Although usually more complicated to set up, retrieving the spectral phase from a SPIDER trace is numerically much simpler than in FROG, but there is no straightforward means to determine the quality of the phase measurement, which strongly depends on the accuracy of the delay between the two replicas. Recent SPIDER-related methods have been devised that allow overcoming this calibration issue [8, 9].

Recently, a new paradigm in pulse characterization based on phase scanning, multiphoton intrapulse interference phase scan (MIIPS) [10–13], was introduced. It consists in applying well-known spectral phases to the pulse to be characterized and measuring the resulting second-harmonic generation (SHG) signal. By finding which locally introduced amount of group delay dispersion (GDD) results in compression at a given wavelength, the original GDD of the pulse can be found, thereby allowing for the reconstruction of the unknown phase.

In all of the above techniques, the characterization of few-cycle laser pulses is still challenging and usually requires specific adaptations and materials in order to accommodate the associated broad bandwidths.

Our method is related to the MIIPS technique in the sense that a phase scan is performed on the pulse to be measured; however both the experimental setup and the phase retrieval method are substantially different, and these will provide major advantages with respect to other methods. In fact, our technique can be implemented using a standard chirped mirror compressor setup: we use chirped mirrors to ensure that the pulse becomes negatively chirped, and then add glass continuously until the pulse becomes as short as possible. Measuring the generated SHG spectra around this optimal glass insertion allows us to fully retrieve the spectral phase of the pulse in a robust and precise way without the need of further diagnostic tools. The alignment is very easy: no beam-splitting at any point, and no interferometric precision or stability are needed. This method is also particularly relaxed with respect to the necessary bandwidth of the SHG process, so relatively thick (tens of micrometers) frequency doubling crystals can be employed even when measuring few-cycle pulses.

2. Method

Consider an ultrashort laser pulse, which can be described by its complex spectral amplitude

#156410 - $15.00 USD Received 14 Oct 2011; revised 18 Nov 2011; accepted 18 Nov 2011; published 23 Dec 2011
(C) 2012 OSA

$$\tilde{U}(\omega) = \left|\tilde{U}(\omega)\right| \exp\{i\phi(\omega)\}. \tag{1}$$

The pulse goes through a piece of transparent glass and then a SHG crystal, and the measured SHG spectral power as a function of thickness is proportional to

$$S(\omega, z) = \left| \int \left(\int \tilde{U}(\Omega) \exp\left\{izk(\Omega)\right\} \exp(i\Omega t) d\Omega \right)^2 \exp(-i\omega t) dt \right|^2 \tag{2}$$

where z is the thickness of the glass and $k(\Omega)$ its frequency-dependent phase per unit length (or wavenumber). Here, we simply take the original spectrum (amplitude and phase), apply a phase, and Fourier transform it to have the electric field in the time domain. Then SHG is performed (the time-dependent field is squared), and an inverse Fourier transform gives us the SHG spectrum. We perform a dispersion scan (we will call it d-scan for short) on the unknown pulse by introducing different thicknesses of glass and measuring the corresponding SHG spectra, which results in a two-dimensional trace. This is analogous to a MIIPS trace, but in our case the phase function is simply the one introduced by a piece of glass.

This model assumes that the SHG process consists simply on squaring the electric field in time, which assumes an instantaneous and wavelength-independent nonlinearity. We will discuss the consequences of this approximation later. For simplicity, we will also use negative values for the glass insertion. While this is obviously unrealistic from an experimental point of view, mathematically it simply results from setting a given reference insertion as zero. Regardless of this definition, if we know the electric field for a given insertion, it will be straightforward to calculate it for any other insertion.

As an example, we show in Fig. 1 calculated dispersion-scanned SHG traces of some representative spectra, where the spectral phase (left) refers to zero insertion in the d-scans (right). In all cases we used the same power spectrum, which is an actual spectrum measured from the few-cycle ultrafast oscillator used in the next section, and applied different phase curves. The assumed glass is BK7, and the corresponding phase was calculated from easily available Sellmeier equations.

The question now arises on how to find the electric field that generated a given scan. In MIIPS it consists on, for each wavelength λ_0 in the SHG spectrum, finding the insertion that maximizes this signal, noting the corresponding GDD at that point, and assuming that the GDD at the corresponding wavelength $2\lambda_0$ in the fundamental spectrum is the negative of this value. In our case, applying the MIIPS retrieval technique gives good results for slowly varying phases, such as pure GDD and/or third-order dispersion (TOD), but fails for complex and structured phases, such as the modulated phase exemplified in Fig. 1(g). While the SHG at a given wavelength is mostly determined by the spectral power and phase at twice that wavelength in the fundamental field, there is always a coupling between all the generating and generated wavelengths. In the case of MIIPS, where a pulse shaper is normally used, an iterative procedure effectively solves the retrieval problem mentioned above, as the phase gets flatter with each iteration.

We used this coupling between generating and generated wavelengths to our advantage: by using the whole trace's information, combined with a numerical iterative algorithm, we are able to retrieve the spectral phase in a robust and precise way.

#156410 - $15.00 USD Received 14 Oct 2011; revised 18 Nov 2011; accepted 18 Nov 2011; published 23 Dec 2011

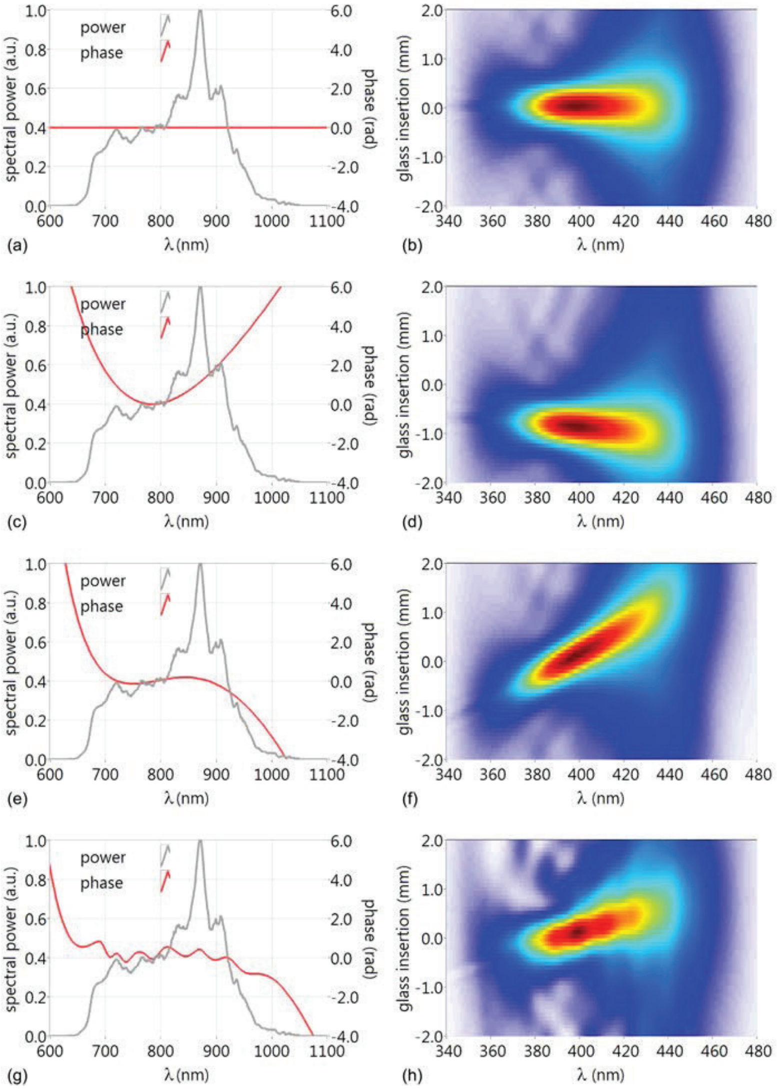

Fig. 1. Example of simulated dispersion scans, where the spectral phase plots on the left correspond to zero insertion in the scans on the right. (a) Fourier limited pulse. (b) Linearly chirped pulse (second-order dispersion only) – this causes mostly a translation of the trace with respect to the glass insertion, but since the glass itself doesn't introduce pure second order dispersion, the pulse is never completely compressed for any insertion, so it appears slightly tilted. (c) Pulse with third-order dispersion only, around 800 nm, which results in a clear tilt in the trace with respect to the previous cases. (d) A more complex phase curve, mostly third-order dispersion and some phase ringing.

The method we used to retrieve the phase, although certainly not the only possible one, proved to be extremely flexible and reliable. It is based on the Nelder–Mead [14] (or downhill simplex) algorithm. We use the measured spectral power density, and by applying different phase curves, try to minimize a merit function (the rms error between the measured and simulated scans, as commonly used in FROG retrievals), given by

$$G = \sqrt{\frac{1}{N_i N_j} \sum_{i,j} \left(S_{meas}(\omega_i, z_j) - \mu S_{sim}(\omega_i, z_j) \right)^2} \tag{3}$$

where S_{meas} and S_{sim} refer to the measured and simulated scans, respectively, and μ is the factor that minimizes the error. This factor, which can be easily found by differentiating the error with respect to μ, is given by

$$\mu = \frac{\sum_{i,j} S_{meas}(\omega_i, z_j) S_{sim}(\omega_i, z_j)}{\sum_{i,j} S_{sim}(\omega_i, z_j)^2}, \tag{4}$$

and must be updated at each iteration. The problem can now be treated as a general multi-dimension optimization problem, where the phase is defined by a function of a set of parameters (or dimensions) and the function to be minimized is the error *G*. To make things easier for the algorithm, the phase function should be described in a convenient basis. We want to minimize the number of dimensions in the problem while still accurately describing the phase, and we want a basis whose functions are as uncoupled as possible, to prevent the algorithm from getting stuck on local minima. Different approaches can be taken here. Some authors choose to allow each point of the sampled complex spectral or time amplitude to be an independent variable (e.g [15].), and as such, the number of dimensions of the problem will be determined by the sampling. Another (very common) choice is to use a Taylor expansion as a basis. In the former case, the large number of parameters makes the algorithm rather slow, while in the latter, there is a high degree of coupling between the even terms (i.e., second order dispersion, fourth order dispersion, etc.) as well as between the odd terms (third order dispersion, fifth order dispersion, etc.). This would still be a good choice (if not optimal) for simple phase functions, as the ones introduced by glasses, gratings, prism compressors, etc., which are accurately described in such a way.

In our case, we chose to write the phase as a Fourier series. This was inspired by the fact that Fourier components are orthogonal. If one could access directly the error between the true phase and its Fourier representation, then each Fourier component could be directly determined by minimizing the error. While we don't have direct access to this error, the overall trace error is a good indicator of the phase error. In fact, for all the cases we tried, the algorithm converged very well. For simple phases (i.e. mostly GDD and TOD) about 6 to 10 coefficients were used, whereas for more complicated phases up to 60 coefficients were used. The highest phase frequencies present on the fundamental spectrum can be estimated from the structure of its dispersion scan.

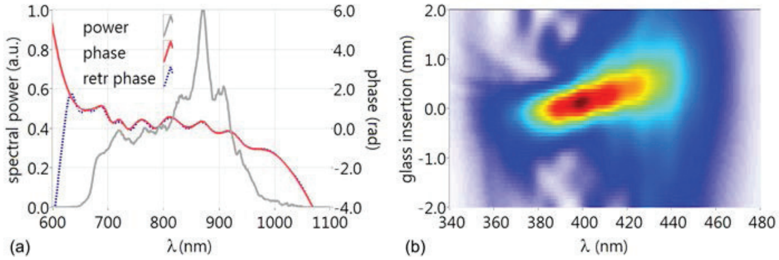

Fig. 2. Example of scan and phase retrievals from Fig. 1 (h).

Figure 2 shows an example of a simulated spectrum (measured power spectrum and simulated phase), its d-scan, and the corresponding retrieved phase. The agreement between the retrieved and original phases is very good typically down to regions where the spectral power is around 2% of the peak spectral power.

Let us now consider a more realistic scenario of particular importance for the case of ultra-broadband few-cycle pulses, where the SHG signal cannot be described by simply squaring the electric field (the SHG process doesn't have infinite bandwidth). Even in this case, the SHG signal is well described by the simple model (Eq. (2), provided the spectrum is multiplied by an adequate spectral filter [16, 17], so the measured signal is simply given by

$$S_{meas}(\omega, z) = S_{ideal}(\omega, z)R(\omega), \qquad (5)$$

where *R(ω)* is the spectral filter and S_{ideal} denotes the ideal, flat response process (Eq. (2). If the spectrometer's response to the SH signal is unknown it can also be included in this response function.

For the discussed algorithm, it is crucial to have a well calibrated signal, the reason being that the algorithm uses the overall error as a merit function. If the spectral response is not flat, the algorithm reacts by introducing fast phase variations on the regions with lower filter response, which makes the signal go out of the calculation box, therefore artificially reducing the overall error. There are several ways around this. The most straightforward would be to measure the spectrometer's response and simulate the SHG crystal spectral curve, but both are unfortunately difficult to obtain accurately. We found numerically that the integral of the trace over the thickness parameter (the frequency marginal)

$$M(\omega) = \int_{-\infty}^{+\infty} S(\omega, z)dz \qquad (6)$$

does not depend on the original spectral phase of the pulse, *ϕ(ω)*. It is then easy to simulate a trace for a Fourier-limited pulse, and use its marginal to calibrate the measured one. Comparing the simulated scan's marginal to the measured scan's marginal it is straightforward to calculate the spectral response *R(ω)*. Knowing the filter response, we can either divide the experimental trace by it, or include it in the retrieval process, by multiplying it by the "ideal" simulated trace, in each iteration. If the filter has zeros in the spectral region of interest, then we are left only with the latter option. We have successfully calibrated experimental scans this way.

We also devised another approach, which proved to be much easier to implement and more flexible. It consists in allowing the error function to be minimized for each wavelength, with the overall error being a weighted function of all these errors. So, given an experimental and simulated scan, the factor that minimizes the error for each frequency component is given by

$$\mu_i = \frac{\sum_j S_{meas}(\omega_i, z_j) S_{sim}(\omega_i, z_j)}{\sum_j S_{sim}(\omega_i, z_j)^2} \qquad (7)$$

and the overall error is

$$G = \sqrt{\frac{1}{N_i N_j} \sum_{i,j} \left(S_{meas}(\omega_i, z_j) - \mu_i S_{sim}(\omega_i, z_j) \right)^2}. \qquad (8)$$

Now, by using this new error function, the algorithm effectively works on matching the trace's features, instead of simply trying to match the trace as a whole. If the trace is successfully retrieved, then the minimizing factors μ_i give us the complete filter response. What is perhaps more remarkable with this approach is that it is possible to correctly retrieve the phase for a certain frequency, even if there is no signal at the corresponding SHG (doubled) frequency. This can be seen from the examples in Fig. 3. Even in the case where the simulated filter response is clipped to zero, like in Fig. 3(d) (therefore making it impossible to

#156410 - $15.00 USD Received 14 Oct 2011; revised 18 Nov 2011; accepted 18 Nov 2011; published 23 Dec 2011

calibrate the signal), the phase is nevertheless correctly retrieved across the whole spectrum (Fig. 3(a)). This would not be possible with the MIIPS retrieval technique.

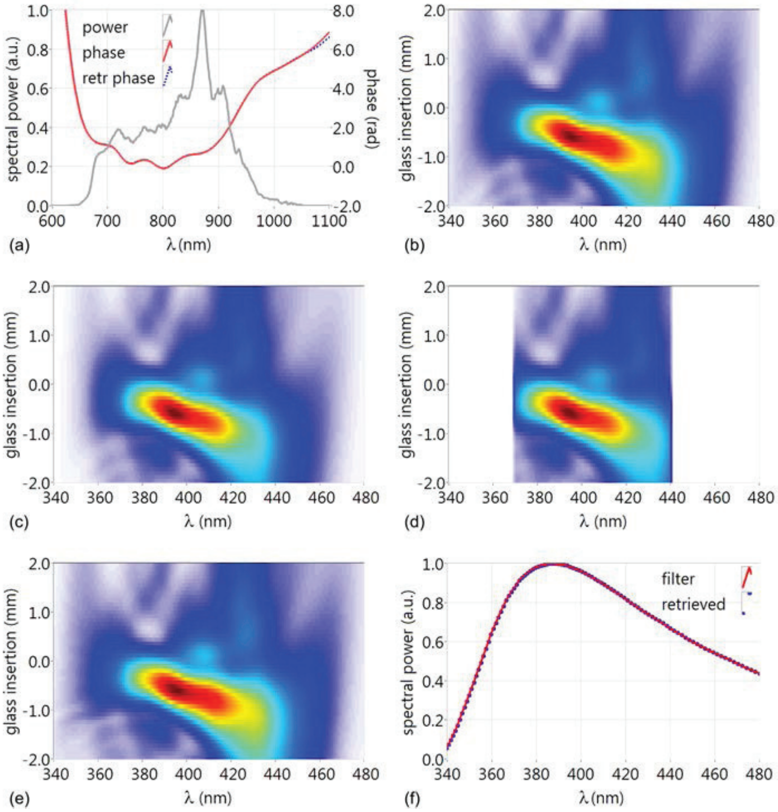

Fig. 3. Example of simulated traces including spectral filters in the SHG process. (a) Simulated spectrum, where the retrieved phase shown is for the worst case scenario, (d). (b) Ideal trace. (c) Ideal trace multiplied by a typical SHG crystal efficiency curve. (d) Same as (c), but clipped at around 370nm and 440nm. (e) Retrieved “ideal” scan from scan (d) – the retrieved scan is supposed to be identical to scan (b). (f) Applied and retrieved spectral filters from (c). The retrieved filter is made up of the error minimizing coefficients μ‘s for each wavelength.

3. Experimental results

A simplified diagram of our experimental setup is given in Fig. 4. It consists on an ultrafast oscillator (Femtolasers Rainbow CEP, not shown), four double-chirped mirror pairs (Venteon GmbH), followed by BK7 AR-coated glass wedges with an 8° angle, an off-axis aluminum-coated parabola (50 mm focal length) and a standard 20 µm thick BBO crystal cut for type I SHG at 800 nm. The chirped mirrors are made in matched pairs to minimize GDD oscillations, and therefore come in two types (described as “blue” and “green” on Fig. 4).

A dispersion scan was performed with very fine sampling in thickness (250 acquired spectra, with a thickness step of about 20 µm). Because of the relatively small angle of the wedges, this thickness step corresponds to a wedge translation step of more than 100 µm (and even this is much more than necessary, as a thickness step of 100 µm is typically enough, which corresponds to a translation step of more than 500 µm) so the positioning precision is

#156410 - $15.00 USD Received 14 Oct 2011; revised 18 Nov 2011; accepted 18 Nov 2011; published 23 Dec 2011

quite undemanding compared to interferometric methods. Depending on the neccessary spectrometer integration time, a typical scan is performed in a few seconds.

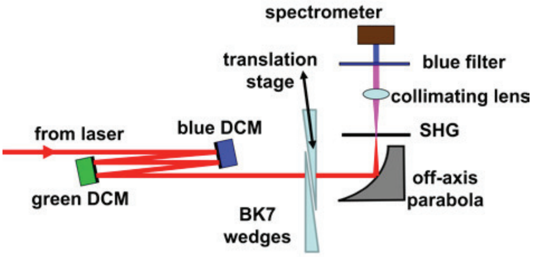

Fig. 4. Experimental setup. The laser is a Femtolasers Rainbow CEP (80 MHz repetition rate, energy per pulse of 2.5 nJ, FWHM Fourier limit of 6 fs), SHG is a 20 µm thick BBO crystal. The double chirped mirrors (DCM) are made in matched pairs to minimize phase ringing, and the aluminum off-axis parabola has a 50 mm focal length.

To test the precision of the method, a bootstrap analysis was performed: from this fine scan, five scans were extracted, all with different data sets, by using every fifth spectrum (i.e., scan 1 uses steps 1,6,11, etc., scan 2 uses steps 2, 7, 12, etc.). The background signal was subtracted, and when the resulting signal was negative, we kept it as such, instead of making it zero. This way we allow for the retrieved data to (correctly) tend to zero where it should, instead of forcing the algorithm to try to converge to half of the noise level.

Two different retrieval techniques were used for each scan thus yielding a total of ten retrievals. In the first case we calibrated the scan from its frequency marginal (i.e., by forcing the integral over z to be the same for the measured scan and for a simulated scan corresponding to the Fourier limit case), and in the second, we allowed the error to adjust to each spectral slice. Typical retrieval times on a standard personal computer range from a few seconds to a few minutes, depending on the number of coefficients used to describe the phase.

In all cases, the retrievals are very similar so we grouped them all together for the statistical analysis (Fig. 5). The “zero” insertion here refers to the insertion at which the pulse is shortest, and for which the phase and time reconstructions are shown. It actually corresponds to about 3 mm of BK7 glass. The retrieved pulse width was 7.1 ± 0.1 fs. The pulses clearly show the effect of residual uncompensated third order dispersion (also evidenced by the tilt in the corresponding d-scan trace) in the form of post-pulses. Note that there is no time-direction ambiguity on the retrieved pulse. Even if the laser and setup as it is don’t allow for any shorter pulses, the precise phase measure allows one to re-design the compressor if necessary, i.e. by using different glasses and/or chirped mirrors.

It is worth noting that the phase retrieval is very robust even in regions of very low spectral power density. And, considering there is very little SHG signal above 470 nm and below 350 nm, it is surprising at first that the phase is consistently retrieved well beyond 940 nm and below 700 nm. Again, this is due to the coupling between all the frequency components on the trace and the original spectrum. As with FROG, the key aspect of this technique is the data redundancy in the dispersion-scanned SHG trace.

As with the simulated scans, it was possible to fully retrieve the filter response of the system as well. With both methods we retrieved very similar curves for all traces.

The phase retrieval technique used in this work is certainly not the only possible one. Even if it worked extremely well for our purposes, better, faster and more elegant numerical approaches are certainly possible and will be studied in future work.

Another advantage of using a multi-dimensional minimization technique is its extreme flexibility. For example, we tried feeding the algorithm the glass thickness spacing as a parameter, and it correctly found the known experimental value.

After having the field well characterized for a given insertion it is straightforward to calculate it for any other insertion by applying the known phase curve of the glass to the

#156410 - $15.00 USD Received 14 Oct 2011; revised 18 Nov 2011; accepted 18 Nov 2011; published 23 Dec 2011

retrieved phase. One can then simply find the insertion that minimized the pulse length and move the wedges into the corresponding position.

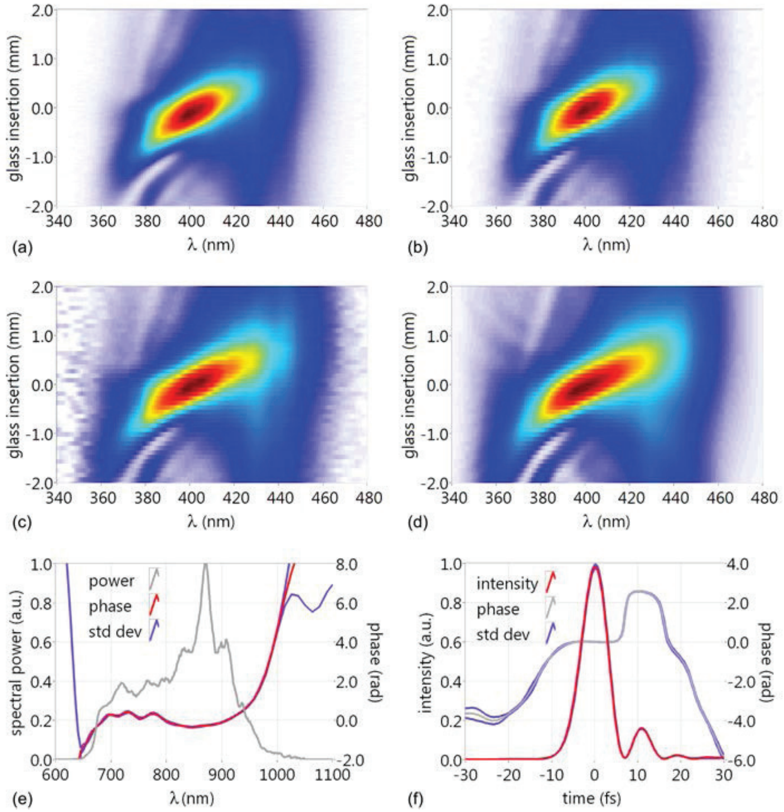

Fig. 5. Measured and retrieved scans. (a) Raw scan, made up of 250 spectra. (b) Scan made from 50 spectra out of the raw scan. (c) Calibrated scan, by using the frequency marginals in Eq. (6)d) Retrieved scan from (c) - either retrieving from (c) or (b), the results are very similar. Plots (e) and (f) show a bootstrap analysis on spectrum and time, from 10 different retrievals. From the original scan with 250 spectra, 5 different scans were obtained using different data sets. The two different techniques were used on each data set. The red curve is the average value, and the blue curves are one standard deviation above and below the average. Retrieved pulse width at FWHM was 7.1 ± 0.1 fs.

4. Conclusion

We have described and demonstrated a simple, inexpensive and robust method to characterize ultrashort laser pulses based on iterative phase retrieval from dispersion scans, using chirped mirrors, wedges and a standard (relatively thick) SHG crystal. The alignment is very easy (no beam-splitting at any point, and no interferometric precision or stability are needed). In our case, the main part of the setup (chirped mirrors and wedges) was already being used for pulse compression, so there was no need to employ other characterization methods. This is the situation where this technique is especially useful. It is of course possible to use the system as a standalone device. Also, we are not as limited by the phase-matching restrictions of the SHG crystal as with other techniques, which allows for the characterization of extremely broad bandwidth pulses without having to sacrifice SHG efficiency by employing

#156410 - $15.00 USD Received 14 Oct 2011; revised 18 Nov 2011; accepted 18 Nov 2011; published 23 Dec 2011

unpractically thin crystals. We believe this technique might be immediately useful for many people working in the field with pulse compressors based on chirped mirrors.

Acknowledgments

This work was partly supported by FCT – Fundação para a Ciência e a Tecnologia and FEDER (grants SFRH/BD/37100/2007 and PTDC/FIS/115102/2009), the European Research Council (ALMA), the Marie Curie Intra-European Fellowship ATTOCO, the Marie Curie Initial Training Network ATTOFEL, the Knut and Alice Wallenberg Foundation, the Joint Research Programme ALADIN of Laserlab-Europe II and the Swedish Research Council.

#156410 - $15.00 USD   Received 14 Oct 2011; revised 18 Nov 2011; accepted 18 Nov 2011; published 23 Dec 2011

(C) 2012 OSA

Paper IV

Characterization of broadband few-cycle laser pulses with the d-scan technique

Miguel Miranda, Cord L. Arnold, Thomas Fordell, Francisco Silva,
Benjamín Alonso, Rosa Weigand, Anne L'Huillier, and Helder Crespo.

Opt. Express **20**, 18732–18743 (2012).

Characterization of broadband few-cycle laser pulses with the d-scan technique

Miguel Miranda,[1,2,*] Cord L. Arnold,[2] Thomas Fordell,[2] Francisco Silva,[1] Benjamín Alonso,[3] Rosa Weigand,[4] Anne L'Huillier,[2] and Helder Crespo[1]

[1] *IFIMUP-IN and Departamento de Física e Astronomia, Universidade do Porto, Rua do Campo Alegre 687, 4169-007 Porto, Portugal*
[2] *Department of Physics, Lund University, P.O. Box 118, SE-221 00 Lund, Sweden*
[3] *Grupo de Investigación en Óptica Extrema (GIOE), Universidad de Salamanca, Pl. de la Merced s/n, E-37008 Salamanca, Spain*
[4] *Departamento de Óptica, Facultad de Ciencias Físicas, Universidad Complutense de Madrid, Avda. Complutense s/n, 28040 Madrid, Spain*
[*] *mmiranda@fc.up.pt*

Abstract: We present an analysis and demonstration of few-cycle ultrashort laser pulse characterization using second-harmonic dispersion scans and numerical phase retrieval algorithms. The sensitivity and robustness of this technique with respect to noise, measurement bandwidth and complexity of the measured pulses is discussed through numerical examples and experimental results. Using this technique, we successfully demonstrate the characterization of few-cycle pulses with complex and structured spectra generated from a broadband ultrafast laser oscillator and a high-energy hollow fiber compressor.

©2012 Optical Society of America

OCIS codes: (320.2250) Femtosecond phenomena; (320.5520) Pulse compression; (320.7090) Ultrafast lasers; (320.7100) Ultrafast measurements.

References and links

1. U. Morgner, R. Ell, G. Metzler, T. R. Schibli, F. X. Kärtner, J. G. Fujimoto, H. A. Haus, and E. P. Ippen, "Nonlinear Optics with Phase-Controlled Pulses in the Sub-Two-Cycle Regime," Phys. Rev. Lett. **86**(24), 5462–5465 (2001).
2. S. Rausch, T. Binhammer, A. Harth, J. Kim, R. Ell, F. X. Kärtner, and U. Morgner, "Controlled waveforms on the single-cycle scale from a femtosecond oscillator," Opt. Express **16**(13), 9739–9745 (2008).
3. T. Fuji, A. Unterhuber, V. S. Yakovlev, G. Tempea, A. Stingl, F. Krausz, and W. Drexler, "Generation of smooth, ultra-broadband spectra directly from a prism-less Ti:sapphire laser," Appl. Phys. B **77**(1), 125–128 (2003).
4. H. M. Crespo, J. R. Birge, E. L. Falcão-Filho, M. Y. Sander, A. Benedick, and F. X. Kärtner, "Nonintrusive phase stabilization of sub-two-cycle pulses from a prismless octave-spanning Ti:sapphire laser," Opt. Lett. **33**(8), 833–835 (2008).
5. A. Dubietis, G. Jonušauskas, and A. Piskarskas, "Powerful femtosecond pulse generation by chirped and stretched pulse parametric amplification in BBO crystal," Opt. Commun. **88**(4-6), 437–440 (1992).
6. A. Dubietis, R. Butkus, and A. P. Piskarskas, "Trends in chirped pulse optical parametric amplification," IEEE J. Sel. Top. Quantum Electron. **12**(2), 163–172 (2006).
7. D. Strickland and G. Mourou, "Compression of amplified chirped optical pulses," Opt. Commun. **56**(3), 219–221 (1985).
8. A. Amani Eilanlou, Y. Nabekawa, K. L. Ishikawa, H. Takahashi, and K. Midorikawa, "Direct amplification of terawatt sub-10-fs pulses in a CPA system of Ti:sapphire laser," Opt. Express **16**(17), 13431–13438 (2008).
9. F. Krausz and M. Ivanov, "Attosecond physics," Rev. Mod. Phys. **81**(1), 163–234 (2009).
10. E. Esarey, C. B. Schroeder, and W. P. Leemans, "Physics of laser-driven plasma-based electron accelerators," Rev. Mod. Phys. **81**(3), 1229–1285 (2009).
11. M. Nisoli, S. De Silvestri, and O. Svelto, "Generation of high energy 10 fs pulses by a new pulse compression technique," Appl. Phys. Lett. **68**(20), 2793 (1996).
12. M. Nisoli, S. De Silvestri, O. Svelto, R. Szipöcs, K. Ferencz, Ch. Spielmann, S. Sartania, and F. Krausz, "Compression of high-energy laser pulses below 5 fs," Opt. Lett. **22**(8), 522–524 (1997).
13. C. P. Hauri, W. Kornelis, F. W. Helbing, A. Heinrich, A. Couairon, A. Mysyrowicz, J. Biegert, and U. Keller, "Generation of intense, carrier-envelope phase-locked few-cycle laser pulses through filamentation," Appl. Phys. B **79**(6), 673–677 (2004).
14. I. Walmsley and C. Dorrer, "Characterization of ultrashort electromagnetic pulses," Adv. Opt. Photon. **1**(2), 308–437 (2009).

#167354 - $15.00 USD Received 25 Apr 2012; revised 25 May 2012; accepted 12 Jun 2012; published 1 Aug 2012

15. J. C. M. Diels, J. J. Fontaine, I. C. McMichael, and F. Simoni, "Control and measurement of ultrashort pulse shapes (in amplitude and phase) with femtosecond accuracy," Appl. Opt. **24**(9), 1270–1282 (1985).
16. C. Iaconis and I. A. Walmsley, "Spectral phase interferometry for direct electric-field reconstruction of ultrashort optical pulses," Opt. Lett. **23**(10), 792–794 (1998).
17. A. S. Wyatt, I. A. Walmsley, G. Stibenz, and G. Steinmeyer, "Sub-10 fs pulse characterization using spatially encoded arrangement for spectral phase interferometry for direct electric field reconstruction," Opt. Lett. **31**(12), 1914–1916 (2006).
18. J. R. Birge, H. M. Crespo, and F. X. Kärtner, "Theory and design of two-dimensional spectral shearing interferometry for few-cycle pulse measurement," J. Opt. Soc. Am. B **27**(6), 1165–1173 (2010).
19. V. V. Lozovoy, I. Pastirk, and M. Dantus, "Multiphoton intrapulse interference. IV. Ultrashort laser pulse spectral phase characterization and compensation," Opt. Lett. **29**(7), 775–777 (2004).
20. B. Xu, J. M. Gunn, J. M. D. Cruz, V. V. Lozovoy, and M. Dantus, "Quantitative investigation of the multiphoton intrapulse interference phase scan method for simultaneous phase measurement and compensation of femtosecond laser pulses," J. Opt. Soc. Am. B **23**(4), 750–759 (2006).
21. Y. Coello, V. V. Lozovoy, T. C. Gunaratne, B. Xu, I. Borukhovich, C.-H. Tseng, T. Weinacht, and M. Dantus, "Interference without an interferometer: a different approach to measuring, compressing, and shaping ultrashort laser pulses," J. Opt. Soc. Am. B **25**(6), A140–A150 (2008).
22. V. V. Lozovoy, B. Xu, Y. Coello, and M. Dantus, "Direct measurement of spectral phase for ultrashort laser pulses," Opt. Express **16**(2), 592–597 (2008).
23. D. J. Kane and R. Trebino, "Characterization of arbitrary femtosecond pulses using frequency-resolved optical gating," IEEE J. Quantum Electron. **29**(2), 571–579 (1993).
24. R. Trebino and D. J. Kane, "Using phase retrieval to measure the intensity and phase of ultrashort pulses: frequency-resolved optical gating," J. Opt. Soc. Am. A **10**(5), 1101–1111 (1993).
25. R. Trebino, K. W. DeLong, D. N. Fittinghoff, J. N. Sweetser, M. A. Krumbugel, B. A. Richman, and D. J. Kane, "Measuring ultrashort laser pulses in the time-frequency domain using frequency-resolved optical gating," Rev. Sci. Instrum. **68**(9), 3277–3295 (1997).
26. M. Miranda, T. Fordell, C. Arnold, A. L'Huillier, and H. Crespo, "Simultaneous compression and characterization of ultrashort laser pulses using chirped mirrors and glass wedges," Opt. Express **20**(1), 688–697 (2012).
27. D. Keusters, H.-S. Tan, P. O'Shea, E. Zeek, R. Trebino, and W. S. Warren, "Relative-phase ambiguities in measurements of ultrashort pulses with well-separated multiple frequency components," J. Opt. Soc. Am. B **20**(10), 2226–2237 (2003).
28. A. Baltuška, M. S. Pshenichnikov, and D. A. Wiersma, "Amplitude and phase characterization of 4.5-fs pulses by frequency-resolved optical gating," Opt. Lett. **23**(18), 1474–1476 (1998).
29. A. Baltuška, M. S. Pshenichnikov, and D. A. Wiersma, "Second-harmonic generation frequency-resolved optical gating in the single-cycle regime," IEEE J. Quantum Electron. **35**(4), 459–478 (1999).
30. J. A. Nelder and R. Mead, "A simplex method for function minimization," Comput. J. **7**, 308–313 (1965).
31. V. S. Yakovlev, P. Dombi, G. Tempea, C. Lemell, J. Burgdorfer, T. Udem, and A. Apolonski, "Phase-stabilized 4-fs pulses at the full oscillator repetition rate for a photoemission experiment," Appl. Phys. B **76**(3), 329–332 (2003).
32. A. Baltuška, A. Pugzlys, M. S. Pshenichnikov, and D. A. Wiersma, "Rapid amplitude-phase reconstruction of femtosecond pulses from intensity autocorrelation and spectrum," in *Conference on Lasers and Electro-Optics*, 1999 OSA Technical Digest Series (Optical Society of America, Washington, D.C., 1999), 264–265.
33. C. Dorrer and I. Walmsley, "Accuracy criterion for ultrashort pulse characterization techniques: application to spectral phase interferometry for direct electric field reconstruction," J. Opt. Soc. Am. B **19**(5), 1019–1029 (2002).
34. G. Stibenz, C. Ropers, Ch. Lienau, Ch. Warmuth, A. S. Wyatt, I. A. Walmsley, and G. Steinmeyer, "Advanced methods for the characterization of few-cycle light pulses: a comparison," Appl. Phys. B **83**(4), 511–519 (2006).
35. A. S. Wyatt, A. Grün, P. K. Bates, O. Chalus, J. Biegert, and I. A. Walmsley, "Accuracy measurements and improvement for complete characterization of optical pulses from nonlinear processes via multiple spectral-shearing interferometry," Opt. Express **19**(25), 25355–25366 (2011).
36. D. R. Austin, T. Witting, and I. A. Walmsley, "Resolution of the relative phase ambiguity in spectral shearing interferometry of ultrashort pulses," Opt. Lett. **35**(12), 1971–1973 (2010).
37. H. Crespo, M. Miranda, P. Oliveira, and R. Weigand are preparing a manuscript to be called "Broadband 5.9-fs Ti:sapphire laser characterized using the dispersion-scan technique."

1. Introduction

Today's femtosecond laser oscillators can easily deliver pulse durations in the few-cycle regime [1–4]. Ultra-broadband oscillators based on Ti:Sapphire usually operate in regimes where strong nonlinearities occur within the gain medium itself, which can lead to broadband and highly structured spectra. On the other hand, there is a strong demand for high-power ultrashort pulses not achievable directly with laser oscillators. These can be produced by optical parametric chirped pulse amplification (OPCPA) [5, 6] or by chirped pulse amplification (CPA) [7, 8]. It is however a complicated task to preserve the short pulse duration in the amplification process in traditional CPA systems, as effects like gain

#167354 - $15.00 USD Received 25 Apr 2012; revised 25 May 2012; accepted 12 Jun 2012; published 1 Aug 2012
(C) 2012 OSA

narrowing reduce the spectral width of the amplified pulses. Thus, external pulse compression schemes are usually employed that can provide energetic pulses in the few- to single-cycle regimes. These pulses have become indispensable tools in attoscience [9] and high-field physics [10]. The most common external compression schemes involve spectral broadening of amplified pulses by self phase modulation (SPM), either in a gas-filled capillary waveguide [11, 12] or in a self-guided filament [13], usually followed by temporal compression with chirped mirrors. The resulting spectra are generally a few hundred nanometers wide, often featuring strong modulations and spectral gaps. Furthermore, the phase acquired by the pulses in the broadening process is complicated due to the interplay between several effects, such as SPM, dispersion, plasma generation, and shockwave formation, and in practice can only be partially compensated for by chirped mirrors. Considering the broadband spectra with complicated structure and phase that normally arise, the characterization of pulses delivered by these external compression schemes is usually quite challenging.

When characterizing ultrashort laser pulses, different methods have different strengths and weaknesses [14]. The existing measurement techniques can be broadly defined to operate in the time domain (i.e., autocorrelations [15]), the spectral domain (spectral phase interferometry for direct electric-field reconstruction - SPIDER - and variants [16–18], and multiphoton intrapulse interference phase scan - MIIPS [19–22]) or both domains (frequency resolved optical gating - FROG [23–25]).

We have recently demonstrated a simple technique to characterize ultrashort pulses while compressing them with chirped mirrors and glass wedges [26]. Since chirped mirrors introduce fixed amounts of dispersion, they're commonly used together with a pair of glass wedges to fine-tune the dispersion so as to reach maximum compression. By measuring the fundamental spectrum and the second-harmonic generation (SHG) spectra around this optimum glass insertion, together with a numerical iterative algorithm, it is possible to fully characterize the pulses without the need for further diagnostics. In this work, we investigate the applicability of the method (which we call *d-scan,* short for dispersion scan) to particularly complex cases, namely sources with complex spectra (both in spectral power and phase), as well as its robustness to measurement bandwidth and noise. We demonstrate, via simulations and experiments, that it is possible to reconstruct the phase of few-cycle pulses generated by ultrabroad bandwidth oscillators and from post-compression in a hollow fiber from a CPA system. The main advantages of this technique are its simplicity (ease of alignment), sensitivity (no need for pulse splitting, so it uses all the available energy), relaxed bandwidth requirements, and the ability to measure the relative phase between well separated frequency components, provided the spectral gap between them is smaller than the largest continuous spectral region [27]. The cases considered here (both simulated and experimental) are of particular relevance for state-of-the-art broadband ultrashort pulse sources, where spectra are the result of complex nonlinear processes (e.g., Kerr effect and plasma interaction).

2. Method

An ultrashort laser pulse can be described by its complex spectral amplitude

$$\tilde{U}(\omega) = \left|\tilde{U}(\omega)\right| \exp\{i\,\phi(\omega)\}. \tag{1}$$

If the pulse goes through a piece of transparent glass and then a SHG crystal, the measured SHG spectral power as a function of thickness is proportional to

$$S(\omega, z) = \left| \int \left(\int \tilde{U}(\Omega) \exp\left\{ izk(\Omega) \right\} \exp(i\,\Omega t) d\,\Omega \right)^2 \exp(-i\,\omega t) dt \right|^2, \tag{2}$$

which can also be written in the spectral domain as a convolution (as usually found in MIIPS literature [19–22])

$$S(\omega,z) = \left| \int \tilde{U}(\Omega)\exp\{izk(\Omega)\}\tilde{U}(\omega-\Omega)\exp\{izk(\omega-\Omega)\}d\Omega \right|^2 \qquad (3)$$

where z is the glass thickness and $k(\Omega)$ is the frequency-dependent wavenumber of the glass. This simple SHG model assumes that the nonlinearity has infinite bandwidth, or at least that the spectral response is flat in the region of interest, which is seldom the case for pulses in the few-cycle regime and under normal experimental conditions. Fortunately the resulting SHG power spectrum is still well described by this simple model, provided that a spectral filter is included [28, 29].

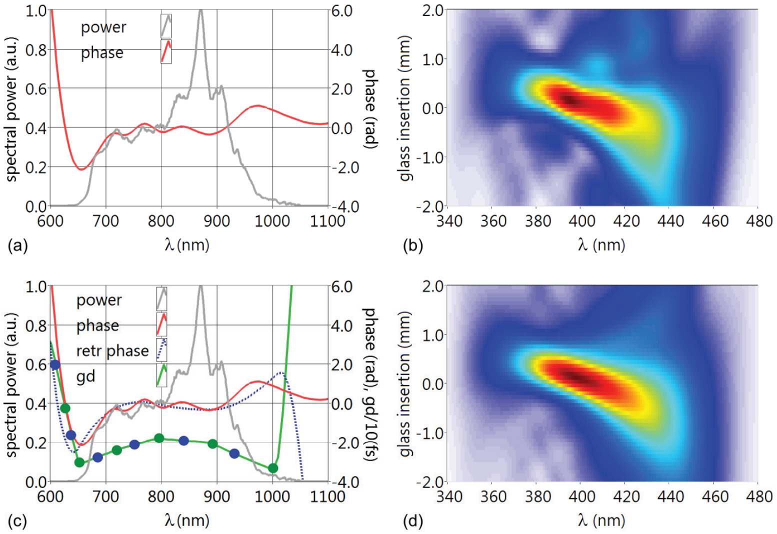

Fig. 1. Measured spectrum and simulated phase (a) and corresponding d-scan trace (b). The algorithm uses a GD representation to try to match the simulated trace (d) to the target trace (b). It starts with a coarse representation which is then interpolated to a finer one as the algorithm reaches a minimum. In (c) a given amount of free parameters are available (green dots), the GD curve is interpolated from those values, and the phase (blue dotted line) is calculated from that GD curve. For this amount of points the best it can do is to produce trace (d). The algorithm then continues by adding more degrees of freedom (blue dots), until it reaches the sampling limit. The previously determined values are still allowed to vary.

Our method consists on measuring the fundamental power spectrum and guessing the spectral phase that reproduces the measured SHG trace, $S(\omega,z)$. As in our previous work [26], we use a general minimization technique (Downhill Simplex [30]), but different basis sets are used to describe the phase. In the original algorithm we used a Fourier series to represent the phase, with the different coefficients of the Fourier series being the optimization parameters. This worked well in most cases but was not enough for others. A simple way to avoid the algorithm getting stuck in local minima is to switch basis whenever this happens: often, a local minimum in a given basis is not a local minimum in another basis, so the simple switching of basis can be a great improvement. For the work presented here, we used several different representations. A good tradeoff between accuracy and speed was obtained by defining the GD values at a given resolution and using spline interpolation in between (similarly to [31, 32]). As the algorithm converges, the resolution is then increased by adding more degrees of freedom. A schematic representation of the algorithm is depicted in Fig. 1, showing an intermediate step of the algorithm while using GD values as a set to represent the guessed phase. The same was done using phase and GDD representations instead of GD values, and switching between those representations whenever the algorithm stalled.

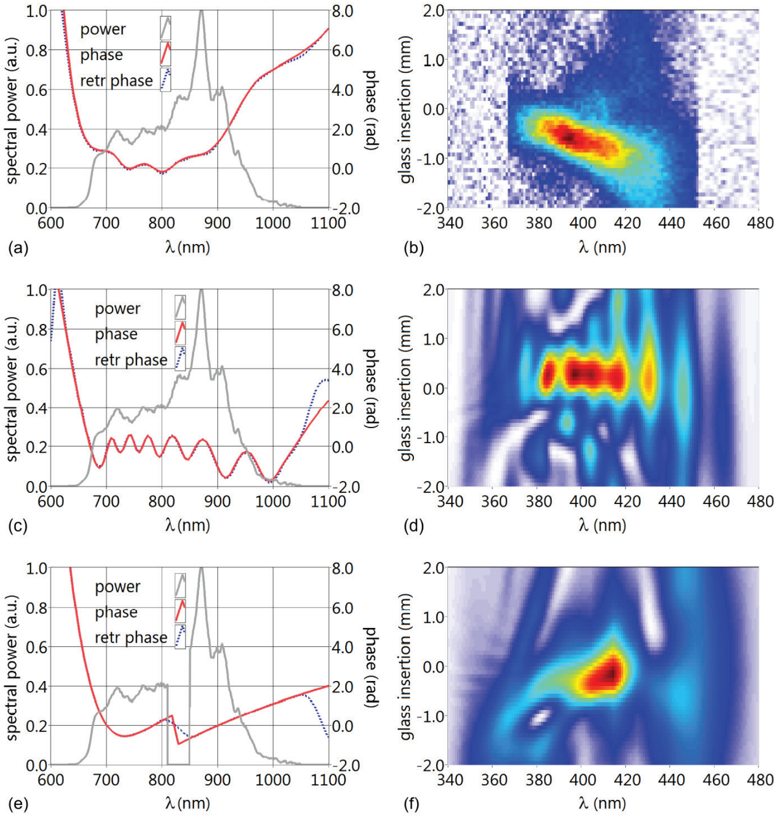

Fig. 2. Example of simulated dispersion scans for different complex cases, where the spectral phase plots on the left correspond to zero insertion in the scans on the right. (a) simulated and retrieved phase and corresponding d-scan (b) multiplied by a crystal response curve, together with hard clipping at the spectral edges and 5% additive noise added. (c) and (d) correspond to relatively small but fast phase variations that heavily distort the trace. (e) and (f) demonstrate the case of a hard-clipped spectrum with phase, group delay and group delay dispersion discontinuities between the resulting two spectral regions. For all of these cases the retrieved phase is in very good agreement with the initial simulated phase.

In previous work we showed that the d-scan method doesn't require an intensity-calibrated SHG signal, and the spectral filter can be retrieved at the same time as the fundamental spectral phase. This is accomplished by using a wavelength-dependent (local) error as the merit function for the minimization algorithm [26].

3. Examples

We briefly study the performance of the method for three different scenarios: measurement noise, strong phase modulation, and spectra with well-separated frequency components (Fig. 2). A d-scan trace is simulated for each different scenario, and the retrieval algorithm is run. In all cases, the "zero" glass insertion on the right side scans corresponds to the shown spectral phase on the left side plots. The fundamental spectrum is an actual measurement from the ultrafast oscillator used in our previous work [26].

#167354 - $15.00 USD Received 25 Apr 2012; revised 25 May 2012; accepted 12 Jun 2012; published 1 Aug 2012
(C) 2012 OSA

3.1 Noise

A systematic analysis to noise tolerance of a given method invariably involves choosing a "representative" pulse, physically simulating the measurement process, adding noise, and trying to retrieve the original pulse. Given the amount of parameters available, and that each measurement technique has its strengths and weaknesses, it is just too easy to find a case where a given method is superior to others with respect to noise. In view of this, we will not be comparing the d-scan technique to other methods but will simply illustrate qualitatively the tolerance to noise using a "representative" example. For this we simulated a d-scan, applied a spectral filter and added Gaussian noise, with a standard deviation equal to 5% of the peak value of the trace. Even under such unfavorable conditions the retrieved phase is still in very good agreement with the original simulated phase, as seen in Figs. 2(a) and 2(b).

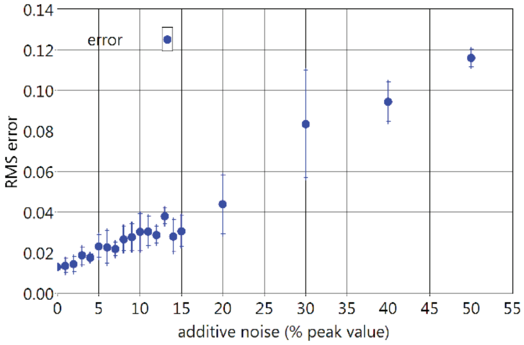

Fig. 3. Error as a function of the added Gaussian noise for the example from Fig. 1(a). For each amount of noise, five retrievals were done. The error bars indicate the standard deviation.

The finer details in the trace will naturally be the first to become "buried" under the noise. Still, even a very noisy signal is often enough to get an estimate of the degree of compression being achieved, since the trace's tilt gives direct indication of uncompensated third and higher order dispersion. This is a very useful feature for real-life situations.

Using the RMS electric field error as defined in [33],

$$\varepsilon = \left\| U_1 - U_2 \right\| = \left[\frac{1}{2\pi} \int \left| \tilde{U}_1(\omega) - \tilde{U}_2(\omega) \right|^2 d\omega \right]^{1/2}, \tag{4}$$

it is possible to study how much the retrieval degrades compared to a noiseless trace for our "representative" pulse (Fig. 3). With the example from Fig. 1(a), with full bandwidth, an RMS noise below 0.02 is readily achievable for a noiseless trace and doesn't appreciably increase up to a noise fraction of about 2%. Then it scales approximately linearly with the added noise, and a retrieval is typically acceptable (RMS error of 0.1) with noise levels as high as 30% of the trace's peak value. It should be pointed out that this depends on many parameters, like the number of samples, scanning range, and the test pulse. The fundamental spectrum is also assumed to be measured without any error.

3.2 Strong phase modulation

Dealing with complex pulses (i.e., pulses with a rapidly varying spectral phase) is a challenging task for all measurement methods [34]. A particularly difficult (and common) situation appears when the generation and/or compression process relies on nonlinear processes like SPM and self-steepening. This increases the time-bandwidth product (TBP) of the pulses, putting higher demands on spectrometer resolution, and increasing the delay range requirements in FROG measurements. Our method makes no assumption about a slowly varying phase, so there isn't in principle a limit for how fast and strong these can be. There

#167354 - $15.00 USD Received 25 Apr 2012; revised 25 May 2012; accepted 12 Jun 2012; published 1 Aug 2012
(C) 2012 OSA

are some practical issues that should be taken into account though: in our case, the spectral resolution requirements increase both for structured spectral power and phase, as necessary to properly sample each spectrum of the scan. In these conditions, the signal is spread over a larger glass insertion scale, therefore increasing the necessary dispersion scanning range. The retrieval time also increases, as a finer spectral sampling is needed, and more parameters are also needed to properly describe the phase. For the case of SPIDER, provided the signal is well sampled, the direct, non-iterative algorithm is quite insensitive to this added complexity.

Figures 2(c) and 2(d) show an example of a trace for a spectrum with a strongly modulated, rapidly varying phase. Our simulations show that, as long as most of the signal is contained within the scanning region, the d-scan method performs well. As with other techniques, very fast and small phase structures might go unnoticed: experimentally, the spectra are resampled to a grid with a reasonable amount of points to keep computational effort low. If not done carefully (i.e., properly sampling all spectra), this might wash out fine details.

3.3 Spectra with well-separated frequency components

It is often difficult to measure the relative phase between spectral components when there is a gap between them. The fundamental limitation in our technique is similar to all other self-referenced methods [27]. Given two well-separated fundamental frequency components, the trace will contain a signal at the corresponding doubled frequencies, and in addition there will be a cross-term, like in the FROG technique. If this cross-term is broad enough to connect the separate individual SHG parts, then its shape depends on the relative phase between them, and that phase can in principle be recovered. Otherwise, the signal is still sensitive to the group delay between separate spectral components. In the case of SPIDER, large shears will be necessary to “connect” different spectral regions, but this sacrifices measurement resolution. Multi-shearing techniques allow overcoming this problem [35, 36], at the expense of added experimental complexity.

On Figs. 2(e) and 2(f) such an example is shown, where the spectrum was clipped to zero at around 820 nm. For such situation, the width of the cross-term around 410 nm is large enough (and the gap at 820 nm is small enough) not to pose any problem to the algorithm: it handles well, without any modification, discontinuities in the phase, group delay, and group delay dispersion.

All the mentioned problems are linked, and there’s a tradeoff between all of them, i.e., a complex spectrum will put more demand on the signal-to-noise ratio, and holes in the spectrum will lead to a longer trace, which in turn requires a larger dispersion range, etc. It is therefore difficult (if not impossible) to make a systematic study on a measurement technique without assuming a particular set of conditions. The cases shown here can be considered “worst case scenarios” within realistic conditions one would usually find in the lab.

4. Experimental results

Two different systems have been characterized for this work. The first is a recently built few-cycle ultrafast laser oscillator, and the second is the output of a hollow fiber compressor. Characterizing such systems is a difficult task for different reasons: in the first case, besides the broad bandwidth, the spectral power is very low at certain wavelengths. In the second case, the spectral power and phase can both be, in some situations, rather complex, due to the nonlinearities involved in the spectral broadening process.

The experimental setup is very similar to the setup described in previous work [26], and consists of a standard pulse compressor made with broadband double-chirped mirrors (IdestaQE, 600-1200 nm bandwidth, GDD ≈-85 fs^2 per bounce at 800 nm) and BK7 glass wedges (Femtolasers GmbH), followed by a focusing off-axis silver parabolic mirror and a SHG crystal (Fig. 4).

In all cases, a full d-scan measurement typically takes a few seconds to perform, and a retrieval can take between a few seconds to a few minutes on a standard personal computer, depending on the complexity of the trace. Both the fundamental and SHG spectra were

#167354 - $15.00 USD Received 25 Apr 2012; revised 25 May 2012; accepted 12 Jun 2012; published 1 Aug 2012
(C) 2012 OSA

resampled to a 256-point linear array, as this was enough to properly sample the spectra. Between 50 to 60 spectra were acquired for each scan. Depending on the system being characterized, minor changes to the setup were done, as described in the following sections.

4.1 Ultrafast oscillator

The home-built Kerr-lens modelocked laser oscillator used in this section will be described in detail elsewhere [37]. This oscillator presents a challenging case due to its broad and structured spectrum. For SHG, both 5 µm and 20 µm thick BBO crystals (cut for type I SHG at 800 nm) were used in different measurements in order to experimentally investigate the relative insensitivity of the d-scan technique to crystal phase-matching bandwidth [26]. The SHG signal was filtered from the fundamental using a colored highpass filter and a lens was used to collect the signal into a fiber-coupled visible-uv spectrometer (Scansci ScanSpec). The energy per pulse was about 1nJ, at 80 MHz repetition rate.

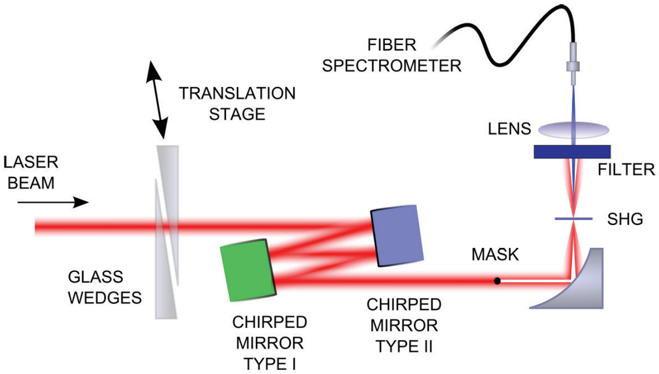

Fig. 4. Experimental setup. The glass wedges are made of BK7, and the chirped mirrors are made in matched pairs to minimize phase ringing. In some cases a mask was used to spatially separate the SHG signal from the fundamental beam at the detector, while in others a blue filter was used to block the fundamental beam (see text). The SHG crystal was either a 5 or 20 µm thick BBO.

Figure 5 shows a comparison between measurements and retrievals made using both crystals. The raw d-scan trace obtained with the 5 µm crystal (Fig. 5(a)) shows a smaller signal-to-noise ratio compared to the 20 µm trace (Fig. 5(f)) due to lower SHG conversion efficiency in the thinner crystal, but also features a larger relative signal in the longer wavelength side due to the larger phase matching bandwidth. The calibrated scans (Figs. 5(b) and 5(g)), obtained by applying the calibration curve given by the d-scan retrieval algorithm to the measured (raw) d-scan traces, are very similar in both cases, apart from the expected higher signal-to-noise ratio for the thicker crystal. For each crystal, five different data sets were used on five different retrievals, allowing us to perform a statistical analysis and to estimate the confidence levels of the result.

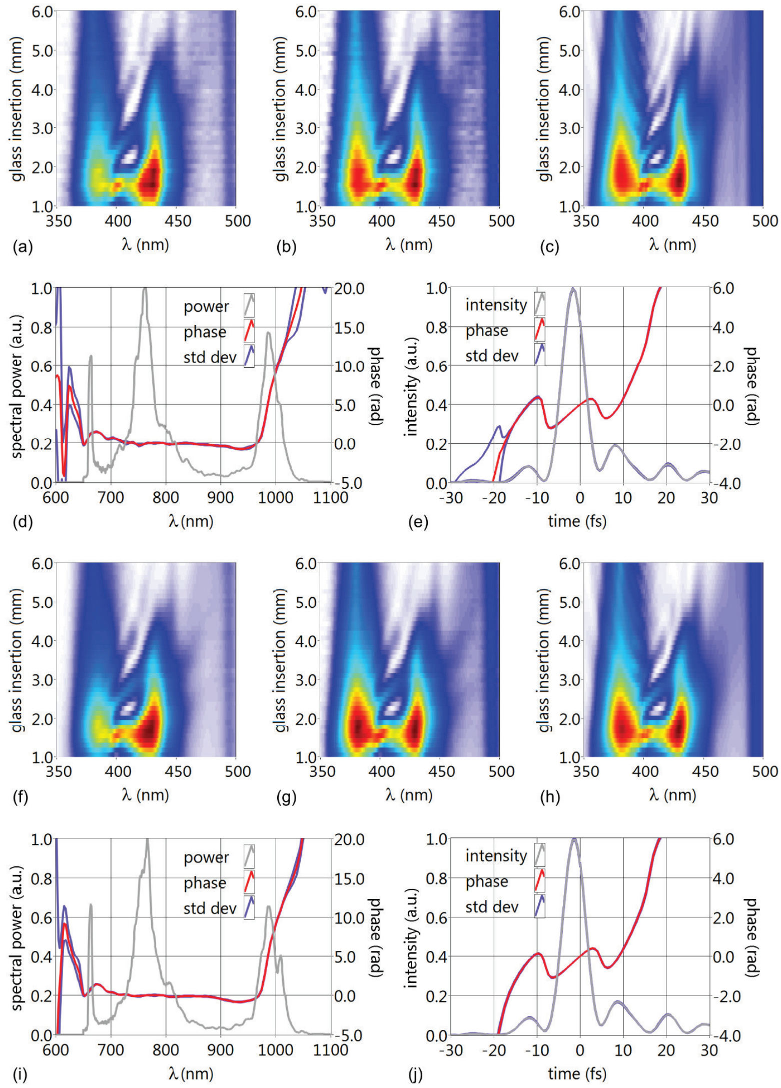

Fig. 5. Measured (a), calibrated (b), and retrieved (c) scans from the home-built ultrafast oscillator, obtained with a 5 μm thick BBO crystal. The retrieved phase statistics in the spectral domain (d) and the corresponding time reconstructions (e) were obtained from 5 different measurements and retrievals. The same applies to plots (f) to (j), but for a 20 μm thick crystal. The measured pulse duration is 6.0 ± 0.1 fs FWHM, with a Fourier limit of 5.2 fs for both cases.

In both cases, the shortest pulse duration obtainable for this chirped mirror set and glass combination was 6.0 ± 0.1 fs FWHM, achieved for a glass insertion of 1.5 mm. The Fourier limit for both spectra is 5.2 fs FWHM.

#167354 - $15.00 USD Received 25 Apr 2012; revised 25 May 2012; accepted 12 Jun 2012; published 1 Aug 2012
(C) 2012 OSA

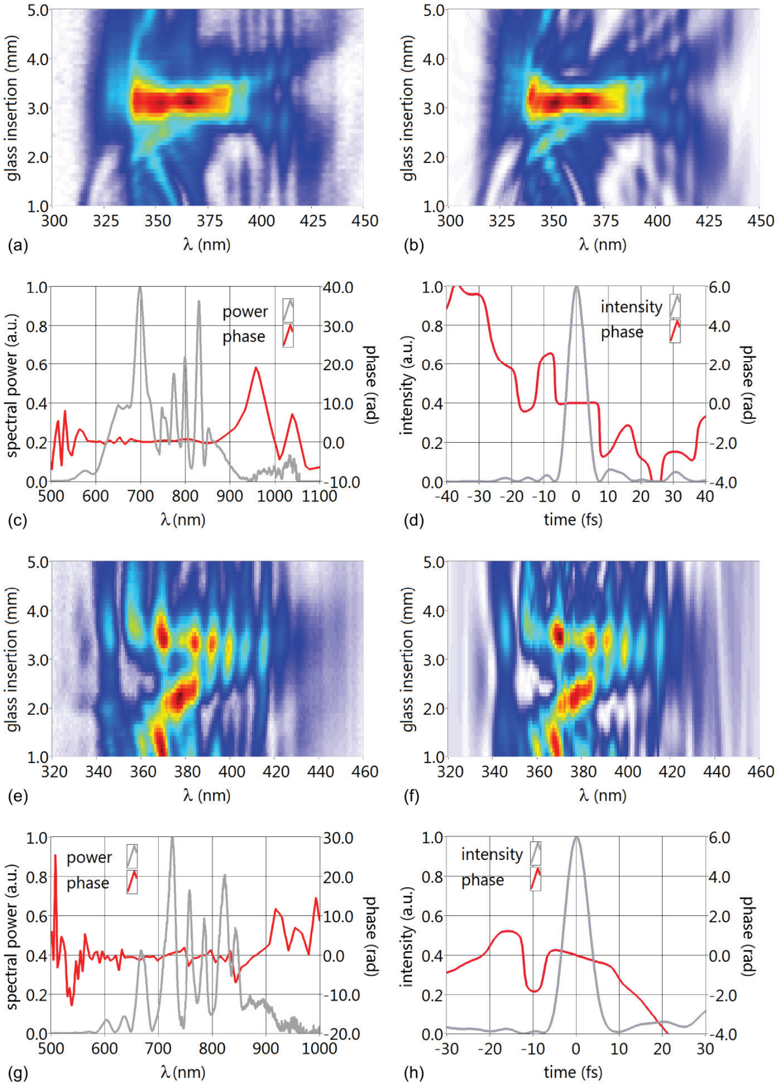

Fig. 6. Measured (a) and (e), and retrieved (b) and (f) scans from a hollow-fiber compressor operating in different regimes. The measured pulse durations are respectively 6.2 and 6.5 fs FWHM, with Fourier limits of 4.7 and 6.1 fs.

Due to UV absorption in the glass filter, the expected SHG signal at around 330 nm (corresponding to the peak at around 660 nm in the fundamental spectrum) is absent from our measurements. This (weak) signal is nevertheless present in the retrieved traces (not shown), which also shows that the phase from that spectral region is encoded in the remaining of the trace. A similar argument holds regarding the peak at 1000 nm: the corresponding SHG signal at around 500 nm varies very little across the insertion scale, thus yielding little information about the fundamental spectral phase; yet, that phase strongly shapes the trace around the 360 to 460 nm region, which allows it to be determined. The fact that all retrievals give very

#167354 - $15.00 USD Received 25 Apr 2012; revised 25 May 2012; accepted 12 Jun 2012; published 1 Aug 2012
(C) 2012 OSA

similar results, independently of factors such as first guesses for the algorithm, chosen basis, etc., further reassures us of the accuracy of the retrievals.

4.2 Hollow-fiber

For the case of ultrashort pulses obtained from spectral broadening in gas-filled hollow-core fibers, the nonlinear processes inherent to the broadening process are responsible for fast and strong oscillations on both spectral power and phase. Different operating conditions that depend on many parameters such as alignment, input power, beam size, etc., might lead to very different spectral structures. We characterized the output of a hollow fiber compressor under two different operating conditions: in the first one, the fiber was aligned so as to get a spectrum as broad as possible, while in the second case it was aligned so as to optimize the quality of the spatial profile of the output beam.

The hollow fiber used had a 250 μm inner diameter, was filled with approximately 500 mbar of Argon, and pumped with 800 μJ, sub-30 fs pulses from a 1 kHz Ti:Sapphire amplifier (Femtolasers FemtoPower Compact PRO CEP). For SHG we used a 5 μm thick BBO crystal.

The output of the fiber usually has measurable spectral wings down to 300 nm. While much weaker than the main spectral part, this is still enough to prevent proper measurement of the SHG signal if not properly filtered.

The blue filter used in the previous case (ultrafast oscillator) blocked too much of the SHG signal, as it also absorbed wavelengths shorter than 360 nm. Instead, we opted to block a small central portion of the fundamental beam with a thin wire (the “mask” shown in Fig. 2) and measured the central part of the SHG signal. The resulting spatial separation was enough to eliminate the fundamental signal, without any additional spectral filtering. Both the fundamental and SHG spectra were measured with a broadband fiber-coupled spectrometer (Ocean Optics HR4000).

The results for both operating conditions are shown in Fig. 6. Figures 6(a) to 6(d) correspond to the case where the hollow fiber was optimized for spectral bandwidth, while Figs. 6(e) to 6(h) are for the case where the spatial mode was best.

5. Conclusion

We have successfully demonstrated the applicability of ultrashort pulse characterization by numerical phase retrieval from second-harmonic dispersion scans for cases that are representative of broadband state-of-the-art sources. Compared to our previous work, the phase retrieval algorithm has been improved by swapping the base and/or the representation of the quantity being retrieved (phase, GD, GDD) whenever calculations would stall. The technique proved to be robust with respect to spectral complexity (power and phase), noise, and bandwidth limitations, not only in simulations but in real laboratory conditions as well. Measurements performed on a home-built broadband few-cycle laser oscillator using two nonlinear crystals of different thicknesses (5 μm and 20 μm) resulted in the same retrieved pulse profile and duration (6.0 ± 0.1 fs FWHM) in spite of the different phase matching bandwidth conditions and signal-to-noise ratios of the corresponding traces. Few-cycle pulses with complex and highly modulated spectra generated by a hollow-fiber compressor under two different alignment conditions (broadest spectrum and best spatial profile) were also successfully retrieved with this technique (6.2 and 6.5 FHWM, respectively).

The main drawbacks of this method are its iterative nature (there is the possibility that the algorithm gets stuck during minimization) and, in its current implementation, its intrinsic multi-shot nature. It is also based on a 1D model, so space-time coupling effects are not presently taken into account.

In principle there is no reason why this method shouldn’t work down to the single-cycle regime. The fact that most of the fundamental phase information is contained within the cross-terms clearly makes the technique very tolerant with respect to bandwidth limitations regarding SHG generation and detection. The intrinsic simplicity (most of the experimental

#167354 - $15.00 USD Received 25 Apr 2012; revised 25 May 2012; accepted 12 Jun 2012; published 1 Aug 2012

(C) 2012 OSA

setup is actually a standard chirped mirror compressor similar to those already existent in many laboratories) and ease of alignment are also some of the most attractive features of this method.

Acknowledgments

This work was partly supported by FCT – Fundação para a Ciência e a Tecnologia and FEDER (grants SFRH/BD/37100/2007, SFRH/BD/69913/2010, PTDC/FIS/115102/2009 and SFRH/BSAB/1100/2010), the ESF - European Science Foundation ("Super-intense laser-matter interactions" grant 4596), grant program Formación de Profesorado Universitario (Benjamín Alonso), Ministerio de Ciencia y Tecnología, Subdirección General de Proyectos de Investigación (Project FIS2009-07870), the European Research Council (ALMA), the Marie Curie Intra-European Fellowship ATTOCO, the Marie Curie Initial Training Network ATTOFEL, the Knut and Alice Wallenberg Foundation, the Joint Research Programme ALADIN of Laserlab-Europe II and the Swedish Research Council. The authors would like to thank Adam Wyatt for valuable comments and insight, and to Scansci for the kind loan of a vis-uv spectrometer.

PAPER V

Spatiotemporal characterization of few-cycle laser pulses

Benjamín Alonso, Miguel Miranda, Íñigo J. Sola, and Helder Crespo.

Opt. Express **20**, 17880–17893 (2012).

Spatiotemporal characterization of few-cycle laser pulses

Benjamín Alonso,[1,*] Miguel Miranda,[2] Íñigo J. Sola,[1] and Helder Crespo[2]

[1] *Universidad de Salamanca, Grupo de Investigación en Óptica Extrema (GIOE) Pl. de la Merced s/n E-37008 Salamanca, Spain*

[2] *IFIMUP-IN and Departamento de Física e Astronomia, Universidade do Porto, Rua do Campo Alegre 687, 4169-007 Porto, Portugal*

[*] *b.alonso@usal.es*

Abstract: In this paper we apply a broadband fiber optic coupler interferometer to the measurement of few-cycle laser pulses. Sub-8-fs pulses delivered by an ultrafast oscillator were characterized spatiotemporally using STARFISH, which is based on spatially resolved spectral interferometry. The reference pulse was measured with the d-scan technique. The pulses were focused by an off-axis parabolic mirror and were characterized at different transverse planes along the focusing region. The evolution of the retrieved pulses is analyzed, exhibiting small variations in the temporal (and spectral) amplitude and phase during propagation. Finally, the peak irradiance evolution is estimated from the integration of the spatiotemporal intensity.

©2012 Optical Society of America

OCIS codes: (320.7100) Ultrafast Measurements; (320.2250) Femtosecond phenomena; (320.5520) Pulse compression; (320.7090) Ultrafast lasers.

References and links

1. I. A. Walmsley and C. Dorrer, "Characterization of ultrashort electromagnetic pulses," Adv. Opt. Photon. **1**(2), 308–437 (2009).
2. R. Trebino and D. J. Kane, "Using phase retrieval to measure the intensity and phase of ultrashort pulses: frequency-resolved optical gating," J. Opt. Soc. Am. A **10**(5), 1101–1111 (1993).
3. C. Iaconis and I. A. Walmsley, "Spectral phase interferometry for direct electric-field reconstruction of ultrashort optical pulses," Opt. Lett. **23**(10), 792–794 (1998).
4. R. V. Shack and B. C. Platt, "Production and use of a lenticular Hartmann screen," in *1971 Spring Optical Meeting of the Optical Society of America*, J. Opt. Soc. Am. **61**, 648–697 (Optical Society of America, 1971), p. 656, paper MG23.
5. P. Bowlan, P. Gabolde, and R. Trebino, "Directly measuring the spatiotemporal electric field of focusing ultrashort pulses," Opt. Express **15**(16), 10219–10230 (2007).
6. E. Rubino, D. Faccio, L. Tartara, P. K. Bates, O. Chalus, M. Clerici, F. Bonaretti, J. Biegert, and P. Di Trapani, "Spatiotemporal amplitude and phase retrieval of space-time coupled ultrashort pulses using the Shackled-FROG technique," Opt. Lett. **34**(24), 3854–3856 (2009).
7. B. Alonso, I. J. Sola, O. Varela, J. Hernández-Toro, C. Méndez, J. San Román, A. Zaïr, and L. Roso, "Spatiotemporal amplitude-and-phase reconstruction by Fourier-transform of interference spectra of high-complex-beams," J. Opt. Soc. Am. B **27**(5), 933–940 (2010).
8. A. Baltuška, Z. Wei, M. S. Pshenichnikov, D. A. Wiersma, and R. Szipöcs, "All-solid-state cavity-dumped sub-5-fs laser," Appl. Phys. B **65**(2), 175–188 (1997).
9. H. M. Crespo, J. R. Birge, E. L. Falcão-Filho, M. Y. Sander, A. Benedick, and F. X. Kärtner, "Nonintrusive phase stabilization of sub-two-cycle pulses from a prismless octave-spanning Ti:sapphire laser," Opt. Lett. **33**(8), 833–835 (2008).
10. T. Udem, R. Holzwarth, and T. W. Hänsch, "Optical frequency metrology," Nature **416**(6877), 233–237 (2002).
11. A. Amani Eilanlou, Y. Nabekawa, K. L. Ishikawa, H. Takahashi, and K. Midorikawa, "Direct amplification of terawatt sub-10-fs pulses in a CPA system of Ti:sapphire laser," Opt. Express **16**(17), 13431–13438 (2008).
12. M. Nisoli, S. De Silvestri, O. Svelto, R. Szipöcs, K. Ferencz, Ch. Spielmann, S. Sartania, and F. Krausz, "Compression of high-energy laser pulses below 5 fs," Opt. Lett. **22**(8), 522–524 (1997).
13. C. P. Hauri, W. Kornelis, F. W. Helbing, A. Heinrich, A. Couairon, A. Mysyrowicz, J. Biegert, and U. Keller, "Generation of intense, carrier-envelope phase-locked few-cycle laser pulses through filamentation," Appl. Phys. B **79**(6), 673–677 (2004).

#169675 - $15.00 USD Received 4 Jun 2012; revised 13 Jul 2012; accepted 16 Jul 2012; published 20 Jul 2012
(C) 2012 OSA

14. G. Stibenz, N. Zhavoronkov, and G. Steinmeyer, "Self-compression of millijoule pulses to 7.8 fs duration in a white-light filament," Opt. Lett. **31**(2), 274–276 (2006).
15. A. S. Wyatt, I. A. Walmsley, G. Stibenz, and G. Steinmeyer, "Sub-10 fs pulse characterization using spatially encoded arrangement for spectral phase interferometry for direct electric field reconstruction," Opt. Lett. **31**(12), 1914–1916 (2006).
16. J. R. Birge, H. M. Crespo, and F. X. Kärtner, "Theory and design of two-dimensional spectral shearing interferometry for few-cycle pulse measurement," J. Opt. Soc. Am. B **27**(6), 1165–1173 (2010).
17. A. Baltuška, M. S. Pshenichnikov, and D. A. Wiersma, "Amplitude and phase characterization of 4.5-fs pulses by frequency-resolved optical gating," Opt. Lett. **23**(18), 1474–1476 (1998).
18. A. Baltuška, M. S. Pshenichnikov, and D. A. Wiersma, "Second-harmonic generation frequency-resolved optical gating in the single-cycle regime," IEEE J. Quantum Electron. **35**(4), 459–478 (1999).
19. S. Akturk, C. D'Amico, and A. Mysyrowicz, "Measuring ultrashort pulses in the single-cycle regime using frequency-resolved optical gating," J. Opt. Soc. Am. B **25**(6), A63–A69 (2008).
20. G. Stibenz and G. Steinmeyer, "Interferometric frequency-resolved optical gating," Opt. Express **13**(7), 2617–2626 (2005).
21. G. Stibenz, C. Ropers, Ch. Lienau, Ch. Warmuth, A. S. Wyatt, I. A. Walmsley, and G. Steinmeyer, "Advanced methods for the characterization of few-cycle light pulses: a comparison," Appl. Phys. B **83**(4), 511–519 (2006).
22. M. Miranda, T. Fordell, C. Arnold, A. L'Huillier, and H. Crespo, "Simultaneous compression and characterization of ultrashort laser pulses using chirped mirrors and glass wedges," Opt. Express **20**(1), 688–697 (2012).
23. M. Miranda, T. Fordell, C. Arnold, F. Silva, B. Alonso, R. Weigand, A. L'Huillier, and H. Crespo, "Characterization of broadband few-cycle laser pulses with the d-scan technique," Opt. Express. submitted.
24. B. Alonso, Í. J. Sola, J. S. Román, Ó. Varela, and L. Roso, "Spatiotemporal evolution of light during propagation in filamentation regime," J. Opt. Soc. Am. B **28**(8), 1807–1816 (2011).
25. A. S. Wyatt, A. Grün, P. K. Bates, O. Chalus, J. Biegert, and I. A. Walmsley, "Accuracy measurements and improvement for complete characterization of optical pulses from nonlinear processes via multiple spectral-shearing interferometry," Opt. Express **19**(25), 25355–25366 (2011).
26. L. Lepetit, G. Cheriaux, and M. Joffre, "Linear techniques of phase measurement by femtosecond spectral interferometry for applications in spectroscopy," J. Opt. Soc. Am. B **12**(12), 2467–2474 (1995).
27. O. Mendoza-Yero, B. Alonso, O. Varela, G. Mínguez-Vega, Í. J. Sola, J. Lancis, V. Climent, and L. Roso, "Spatio-temporal characterization of ultrashort pulses diffracted by circularly symmetric hard-edge apertures: theory and experiment," Opt. Express **18**(20), 20900–20911 (2010).
28. B. Alonso, R. Borrego-Varillas, O. Mendoza-Yero, I. J. Sola, J. San Román, G. Mínguez-Vega, and L. Roso, "Frequency resolved wavefront retrieval and dynamics of diffractive focused ultrashort pulses," J. Opt. Soc. Am. B. submitted.

1. Introduction

The field of ultrashort laser pulses is rapidly evolving both from the point of view of the development of laser sources and from their applications. As a consequence, the techniques for the characterization of such pulses are also in constant development. The temporal characterization of ultrashort pulses is a well-established field, with several techniques allowing for the retrieval of pulse amplitude and phase in the temporal domain [1]. Among these techniques, FROG (Frequency-Resolved Optical Gating) [2] and SPIDER (Spectral phase interferometry for direct electric-field reconstruction) [3] are the most widely used today. The spatial phase of the pulses can also be obtained with standard methods, as for example using the Hartmann-Shack wavefront sensor [4].

During the last few years, a huge progress has been done to extend these techniques to characterize the spatiotemporal amplitude and phase (or equivalently, the spatiospectral amplitude and phase) of the pulses. This full characterization is often required in applications where the spatial and temporal dependence of the pulses is coupled and of extreme importance. For this purpose, the following techniques can be underlined: Spatially Encoded Arrangement for Temporal Analysis by Dispersing a Pair Of Light E-fields (SEA TADPOLE) [5], Hartmann-Shack combined with FROG (Shackled-FROG) [6], and SpatioTemporal Amplitude-and-phase Reconstruction by Fourier-transform of Interference Spectra of High-complex-beams (STARFISH) [7].

Regarding the duration of the pulses, currently available technology routinely provides few-cycle near-infrared ultrafast laser pulses (with durations well below 10 fs) either using post-compression schemes or directly from broadband and octave-spanning Ti:sapphire laser oscillators (see, e.g., [8,9]). Octave-spanning oscillators have many applications, for example,

#169675 - $15.00 USD Received 4 Jun 2012; revised 13 Jul 2012; accepted 16 Jul 2012; published 20 Jul 2012
(C) 2012 OSA

in optical frequency metrology and high-precision optical spectroscopy [10]. Moreover, the production of high-energy few-cycle laser pulses has also been recently achieved through direct chirped pulse amplification [11] as well as in post-compression schemes based on hollow-core fibers [12] and filamentation [13,14].

The temporal characterization of few-cycle pulses, which have ultra-broad bandwidths, is very demanding for common techniques. Many efforts have been done in adapting these techniques to this regime, where very thin nonlinear crystals and second-harmonic-generation (SHG) spectral signal calibration are required. For example, spatially encoded arrangement of SPIDER (SEA-SPIDER) [15] and two-dimensional spectral shearing interferometry [16] have been applied to the measurement of few-cycle pulses. Also, careful calibration of SHG-FROG [17–19] and the use of interferometric FROG [20] have also been demonstrated in the few-cycle regime. A comparison of the experimental results for these techniques is given in [21]. Recently a new technique known as d-scan (dispersion-scan) has been introduced [22,23]. It achieves the simultaneous compression and characterization of the pulses by tracking the spectrum of the SHG signal during a continuous insertion of dispersion (from negative to positive chirp) and applying an iterative retrieval procedure. The SHG signal can be self-calibrated and the up-converted bandwidth requirements are more relaxed compared to other techniques.

The adaptation of techniques for pulse characterization in the spatiotemporal domain is also a challenge. There is a strong interest in the full spatiotemporal characterization of ultrashort pulses to be used in applications, for example in filamentation [24]. SEA-SPIDER has been recently shown to provide space-time information (excluding the pulse-front tilt) of 10.2 fs pulses [25]. In this paper, we used the technique STARFISH [7] to measure few-cycle pulses delivered by an oscillator. The phase of the test pulse can be extracted by combining it with a known reference pulse in a spectral interferometer (SI). Here, we used the d-scan technique [22] to measure the spectral phase of the reference pulse. Due to the large bandwidth of the pulses, we had to calibrate the spectral response (in amplitude and phase) of the fiber optic coupler used in the SI setup, as well as the spectrometer's response, in order to correct the spectral amplitude and phase retrieved with STARFISH.

2. Experimental setup

The experiments were performed with a Ti:sapphire ultrafast oscillator (Femtolasers Rainbow CEP) at a repetition rate of 80 MHz, with a central wavelength around 800 nm, a Fourier-transform limit of ≈ 7 fs and an energy per pulse of 2.5 nJ. The experimental setup for the full characterization of these pulses is divided into two main parts, corresponding to the combination of the d-scan technique [22] for measurement of the reference pulse, and the STARFISH technique [7] for the spatiotemporal characterization of the test pulse (see Fig. 1).

The d-scan setup is based on a glass wedge pair and a set of chirped mirrors and allows us to obtain dispersion scans of the pulses around their optimum compression point. We used BK7 wedges (Femtolasers GmbH) with antireflection-coating and an angle of 8°. The chirped mirrors are two pairs of double-chirped mirrors (DCM, Venteon GmbH), with each pair composed of two types of mirrors, named 'blue' and 'green', designed to compensate for the phase ringing. The group delay dispersion (GDD) introduced by the DCMs is approximately $120 fs^2$ per two bounces at 800 nm. Simultaneously to the d-scan, the pulse is focused in a nonlinear crystal (BBO, type I, 20 μm thick) by an off-axis parabolic (OAP) mirror with a focal length of 5 cm. The SHG signal produced in the BBO crystal is collimated by a lens and a blue filter is used to remove residual infrared radiation before detection with a calibrated fiber-coupled spectrometer (HR4000, Ocean Optics Inc.).

#169675 - $15.00 USD Received 4 Jun 2012; revised 13 Jul 2012; accepted 16 Jul 2012; published 20 Jul 2012
(C) 2012 OSA

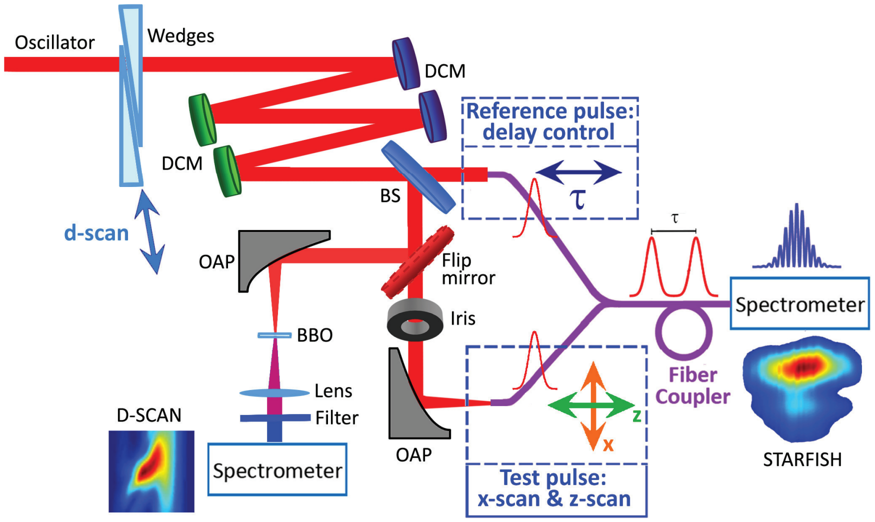

Fig. 1. Experimental setup for the spatiotemporal characterization of few-cycle pulses focused by an off-axis parabola (OAP) of 5-cm focal length. The pulses are simultaneously compressed and characterized using the dispersion scan (d-scan) technique, where a compressor based on a wedge pair and two pairs of double chirped mirrors (DCM) enables tracking the SHG signal generated in a nonlinear crystal (BBO) as a function of dispersion. The pulses are divided by a broadband beam splitter (BS) and coupled to the SI of STARFISH. The test and reference pulses are combined in a fiber optic coupler and sent to the spectrometer. The position of the test fiber performs the scan (in the spatial, x, and the longitudinal, z, coordinates).

Regarding the STARFISH setup, a broadband beam splitter (BS, Venteon GmbH) is used to produce a replica of the oscillator pulses, to be used as reference pulse in the SI. A flip mirror is used to obtain the calibration of the reference pulses using d-scan. The test pulse is focused by a 5-cm focal length OAP after an iris that selects the most energetic part of the pulse's profile (diameter of 5 mm). The pulses focused by the OAP are spatiotemporally characterized by scanning their spatial profile along the x-axis with the test pulse fiber. This is performed for different propagation distances around the focus by scanning the z-axis with the fiber. The position of the fiber that collects the reference pulse allows for adjusting the delay in the SI. The single-mode fiber coupler acts as an interferometer, effectively combining the test and reference pulses; it is directly connected to the spectrometer (HR4000), where the resulting spectral interferences are detected. The small diameter of the fiber core ($4\mu m$) provides high spatial resolution in the measurements.

The spectral phase of the reference pulse is retrieved by d-scan [22]. For this purpose, the SHG trace in a dispersion scan with the glass wedges around the shortest compressed pulse is measured. The dispersion introduced by the wedges is known from the Sellmeier equations of the material (in this case BK7). The fundamental spectrum is separately measured. The SHG trace is simulated for a seed phase and is compared with the experimental d-scan. An iterative algorithm is used to optimize the retrieved phase until the simulated trace converges to the experimental one. This way, the spectral phase of the pulse is univocally determined. Since the dispersion of the wedges is known, the glass insertion that gives the shortest pulse can be obtained simultaneously to the pulse characterization.

The spatiotemporal amplitude and phase characterization is obtained by the STARFISH technique [7]. For each propagation distance, the fiber scans the pulse profile to measure the spatially resolved spectral interferometry with a reference pulse, previously characterized

#169675 - $15.00 USD Received 4 Jun 2012; revised 13 Jul 2012; accepted 16 Jul 2012; published 20 Jul 2012

using d-scan. The spectral interferences are analyzed with a Fourier-transform algorithm [26] to retrieve the spectral phase of the test pulse. The spatially-resolved spectrum (amplitude) is measured in another scan with the fiber. After inverse Fourier-transforming in the frequency coordinate, the spatiotemporal amplitude and phase of the pulses is characterized.

The few-cycle laser pulses delivered by the oscillator have an ultra-broadband spectrum extending from 630 to 980 nm. Since fiber optic couplers are designed to transmit light in a finite bandwidth, checking the transmission of the fiber coupler, as described in the next section, is vital for broadband applications.

3. Calibration of the fiber coupler for ultra-broadband experiments

3.1 Transmission as a function of the wavelength

We measured the spectral transmission of the coupler with a white-light calibration lamp (300-1050 nm, LS1-CAL, Ocean Optics Inc.). The transmission function, $\eta(\lambda)$, was obtained by comparing the power spectral density with and without the fiber, measured with a calibrated broadband spectrometer (HR4000, Ocean Optics). The result is given in Fig. 2, where the experimental data is plotted in blue. We fitted an exponential function to the measured data, $\exp(a\lambda^4+b\lambda^3+c\lambda^2+d\lambda+e)$, where we determined five free parameters (in order to avoid restrictions in the fit of the experimental curve) by least squares optimization. Only the gray shaded area was considered for the fit in order to avoid the noise in the tails. The red curve is the resulting transmission $\eta(\lambda)$ that will be taken into account to correct the amplitude response of the fiber coupler. From this curve, we see that wavelengths below 500 nm and above 1000 nm will not be coupled. Nevertheless, the broadband transmission of the coupler is still adequate for measuring few-cycle, near infrared pulses.

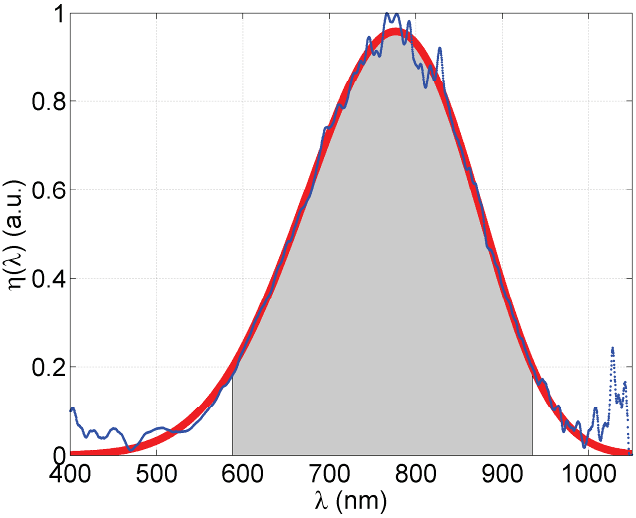

Fig. 2. Calibration of the spectral transmission of the fiber coupler measured with a white-light source.

The two interferometer arms are of almost equal length (difference $< 2\,mm$), and so the dispersion introduced in the reference and test pulses is practically balanced. The slight difference in length gives rise to an actual phase difference but this is calibrated in the SI and is taken into account when retrieving the correct phase from STARFISH. The dispersion of

#169675 - $15.00 USD Received 4 Jun 2012; revised 13 Jul 2012; accepted 16 Jul 2012; published 20 Jul 2012
(C) 2012 OSA

additional optics, e.g. the beam splitter, was also calibrated with SI and introduced in the phase retrieval. Our fiber with almost equal length arms allows their phase difference to be calibrated and the application to SI. If the arms length were not well-balanced, the relative dispersion between the two arms of the interferometer would be arbitrarily large to the point that it caused a large broadening of the side-peaks after calculating the Fourier-transform of the interference [26]. These two peaks may overlap and this fact may enter in conflict with the longer measurable pulses due to the limitations imposed by the experimental spectral resolution. In our case, the signal broadening is well below this limit.

3.2 Transmission as a function of the angle of incidence and the wavelength

We will use STARFISH for the measurement of non-collimated pulses, such as those focused by an off-axis parabola (see Section 4). In these cases, *k*-vectors with different directions will be coupled with different efficiency into the optical fiber due to its limited numerical aperture (NA). In general, the transmission of the fiber is a function of the angle of incidence of the light, with the highest efficiency occurring for normal incidence with respect to the fiber axis. The transmission decreases as the angle of incidence increases, which determines a cone of coupled light related to the NA .

Since the NA of single-mode fibers also depends on the refractive indices of the fiber core and cladding, and we are dealing with ultra-broadband spectra, the NA is expected to show a dependence on material dispersion. In this case, the transmission of the fiber depends not only on the angle of incidence θ, but also on the wavelength λ . Such situation would imply a spatiospectral distortion in the measurement of focused pulses.

For this reason, we calibrated the coupling efficiency of the fiber as a function of the angle of incidence and the wavelength. We used a white-light source (LS1-CAL, Ocean Optics) and a rotation stage to vary the angle of the fiber with respect to the source while keeping the fiber input in the axis of rotation. The signal was detected with a fiber-coupled spectrometer (AvaSpec-2048, Avantes). The transmission function $\xi(\theta,\lambda)$, where the signal has been normalized for each wavelength, is represented in Fig. 3(a). The angular dependence of $\xi(\theta,\lambda)$ is roughly constant with wavelength. In Fig. 3(b) we plot the integral of $\xi(\theta,\lambda)$ in the wavelength axis $\xi_m(\theta)=\int_\lambda \xi(\theta,\lambda)\,d\lambda$, obtaining a full-width at half-maximum (FWHM) of the acceptance cone $\Delta\theta = 10.06^\circ$. To study the dispersion of the acceptance angle (see Fig. 3(c)), we calculated the angle for which the signal falls to half the maximum from the center, $\theta_{50\%}$, as a function of wavelength (blue dots), and compared it to $\Delta\theta/2$ (red curve). If the noisy regions in the extremes of the spectrum are discarded, it can be concluded that the angular response is not dispersive in a broad spectral bandwidth. This means that the angular dependence of the light coupling in the fiber does not depend on the wavelength, so $\xi(\theta,\lambda)\approx\xi_m(\theta)$. We therefore conclude that spatiospectral distortions do not occur when measuring few-cycle focused pulses with the fiber. In Fig. 3(d) the numerical aperture for the half-maximum of the cone, $NA_{50\%}=\sin\theta_{50\%}$, is given. In the case of measuring pulses with higher numerical apertures, the detection modifies the measured pulse with the function $\xi_m(\theta)$, so the signal coming from the peripheral part of the profile of the focused pulse will be detected with less efficiency, as verified experimentally in the near-field of a zone plate [27]. In this work, we measured the oscillator pulses focused with a focal length $f = 50mm$, so the radius $r_{50\%}$ corresponding to $\theta_{50\%}$ is given by $\tan\theta_{50\%} = r_{50\%}/f$. This radius is $r_{50\%} = 4.40mm$ and the condition $r < r_{50\%}$ in the input profile is fulfilled within the 2.5-mm radius iris used in the experiments. To prove this, we simulated the focus of an ideal plane wave using a 5-mm diameter diaphragm, with and without the effect of the NA , obtaining a

#169675 - $15.00 USD Received 4 Jun 2012; revised 13 Jul 2012; accepted 16 Jul 2012; published 20 Jul 2012
(C) 2012 OSA

focal spot size (FWHM) of 7.42 and $7.35\mu m$, respectively. We conclude that the effect is almost negligible in our case, even more taking into account that the outer part of the spatial profile before focusing (the region more afflicted) is the less intense part of the pulse profile.

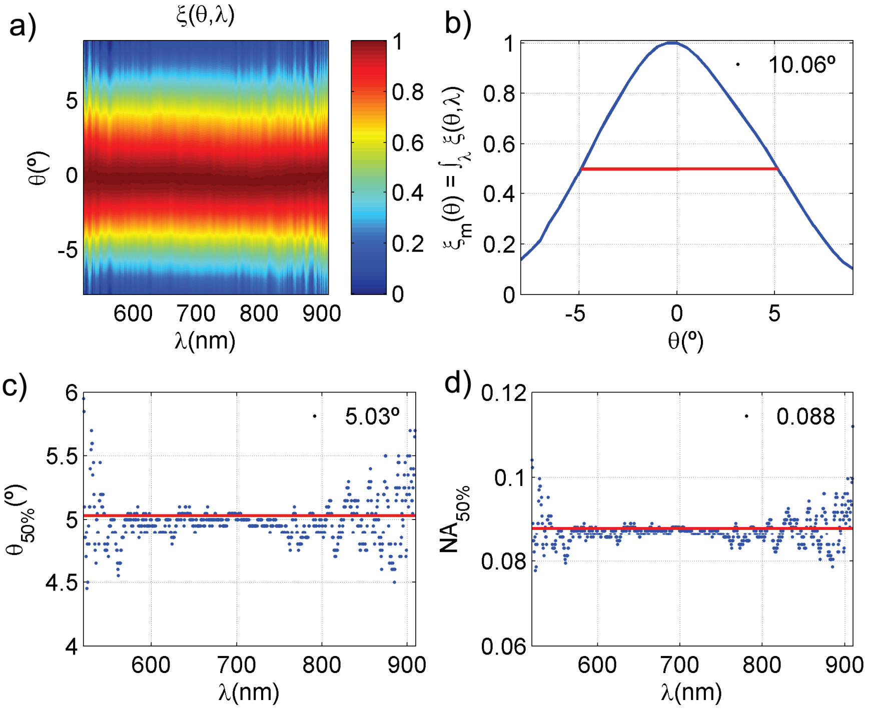

Fig. 3. (a) Transmission of the fiber as a function of the angle of incidence and the wavelength. (b) Transmission integrated in wavelength. (c) Angle of incidence for a decrease in efficiency of 50% with respect to the maximum. (d) Numerical aperture corresponding to the angle in (c).

4. Experimental characterization of few-cycle pulses delivered by an oscillator

4.1 Measurement of the reference pulse: d-scan

The reference pulse required by STARFISH was characterized with the d-scan technique. The compressor was composed of two pairs of chirped mirrors and a pair of BK7 wedges with an angle of 8°. The dispersion scan was done, as usual, by translating one wedge along the direction illustrated in Fig. 1. The total scan corresponds to 59 points with a step of $0.6mm$ in the direction of the scan. This translates into a total glass insertion of $d = 4.84mm$ in the propagation direction of the pulse. We measured three independent d-scans of the pulse in order to perform several pulse retrievals.

An experimental d-scan trace is shown in Fig. 4(a). The corresponding retrieved trace is given in Fig. 4(b) and shows a good matching to the measurement. The spectrum and phase of the retrieved pulse for the best achieved compression are shown in Fig. 4(c). The full width at $1/e^2$ of the characterized spectrum is $267nm$. The standard deviation of the phase (gray curve) for the different retrievals shows the small precision error present in the retrieval. In Fig. 4(d) the temporal intensity and phase of the pulse is depicted. The Fourier-limited duration of the measured spectrum is $6.7fs$ (FWHM) and the duration of the retrieved pulse

Received 4 Jun 2012; revised 13 Jul 2012; accepted 16 Jul 2012; published 20 Jul 2012

is $7.8\pm0.1\,fs$ (FWHM). The gray curves are the standard deviation of the amplitude and phase calculated from the different traces, showing a small variation between them: $<0.4\,rad$ for the spectral phase, $<0.1\,rad$ for the temporal phase and <0.035 for the normalized temporal intensity.

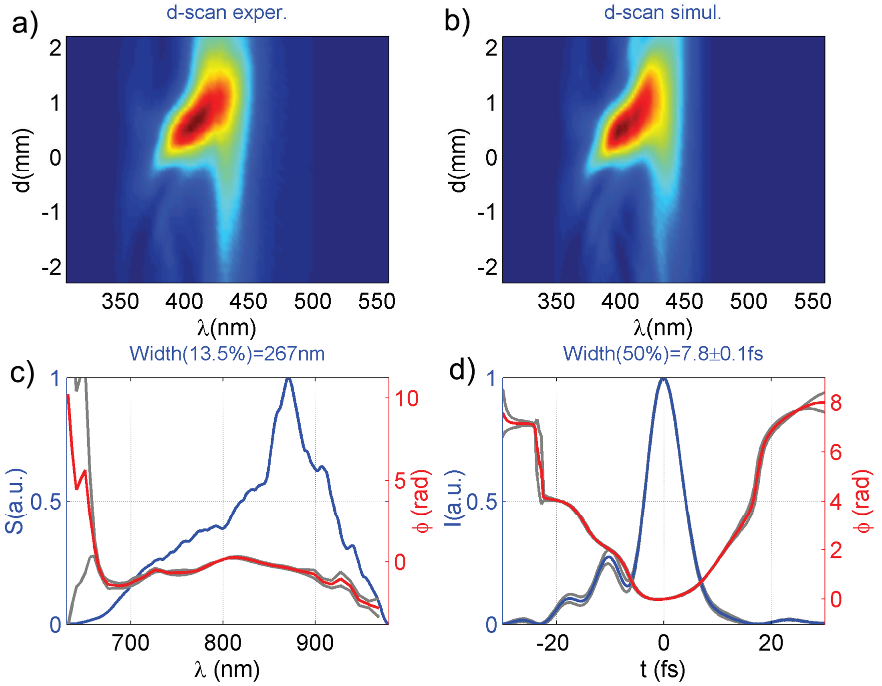

Fig. 4. (a) Experimental and (b) retrieved d-scan trace of the reference pulse. (c) Spectrum (blue) and phase (red) of the retrieved pulse. (d) Intensity (blue) and phase (red) of the reference pulse. The gray curves in (c) and (d) represent the standard deviation of the retrievals.

4.2 Spatiospectral and spatiotemporal characterization: STARFISH

We used STARFISH to characterize the focusing region of the oscillator after the OAP ($f=50\,mm$). The measurements were done for 7 consecutive propagation distances z around the focus, in order to track the evolution of the focused pulses: $z=f+\{-1.5\;-1.0\;-0.5\;0\;0.5\;1.0\;1.5\}\,mm$. The spatiospectral (and spatiotemporal) amplitude and phase were retrieved for each z-plane. The spatial features in the transverse plane were measured in one axis (x-axis), since the system was assumed to have cylindrical symmetry. Similar sets of measurements can be performed in the full x-y plane just by spatially scanning with two perpendicular actuators.

The evolution of the spatially-resolved spectrum is shown in Fig. 5(a) as a function of the longitudinal position z. The x-axis extends from –50 to 50 mm in all cases. The x-scan was done in steps of $1\,\mu m$. During propagation, it is mainly the spatial width (x-axis) that is changing, whereas the spectrum is almost undistorted. Due to the pulses' broad bandwidth, the effect of smaller focal spot size for the shorter wavelengths is visible in the spatially-resolved spectrum at the focus of the OAP [Fig. 5(a)]. Apart from this effect, the main

#169675 - $15.00 USD Received 4 Jun 2012; revised 13 Jul 2012; accepted 16 Jul 2012; published 20 Jul 2012

consequence is a change of the relative amplitude of the spectral components, in particular the fact that shorter wavelengths exhibit slightly larger amplitudes with respect to longer wavelengths. Other small distortions can be attributed to a misalignment of the OAP or to a non-homogeneous spatial profile of the oscillator (before the OAP).

In Fig. 5(b), the spatiospectral phase (or wavefront) is represented for the same set of axial distances. Since STARFISH retrieves the frequency-resolved wavefront [28] (with a small noise due to phase drifts), we represent the phase $\phi(x)$ for different wavelengths λ_0. For clarity, we represent these wavefronts, $\phi(x;\lambda=\lambda_0)$, using a different color for each wavelength and shifted to $\phi(x;\lambda=\lambda_0)=0$ in $x=0$, what is equivalent to remove the spectral phase on-axis. To corroborate the result, we did two independent measurements (x-scans) for each position z, so we also represent the error (black curves) calculated from their difference. In spite of the presence of some noise, these measurements can be used to determine qualitatively and quantitatively the convergence and divergence of the pulse, thus helping to identify the propagation distance analyzed in each measurement. As observed in the measurements, for the pulses focused by the OAP the reddish wavelengths have smaller curvature than the bluer ones, as given by the dependence of the wavenumber on wavelength, $k \propto \lambda^{-1}$.

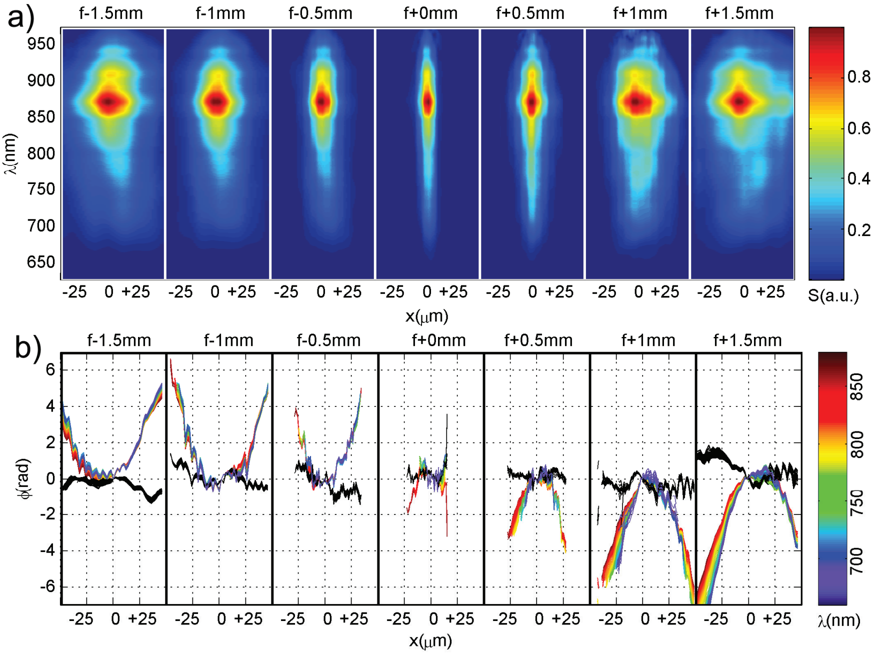

Fig. 5. (a) Normalized spatiospectral intensity and (b) frequency-resolved wavefront at different propagation distances z around the focus of the OAP, the latter represented in different colored curves for each wavelength (see the colorbar). The black curves are the error obtained in the wavefronts from two independent measurements.

In the spatiotemporal domain, the intensity of the pulses along the focusing region is given in Fig. 6(a). Here, the temporal features are also roughly constant both in the x-axis and along z, with the spatial width (x-axis) of the pulses exhibiting the largest variation as the pulse approaches and moves away from the focus. Figure 6(b) depicts slices of the on-axis (x = 0) temporal intensity, with the instantaneous wavelength (calculated from the inverse of the derivative of the temporal phase) shown in different colors that give us information on the temporal chirp of the pulses. Due to the overall positive chirp of the pulses, combined with the relative amplitude decrease of redder wavelengths with respect to the bluer part of the spectrum (as mentioned above), the temporal intensity presents a small decrease in the leading part of the pulse in the planes closer to the focus. The chirp is almost constant along the direction of propagation. These results are consistent with the expected almost constant temporal profile in the focusing region.

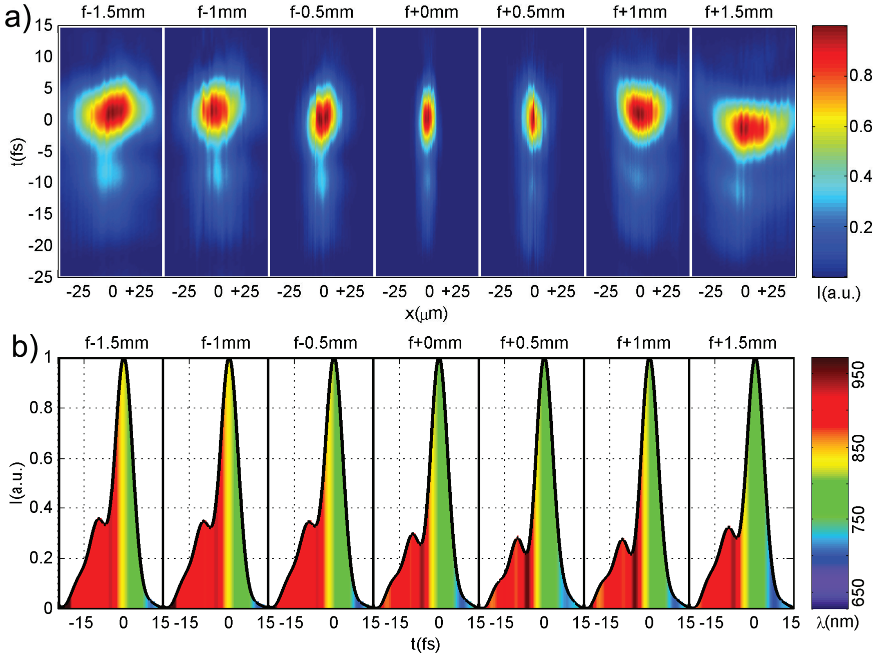

Fig. 6. (a) Normalized spatiotemporal intensity at different propagation distances z around the focus of the OAP. (b) Normalized on-axis intensity (x = 0) colored by the instantaneous wavelength of the pulse for the same propagation distances.

4.3 Comparison of the on-axis results

Here, we compare the spectral and temporal retrievals obtained on-axis (x = 0) for the 7 propagation distances considered. In Fig. 7(a), we represent the mean spectral power (blue curve) and corresponding standard deviation (gray curves), together with the spectral phase (red curve) and standard deviation (gray curves). From the results, it is clear that the spectral amplitude deviation is higher than the phase deviation, indicating that the differences observed in the temporal profiles of Fig. 6(b) are mainly originated by the differences in the spectral amplitude. In Fig. 7(b), the temporal duration (FWHM) of the on-axis pulses is plotted as a function of the propagation distance. The variation of these widths is compared with the FWHM of the Fourier-transform limit (FTL) of the corresponding spectra, exhibiting a correlation between the width of the FTL and the actual width of the pulses. This result again supports the idea that the differences mainly come from the amplitude and not from the phase. The explanation of this result is that the spectral amplitude reshaping due to the focusing flattens the spectrum close to the focus (since the shape of the input spectrum on Fig. 4(c) has lower signal for shorter wavelengths) and this induces a small reduction in the FTL and the duration of the pulse, as seen in Fig. 7(b).

#169675 - $15.00 USD Received 4 Jun 2012; revised 13 Jul 2012; accepted 16 Jul 2012; published 20 Jul 2012
(C) 2012 OSA

As mentioned above, the variations observed in the spectral domain are also present in the temporal domain. In Fig. 7(c), we show the mean temporal intensity (blue) and its standard deviation (gray). The same applies for the temporal phase (red) and its deviation (gray). Here, it is also observed that the difference in the phase is smaller than the difference in the amplitude. The statistics of the pulse width retrieved on-axis gives a FWHM of $8.0 \pm 0.3 fs$, which is consistent with the retrieval of the d-scan. In Fig. 7(d), we also represent the (mean) temporal profile colored with the (mean) instantaneous wavelength to show the good match with the results of Fig. 6(b).

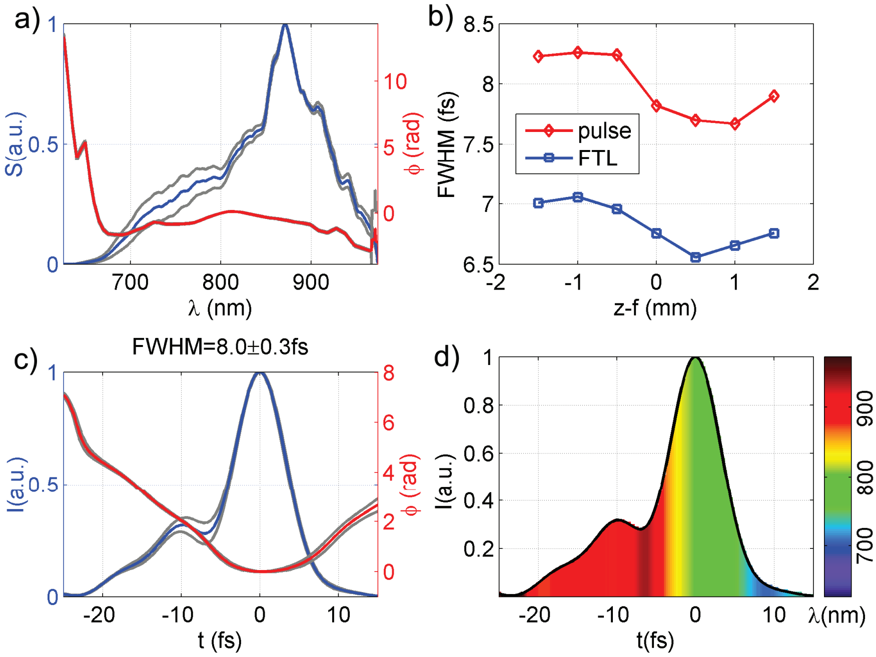

Fig. 7. (a) Mean of the spectral amplitudes (blue curve) and phases (red curve) retrieved on-axis for the five propagation distances, and corresponding standard deviation (gray curves). (b) Temporal width (FWHM) of the on-axis intensity reconstructions of the pulses for different propagation distances, and comparison with the FWHM of the Fourier-transform limit (FTL) of the corresponding spectra. (c) Mean of the temporal amplitudes (blue curve) and phases (red curve) retrieved on-axis for the five propagation distances, and standard deviation (gray curves). (d) Intensity colored by the instantaneous wavelength (see colorbar) of the mean of the on-axis measured pulses.

These results can be interpreted as the validation of the current experimental implementation of the d-scan technique (and could also be extrapolated to other techniques, in which the pulses to be characterized are focused in the nonlinear crystal with an OAP), in the sense that it is assumed that the focus of the OAP does not distort the temporal (or equivalently spectral) amplitude and phase of the pulse. Here, we have found that small differences can occur, although they do not hinder proper pulse retrieval.

4.4 Measurement of the peak irradiance of ultrashort laser pulses

The measurement of the peak intensity of ultrashort laser pulses is often difficult to be addressed, many times due to the high intensities involved. We will show how the characterization of the spatiotemporal intensity of the pulses can be used to calculate an estimation of the peak intensity. Although the results presented in Fig. 6(a) are commonly called intensity, they are actually the irradiance of the pulse, measured in W/cm^2 units. It is usually represented in arbitrary units (a.u.) whenever the absolute value is unknown or irrelevant.

The integral in the two spatial coordinates and the temporal dimension gives the energy of the pulse E, as given in Eq. (1), where $I_E(r,t)$ represents the experimental normalized spatiotemporal intensity at a certain z and κ_{rt} is a constant that gives the peak irradiance of the pulse:

$$E = \kappa_{rt} \int_{-\infty}^{\infty} \left[\int_{0}^{\infty} I_E(r,t) 2\pi r \, dr \right] dt \qquad (1)$$

Since we are assuming cylindrical symmetry, the characterization was done only in one spatial dimension (x-axis). The scan was done in the full axis, i.e., over the two sides of the beam profile with respect to the center (x = 0). Consequently, we have double information and we can obtain two values of the peak irradiance per measurement, corresponding to the polar radius $r_1 = \{x / x \geq 0\}$ and $r_2 = \{x / x \leq 0\}$, respectively.

Often, this full information is not available and we have to make approximations to obtain the peak intensity. Here, we will do a first rough calculation just for comparison. To simplify, we can consider a focused pulse with a Gaussian profile both in the temporal and in the spatial coordinates, thus with separable dependence in time and space. In this case, the irradiance $I_G(r,t)$ is given by

$$I_G(r,t) = \kappa_G \exp\left\{-(4\ln 2)\, r^2 \big/ FWHM_x^2\right\} \exp\left\{-(4\ln 2)\, t^2 \big/ FWHM_t^2\right\} \qquad (2)$$

where $FWHM_t$ and $FWHM_x$ are, respectively, the pulse full widths in the temporal and the spatial coordinates. We take the $FWHM_t$ from the on-axis intensity widths, whose results are shown in Fig. 7(b). For the spatial width $FWHM_x$, we consider the full width in the x-axis after integration in wavelengths of the spatiospectral traces shown in Fig. 5(a). The results for $FWHM_x$ are shown in Fig. 8(a) as a function of the propagation distance. After integrating the Gaussian irradiance $I_G(r,t)$, we obtain the following relation between the pulse energy, the x- and t-widths, and the peak irradiance:

$$E = \int_{-\infty}^{\infty} \left[\int_{0}^{\infty} I_G(r,t) 2\pi r \, dr \right] dt = 1.536 \kappa_G \left(\pi \frac{FWHM_x^2}{4} \right) FWHM_t \qquad (3)$$

From Eq. (3) we see that the Gaussian peak irradiance κ_G actually corresponds to the pulse energy divided by the spatiotemporal volume above half the peak intensity, that is, the pulse energy divided by the temporal duration, $FWHM_t$, by the spatial section, $(\pi/4) FWHM_x^2$, and corrected by a factor of $1/1.536$.

The energy per pulse $E = P / f_{rep}$ is calculated from the measured average power P and the pulse repetition rate $f_{rep} = 80MHz$. The power measured after the $5mm$ iris and the OAP was $P = 80\,mW$, so the energy per pulse was $E = 1nJ$. We consider that the fraction of this energy that is lost (spatially spread) in the focus is negligible. Also, there are other factors that can affect the result, for example part of the radiation being incoherent (e.g. amplified spontaneous emission) or small pre- or post-pulses that are not measured. Therefore, the peak irradiance obtained by this procedure should be considered as an estimate of the actual value.

#169675 - $15.00 USD Received 4 Jun 2012; revised 13 Jul 2012; accepted 16 Jul 2012; published 20 Jul 2012

(C) 2012 OSA

The comparison of the results for the peak irradiance as a function of the propagation distance is shown in Fig. 8(b). As expected, the peak irradiance is higher closer to the focus, where the spatial width decreases. The values obtained at the focus ($z = f$) are $\kappa_G = 6.92 \cdot 10^{10} W / cm^2$, $\kappa_{rt1} = 5.67 \cdot 10^{10} W / cm^2$ and $\kappa_{rt2} = 5.63 \cdot 10^{10} W / cm^2$ in the Gaussian irradiance approximation, for the measured spatiotemporal irradiance from the set $r_1 = \{x / x \geq 0\}$ and from the set $r_2 = \{x / x \leq 0\}$, respectively. The two values for the full spatiotemporal calculation are overlapped, whereas the Gaussian estimation gives higher values. This occurs because the irradiance is more spread in the temporal dimension than in a Gaussian function with the same $FWHM_t$ and accordingly the actual peak irradiance is lower.

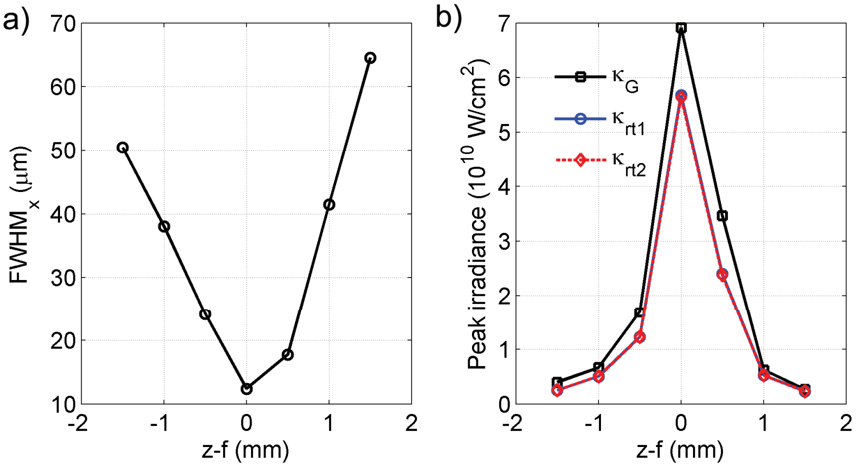

Fig. 8. (a) Experimental spatial width (FWHM) as a function of the propagation distance. (b) Peak irradiance as a function of the propagation distance calculated from the assumption of spatial and temporal Gaussian shape (black curve-squares) and from the measured spatiotemporal intensity using the right-hand-side (blue curve-circles) and the left-hand-side (red dashed curve-diamonds) of the x-axis.

5. Conclusions

Current techniques for the temporal characterization of laser pulses have already reached the few-cycle regime. In particular, the d-scan technique is very powerful due to its simple and low-demanding experimental implementation. The STARFISH technique for the spatiotemporal characterization of the pulses is based in spectral interferometry, and thus requires a calibrated reference pulse. Firstly, we have shown the capabilities of fiber optic coupler based interferometry for ultra-broadband pulse measurements in terms of the operating spectral bandwidth. Then, we have demonstrated the application of STARFISH to few-cycle pulses, using the d-scan to measure the reference pulse.

We have reconstructed spatiotemporally the pulses delivered by an ultrafast oscillator (6.7 fs FWHM Fourier-transform limit) focused by an OAP. The full retrieval of the amplitude-and-phase in the spatiotemporal and spatiospectral domains gives additional information that is lost with usual temporal characterization techniques. We have measured pulses with durations below 8 fs (FWHM) and have studied the evolution of the pulses along the focusing region. We found that temporal dependence of the pulses is practically preserved around the focus of the OAP, presenting small changes in the spectral and temporal amplitude (due to the dependence of the focal spot size for different wavelengths in ultra-broadband pulses), and almost invariant spectral and temporal phases. OAPs are important devices that find many uses in pulse focusing and characterization (especially of ultra-broadband pulses), precisely because of the absence of dispersion and chromatic aberrations, provided that they are properly aligned. STARFISH allows us to know whether the focusing is being properly performed in both the xy-plane (actually, we measured the x-axis) and the z-axis.

We have calculated the peak irradiance of the pulses from the spatiotemporal reconstruction. We have checked that assuming Gaussian profiles and uncoupled space-time dependence is not enough to estimate the peak irradiance. This will be absolutely relevant in pulses with stronger spatiotemporal coupling.

We expect the availability of spatiotemporal characterization techniques in the few-cycle regime to be extremely helpful to study processes involving ultrafast oscillators, as well as processes employing high-energy pulses such as pulse post-compression and high-order harmonic generation, among others.

Acknowledgments

We acknowledge support from Spanish Ministerio de Ciencia e Innovación (MICINN) through the Consolider Program SAUUL (CSD2007-00013), Research projects FIS2009-09522, and grant programs Formación de Profesorado Universitario (No. AP2007-00236 for B. Alonso) and Ramón y Cajal (for I. J. Sola); and from the Junta de Castilla y León through the Program for Groups of Excellence (GR27). H. Crespo acknowledges Fundos FEDER, through Programa Operacional Factores de Competitividade – COMPETE, and Fundação para a Ciência e a Tecnologia (FCT) under grants No. PTDC/FIS/115102/2009 and PTDC/FIS/122511/2010. M. Miranda acknowledges FCT and FEDER grant No. SFRH/BD/37100/2007. We also acknowledge support from Centro de Láseres Pulsados (CLPU), Salamanca, Spain.

PAPER VI

Generation and spatiotemporal characterization of 4.5-fs pulses from a hollow-core fiber compressor

Benjamín Alonso, Miguel Miranda, Francisco Silva, Vladimir Pervak, Jens Rauschenberger, Julio San Román, Íñigo J. Sola, and Helder Crespo.

(2012) *Manuscript in preparation.*

Generation and spatiotemporal characterization of 4.5-fs pulses from a hollow-core fiber compressor

Benjamín Alonso[1,*], Miguel Miranda[2], Francisco Silva[2], Vladimir Pervak[3,4], Jens Rauschenberger[3], Julio San Román[1], Íñigo J. Sola[1], and Helder Crespo[2]

[1] *Universidad de Salamanca, Grupo de Investigación en Óptica Extrema (GIOE) Pl. de la Merced s/n E-37008 Salamanca, Spain*
[2] *IFIMUP-IN and Departamento de Física e Astronomia, Universidade do Porto, Rua do Campo Alegre 687, 4169-007 Porto, Portugal*
[3] *UltraFast Innovations GmbH, Am Coulombwall 1, 85748 Garching, Germany*
[4] *Ludwig-Maximilians-Universität München, Department für Physik, Am Coulombwall 1, 85748 Garching, Germany*
[*] *Corresponding author: b.alonso@usal.es*

Abstract: We have post-compressed 25 fs (Fourier-limit) amplified pulses in an argon-filled hollow-core fiber. The output pulses were compressed using a pair of wedges and chirped mirrors down to 4.5 fs (Fourier-limit of 4.1 fs), which corresponds to less than two optical cycles. The spatiotemporal and spatiospectral amplitude and phase of the pulses were characterized with a combination of STARFISH and d-scan. The spatial dependence of the spectral broadening and the pulse duration was studied, revealing a near-Gaussian output spatial mode. Spatiotemporal characterization of the focus of an off-axis parabolic mirror yielded a peak intensity of $8.3\cdot10^{15}$ W/cm^2 with a 4.8 to 5.3 fs pulse duration across the beam profile, checking the potential applicability of the focused pulses for strong field experiments.

OCIS codes: (320.7100) Ultrafast Measurements; (320.7110) Ultrafast nonlinear optics; (320.5520) Pulse compression; (320.7090) Ultrafast lasers.

References and links

1. A. Baltuška, Th. Udem, M. Uiberacker, M. Hentschel, E. Goulielmakis, Ch. Gohle, R. Holzwarth, V. S. Yakovlev, A. Scrinzi, T. W. Hänsch, F. Krausz, “Attosecond control of electronic processes by intense light fields,” Nature **421**, 611-615 (2003).
2. S. Baker, J. S. Robinson, C. A. Haworth, H. Teng, R. A. Smith, C. C. Chirilã, M. Lein, J. W. Tisch, and J. P. Marangos, “Probing proton dynamics in molecules on an attosecond time scale,” Science **312**, 424-427 (2006).
3. K.W.D. Ledingham, P. McKenna, R.P. Singhal, “Applications for nuclear phenomena generated by ultra-intense lasers,” Science **300**, 1107-1111 (2003).
4. T. Brabec and F. Krausz, “Intense few-cycle laser fields: Frontiers of nonlinear optics,” Rev. Mod. Phys. **72**, 545-591 (2000).
5. M. Hentschel, R. Kienberger, Ch. Spielmann, G.A. Reider, N. Milosevic, T. Brabec, P. Corkum, U. Heinzmann, M. Drescher, F. Krausz, “Attosecond metrology,” Nature **414**, 509-513 (2001).
6. Y. Mairesse, A. de Bohan, L. J. Frasinski, H. Merdji, L. C. Dinu, P. Monchicourt, P. Breger, M. Kovačev, R. Taïeb, B. Carré, H. G. Muller,P. Agostini, and P. Salières, “Attosecond Synchronization of High-Harmonic Soft X-rays,” Science **302**, 1540-1543 (2003).
7. G. Sansone, E. Benedetti, F. Calegari, C. Vozzi, L. Avaldi, R. Flammini, L. Poletto, P. Villoresi, C. Altucci, R. Velotta, S. Stagira, S. D. Silvestri, and M. Nisoli, “Isolated single-cycle attosecond pulses,” Science **314**, 443–446 (2006).
8. I. J. Sola, E. Mevel, L. Elouga, E. Constant, V. Strelkov, L. Poletto, P. Villoresi, E. Benedetti, J. P. Caumes, S. Stagira, C. Vozzi, G. Sansone, and M. Nisoli, “Controlling attosecond electron dynamics by phase-stabilized polarization gating,” Nature Phys. **2**, 319–322 (2006).

9. A. A. Eilanlou, Y. Nabekawa, K. L. Ishikawa, H. Takahashi, and K. Midorikawa, "Direct amplification of terawatt sub-10-fs pulses in a CPA system of Ti:sapphire laser," Opt. Express **16**, 13431-13438 (2008).
10. S. Witte, R. Zinkstok, W. Hogervorst, and K. Eikema, "Generation of few-cycle terawatt light pulses using optical parametric chirped pulse amplification," Opt. Express **13**, 4903-4908 (2005).
11. M. Nisoli, S. De Silvestri, O. Svelto, R. Szipöcs, K. Ferencz, Ch. Spielmann, S. Sartania, and F. Krausz, "Compression of high-energy laser pulses below 5 fs," Opt. Lett. **22**, 522-524 (1997).
12. B. Schenkel, J. Biegert, U. Keller, C. Vozzi, M. Nisoli, G. Sansone, S. Stagira, S. De Silvestri, and O. Svelto, "Generation of 3.8-fs pulses from adaptive compression of a cascaded hollow fiber supercontinuum," Opt. Lett. **28**, 1987-1989 (2003).
13. C. P. Hauri, W. Kornelis, F.W. Helbing, A. Heinrich, A. Mysyrowicz, J. Biegert, and U. Keller, "Generation of intense, carrier-envelope phase-locked few-cycle laser pulses through filamentation," Appl. Phys. B **79**, 673-677 (2004).
14. A. Zaïr, A. Guandalini, F. Schapper, M. Holler, J. Biegert, L. Gallmann, A. Couairon, M. Franco, A. Mysyrowicz, and U. Keller, "Spatio-temporal characterization of few-cycle pulses obtained by filamentation," Opt. Express **15**, 5394-5404 (2007)
15. D. Faccio, A. Lotti, A. Matijosius, F. Bragheri, V. Degiorgio, A. Couairon, and P. Di Trapani, "Experimental energy-density flux characterization of ultrashort laser pulse filaments," Opt. Express **17**, 8193-8200 (2009).
16. J. Odhner and R. J. Levis, "Direct phase and amplitude characterization of femtosecond laser pulses undergoing filamentation in air," Opt. Lett. **37**, 1775-1777 (2012).
17. B. Alonso, I. J. Sola, J. San Román, Ó. Varela, and L. Roso, "Spatiotemporal evolution of light during propagation in filamentation regime," J. Opt. Soc. Am. B **28**, 1807-1816 (2011).
18. X. Sun, S. Xu, J. Zhao, W. Liu, Y. Cheng, Z. Xu, S. L. Chin, and G. Mu, "Impressive laser intensity increase at the trailing stage of femtosecond laser filamentation in air," Opt. Express **20**, 4790-4795 (2012)
19. L. Gallmann, T. Pfeifer, P. M. Nagel, M. J. Abel, D. M. Neumark and S.R. Leone, "Comparison of the filamentation and the hollow-core fiber characteristics for pulse compression into the few-cycle regime," Appl. Phys. B. **86**, 561-566 (2007).
20. T. Witting, F. Frank, C. A. Arrell, W. A. Okell, J. P. Marangos, and J. W. G. Tisch, "Characterization of high-intensity sub-4-fs laser pulses using spatially encoded spectral shearing interferometry," Opt. Lett. **36**, 1680-1682 (2011).
21. I. A. Walmsley and C. Dorrer, "Characterization of ultrashort electromagnetic pulses," Adv. Opt. Photon. **1**, 308-437 (2009).
22. A. Baltuška, M. S. Pshenichnikov, and D. A. Wiersma, "Amplitude and phase characterization of 4.5-fs pulses by frequency-resolved optical gating," Opt. Lett. **23**, 1474–1476 (1998).
23. A. S. Wyatt, I. A. Walmsley, G. Stibenz, and G. Steinmeyer, "Sub-10 fs pulse characterization using spatially encoded arrangement for spectral phase interferometry for direct electric field reconstruction," Opt. Lett. **31**, 1914–1916 (2006).
24. J. R. Birge, H. M. Crespo, and F. X. Kärtner, "Theory and design of two-dimensional spectral shearing interferometry for few-cycle pulse measurement," J. Opt. Soc. Am. B **27**, 1165–1173 (2010).
25. M. Miranda, T. Fordell, C. Arnold, A. L'Huillier, and H. Crespo, "Simultaneous compression and characterization of ultrashort laser pulses using chirped mirrors and glass wedges," Opt. Express **20**, 688-697 (2012).
26. B. Alonso, I. J. Sola, O. Varela, J. Hernández-Toro, C. Méndez, J. San Román, A. Zaïr, and L. Roso, "Spatiotemporal amplitude-and-phase reconstruction by Fourier-transform of interference spectra of high-complex-beams," J. Opt. Soc. Am. B. **27**, 933-940 (2010).
27. B. Alonso, M. Miranda, I. J. Sola, and H. Crespo, "Spatiotemporal characterization of few-cycle laser pulses," Opt. Express **20**, 17880-17893 (2012).
28. M. Miranda, T. Fordell, C. Arnold, F. Silva, B. Alonso, R. Weigand, A. L'Huillier, and H. Crespo, "Characterization of broadband few-cycle laser pulses with the d-scan technique," Opt. Express **20**, 18732-18743 (2012).
29. B. Alonso, R. Borrego-Varillas, Í. J. Sola, Ó. Varela, A. Villamarín, M. V. Collados, J. San Román, J. M. Bueno, and L. Roso, "Enhancement of filamentation postcompression by astigmatic focusing," Opt. Lett. **36**, 3867-3869 (2011)
30. V. Pervak, I. Ahmad, M. K. Trubetskov, A. V. Tikhonravov, and F. Krausz, "Double-angle multilayer mirrors with smooth dispersion characteristics," Opt. Express **17**, 7943-7951 (2009).
31. J. Paye and A. Migus, "Space-time Wigner functions and their application to the analysis of a pulse shaper," J. Opt. Soc. Am. B **12**, 1480-1490 (1995).
32. B. Alonso, R. Borrego-Varillas, O. Mendoza-Yero, I. J. Sola, J. San Román, G. Mínguez-Vega, and L. Roso, "Frequency resolved wavefront retrieval and dynamics of diffractive focused ultrashort pulses," J. Opt. Soc. Am. B **29**, 1993-2000 (2012).
33. E. Kim, H. Kim and J. Noh, "Measurement of the Spatial Wigner Distribution Function of Laser Light by Using a Sagnac Interferometer," J. Korean Phys. Soc. **46**, 1342-1346 (2005).

1. Introduction

The advent of sources capable of delivering ultrashort and ultra-intense light pulses has led to numerous applications in atomic, molecular and nuclear physics [1-3]. In particular, intense few-cycle pulses have opened the way for attosecond physics [4] and metrology [5] via the extreme ultraviolet (XUV) attosecond pulse trains that can be obtained by high-harmonic generation (HHG) [6]. Intense near-infrared pulses close to the single-cycle regime have enabled the generation of isolated attosecond pulses [5,7,8].

The technique of chirped pulse amplification (CPA) combined with Ti:sapphire laser technology has provided many laboratories with intense ultrashort pulses in the 20 to 100 fs range (the lower limit essentially imposed by gain narrowing effects). Although sub-10-fs pulses can be directly obtained from CPA [9] and optical parametric CPA systems [10], they have proven challenging and are still the subject of much research and development. For this reason, two post-compression techniques are usually employed for the generation of intense few-cycle pulses, based on the spectral broadening of light either during propagation in a gas-filled hollow-core fiber (HCF) [11,12] or during the self-guiding due to the filamentation of light [13]. The nonlinear nature of the spectral broadening process, originating mainly from self-phase modulation (SPM), provides a broader spectrum in the center of the beam where the intensity of the pulse is higher. As a consequence, the post-compressed pulses are inhomogeneous and present spatial chirp. The temporal profile of filament-compressed pulses has been shown to depend on the radial coordinate [14]. Also, many efforts are being devoted to the characterization of the filament propagation in terms of temporal [15], spatiotemporal [16,17] and intensity dynamics [18]. The spatial chirp after filamentation and HCF post-compression has been compared experimentally through analysis of the corresponding spectral contents, with more even and less chirped spectra being reported for the HCF case [19]. Recently, a spatially resolved measurement of the spectral and temporal profile of the output mode of a HCF has been performed [20].

Over the last decades, different optical techniques have been introduced for the temporal characterization of ultrashort laser pulses [21]. Most of these now "standard" techniques have been adapted for the temporal measurement of ultra-broadband few-cycle pulses [22-24]. Very recently, the new technique of d-scan (dispersion scan) was introduced, enabling the simultaneous compression and temporal characterization of few-cycle pulses [25]. However, solely temporal characterization of the pulse in a small section of the beam, without accounting for possible variations across the whole pulse front, is generally insufficient, due to the spatiotemporal coupling effects typical of the nonlinear phenomena employed in the post-compression process. For this purpose, the technique of STARFISH (SpatioTemporal Amplitude-and-phase Reconstruction by Fourier-transform of Interference Spectra of Highly-complex-beams) was proposed [26]. Very recently, STARFISH has been demonstrated with sub-8-fs pulses delivered by an ultrafast oscillator, and its capabilities for the study of ultra-broadband pulses have been analyzed [27]. The d-scan technique – initially demonstrated with a few-cycle oscillator – was also very recently used to temporally characterize pulses post-compressed in a HCF [28], which present additional difficulties due to the higher energy, larger spectral bandwidth, stronger phase modulations, and higher instability compared to pulses from an oscillator.

In this work, we generated and characterized sub-two-cycle 4.5 fs pulses (4.1 fs Fourier-limited) from post-compression of 25 fs (Fourier-limit) amplified pulses in an argon-filled HCF. We used the d-scan technique to measure the reference pulse required by STARFISH and applied the latter for the spatiotemporal characterization of the mode compressed at the output of the fiber, where the pulse structure and spatial chirp were studied. These pulses were also focused using an off-axis parabolic mirror and measured around the focal spot in the spatiotemporal domain.

The full spatiotemporal characterization of intense few-cycle lasers provide useful information for the study of the dynamics and characteristics of filamentation [17,29] and HCF post-compressed pulses. In future experiments, it may be used to tackle the comparison between both post-compression techniques. This information is relevant for the optimization of the process itself and for applications (e.g., HHG) of the generated pulses.

2. Experimental setup for post-compression and spatiotemporal characterization

We post-compressed pulses delivered by a $1 kHz$ Ti:sapphire CPA amplifier (Femtolasers FemtoPower Compact PRO CEP) in a gas-filled HCF and chirped mirror compressor. The complete experimental setup is depicted in Fig. 1. The amplified pulses, with a Fourier-transform limit (FTL) of 25 fs, were coupled into the hollow fiber with a 1.5-m focal length lens. The HCF had an inner diameter of $250\mu m$, a length of $1m$, and was filled with argon at a pressure of 960 mbar. The pulse energy before the HCF was $375\mu J$ and the output of the fiber was $150\mu J$ (transmission of 40 %). The amplifier's compressor (the input pulse chirp on the HCF) was adjusted to optimize the spectral broadening (Fig. 3(c)) and the transverse mode profile (Fig. 2(b)) at the fiber output. Additionally, we also optimized the fiber output with an iris (7-mm diameter) placed just before the lens for the fine control of the input energy and the input mode being coupled into the HCF (Fig. 2(a)). Moreover, the post-compression was optimized for a very stable output mode, as required both for subsequent applications and for (multi-shot) pulse characterization. The quality of the d-scan and STARFISH traces is an indication of this stability, since shot-to-shot variations would strongly affect them. In parallel, the raw d-scan traces already provided a fast diagnostic to ensure that the temporal profile corresponded to clean compressed pulses without satellites that could occur in the HCF, given that it only takes a few seconds to acquire them and the shape of the trace gives direct interpretable insight over the structure of the pulse [25]. Due to the nonlinearity of the argon gas inside the HCF, the input spectrum was broadened to a 4.1-fs FTL spectrum extending from 540 to 990 nm (Fig. 3(c)). A spherical silver mirror at near-normal incidence ($ROC = -3000mm$) was placed after the HCF to collimate the spectrally broadened pulses. To complete the post-compression of the pulses, a compressor made of a glass wedge pair and a set of ultra broadband chirped mirrors (CMs) was used. The wedges (Femtolasers GmbH) were made of BK7 with an antireflection-coating and an angle of 8º. The CMs (UltraFast Innovations GmbH) are designed in such a way that when two bounces are combined, with angles of incidence of 5º and 19º, the residual phase ringing is minimized [30]. We used five pairs of mirrors for a total number of five bounces at each angle, as illustrated in Fig. 1 (we have identified the CMs with different colors, orange and purple, for 5º and 19º incidence, respectively). The nominal group delay dispersion (GDD) of the CMs was around $-50 fs^2$ per bounce at 800 nm. The variable insertion of one of the wedges allowed us to fine tune the ultimate post-compressed duration of the pulses, and was also used as part of the d-scan technique, as described below. Notice that for the post-compression we have used a higher gas pressure than in our previous work [27], which provided a broader spectrum here. Also, the compression in [28] was performed using different CMs.

For the characterization of the post-compressed pulses, we used the STARFISH technique [26] assisted by the d-scan technique [25] to measure the reference pulse, in a configuration recently introduced for few-cycle pulses [27]. A replica of the pulse to be characterized was created with a dispersion-balanced (same dispersion in the reflected and transmitted beams) broadband beam splitter (600-1500 nm), BS (Venteon GmbH). One pulse was measured with the d-scan (after the flip mirror) and subsequently used as the reference pulse in STARFISH.

The experimental implementation of the d-scan consists in measuring the second harmonic generation (SHG) spectrum of the pulse while the dispersion is varied via the translation of one of the wedges around the point of maximum compression (minimum pulse duration). As a result, a spectrally resolved SHG trace as a function of wedge insertion (dispersion) is obtained. In the present setup, we focus the pulses with an off-axis parabolic (OAP) mirror (focal length of 5 cm) in a nonlinear crystal (BBO, 20 µm thick, cut for type I SHG at 800 nm). The SHG signal is collimated with a lens and a blue filter is used to remove the remaining fundamental frequency signal before detection with the spectrometer (HR4000, Ocean Optics Inc.).

In STARFISH, a single-mode, $4\mu m$ core diameter, broadband fiber optic coupler [26,27] is used to combine the reference pulse (already characterized by the d-scan) and the (unknown) test pulse. A spectral interferogram (SI) of the pulses with a relative delay τ is measured in a standard fiber-coupled spectrometer (S2000, Ocean Optics Inc.). This information will allow us to obtain the temporal reconstruction of the pulses. The test pulse fiber input is scanned over the spatial profile of the pulse in one axis (x-scan), where cylindrical symmetry is assumed. This allows for the spatiotemporal characterization of the pulses.

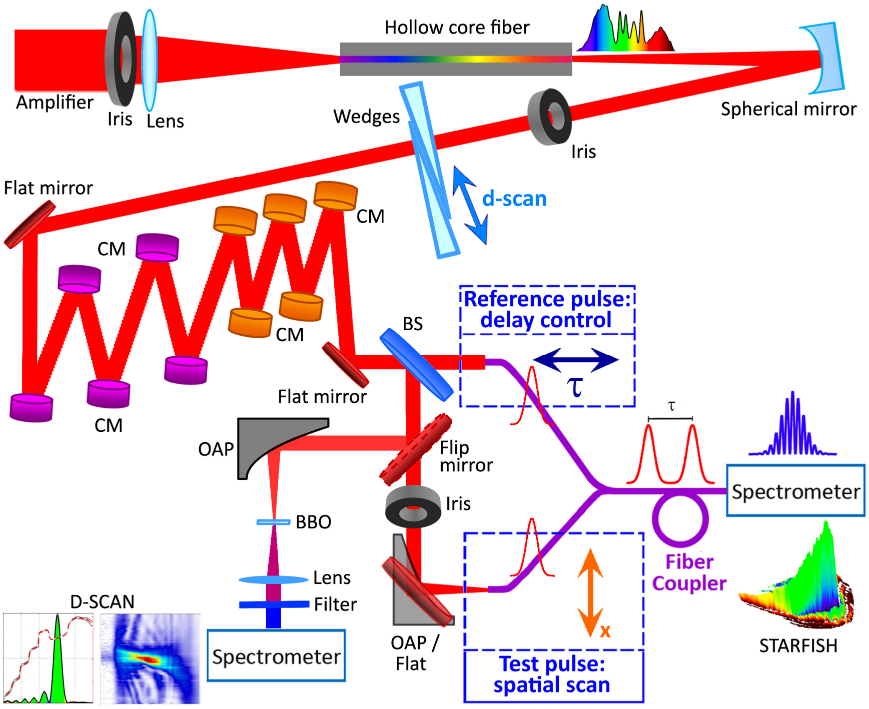
Hollow core fiber
Amplifier
Iris
Lens
Wedges
Spherical mirror
Iris
Flat mirror
d-scan
CM
CM
CM
CM
Reference pulse:
delay control
τ
BS
Flat mirror
OAP
Flip
mirror
Iris
τ
Spectrometer
BBO
Lens
Filter
D-SCAN
Spectrometer
OAP /
Flat
Test pulse:
spatial scan
x
Fiber
Coupler
STARFISH

Fig. 1. Experimental setup for the generation and spatiotemporal characterization of post-compressed pulses. The amplified pulses are spectrally broadened in a hollow-fiber and the output mode is collimated with a spherical mirror. The pulses are divided with a dispersion-balanced broadband 50/50 beam splitter (BS) to perform the spectral interferometry of STARFISH. Using a flip mirror, the reflected pulses can be simultaneously compressed and characterized by dispersion scan (d-scan) where a compressor made of a pair of glass wedges and 5 pairs of chirped mirrors (CM) is used to track the SHG signal generated in a nonlinear crystal (BBO) as a function of wedge insertion. The test and reference pulses are then combined in a fiber optic coupler and sent to the spectrometer. The position of the test fiber is scanned over the spatial coordinate (x-axis). The hollow-fiber output (test pulse) is measured without focusing (flat mirror) and with focusing (off-axis parabola, OAP, 5 cm focal length).

The spatiotemporal STARFISH characterization of the few-cycle pulses is first performed directly after the CM setup, so a flat mirror is used to direct the pulses to the test fiber. We then replace this mirror with a 5-cm focal length OAP to study the focusability of the pulses, and to characterize them around the focal region.

Before the wedges and CM compressor, an iris of 10-mm diameter is used to select the spatial mode after collimation of the fiber output (see Fig. 2(b)). Due to the 10-mm iris before the wedges and the losses inside the compressor itself, the pulse energy decreased from $150\mu J$ to $90\mu J$ before the BS. The beam was not perfectly collimated after the spherical mirror, since it diverged more than would be expected for a collimated beam with the same waist. Actually, the beam size of the pulses increased up to 13 mm just before the last mirror prior to the test fiber (the optical path in the CM setup was 169 cm). At this position, we selected the spatial mode with a diaphragm to eliminate the residual (mostly conical) emission around the main portion of the beam.

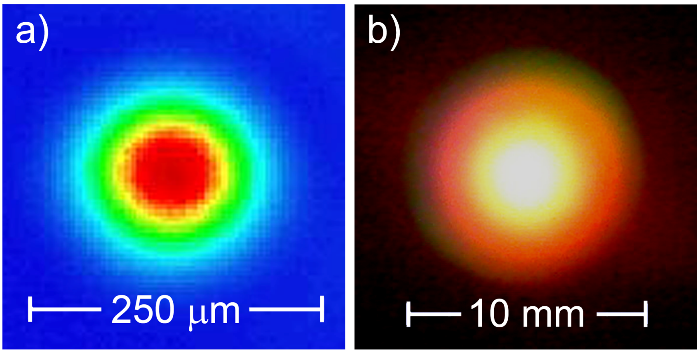

Fig. 2. (a) Input mode coupled at the entrance of the HCF with an inner diameter of $250\mu m$.
(b) Spatial profile of the output mode of the HCF after collimation with the spherical mirror.

The spectral phase of the reference pulse is retrieved by the d-scan technique by optimizing the simulated SHG trace compared with the experimental trace using an iterative algorithm [25]. The spatiotemporal amplitude and phase characterization is obtained by an algorithm based on the Fourier-transform of the spectral interferences given by the STARFISH technique [26].

3. Spatiotemporal analysis of sub-5-fs pulses after hollow-fiber post-compression

3.1 Characterization of the reference pulse using d-scan

As said before, the spectrally broadened amplified pulses are compressed with five pairs of broadband chirped mirrors and a pair of BK7 glass wedges (angle 8°). This compressor is also a part of the d-scan technique setup for the characterization of the reference pulse, which is required for the spectral interferometry. The d-scan trace was taken by measuring the SHG signal for varying glass insertion. The total range of insertion (in the propagation direction) was $d = 4.34mm$ using a lateral insertion step of $0.215mm$, which corresponds to 146 sampling points. The resulting experimental d-scan trace is shown in Fig. 3(a).

The d-scan algorithm was executed five times with different input conditions (five different starting guesses) in order to ensure the convergence of the retrieved phase. The retrieved trace is given in Fig. 3(b), and is in very good agreement with the experimental trace. The experimental spectrum and the retrieved phase of the pulse for maximum compression are shown in Fig. 3(c). The full width at $1/e^2$ of the maximum (in intensity) of the hollow-fiber spectrum is $402nm$. The standard deviation of the phase (gray curves) for the different runs of the algorithm provides the information of the precision error. The spectral phase retrieved is precise except for the shorter wavelengths due to the experimental d-scan trace being cropped in the bluer part of the spectrum, as we will explain below. In Fig. 3(d), we represent the retrieved temporal intensity and phase of the corresponding pulse. The optimum spectral phase has a small contribution of negative third-order dispersion that produces the pre-pulses. The corresponding standard deviations (gray curves) are very small, which means that the spectral phase deviation for shorter wavelengths hardly affects the temporal retrieval. The duration of the pulse is $4.5 \pm 0.1 fs$ (intensity FWHM), close to its FTL of $4.1 fs$. The carrier wavelength calculated from the center of gravity of the spectral power density (in frequency) is $\lambda_g = 739nm$. The temporal intensity in Fig. 3(d) has been color-filled with the instantaneous wavelength of the pulse λ_t. From the tilt of the phase in the pre-pulses we see that they are slightly redder than the main pulse (centered at $\lambda_t = 739nm$), as illustrated by the color fill. The small deviation of the instantaneous wavelength from the carrier wavelength is an evidence of the good compression achieved. The main reason why the final pulse duration deviates from the FTL is the divergence in the spectral phase introduced by the broadband beamsplitter for wavelengths below 600 nm, since this element is designed to work above this wavelength.

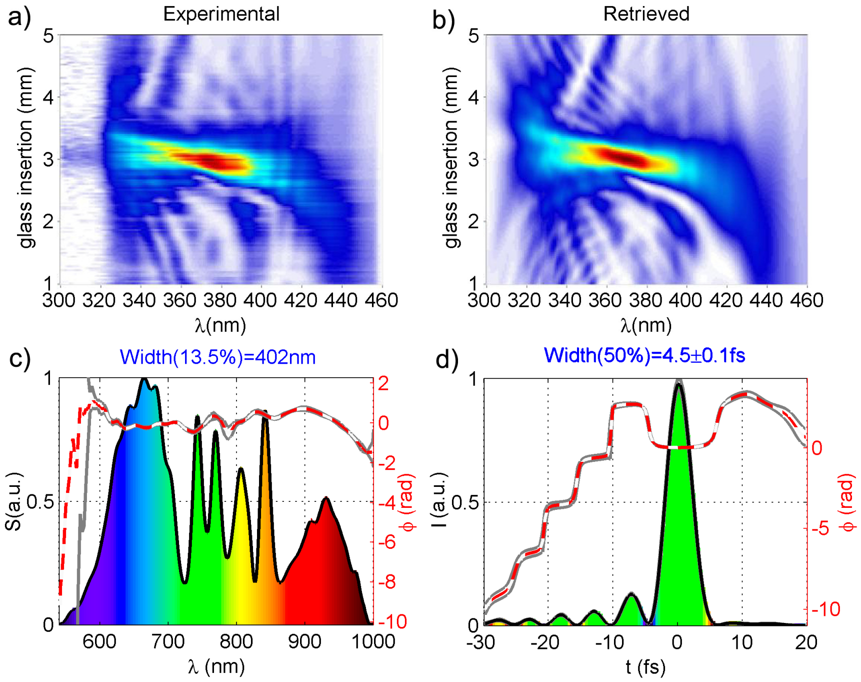

Fig. 3. (a) Experimental and (b) retrieved d-scan traces of the reference pulse. (c) Spectral intensity (black) and phase (dashed red) of the retrieved pulse. (d) Temporal intensity (black) and phase (dashed red) of the reference pulse. The gray curves in (c) and (d) represent the standard deviation of the spectral phase, and of the temporal intensity and phase, respectively. The intensity profile (d) is color-filled by the instantaneous wavelength following the same color scale than in (c).

The lack of signal below 320 nm in the experimental trace may be partly due to the cut-off of the blue filter and by UV absorption in the collimating lens. This justifies the difference between measured and retrieved traces in that spectral region. To minimize this effect, a spatial mask can be used instead of the filter or lens [28]. The phase distortion introduced by the beamsplitter for wavelengths below 600 nm may also contribute to the smaller SHG signal observed at shorter wavelengths. In spite of this, thanks to the trace redundancy in the d-scan technique, it is possible to recover phase information for regions where no SHG signal has been measured at all, as it was shown in [25,28].

As mentioned above, the optimal pulse compression with this system is close to the FTL. To further analyze this compression, we calculated the temporal Wigner distribution function of the pulse and the FTL of the spectrum. For a certain function defined in the time domain (in our case the electric field of the pulses, $E(t)$), the temporal Wigner distribution can be interpreted as the probability (despite it taking positive and negative values) to find a certain wavelength (or frequency ω) at a given time t , i.e., it gives us the spectral distribution within the pulse. The definition of the temporal Wigner distribution function W_T is [31]

$$W_T\left(t,\omega\right)=\int_{-\infty}^{\infty} E\left(t+\frac{t'}{2}\right)E^*\left(t-\frac{t'}{2}\right)e^{i\omega t'}dt' \qquad (1)$$

The calculations for the pulse retrieved by the d-scan and for the FTL of the spectrum are shown in Fig. 4(a) and 4(b), respectively. The information given by W_T is related to the instantaneous frequency (see Fig. 3(d)), although W_T provides the whole information of the temporal distribution of wavelengths, in contrast to the single value of the effective instantaneous wavelength. This gives further insight on the pulse structure and compression, and can give a visual and intuitive idea of how far we are from the FTL by comparing the temporal Wigner distributions of the retrieved pulse and of its FTL (Figs. 4(a) and 4(b)). In our case, the fact that most of the spectrum is contained in the main peak of the pulse (like in the FTL pulse, except for the tails of the spectrum) means that almost the whole spectrum is well compressed (i.e., its spectral phase is well compensated for). Moreover, when comparing the scales of the plots, there is a small loss of signal in the measured pulse with respect to its FTL. This is in agreement with the fact that the peak intensity of the pulse for the d-scan retrieval is 0.8 times the FTL peak intensity. The marginals of W_T are also given in the plots, where integration of the Wigner function of the pulse over the frequency and time axes provides the temporal intensity (left) and power spectral density (bottom), respectively.

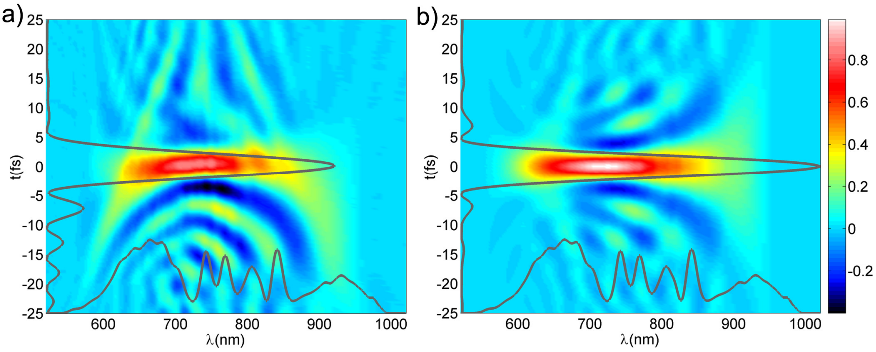

Fig. 4. Wigner distribution functions and corresponding marginals for the electric field of the (a) experimental pulse and (b) Fourier-transform limit of the spectrum. The two functions are represented in the same (arbitrary) units in order to compare the respective signal strength.

3.2 Spatiospectral and spatiotemporal characterization of the output mode using STARFISH

The output mode of the post-compression of the intense pulses in the HCF was characterized in the spatiotemporal domain. The spatial profile was scanned with the fiber across the 13-mm diameter of the pulse with steps of $50 \mu m$ (261 sampling points). The spatially-resolved spectrum (Fig. 5(a)) shows that the spectral distribution is fairly constant across the x-coordinate, only presenting less broadening in the bluer part of the spectrum for the outermost part of the spatial profile. The frequency-resolved wavefront (Fig. 5(b)) presents a curvature responsible for the beam divergence (already observed during beam propagation), which will be taken into account to simulate the focus of the pulse in Section 3.3.

The pulse-front curvature in the spatiotemporal intensity (Fig. 5(d)) corresponds to the expected curvature of a diverging beam. It exhibits a relatively small variation of $\approx 30 fs$ from the center to the periphery of the beam ($\approx 13 mm$ diameter), although it is large compared to the pulse duration. Nevertheless, we will see that the presence of wavefront and pulse-front curvature do not compromise the focusability of the beam and a tight focus is achieved. The spatiotemporal intensity is shown in Fig. 5(e), color-filled with the instantaneous wavelength to better illustrate the spatial dependence of the temporal chirp. The main peak color shifts from bluer to redder values as we move away from the center of the pulse ($x = 0$), as expected from the spatially-resolved spectrum in Fig. 5(a).

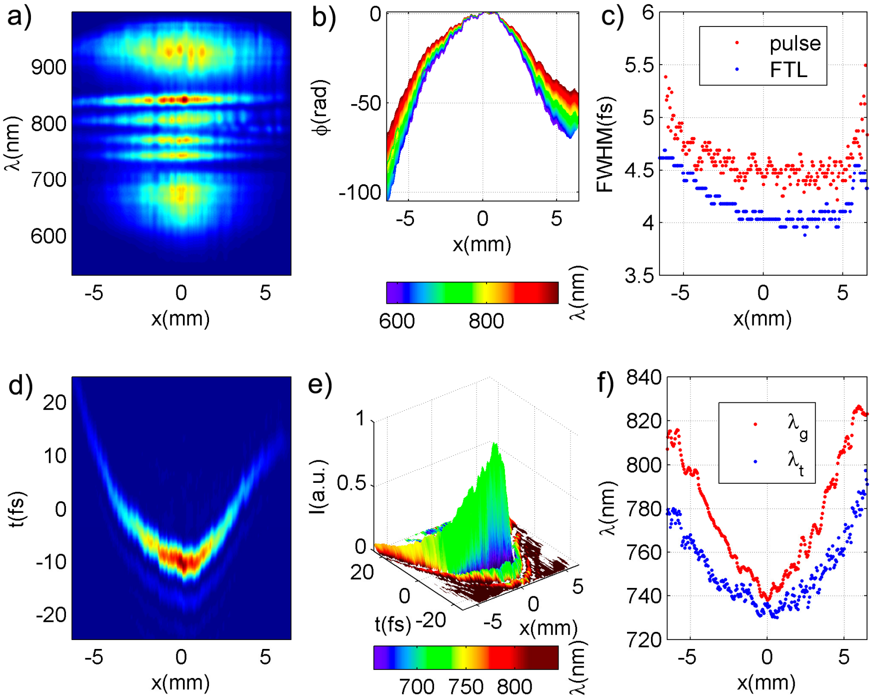

Fig. 5. Intense pulse post-compressed in a HCF; experiment: (a) Normalized spatiospectral intensity and (b) frequency-resolved wavefront, the latter represented in different colored lines for each wavelength (see the colorbar). (c) Fourier-limit (blue) and retrieved pulse duration (red). (d) Normalized spatiotemporal intensity and (e) same as (d), but color-filled with the instantaneous wavelength (see the colorbar). (f) Instantaneous wavelength at the pulse-front (blue) and center wavelength (red).

The pulse duration (intensity FWHM) as a function of x is presented in Fig. 5(c) for the retrieved pulse and for the FTL of the spectrum. The pulse duration varies approximately from 4.5 fs on-axis to 5.0 fs in the wings, whereas the FTL varies from 4.0 fs to 4.5 fs. In Fig. 5(f), we show the carrier wavelength dependence on x, both for the center of gravity of the spectrum (λ_g) and the instantaneous wavelength (λ_t) evaluated at the maximum of the pulse (i.e. at the pulse front). We see that λ_g varies from 740 nm (on-axis) to 820 nm (wings), whereas λ_t varies from 735 nm (on-axis) to 790 nm (wings). This difference is explained by the redistribution of frequencies inside the pulse due to the temporal chirp. These results are in agreement with previous works where blue-shift and larger spectral broadening and pulse shortening were observed on-axis in comparison with the outer part of the spatial profile [19]. Redder pre-pulses with the same curvature than the main pulse (the pulse front) are observed, similarly to the reference pulse. There is almost no chromatic aberration in the wavefront (Fig. 5(b)) since all wavelengths have practically the same curvature, except for the intrinsic wavenumber dependence $\phi(x_0,\lambda) \propto k \propto \lambda^{-1}$ (similar to the results given in [32] for a focusing refractive lens), as we will calculate in the next section.

3.3 Spatiospectral and spatiotemporal characterization of the focus using STARFISH

The pulses were focused with an OAP (f = 5 cm). The focus was spatially resolved with the test fiber, which scanned the transverse profile across $30\mu m$ in steps of $1\mu m$ (x-axis). Despite the $4\mu m$ fiber core diameter, we have demonstrated in previous work that using a smaller step allows us to recover the structure and size of focused pulses [31]. In this experiment, a neutral-density filter was placed before the interferometer (before the BS) to avoid damage or nonlinear effects in the collecting fiber, so the linear focus was characterized. The spectrum as a function of the x-coordinate (Fig. 6(a)) presents a spatial chirp, with increasing red-shift for increasing values of x. The spatiotemporal distribution corresponds to a well-defined focus in space and time (Fig. 6(d)), with a spatial width of $10\mu m$ (FWHM) and a temporal duration on-axis of $4.5\,fs$ (FWHM). The instantaneous wavelength combined with the intensity (Fig. 6(e)) inherits the spatial chirp from the frequency domain (shown in Fig. 6(a)). Since the input pulse is symmetric in x (Fig. 5), the spatial chirp may be originated by a slight misalignment in the OAP. The frequency-resolved wavefronts (Fig. 6(b)) show a slight divergence, meaning that the measurement was not taken exactly at the focus, but just before it. Also, the wavefronts for the different wavelengths have a gradual relative tilt, which is an evidence of the spatial chirp originated by the asymmetric focusing phase introduced by the misalignment.

An estimation of the peak irradiance of the pulses focused with the OAP can be obtained in terms of the pulse duration and the spot size, assuming Gaussian beams and pulse shapes with widths given by the experimental spatial and temporal FWHM, respectively. The expression for the peak irradiance is $I_{\max} = 0.651 \cdot E/(\Delta t \cdot S)$ [27], where $E = 45\mu J$ is the pulse energy after the beam splitter, $\Delta t = 4.5 fs$ is the temporal FWHM, $S = \pi(\Delta x/2)^2$ is the spot section (since $\Delta x = 10\mu m$ is the spatial FWHM) and 0.651 is the factor coming from the assumption of Gaussian shapes. In our case, we estimate a peak irradiance of $I_{\max} = 8.3\times10^{15}\, W/cm^2$.

The FWHM intensity of the Fourier-transform limited (FTL) pulse increases along the x-axis from 4.5 to 4.9 fs and the retrieved pulse duration from 4.8 to 5.3 fs (Fig. 6(c)). Similar behavior is observed for the carrier (central) wavelength λ_g that varies from 760 nm to 810 nm (Fig. 6(f)). Again, the instantaneous wavelength at the pulse-front, λ_t, is blue-shifted with respect to λ_g.

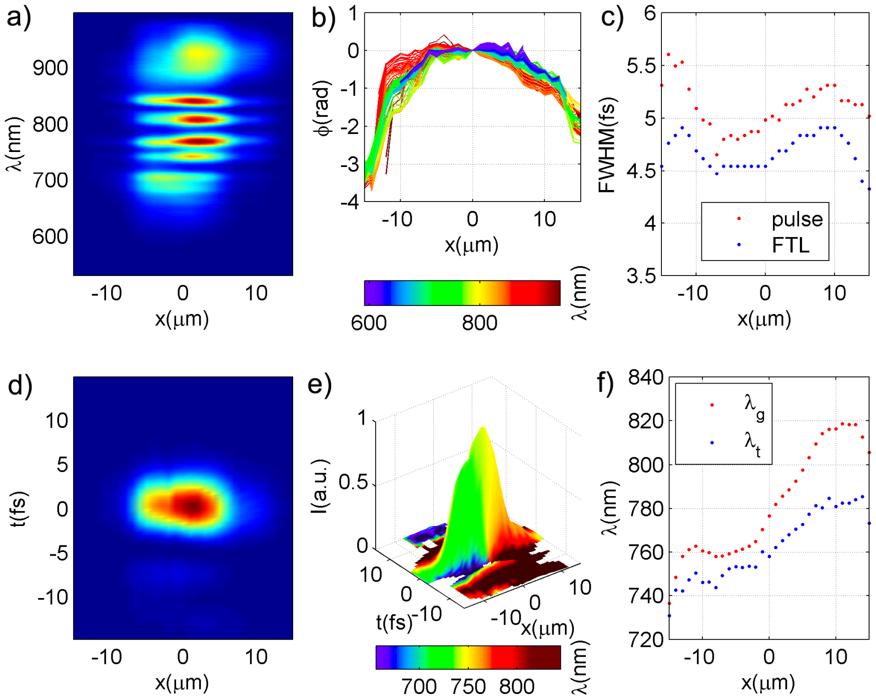

Fig. 6. Post-compressed pulses focused with an OAP; experiment: (a) Normalized spatiospectral intensity and (b) frequency-resolved wavefront, the latter represented in different colored lines for each wavelength (see the color-bar). (c) Fourier-limit (blue) and pulse duration (red). (d) Normalized spatiotemporal intensity and (e) same as (d), color-filled by the instantaneous wavelength (see the color-bar). (f) Instantaneous wavelength at the pulse-front (blue) and center wavelength (red).

We studied the effect of the spatiospectral phase (or wavefront) of the mode before focusing (Fig. 5(b)). This phase is mainly quadratic and can be written as $\phi(x;\lambda)=(\pi/\lambda)(x^2/f_{in})$, corresponding to a diverging beam with a focal length f_{in}. From the fit to the phase $\phi(x;\lambda)$ for each wavelength, we extracted the focal length $f_{in}=-4724\pm 26mm$ (regression coefficient $R=0.9989$). When combined with the focal length of the OAP, $f_{OAP}=50mm$, we obtained the effective focal length $f_{eff}=50.53\,mm$. Assuming that only this quadratic phase is present, this will simply cause a shift in the focal position along the propagation axis, but higher order curvature terms in the wavefront may distort the focal spot.

Finally, we analyzed the effect of the numerical aperture (NA) of the fiber coupler (the test pulse fiber arm). In a previous work we measured a coupling efficiency of 50% at an angle of incidence of $\theta=5°$ [27]. Here, we used the experimental dependence of the coupling on the angle θ, denoted by $T(\theta)$, to study its effect in the measurement of the focus of the OAP. In the ray-tracing approximation, the angle θ is translated to the input spatial plane as $\tan\theta\approx r/z$, where $z=f$ for observation at the focus (this gives the function $T(r)$ in Fig. 7(a)). In the present case, the spatial intensity profile has a Gaussian-like shape, so the less efficiently coupled part of the profile, the periphery, is the part with less contribution. Figure 7(a) shows the spatial intensity profile $I(r)$, the fiber transmission $T(r)$, and the modified spatial profile $I(r)\cdot T(r)$ considering ray tracing. The experimental spatially-resolved spectrum before the focus is shown in Fig. 7(b), which can be compared with the same magnitude modified by $T(r)$ in Fig. 7(c). From Fig. 7, it can be seen that the parts actually affected are the wings of the spatial profile.

The distribution of the orientation of the wave vectors inside a focused monochromatic Gaussian beam (far from the Rayleigh zone) corresponds to a defined (with a narrow angular spreading) angle, which can be simply calculated by ray tracing, as a function of the spatial coordinate (in the transverse plane) [33]. Since larger angles occur in the periphery of the beam, outside the focal region the angular filtering of the NA of the fiber results in a reduction of the spatial width that can be estimated as explained in the previous paragraph (see Fig. 7). Contrarily, at the focus position all the wave vectors (from the ray tracing) are overlapped and the wave vector spreading is independent on the spatial coordinate, so the ray tracing approximation is obviously unacceptable there [33]. For this reason, in the focus (where we measured the pulse), the effect of the NA coupling will be ideally a reduction in the collected signal without spatial distortion. Anyway, in our case the NA of the pulse is comparable to the NA of the detection fiber, so the effect on the spatiotemporal measurements will be small (for instance, see the decrease in spatial width in Fig. 7).

The present analysis will be more complex in the case of polychromatic non-Gaussian beams, which may also be inhomogeneous and present wavefront aberrations. This will cause a less predictable propagation (if the unfocused pulse is known, numerical simulations can still be performed). However, ray tracing can still give a first approximation of the wavevector distribution and an upper bound for the maximum angle $\theta_{\max}$ can be estimated by the relation $\tan\theta_{\max} \simeq r_{\max}/f$, where $r_{\max}$ is the radius of the unfocused pulse and f is the focal length. Naturally, the effect of the NA will not be felt by smaller beams or longer focal lengths. Finally, the rather homogeneous mode at the output of the hollow-fiber plays to our advantage in the sense that distortions (due to the NA) at the focus of the beam will be reduced.

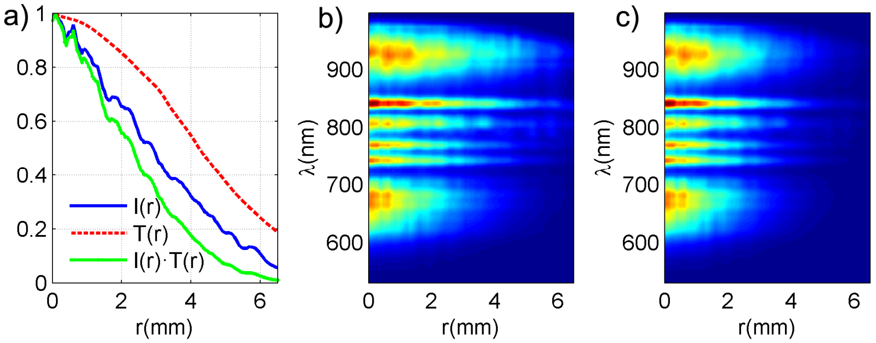

Fig. 7. (a) Spatial profile of the pulse (blue), transmission of the fiber due to the numerical aperture (red) and corrected spatial distribution (green). (b) Experimental spatially-resolved spectrum. (c) Spatially-resolved spectrum modified by T(r).

4. Conclusions

We have generated sub-two-cycle pulses by post-compression in an argon-filled hollow-core-fiber of 25-fs (Fourier-transform limited) amplified pulses from a 1 kHz Ti:sapphire laser. The post-compression was optimized to have a broadband spectrum corresponding to few-cycle pulses (4.5 fs FWHM, 4.1 fs FTL) and a homogeneous (near-Gaussian) spatial profile with a significantly stable mode. The optimum compression was achieved by compensating the spectral phase with a pair of wedges and ultra-broadband chirped mirrors. The post-compressed pulses were characterized in the spatiotemporal domain using the STARFISH technique and the reference pulse was measured with the d-scan technique. We first studied the output mode of the hollow-fiber and found that the spectral broadening and the blue-shift are significantly larger at the center (x=0) of the pulse than in the periphery. This resulted in an increase in pulse duration from 4.5 fs at the beam center up to 5 fs at the periphery. A symmetric spatial chirp (relative to x=0) was consequently observed in the spatiotemporal reconstruction. Also, the measured wavefront corroborated the divergence predicted from the observation of the spatial size growth during the propagation.

The pulse was also focused with an off-axis parabolic mirror (f = 5 cm) producing a measured focal spot size of $10\mu m$ (FWHM). In this case, an asymmetric spatial chirp was observed, which was attributed to a slight misalignment of the mirror. The experimental spectrum, wavefront, intensity and temporal chirp are consistent with this statement. The effect of the numerical aperture of the collection fiber on the focused pulse measurement was also studied. Although not negligible, it did not prevent us from obtaining detailed information on the structure of the focused pulse.

The broadband, intense 4.5 fs pulses (4.1 fs Fourier-limited) that were characterized in the spatiotemporal domain using STARFISH in conjunction with d-scan are already at the limit of most temporal characterization techniques in the near-infrared range. The possibility of measuring high-energy, low repetition rate pulses in this range shows promise for future applications to the further study and optimization of filament and hollow-fiber compressed pulses.

Acknowledgements

We acknowledge support from Spanish Ministerio de Ciencia e Innovación (MICINN) through the Consolider Program SAUUL (CSD2007-00013), Research projects FIS2009-09522, and grant programs Formación de Profesorado Universitario (No. AP2007-00236 for B. Alonso) and Ramón y Cajal (for I. J. Sola); and from the Junta de Castilla y León through the Program for Groups of Excellence (GR27). H. Crespo acknowledges Fundos FEDER, through Programa Operacional Factores de Competitividade – COMPETE, and Fundação para a Ciência e a Tecnologia (FCT) under grants No. PTDC/FIS/115102/2009 and PTDC/FIS/122511/2010. M. Miranda and F. Silva acknowledge FCT and FEDER grants No. SFRH/BD/37100/2007 and SFRH/BD/69913/2010, respectively. We also acknowledge support from Centro de Láseres Pulsados (CLPU), Salamanca, Spain.

PAPER VII

Space-time focusing of phase-stabilized nanojoule-level 2.5-cycle pulses to peak intensities $> 3 \times 10^{13}$W/cm^2 at 80 MHz

Miguel N. Miranda, Pedro B. Oliveira, L. M. Bernardo,
Franz X. Kärtner, and Helder M. Crespo.

CLEO/Europe and EQEC 2009 Conference Digest **CF1 2**, (2009).

Space-time focusing of phase-stabilized nanojoule-level 2.5-cycle pulses to peak intensities >3×10^{13} W/cm^2 at 80 MHz

Miguel N. Miranda[1], Pedro B. Oliveira[1], L. M. Bernardo[1], Franz X. Kärtner[2], Helder M. Crespo[1]

1. IFIMUP and IN - Institute of Nanoscience and Nanotechnology, Departamento de Física, Faculdade de Ciências, Universidade do Porto, Rua do Campo Alegre, 687, 4169-007 Porto, Portugal.

2. Department of Electrical Engineering and Computer Science and Research Laboratory of Electronics, Massachusetts Institute of Technology, Cambridge, Massachusetts 02139-430, USA.

Tight focusing of laser light down to near diffraction limited spot sizes can be easily achieved with high numerical aperture microscope objectives, and state-of-the-art ultrafast laser technology has made possible the generation of sub-two-cycle pulses directly from laser oscillators [1, 2]. In applications such as OCT, the spot size translates into lateral resolution, while techniques relying on nonlinear optical effects, such as CARS spectroscopy and two-photon microscopy, rely on both the spatial and temporal confinement of radiation, which leads to high peak intensities. Space-time focusing of carrier-envelope phase stabilized few-cycle laser pulses plays a crucial role in the study of phase-dependent nonlinear optical phenomena [3]. However, such focusing is not easily achieved, mostly due to the very broad bandwidths of few-cycle pulses and the dispersion introduced by the large amounts of glass present in high-quality microscope objectives. Non-dispersive reflective objectives have been used for this purpose [3], but their intrinsic obscuration usually limits the coupling efficiency to less than 10%, with a consequent decrease in peak intensity. Dispersion compensation of microscope objectives using chirped mirrors has resulted in sub-14-fs pulses [4], and very recently, sub-8-fs pulses were obtained with a 4-f pulse shaper arrangement based on a mechanically deformable mirror [5].

In this work we demonstrate the efficient focusing of 2.5-cycle laser pulses from a phase-stabilized broadband laser oscillator with a repetition rate of 80 MHz (Femtolasers Rainbow) using a simple and compact setup based on octave-spanning double-chirped mirrors [6] to pre-compensate the dispersion of microscope objectives. The beam diameter was kept at <2 mm at the entrance of the objectives in order to minimize undesirable radius-depend group-delay dispersion effects [7]. Temporal characterization was performed with a modified SHG interferometric autocorrelator capable of measuring the pulse duration directly at the focus of the objectives, and the spot size was measured by imaging it with another microscope objective and CCD camera. For an input pulse energy of 2.5 nJ, a 63× microscope objective (N.A.= 0.85) resulted in clean 6.8 fs (FWHM) pulses with spot sizes as small as 1.1 μm (FWHM), as shown in Fig. 1.

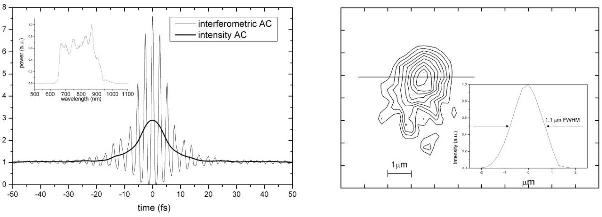

Fig. 1 Measured focused pulses obtained with a 63× microscope objective (N.A. = 0.85): (left) Interferometric and intensity autocorrelations at the focus (inset: intensity spectrum). The retrieved pulse width assuming a sech^2 shape is 6.8 fs FWHM. (right) Beam intensity profile at the focus, with x-cut slice inset. The beam diameter is 1.1 μm FWHM.

Thin glass slides were used to fine tune the dispersion and optimize the final pulse width. The overall system efficiency is >95%, corresponding to a peak intensity >3.7×10^{13} W/cm^2, already at the onset of extreme phase-dependent nonlinear effects such as high-harmonic generation (HHG). To our knowledge, these are the highest peak intensities and shortest pulse durations ever obtained for focused low-energy phase-stabilized pulses at multi-MHz repetition rates, which should have an impact on a number of applications. The estimated peak intensities open the possibility of studying phase-dependent extreme nonlinear optical phenomena such as HHG directly with a few-cycle laser oscillator at MHz repetition rates.

References

[1] F. X. Kärtner et al., "Few-Cycle Pulses Directly from a Laser", in "Few-Cycle Laser Pulse Generation and Its Applications," pp. 73-136 (Springer, 2004).
[2] H. M. Crespo et al., Opt. Lett. **33**, 833-835 (2008).
[3] O. D. Mücke et al., Phys. Rev. Lett. **85**, 057401 (2001).
[4] G. Tempea et al., "Dispersion Management for Microscope Objectives", CLEO (OSA, 2005), paper CThBB6.
[5] Y. Ozeki et al., Opt. Express **16**, 2778 (2008).
[6] F. X. Kärtner et al., J. Opt. Soc. Am. B **18**, 882-885 (2001).
[7] J. Jasapara and W. Rudolph, Opt. Lett. **24**, 777 (1999).

Paper VIII

Spatial and spectral properties of the high-order harmonic emission in argon for seeding applications

X. He, M. Miranda, J. Schwenke, O. Guilbaud, T. Ruchon, C. Heyl,
E. Georgadiou, R. Rakowski, A. Persson, M. B. Gaarde, and
A. L'Huillier.

Phys. Rev. A **79**, 063829 (2009).

PHYSICAL REVIEW A **79**, 063829 (2009)

Spatial and spectral properties of the high-order harmonic emission in argon for seeding applications

Xinkui He,[1] M. Miranda,[1,*] J. Schwenke,[1,2] O. Guilbaud,[1,†] T. Ruchon,[1,‡] C. Heyl,[1] E. Georgadiou,[1] R. Rakowski,[1]
A. Persson,[1] M. B. Gaarde,[3] and A. L'Huillier[1]
[1]*Department of Physics, Lund University, P.O. Box 118, SE-221 00 Lund, Sweden*
[2]*Max-lab, Lund University, P.O. Box 118, SE-221 00 Lund, Sweden*
[3]*Department of Physics and Astronomy, Louisiana State University, Baton Rouge, Los Angeles 70803-4001, USA*

(Received 24 November 2008; published 22 June 2009)

We characterize and control the harmonic emission in the spectral and spatial domains in order to define in which conditions the harmonic radiation can be a high-quality seed for soft x-ray and x-ray free-electron lasers. The length of the gas cell, where harmonics are generated, was optimized and the energy per pulse was determined in absolute value with a calibrated x-ray photodiode. The beam spatial profile was measured and, in some conditions, a very collimated beam with a half-angle divergence below 1 mrad could be obtained. We also show that increasing the intensity of the fundamental laser field leads to a considerable broadening of the bandwidth of the harmonic radiation, allowing us to cover a large spectral range. This effect is due to fundamental reshaping leading to an efficient phase matching of both short- and long-trajectory contributions.

DOI: 10.1103/PhysRevA.79.063829 PACS number(s): 42.65.Ky, 32.80.Rm, 32.80.Qk

I. INTRODUCTION

A lot of effort is devoted world wide to the development of coherent light sources in the extreme ultraviolet (xuv) range with laserlike properties. Different paths are being explored, from x-ray free-electron lasers (XFELs), based on the self-amplification of the synchrotron radiation emitted by relativistic electron bunches [1] to soft x-ray lasers (SXRLs), relying on the realization of a population inversion in highly charged ions obtained in a hot dense plasma [2]. These two approaches lead to high-energy xuv pulses with, in general, poor coherence properties compared to conventional lasers since the xuv beams result from the direct amplification of the spontaneous emission emitted at one extremity of the medium. High-order harmonics emitted during the nonlinear interaction between an intense ultrashort laser and a gas [3,4] inherit most of the desirable properties of the driving laser in terms of the spatial and temporal coherence but suffer from low conversion efficiencies, resulting in pulse energies typically in the nJ range [5]. A straightforward idea explored in several laboratories around the world [6–8] is to use harmonic radiation to seed the first mentioned sources, thus combining the coherence and flexibility of the harmonics with the high output energy of XFELs or SXRLs.

Seeding requires well-characterized and optimized harmonics. The spatial wave front and spectral content should be of high quality and the energy per unit of bandwidth as high as possible to overcome the spontaneous emission in the amplifier. Many studies have been devoted to characterize the harmonic spectra [9,10] or the spatial profile [11,12] of high-order harmonics, however, often separately. In addition, the harmonic frequency should be matched to a given x-ray plasma spectral line. Previous work uses a high-intensity frequency-chirped fundamental field to spectrally modulate and, to some extent, tune the high-energy part of the high-order harmonic generation spectrum [13,14]. An adaptive spectral filter (DAZZLER) has also been used to provide some tunability of the high-harmonic spectrum [15].

In the present paper, we discuss the characteristics of the harmonic radiation generated in argon around 30 nm by a rather high-energy laser driver with about 100 mJ per pulse in 40 fs at 800 nm wavelength. The spectrum, spatial profile, and energy per pulse are determined and optimized for different focusing geometries and medium lengths. We also show that the spectral bandwidth is considerably increased by simply using a higher laser intensity. We concentrate on the wavelength range between 20 and 40 nm, which can be reached using Ar as generating gas. In Sec. II, we describe the main physics of harmonic generation useful for this work. In Sec. III, we present the experimental method and results.

II. BRIEF SUMMARY OF THE PHYSICS OF HIGH-ORDER HARMONIC GENERATION

A. Single-atom response

The physical origin of harmonic generation can be easily understood by a simple semiclassical picture [16,17]. When an atom is exposed to an intense infrared laser field, the atomic potential is considerably distorted by the strong electric field. An electron from the outer shell may tunnel through the Coulomb barrier and ionize. This electron is then accelerated by the laser field, driven back to the parent ion when the direction of the electric field changes sign, and may recombine to the ground state, thereby emitting a high-energy photon. This energy is equal to the atomic ionization energy (I_p) plus the energy acquired during the acceleration.

---

[*] Also at IFIMUP/IN, Department of Physics, University of Porto, Portugal.

[†] Also at LIXAM, CNRS, Univ Paris-Sud, UMR n 8624, Orsay F-91405, France.

[‡] Also at CEA-Saclay, DSM, Service des Photons, Atomes et Molécules, 91191, Gif-sur-Yvette, France.

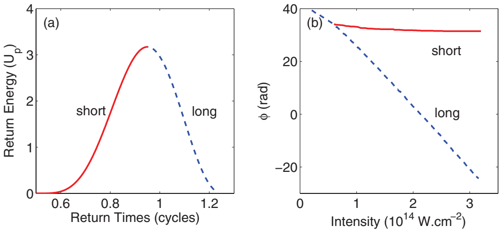

FIG. 1. (Color online) (a) Classical calculation of the kinetic energy of the electron as a function of the return time. (b) Calculation of the intensity dependence of the 19th harmonic phase for the short and long trajectories using the strong-field approximation [19].

This process occurs every half cycle of the driving laser, so that the emitted radiation is periodic with a periodicity equal to 1.3 fs, for a 800 nm fundamental laser field. The spectrum consists of harmonic peaks at odd multiples of the incident frequency. The kinetic energy (E_c) acquired during the electron excursion in the continuum can be calculated using a simple classical calculation, which provides to the experimentalist a useful guide to estimate the available spectral range (W) according to the formula $W=I_p+E_c$. Results of such calculations are presented in Fig. 1(a). The kinetic energy gained is plotted in units of the ponderomotive energy U_p related to the laser field amplitude (E) by $U_p=e^2E^2/4m\omega^2$ where e and m are the charge and mass of electron and ω laser frequencies. U_p (expressed in eV) can also been written as $9.34\lambda^2 I$ where the laser wavelength λ is in μm and the laser intensity I is in 10^{14} W/cm^2 units. For example, for $\lambda=0.8$ μm, $I=2\times 10^{14}$ W/cm^2, the maximum kinetic energy is 38 eV, and the maximum photon energy generated in Ar is about 54 eV. The abscissa in Fig. 1(a) indicates the return time of the electron in units of the laser cycle (2.7 fs). This figure shows that there are two possible electron trajectories leading to the same return energy below the maximum energy. The trajectory with the longer excursion time is called the long trajectory, while that with the shorter excursion time is called short.

The phase accumulated by the electron on these trajectories is transferred to the emitted radiation field. The phase of the harmonic light is therefore not simply related to the phase of the driving laser but also includes an intrinsic phase component that can vary rapidly with laser intensity. This intrinsic phase, which is weakly dependent on the process order, has consequences for both spatial and spectral emission characteristics, and we indicate in Fig. 1(b) its variation with the intensity for the 19th harmonic generated in Ar calculated using the strong-field approximation [18,19]. The two branches refer to the short (red) and long (blue) trajectories. For $I>10^{14}$ W/cm^2, in the so-called plateau region, the intrinsic phase can be approximated by $\Phi_j(\mathbf{r},t)=\alpha_j I(\mathbf{r},t)$, where j refers to the trajectory (short or long). The harmonic field is the coherent sum of two contributions,

$$E_h(\mathbf{r},t)=\sum_{s,l} A_{hj}(\mathbf{r},t)e^{i\omega_h t-i\alpha_j I(\mathbf{r},t)}, \tag{1}$$

where A_{hj} denotes the amplitude of the contribution of the trajectory j to the harmonic field with frequency ω_h. We also indicate in Table I the values of these α coefficients for the short and long trajectories, for a few harmonics discussed in the present work [19]. Assuming a Gaussian distribution for the fundamental and harmonic fields, both in space and time, we can estimate the divergence and spectral bandwidth of the harmonic field according to

$$\theta_j=\frac{\lambda_h}{\pi w_h}\sqrt{1+4\alpha_j^2 I_0^2\frac{w_h^4}{w_f^4}}, \tag{2}$$

and

$$\Delta\lambda_j=\frac{\lambda_h^2}{\pi c\tau_h}\sqrt{1+4\alpha_j^2 I_0^2\frac{\tau_h^4}{\tau_f^4}}. \tag{3}$$

λ_h, w_h, and τ_h denote the wavelength, beam waist, and pulse width of the harmonic field and w_f, τ_f, and I_0 are the beam waist, pulse width, and peak intensity of the fundamental field. If the second terms in the roots are negligible, the harmonic field is Fourier transform limited in the time domain and diffraction limited in space. In general, phase effects lead to the deviation from the Fourier limit, especially for high intensities and long trajectories. Upper values for $\theta_j(j=s,l)$ and $\Delta\lambda_j$ are given in Table I using $w_f=150$ μm, $\tau_f=40$ fs, and $I_0=1.5\times 10^{14}$ W/cm^2, representing typical experimental values and assuming $w_h/w_f=\tau_h/\tau_f=1$. In reality, these ratios are slightly below one and decrease with the process order since high-order harmonics require higher laser intensity to be generated and are emitted over a smaller diameter and shorter pulse duration. The values indicated in Table I might

TABLE I. Useful parameters for the 19th to the 31st harmonics in Ar. The intensity of the laser field used for the calculation is 1.5×10^{14} W/cm^2 and the unit for α is 10^{-14} W^{-1} cm^2.

Order	19	21	23	25	27	29	31
λ_h (nm)	42.1	38.1	34.8	32.0	29.6	27.6	25.8
α_s	−1.0	−1.8	−2.7	−3.8	−5.1	−6.9	−9.8
α_l	−22.9	−22.2	−21.5	−20.5	−19.2	−17.5	−14.8
θ_s (mrad)	0.3	0.4	0.6	0.8	1.0	1.2	1.6
θ_l (mrad)	6.1	5.4	4.8	4.2	3.6	3.1	2.4
$\Delta\lambda_s$ (nm)	0.2	0.2	0.2	0.3	0.4	0.5	0.5
$\Delta\lambda_l$ (nm)	3.2	2.6	2.1	1.7	1.4	1.0	0.8

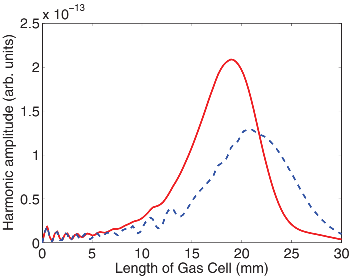

FIG. 2. (Color online) Phase matching contribution to the harmonic intensity as a function of cell length for short (red solid) and long (blue dashed) trajectories.

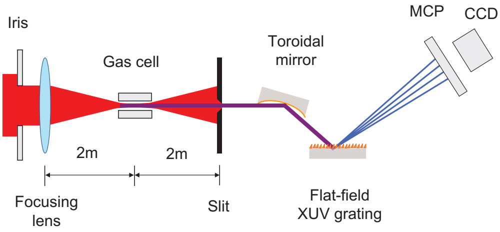

FIG. 3. (Color online) Experimental setup.

be used as a guide to estimate upper values for the spatial and spectral widths of the HHG radiation.

B. Propagation

The optimization of the harmonic emission requires not only a strong single-atom response but also that all of the atoms in the medium emitted in phase. For the sake of simplicity, we here give a simple description of propagation using a one-dimensional approximation, along the propagation axis (z). More advanced calculations accounting also for off-axis effects will be presented in Sec. III. Phase matching is realized when the variation in the difference between the phase of the qth harmonic field generated in the medium and that of the polarization driving it, equal to

$$\delta\Phi_q(z,t) = \int \Delta k_q(z',t)dz' + q \arctan(z/z_R) + \alpha_j I(z,t), \tag{4}$$

is minimized over the medium length [20]. In the right-hand side of Eq. (4), the first term denotes the influence of dispersion, which includes two opposite contributions, from the neutral medium and the free electrons. The second term indicates the influence of focusing (z_R denoting the Rayleigh length of the fundamental beam). Finally, the third term is the single-atom phase described above, which strongly depends on the trajectory. For loose focusing geometries, in general, the contribution of dispersion effects is stronger than the geometrical and single-atom phase variations, both for a neutral medium and for a strongly ionized medium. The first condition to achieve phase matching is to (approximately) cancel the neutral atom and free-electron dispersion, which is achieved for a degree of ionization of the medium of approximately 7% in argon. The phase variation due to the geometrical phase and to the single-atom phase (especially in the case of the long trajectory) needs to be included for a correct description of phase matching [21,22]. In addition, the absorption in general limits the conversion efficiency [23].

Figure 2 shows the results of calculations performed for the 21st harmonic in argon using a one-dimensional model described in [24], including all of the phase terms in Eq. (4), and consisting in summing all of the microscopic contributions over a certain length. The red and blue curves refer to the contribution of the short and long trajectories considered separately in the calculation, with the same single-atom response amplitude. The oscillations observed for short length media indicate that phase matching is not realized and that the field generated at some location in the medium is canceled by that generated in another location. The quadratic increase from $L=12$ mm is characteristic of phase matching. The harmonic yield saturates and eventually decreases when the absorption limit is reached. The phase variation for the long-trajectory contribution leads to a shift in the optimal medium length. The curves shown in Fig. 2 depend only weakly on the process order; for example, the short trajectory contribution of the 15th (respectively, 25th) harmonic is maximized for $L=16$ mm (respectively, $L=20$ mm). These results obtained with a one-dimensional model might change a little when generalizing to three dimensions, when considering other laser intensities and gas pressures. Our aim here was to illustrate the physics of phase matching of high-order harmonics rather than simulate a realistic experimental situation.

The conclusion of our model is that efficient, absorption-limited, and phase matching of high-order harmonics may be achieved by using sufficiently long media. Another way would be to have a cell with a length corresponding to the absorption length (or equal to a few times the absorption length) and to locate it at the position where the intensity is such that phase matching can be achieved. Experimentally, the first solution is much easier. Other effects, such as a spatiotemporal modification of the fundamental field [25], leading in particular to defocusing, could also favor phase matching of high-order harmonic generation in long media [26] (see also the discussion below).

III. EXPERIMENTAL METHOD AND RESULTS

A. Measurement of spatial and spectral profiles

Our experimental setup is shown in Fig. 3. The laser is an amplified Ti:sapphire 10 Hz system delivering 40 fs pulses around 800 nm with an energy up to 1 J. The results presented below are obtained with only a fraction of this energy less than 100 mJ. Furthermore, the 50-mm-diameter beam is apertured down by an iris with variable diameter (with a diameter typically between 11 and 16 mm), so that only about a few mJ infrared energy is actually sent into our ex-

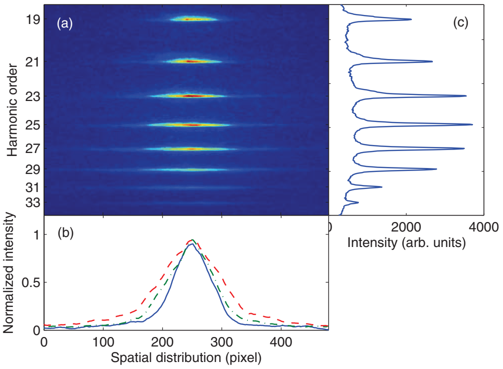

FIG. 4. (Color online) (a) Experimental measurement using a 21 mm Ar gas cell and a fundamental intensity of $I=10^{14}$ W/cm^2; (b) spatial profile of the 19th (blue solid), 23rd (green dash dotted), and 27th (red dashed) harmonic. (c) Spatially integrated spectrum.

perimental setup. The beam is focused by a lens with 2 m focal length into a gas cell with 1 mm transverse diameter and variable length (from 3 to 20 mm). The harmonic spectra are detected by a flat-field xuv spectrometer, with a 100 μm entrance slit, located at approximately 2 m from the gas jet. An xuv microchannel plate (MCP) combined with a charge-coupled device camera is used to capture the final image. In contrast to many previous measurements [11,12], we do not image the harmonic source but a slice of its profile at a relatively long distance (2 m) from the source, which gives us the possibility to measure the spatial profile in the far field (and therefore the divergence) of the beam [27,28]. Our spectral resolution is estimated to be 0.2 nm.

A typical experimental spectrum is shown in Fig. 4. Harmonics are shown from the 19th to the 33rd, corresponding to a spectral range of 42–24 nm or in energy 29–51 eV. Spatial profiles are shown in the horizontal direction, while the vertical one shows spectra. Figure 4(b) shows some spatial profiles, while the spatially-integrated spectrum is presented in (c). These measurements show evidence for contributions from the short trajectory, leading to a narrow collimated beam and also from the (weaker) long trajectory, with much higher divergence. In the cut-off region, both contributions merge together.

In order to avoid any influence of the spectrometer collecting optics on the harmonic spatial profile, we have measured it directly by taking an image with the MCP at about 2 m from the gas cell. The fundamental field and the low-order harmonics (up to the 11th) were removed by an absorption in a 200-nm-thin Al filter. A typical result is shown in Fig. 5. A relatively narrow peak is superposed on a broad pedestal, which can be attributed to the main two quantum paths responsible for harmonic generation. The harmonic beam diameter could be measured by comparing with the diameter of the aperture on which the filter was mounted and which could be observed on the MCP. The full width at half maximum is 1.4 mm and the corresponding beam divergence is 0.7 mrad. This agrees with the predictions presented above

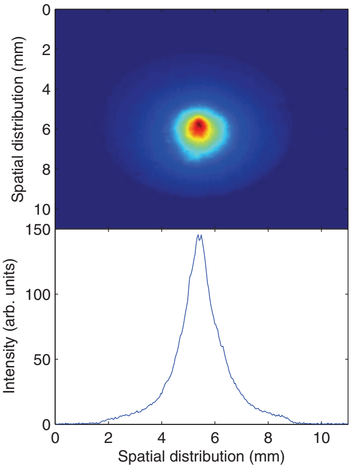

FIG. 5. (Color online) Spatial profile of the total harmonic yield transmitted through the Al filter measured at 2 m from the 15 mm gas cell. The infrared beam was focused just at the beginning of the cell. The aperture was 14 mm.

(Table I) for the (dominant) short trajectory and for the strong 23rd–25th harmonics. The ratio between the short- and long-trajectory contributions is affected by the position of the focus of the infrared beam in the gas cell. In agreement with previous work [21], we find that the short trajectory is enhanced compared to the long one when the focus position is before the gas cell.

B. Measurement of the harmonic pulse energy

The pulse energy of the high-order harmonic radiation was measured by using a calibrated xuv photodiode, with good sensitivity from 1 eV to 6 keV. The diode could be moved under vacuum before the flat-field xuv spectrometer, so that we could measure the energy and the corresponding spectrum within the same series of measurements. Two 200 nm Al filters were needed to block the fundamental beam. The number of the electrons N_e generated from the photodiode is the integral of the measured current. The number of the photons at each harmonic frequency is obtained through the equation

$$N_e = \sum_q \eta_q t_q N_q, \tag{5}$$

where N_q denotes the number of photons generated at the qth harmonic frequency, t_q is the transmission by the Al filters and η_q is the quantum efficiency of the photodiode for the qth harmonic. The absorption from the Al filters can be estimated by calculating the transmission function of Al, accounting for the effect of a thin layer of oxide, which unfortunately reduces the transmission and introduces an uncertainty in the energy determination. Figure 6 shows the transmission of 200 nm Al (blue line), as well as that of 200 nm Al, plus 20 nm oxide (10 nm on each side), which is a

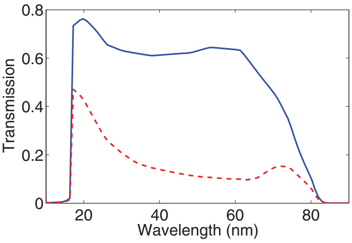

FIG. 6. (Color online) Calculated transmission function for 200 nm Al filter (blue solid) and with 10 nm oxidation layer on each side (red dashed).

rough estimation of the oxide layer on the filters used in this experiment [29]. From the relative ratios between the generated harmonics obtained from spectral measurements, the number of photons per harmonic, the pulse energy, as well as the conversion efficiency can be deduced. Results of measurements performed in optimized conditions [with a 19-mm-length gas cell (see below)] are presented in Table II.

C. Optimization of the output energy by varying the cell length

Figure 7(a) shows the variation in the harmonic energy as a function of cell length for a few harmonics. The focus was located at the center of the cell. The saturation effect observed is attributed to absorption, which is more important for the low-order harmonics than for the high-order ones. Figure 7(b) shows the 23rd harmonic spatial profile obtained at $\sim 2\times 10^{14}$ W/cm^2, with gas cells of different lengths and an aperture before the lens equal to 13 mm. The central part of the angular profile, which reflects the contribution from the short trajectory, is approximately constant with order and with cell length, on the order of 1 mrad.

Increasing the cell length results in an increased harmonic energy as well as the appearance of the long-trajectory contribution, with higher divergence. The predictions of our model (see Fig. 2) agree quite well with the experimental observation, showing a saturation for medium lengths of 20 mm and an increase in the contribution of the long trajectory as the length increases. The latter effect is of interest for seeding applications since the contribution of the long trajectory can be made spectrally broader at high laser intensity, thus, providing increased possibility to match the gain profile of an amplifier, as explained below.

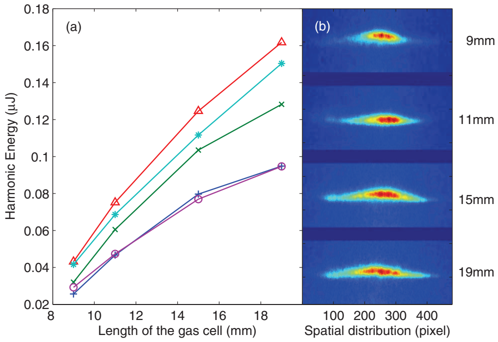

FIG. 7. (Color online) (a) Harmonic energy as a function of cell length for the 13th (line with plus), 17th (line with x mark), 21st (line with triangle), 23rd (line with star), and 27th (line with circle) order. (b) Spatial distribution of 23rd harmonic for different gas cell lengths.

D. Increasing the spectral range between consecutive harmonics

Spectra obtained from two different fundamental energies by changing iris diameters are shown in Fig. 8. The harmonic spectra get broadened as the input energy increases more than the prediction of Eq. (3) for a single trajectory. In addition, interference structures appear. This complicated structure appears in connection with an ionization-induced spatiotemporal reshaping of the laser beam, which improves the phase matching conditions for the long trajectory. The short trajectory is well phase matched both before and after the reshaping, and we therefore see spectral interference between the contributions from both trajectories [30]. Similar structures have been observed in previous work [27,28] and interpreted in terms of interference between the contribution of the two (short and long) trajectories, without—however—explaining the reason for both contributions to be of the same strength.

Our interpretation is supported by theoretical calculations including both the microscopic and macroscopic responses of the argon gas to the intense laser pulse. The results were calculated via the coupled nonadiabatic solutions of the time-dependent Schrödinger equation, within the strong-field approximation [17], and the Maxwell wave equation. Our approach is described in detail in [20]. As initial conditions for the calculation, we use similar parameters as the experiment, in terms of peak intensity, duration, and focusing conditions for the laser beam, and density and length of the argon cell.

TABLE II. Optimized high-order harmonic energy and conversion efficiency.

Harmonic order	17	19	21	23	25	27
Transmission	0.12	0.13	0.15	0.16	0.19	0.21
Photon number ($\times 10^{10}$)	3.03	2.98	3.10	2.63	1.60	1.41
Energy (μJ)	0.13	0.14	0.16	0.15	0.10	0.09
Efficiency ($\times 10^{-6}$)	6.8	7.5	8.6	8.0	5.3	5.0

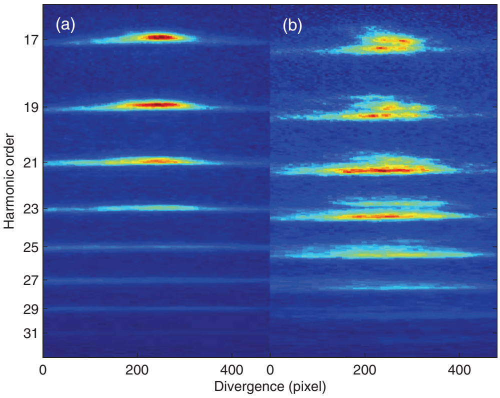

FIG. 8. (Color online) Harmonic spectra at two different intensities measured to be (a) 2×10^{14} W/cm^2 and (b) $\sim5\times10^{14}$ W/cm^2. A 21 mm gas cell was used and the focus point of the infrared beam was in the middle of the cell. Note the significant blue shift of the spectral distribution at high intensity.

The calculated far-field spatiospectral profiles of harmonics 17–21 are shown in Figs. 9(a) and 9(b). At low intensity, the very loose focusing conditions strongly favor phase matching of the short trajectory, and the resulting harmonics are spectrally narrow and well behaved. The contribution from the long trajectory in these conditions can barely be seen in Fig. 9(a) as a faint halo around the 19th harmonic, most prominent on the low-frequency side and at divergences above 0.6 mrad. At high intensity, the harmonic spectra are much broader, exhibit interference fringes, and are blueshifted relative to the low-intensity case. As mentioned above, the interference is the result of both short- and long-trajectory contributions being well phase matched by the strongly reshaped laser beam. Figures 9(c) and 9(d) show the spatiotemporal profile of the laser beam in the near field, at the end of the argon medium. The high-intensity beam has undergone violent spatiotemporal reshaping which results in defocusing, strong blueshifting on axis, and the overall change in shape where the laser envelope reaches its maximum at different times for different radii. The reshaping happens after a few mm of propagation and then does not change much through the remainder of the medium. In the calculations, we see a strong increase in the long-trajectory contribution around the propagation distances where the reshaping sets in, with a significant component on axis. The short- and long-trajectory contributions thus interfere in the far field, leading to the two or three horizontal stripes observed in Figs. 9(b) and 8(b).

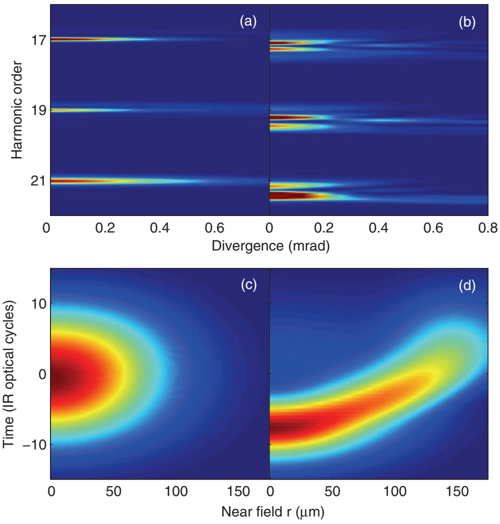

FIG. 9. (Color online) Calculated far-field spatial profile of different harmonic for two different peak intensities (a) 1×10^{14} W/cm^2 and (b) 3.3×10^{14} W/cm^2. Spatiotemporal distribution of corresponding fundamental beam at the exit of the medium (c) and (d).

This effect provides an easy way for covering a larger spectral range, which is very important for seeding x-ray laser plasmas. For example, the 25th harmonic (32 nm) is close to the x-ray lasing lines of 31.2 nm (Ne-like Sc), 32.6 nm (Ne-like Ti), and 32.8 nm (Ni-like Kr) and can be broadened to reach these lines simply by increasing the laser intensity. It has been suggested previously [13,14] that harmonics could be tuned by changing the chirp of the fundamental field. In such an experiment, several parameters are varied at the same time: chirp, pulse duration, and laser intensity. We believe that the main effect is due to the variation in the laser intensity. In addition, the fundamental chirp may induce additional or reduced spectral broadening depending on the sign of the chirp.

IV. CONCLUSION

In this work, we have studied the spectral and spatial properties of high-order harmonics generated in argon gas. The absolute value of the energy emitted per harmonic pulse was estimated in optimized conditions. We found that the use of long gas cells (20 mm) led to higher energies and more collimated xuv beams. Large spectral bandwidths, close to the interval between consecutive harmonics, could be achieved by increasing the intensity of the infrared beam in the gas cell leading to an improved phase matching of the long trajectory.

ACKNOWLEDGMENTS

This research was supported by the European Union project NEST-ADVENTURE under Grant No. 012843-2 TUIXS, the Marie Curie actions EST MAXLAS, IIF OHIO, and EIF Attotech, the Knut and Alice Wallenberg Foundation, the Swedish Science Council, and the U.S. National Science Foundation through Grant No. PHY-044923. We thank B. Schütte, T. Eberle, J. Klemmer, F. Geier, and E. Pourtal, for their help in some early stage of this experiment.

[1] J. Feldhaus, J. Arthur, and J. B. Hastings, J. Phys. B **38**, S799 (2005).
[2] D. L. Matthews *et al.*, Phys. Rev. Lett. **54**, 110 (1985).
[3] A. McPherson *et al.*, J. Opt. Soc. Am. B **4**, 595 (1987).
[4] M. Ferray *et al.*, J. Phys. B **21**, L31 (1988).
[5] Harmonic energies per pulse on the order of a μJ have been reached by several groups; see, for example, J.-F. Hergott *et al.*, Phys. Rev. **66**, 021801 (2002); E. Takahashi *et al.*, J. Opt. Soc. Am. **20**, 158 (2003).
[6] P. Zeitoun *et al.*, Nature (London) **431**, 426 (2004).
[7] Y. Wang *et al.*, Nat. Photonics **2**, 94 (2008).
[8] G. Lambert *et al.*, Nat. Phys. **4**, 296 (2008).
[9] L. Nugent-Glandorf, M. Scheer, M. Krishnamurthy, J. W. Odom, and S. R. Leone, Phys. Rev. A **62**, 023812 (2000).
[10] H. T. Kim *et al.*, J. Phys. B **37**, 1141 (2004).
[11] J. W. G. Tisch, R. A. Smith, J. E. Muffett, M. Ciarrocca, J. P. Marangos, and M. H. R. Hutchinson, Phys. Rev. A **49**, R28 (1994).
[12] P. Salières *et al.*, J. Phys. B **27**, L217 (1994).
[13] H. T. Kim, D. G. Lee, K. H. Hong, J. H. Kim, I. W. Choi, and C. H. Nam, Phys. Rev. A **67**, 051801(R) (2003).
[14] Z. Chang, A. Rundquist, H. Wang, I. Christov, H. C. Kapteyn, and M. M. Murnane, Phys. Rev. A **58**, R30 (1998).
[15] D. H. Reitze *et al.*, Opt. Lett. **29**, 86 (2004).
[16] P. B. Corkum, Phys. Rev. Lett. **71**, 1994 (1993).
[17] M. Lewenstein, P. Balcou, M. Y. Ivanov, A. L'Huillier, and P. B. Corkum, Phys. Rev. A **49**, 2117 (1994).
[18] M. Lewenstein, P. Salieres, and A. L'Huillier, Phys. Rev. A **52**, 4747 (1995).
[19] K. Varju *et al.*, J. Mod. Opt. **52**, 379 (2005).
[20] M. B. Gaarde, J. L. Tate, and K. J. Schafer, J. Phys. B **41**, 132001 (2008).
[21] P. Salières, A. L'Huillier, and M. Lewenstein, Phys. Rev. Lett. **74**, 3776 (1995).
[22] F. Lindner, W. Stremme, M. G. Schatzel, F. Grasbon, G. G. Paulus, H. Walther, R. Hartmann, and L. Struder, Phys. Rev. A **68**, 013814 (2003).
[23] E. Constant, D. Garzella, P. Breger, E. Mevel, C. Dorrer, C. Le Blanc, F. Salin, and P. Agostini, Phys. Rev. Lett. **82**, 1668 (1999).
[24] T. Ruchon *et al.*, New J. Phys. **10**, 025027 (2008).
[25] M. B. Gaarde, M. Murakami, and R. Kienberger, Phys. Rev. A **74**, 053401 (2006).
[26] Y. Tamaki *et al.*, Phys. Rev. Lett. **82**, 1422 (1999).
[27] E. Brunetti, R. Issac, and D. A. Jaroszynski, Phys. Rev. A **77**, 023422 (2008).
[28] H. Xu, H. Xiong, Z. Zeng, Y. Fu, J. Yao, R. Li, Y. Cheng, and Z. Xu, Phys. Rev. A **78**, 033841 (2008).
[29] K. Varjú *et al.*, Laser Phys. **15**, 888 (2005).
[30] A. Zair *et al.*, Phys. Rev. Lett. **100**, 143902 (2008).

PAPER IX

Single-shot holography using high-order harmonics

J. Schwenke, A. Mai, M. Miranda, X. He, G. Genoud, A. Mikkelsen, S.-G. Pettersson, A. Persson, and A. L'Huillier.

J. Mod. Opt. **106**, 2723–2730 (2008).

Journal of Modern Optics
Vol. 55, No. 16, 20 September 2008, 2723–2730

Single-shot holography using high-order harmonics

J. Schwenke[a,b]*, A. Mai[a], M. Miranda[a], X. He[a], G. Genoud[a], A. Mikkelsen[a], S.-G. Pettersson[a], A. Persson[a] and A. L'Huillier[a]

[a]*Deparment of Physics, Lund University, Lund, Sweden;* [b]*MAX-lab, Lund University, Lund, Sweden*

(*Received 23 April 2008; final version received 6 August 2008*)

This work demonstrates single-shot holography with ultrashort XUV pulses. The pulses are generated by high-harmonic generation in an Ar gas cell and focused to produce a strongly divergent reference beam suitable for in-line holography of micrometer size objects. The achieved intensity of the high-order harmonics in the XUV regime is sufficient for single-shot holography with good signal-to-noise ratio. A numerical algorithm is applied to reconstruct real images from the recorded holograms, which also includes an iterative process to reduce the twin-image blurring. Holograms and reconstructed images of microscope tips are presented and a description of the algorithm is given.

Keywords: holography; high-harmonic generation; time-resolved imaging

1. Introduction

Coherent light sources in the XUV and X-ray ranges are being actively developed for imaging objects of nanometer size in various conditions. An additional interesting feature is the combination of spatial and temporal resolution. This often requires intense short pulses, in order to perform single-shot time-resolved measurements. These requirements are fullfilled by free electron lasers, as beautifully shown in experiments performed at FLASH in Hamburg [1–3]. Single-shot experiments were also recently carried out at BESSY in Berlin and SSRL at Stanford University [4].

High-order harmonics generated when an intense laser interacts with a gas target constitute another interesting source with the advantage of being table-top and affordable in university laboratories. Using Ar or Xe gas, pulse energies of up to a hundred nJ between 30 and 50 nm can be achieved. High-order harmonics are now being developed for time-resolved coherent-imaging applications by several groups [5–8]. The energy range varies from the ultraviolet to the soft X-ray region (>100 eV) and pulses can be as short as a few hundred attoseconds.

In the present work we describe a coherent imaging setup developed in Lund, based upon digital in-line holography [9]. The coherent light, produced by high-order harmonic generation in Ar gas, is both spectrally selected and tightly focused with a Schwarzschild objective, manufactured with multilayer mirrors reflecting 38 nm. Our optimized harmonic

---

*Corresponding author. Email: jorg.schwenke@maxlab.lu.se

ISSN 0950–0340 print/ISSN 1362–3044 online
© 2008 Taylor & Francis
DOI: 10.1080/09500340802398236
http://www.informaworld.com

generation setup allows us to obtain high quality single shot holograms. An algorithm has also been developed to recover amplitude and phase of the object. This article is organized as follows. In Section 2 the experimental setup is described in detail, while in Section 3 our reconstruction algorithm is presented. The reconstructed images are shown and discussed in Section 4.

2. Experiment

The experimental setup is shown in Figure 1. The incident infrared laser beam at 800 nm is provided by a low energy (100 mJ) arm of a powerful 40 TW laser system, operating at 10 Hz repetition rate and with pulses of 40 fs duration. An iris is used to optimize the HHG efficiency. In general the beam is clipped to a diameter of 12 mm, so that 10 mJ are actually used for the nonlinear conversion. A lens with a focal length of 2 m focuses pulses into the gas target, which is a cylindrical cell with variable length. The diameter of the gas cell is 1 mm, and a cell length of 15 mm was used in this experiment. The cell is filled with Ar gas through a piezo-driven injection system synchronized with the incident laser pulse. The harmonic beam created is emitted along the laser axis, with a divergence of 0.7 mrad. The infrared pulses are blocked after the gas cell by a 200 nm-thick Al filter. About 2 m after the gas cell the beam is focused by a Schwarzschild objective, which includes two spherical mirrors, convex and concave, centred at the same point. The mirrors are coated with multiple layers to select a narrow bandwidth around the 21st harmonic (38 nm). The bandwidth is, unfortunately, large enough to let through small fractions of the 19th and 23rd harmonics as well. The maximum reflection, which occurs at $\lambda = 37$ nm, is about 40%. The focal length of the objective is 26.9 mm. The setup is used off-axis in order to reduce intensity loss due to back reflection. The focal point is located at a distance of 48 mm behind the objective, and the harmonic beam is divergent with a half angle $\theta = 75$ mrad. A micro channel plate (MCP) is used to record the intensity distribution of the divergent beam. The MCP is coupled to a phosphor screen, imaged by a CCD camera. If an object is placed into the divergent beam, interference occurs between the direct beam and parts of the beam diffracted from the object, and an interference pattern can be observed and recorded on the MCP. Based on the divergence of the beam, and the distance and dimensions of the detector, the theoretical resolution limit of the setup is 250 nm.

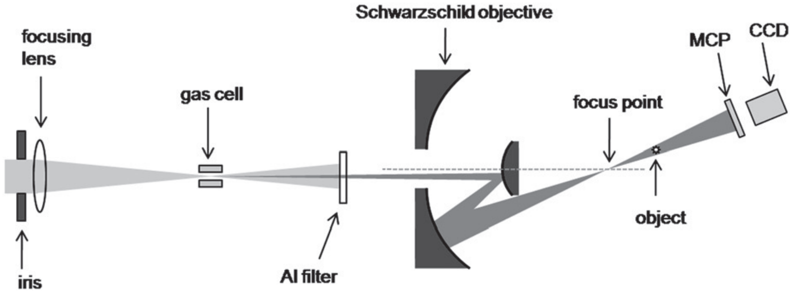

Figure 1. Experimental setup.

The method presented here requires a strongly divergent beam to achieve a magnified interference pattern. The Schwarzschild objective allows for tight focusing in a compact design and was therefore chosen over conventional spherical mirror setups. Objects are mounted on a motorized translation stage that allows for accurate positioning. In these experiments, tungsten tips for a scanning tuneling microscope (STM) [10] were used. Figure 2 shows recorded holograms after background subtraction. The left image shows a straight tip, where just a single shot of the setup was used. The middle image shows the same tip, but here the hologram was averaged over a large number of shots. Figure 2(*c*) shows a deformed tip, also averaged over many shots. In all three cases, the background was averaged over multiple images recorded in the absence of the object.

3. The reconstruction algorithm

The recorded holograms show the interference of the direct beam (or reference beam) and that diffracted by the object. According to the Huygens–Fresnel principle, each point in

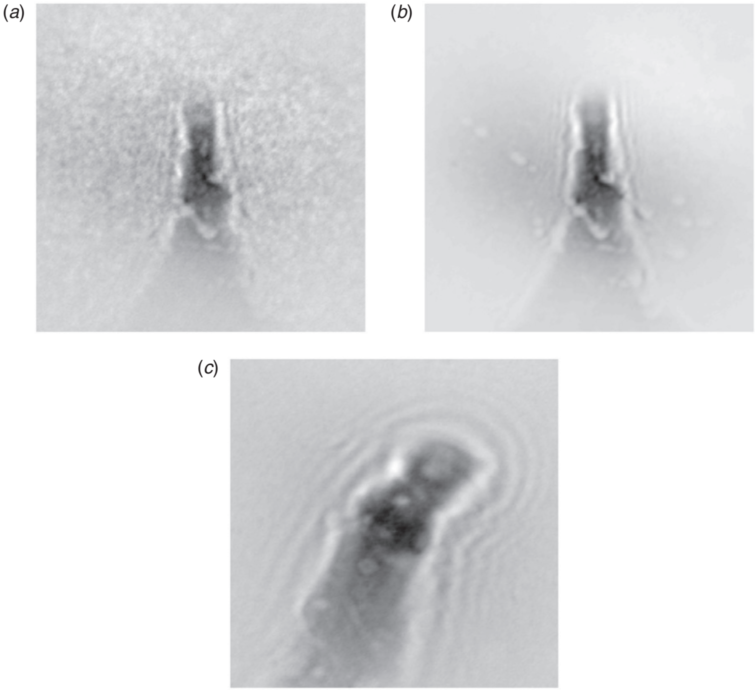

Figure 2. Recorded holograms of tungsten mircoscope tips. (*a*) Straight tip, single-shot hologram after subtraction of an averaged background. (*b*) Straight tip and (*c*) deformed tip, multiple shot holograms after subtraction of an averaged background.

the object plane is the origin of a spherical wave contributing to the interference pattern in the hologram plane. The electromagnetic field at a point (x_h, y_h) in the hologram plane can be calculated from the field in the object plane by adding up the individual waves at points (x_o, y_o), as stated by the Fresnel–Kirchoff integral:

$$E_H(x_h, y_h) = \frac{i}{\lambda}\int_S E_O(x_o, y_o)\frac{\exp(-ikr)}{r}\cos\theta\,dx_o\,dy_o, \tag{1}$$

where r is the distance between the points with the angle θ to the normal of the planes. The integration is carried out over the area of the object, S. If the angle θ is small, the paraxial approximation can be used, which greatly simplifies the integration in Equation (1). Unfortunately, this is not the case in our configuration since the harmonic beam is focused by the Schwarzschild objective and therefore divergent after the focus. Our numerical approach introduces a third plane, called the far field plane, which is at a large distance from the other two planes. The paraxial approximation is used between the far field plane and the object or hologram planes. Fast Fourier Transformation techniques are used to integrate Equation (1), where the harmonic beam is approximated by a Gaussian profile [9]. This method allows us to simulate a hologram from an object, as well as to reconstruct the electromagnetic field in the object plane from a recorded hologram.

In our experiment, the interference pattern on the MCP is recorded as an intensity distribution, so that the phase information is lost. After subtracting a background image (recorded in the absence of the object), the method described above can be used to obtain the field distribution in the object plane. However, since no phase information was recorded, the reconstructed image is blurred due to the twin image problem inherent to the in-line geometry [11]. We therefore apply an iterative algorithm to recover the phase of the hologram and thereby reduce the blurring of the image. This algorithm was inspired from Latychevskaia and Fink [12].

The first iteration loop begins with the recorded intensity distribution $I(x_h, y_h)$. This is the square of the amplitude of the electromagnetic field in the hologram plane, $A(x_h, y_h) = [I(x_h, y_h)]^{1/2}$. To build a hologram, we combine the amplitude with the phase of the reference wave in the hologram plane, $\phi_{H,\mathrm{ref}}$:

$$E_H(x_h, y_h) = A(x_h, y_h)\exp[i\phi_{H,\mathrm{ref}}(x_h, y_h)]. \tag{2}$$

This complex field is used as the input data for the reverse propagation, by which the total electromagnetic field $E_O(x_o, y_o)$ in the object plane is found. The total field can be described as

$$E_O(x_o, y_o) = t(x_o, y_o)\exp[i\phi_{O,\mathrm{ref}}(x_o, y_o)], \tag{3}$$

where $t(x_o, y_o)$ is a complex transmission function, and $\phi_{O,\mathrm{ref}}(x_o, y_o)$ is the phase of the reference wave in the object plane. We remove the phase of the reference wave by multiplying with the complex conjugate, and rewrite the transmission function as

$$t(x_o, y_o) = E_O(x_o, y_o)\exp[-i\phi_{O,\mathrm{ref}}(x_o, y_o)] = [1 - a(x_o, y_o)]\exp[i\phi_O(x_o, y_o)]. \tag{4}$$

The real part on the right side of the equation contains the absorption $a(x_o, y_o)$, while the complex part describes the phase shift $\phi_O(x_o, y_o)$ induced by the transmission through the object. We now impose a constraint on the absorption, namely that it must not be negative. For the expression $[1 - a(x_o, y_o)]$ we therefore consider values larger than 1 to be undesirable contributions of the twin image and consequently replace them by 1. This gives the adjusted transmission function $a'(x_o, y_o)$, which is recombined with the phase shift to form a new object:

$$[1 - a'(x_h, y_h)]\exp[i\phi_O(x_o, y_o)] = t'(x_o, y_o). \tag{5}$$

This object is used to simulate a hologram,

$$E_{H,sim} = A_{sim}(x_h, y_h)\exp[i\phi_{sim}(x_h, y_h)], \tag{6}$$

from which the simulated phase $\phi_{sim}(x_h, y_h)$ is extracted. This concludes the first iteration loop. For all consecutive iterations, the initial hologram is composed of the recorded diffraction pattern and the simulated phase from the last iteration (rather than the phase of the reference wave). Our reconstruction algorithm can be summarized as follows:

(1) A hologram is composed of the experimentally recorded intesnsity, and phase information, which is acquired by extraction from a simulated hologram. For the first reconstruction, the phase of the reference wave is used instead.
(2) The Fresnel–Kirchhoff algorithm is used to find the total field in the object plane, and the field is divided by the reference wave, to obtain the transmission function of the object.
(3) The absorption function is extracted, and adjusted so that negative absorption does not occur. The resulting function is recombined with the phase to form a new transmission function and thus a new object.
(4) The new object is propagated forward to the hologram plane to simulate a hologram. The phase of this simulated hologram is used for the next iteration.

The iteration process in theory completely removes the blurring of the reconstructed image, and at the same time causes the absorption and phase properties of the object to develop towards their true values. However, when applied to experimentally recorded holograms, the performance of the iteration process is limited by the stability of the light source. In our setup, beam direction and intensity vary from shot to shot which impairs background subtraction. As a result, the reconstructed transmission function in the object plane is distorted, and clean separation and removal of twin image contributions becomes difficult. In this work, we have adjusted the constraint to values lower than 1 in order to counteract the effects of intensity and beam position variation.

4. Reconstruction of experimental holograms

Figure 3 shows the results of the reconstruction algorithm on holograms of a straight tungsten tip. The hologram in Figure 2(*a*) is obtained by subtracting a single shot image with a background averaged over 200 shots. The first reconstruction from this hologram yields Figure 3(*a*). The shape of the tip is clearly visible, but the image is blurred, and fringes are still present. Figure 3(*b*) shows the object after application of the iteration algorithm (100 iterations). Even though the blurring is not removed completely, the image is of higher quality. The details at the end of the tip have a higher contrast, while the fringes have almost disappeared. The FWHM of the tip profile, which gives an upper estimate of the spatial resolution, is measured to be 4.3 µm. The second row of Figure 3 shows the reconstruction of a hologram averaged over 200 images (Figure 2(*b*)). Compared with the single-shot hologram in Figure 2(*a*), the noise is much lower, and the fringes have a better contrast to the background. The first reconstruction, Figure 3(*c*), already shows the object clearly, although fringes are visible on both sides of the tip. Figure 3(*d*) shows the object after 100 iterations. Again, the image quality is improved, but still some blurring remains, and the aforementioned fringes are also still visible. The width of the profile is now 4.7 µm. The limited effect of the iterative process can be partly attributed to the usage of multiple shot backgrounds. Since the beam direction changes slightly from shot to shot, the averaged background does not accurately match the hologram.

Figure 4 shows the hologram (Figure 4(*a*)) and reconstruction (Figure 4(*b*), 100 iterations) of a deformed tungsten tip, as well as a scanning tuneling microscope (STM) image (Figure 4(*c*)) of the same tip in a similar orientation. As can be seen on the STM-image, the end of the tip is bent to a hook. The overall shape can be readily identified on the reconstructed image, but the hook is very blurred. In this case, the object blocks

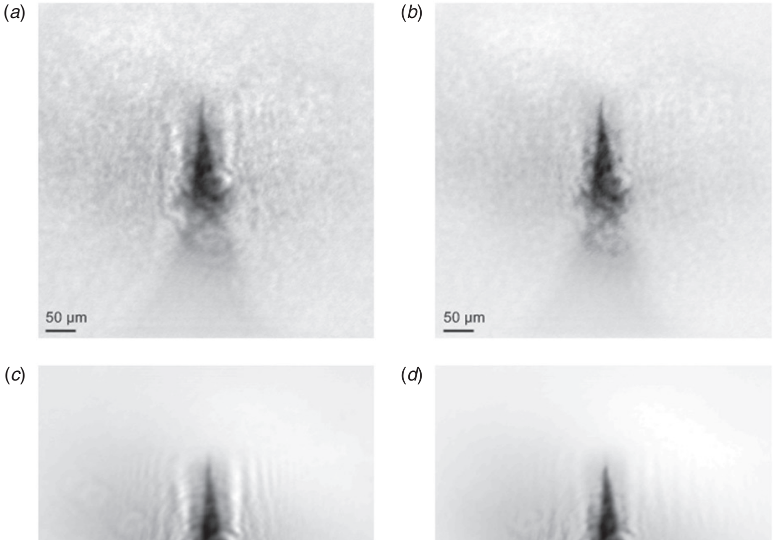

Figure 3. Reconstructed images of a straight microscope tip with and without iteration. (*a*), (*b*) Reconstructed from a single-shot hologram, and (*c*), (*d*) reconstructed from an averaged hologram.

a larger area of the beam, which reduces the intensity and the contrast on the detector. Figure 5(*a*) shows a single-shot hologram of the same object, and Figure 5(*b*) the reconstruction thereof (100 iterations). Here the single-shot image looks slightly better even than the multi-shot image.

The spatial resolution is primarily limited by the digital capturing of the hologram, as the CCD does not resolve the maximal resolution displayed by the MCP. As a result, smaller fringes in the outer areas of the hologram are not observed. The situation can be improved by using a back-illuminated X-ray CCD instead of the MCP setup, and also by adjusting the ratio between object beam and reference beam, which affects the contrast of the fringes. Another factor is possibly the bandwidth of the focusing optics, where the transmission of multiple harmonic orders results in superimposed (and therefore blurred) diffraction patterns. It is, however, still possible to reconstruct the object with a single

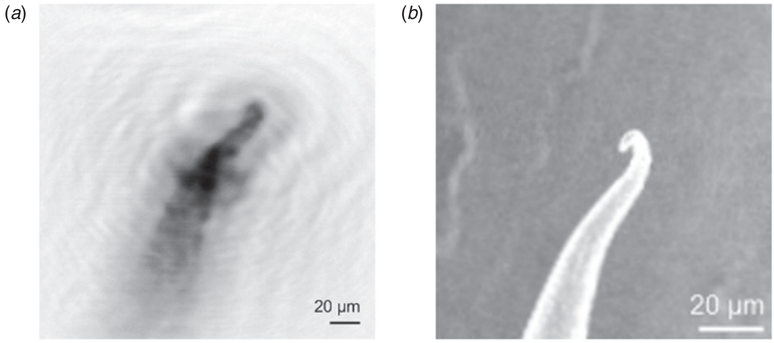

Figure 4. Images of a deformed microscope tip, hologram averaged over multiple shots: (*a*) object after reconstruction, and (*b*) STM-image for comparison.

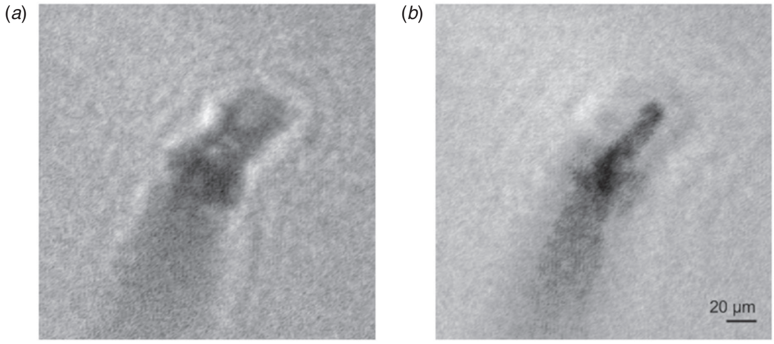

Figure 5. Hologram and reconstructed image of a deformed microscope tip. (*a*) Single-shot hologram, and (*b*) reconstructed image after 100 iterations.

wavelength and thereby select to some extent the image obtained with the dominant harmonic order. Lastly, the beam stability needs to be improved in order to enhance the effectiveness of the iterative algorithm and thereby increase the quality of the reconstructed images. This is especially important for the imaging of transmissive objects.

5. Conclusions

The recent experiments show that the setup is capable of producing single-shot images of good quality in the low micrometer range. The spatial resolution is not as good as expected, but it can be improved by careful optimization of the setup. A spatial resolution of below 1 μm seems to be readily achievable. Future work will be targeted at demonstrating time-resolved holography in pump–probe experiments, effectively reaching the femtosecond time scale with a table-top setup. Furthermore, the capability of the experimental technique and reconstruction algorithm to retrieve the phase properties of transmissive objects will be explored.

Acknowledgements

This research was supported by the Marie Curie Early Stage Training Site (MAXLAS), the Knut and Alice Wallenberg Foundation and the Swedish Research Council. We also thank Ulf Johansson and Ralf Nyholm for fruitful discussions and support.

References

[1] Chapman, H.N.; Barty, A.; Bogan, M.J.; Boutet, S.; Frank, M.; Hau-Riege, S.P.; Marchesini, S.; Woods, B.W.; Bajt, S.; Benner, W.H., et al. *Nature Physics*. **2006,** *2,* 839–843.

[2] Chapman, H.N.; Hau-Riege, S.P.; Bogan, M.J.; Bajt, S.; Barty, A.; Boutet, S.; Marchesini, S.; Frank, M.; Woods, B.W.; Benner, W.H., et al. *Nature*. **2007,** *448,* 676–680.

[3] Bogan, M.J.; Benner, W.H.; Boutet, S.; Rohner, U.; Frank, M.; Barty, A.; Seibert, M.M.; Maia, F.; Marchesini, S.; Bajt, S., et al. *Nano Lett*. **2008,** *8,* 310–316.

[4] Schlotter, W.F.; Lüning, J.; Rick, R.; Chen, K.; Scherz, A.; Eisebitt, S.; Günther, C.M.; Eberhardt, W.; Hellwig, O.; Stöhr, J. *Opt. Lett*. **2007,** *32,* 3110–3112.

[5] Bartels, R.A.; Paul, A.; Green, H.; Kapteyn, H.C.; Murnane, M.M.; Backus, S.; Christov, I.P.; Liu, Y.; Attwood, D.; Jacobsen, C. *Science*. **2002,** *297,* 376–378.

[6] Morlens, A.-S.; Gautier, J.; Rey, G.; Zeitoun, P.; Caumes, J.-P.; Kos-Rosset, M.; Merdji, H.; Kazamias, S.; Cassou, K.; Fajardo, M. *Opt. Lett*. **2006,** *31,* 3095–3097.

[7] Sandberg, R.L.; Paul, A.; Raymondson, D.A.; Hädrich, S.; Gaudiosi, D.M.; Holtsnider, J.; Tobey, R.I.; Cohen, O.; Murnane, M.M.; Kapteyn, H.C. *Phys. Rev. Lett*. **2007,** *99,* 098103-1–4.

[8] Tobey, R.I; Siemens, M.E.; Cohen, E.; Murnane, M.M.; Kapteyn, H.C.; Nelson, K.A *Opt. Lett*. **2007,** *32,* 286–288.

[9] Genoud, G.; Guilbaud, O.; Mengotti, E.; Petterson, S.-G.; Georgiadou, E.; Pourtal, E.; Wahlström, C.-G.; L'Huillier, A. *Appl. Phys. B* **2008,** *90,* 533–538.

[10] Ekvall, I.; Wahlström, E.; Claesson, D.; Olin, H.; Olsson, E. *Meas. Sci. Technol*. **1999,** *10,* 11–18.

[11] Gabor, D. *Nature*. **1948,** *4098,* 777–778.

[12] Latychevskaia, T.; Fink, H.-W. *Phys. Rev. Lett*. **2007,** *98,* 233901-1–4.

[13] Huang, X.M.H.; Zuo, J.M.; Spence, J.C.H. *Appl. Surf. Sci*. **1999,** *148,* 229–234.

Paper X

Phase Measurement of Resonant Two-Photon Ionization in Helium

M. Swoboda, T. Fordell, K. Klünder, J. M. Dahlström, M. Miranda,
C. Buth, K. J. Schafer, J. Mauritsson, A. L'Huillier, and
M. Gisselbrecht.

Phys. Rev. Lett. **104**, 103003 (2010).

PRL **104,** 103003 (2010) PHYSICAL REVIEW LETTERS week ending
12 MARCH 2010

Phase Measurement of Resonant Two-Photon Ionization in Helium

M. Swoboda,[1] T. Fordell,[1] K. Klünder,[1] J. M. Dahlström,[1] M. Miranda,[1,2] C. Buth,[3,4] K. J. Schafer,[3,4] J. Mauritsson,[1]
A. L'Huillier,[1,*] and M. Gisselbrecht[1]
[1]*Department of Physics, Lund University, P.O. Box 118, 22100 Lund, Sweden*
[2]*Departamento de Física, Universidade do Porto, Rua do Campo Alegre 687, 4169-007 Porto, Portugal*
[3]*Department of Physics and Astronomy, Louisiana State University, Baton Rouge, Louisiana 70803, USA*
[4]*PULSE Institute, SLAC National Accelerator Laboratory, Menlo Park, California 94025, USA*
(Received 18 December 2009; published 12 March 2010)

We study resonant two-color two-photon ionization of helium via the $1s3p\ ^1P_1$ state. The first color is the 15th harmonic of a tunable Ti:sapphire laser, while the second color is the fundamental laser radiation. Our method uses phase-locked high-order harmonics to determine the *phase* of the two-photon process by interferometry. The measurement of the two-photon ionization phase variation as a function of detuning from the resonance and intensity of the dressing field allows us to determine the intensity dependence of the transition energy.

DOI: 10.1103/PhysRevLett.104.103003 PACS numbers: 32.80.Rm, 32.70.Jz, 32.80.Qk, 42.65.Ky

Multicolor resonant ionization is at the heart of numerous and diverse applications in fundamental and applied sciences. Examples are studies of very high Rydberg states [1], investigations of biomolecules [2] and specific selection of radioactive species [3]. In the simplest scheme, resonantly enhanced two-photon ionization (R2PI) occurs via the absorption of two photons, generally of different colors, one tunable (ω_1) used to scan across a resonant state (r), and the second (ω) ionizing from the excited state. In traditional R2PI, the *yield* of the produced ion species is recorded as a function of laser wavelength, and the position and shape of the observed resonance provides information on the underlying electronic and rovibrational structures. These studies rely on spectroscopic information using narrow-bandwidth lasers, which do not allow any temporal resolution. Here, we present an ultrafast time-resolved-technique to retrieve also the *phase* of R2PI when sweeping through the resonance. We demonstrate it by studying R2PI of He via the $1s3p\ ^1P_1$ state which lies 23.087 eV above the ground state.

The basic principle of our experiment is illustrated in Fig. 1. We study the interference between two pathways to the same ionized final state (f_1), one through the resonance with absorption of two photons with frequency ω_1 and ω, and the second through a continuum path, using a third color (ω_2), involving absorption of a photon with frequency ω_2 and emission of a photon with frequency ω. The phase of the R2PI is encoded in the modulation of the photoelectron signal S_{f_1} as a function of the delay τ between the (ω_1, ω_2) fields and the ω field [Fig. 1(b)]. When the energy of the exciting radiation ω_1, and thus the detuning from the resonance is changed, the phase variation of the resonant transition leads to a measurable shift of the S_{f_1} oscillation. This phase shift needs to be referenced against another modulation S_{f_2} that is independent of the resonance and thus providing a *clock* to our measurement. A process providing an independent modulation requires a fourth color (ω_3) and involves another final state (f_2) (see Fig. 1).

An essential requirement for our measurement is the use of phase-locked radiation fields with commensurate frequencies, and a temporal precision better than the periodicity of the interference signal, in our case 1.3 fs. Another requirement, is a high spectral resolution for the excitation of a narrow resonance. These requirements can be simultaneously fulfilled by using the high-order harmonic frequency combs produced when an intense laser field interacts with a gas of atoms or molecules [4]. As is now well understood [5,6], harmonics arise due to interferences

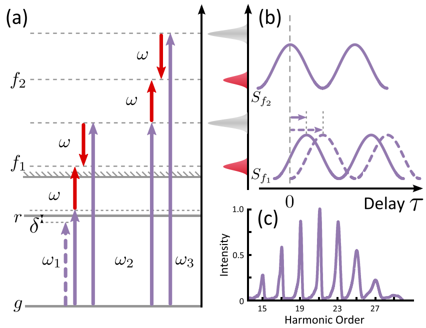

FIG. 1 (color online). (a) Schematic diagram illustrating the phase measurement of R2PI. The dashed and solid ω_1 lines represent two excitation energies on either side of the resonance. The photoelectron peaks used in the measurement are S_{f_1} and S_{f_2}. (b) Illustration of modulated sideband signals S_{f_1} and S_{f_2}. Two S_{f_1} modulations are indicated, corresponding to the two excitation energies in (a). (c) Experimental harmonic spectrum used in the measurements.

© 2010 The American Physical Society

between attosecond pulses produced by tunnel ionization, acceleration of the created wave packet in the field and recombination back to the ground state at each half cycle of the laser field. The spectral width of the individual harmonics is thus related to the number of attosecond pulses, and decreases as the laser pulse duration increases [7]. In this process, a comb of phase-locked harmonics of odd order is generated.

In the present work, we use high-order harmonics to study two-color photoionization of He via the $1s3p\ ^1P_1$ state [8,9]. In contrast to the "reconstruction of attosecond bursts by interference of two-photon transition" (RABITT) technique, used to determine the pulse duration of attosecond pulses [10,11] and similarly to previous work performed in Ne [12] and N_2 [13], we eliminate the influence of the temporal characteristics of the attosecond pulses to concentrate on the influence of the atomic properties. We study the R2PI phase as a function of detuning from the resonance, by varying the fundamental wavelength (around 805 nm) or alternatively by increasing the fundamental intensity. We apply these measurements to determine the intensity-dependence of the energy of the $1s^2 \rightarrow 1s3p$ transition, and interpret the results using theoretical calculations consisting of solving the time-dependent Schrödinger equation (TDSE) in conditions close to the experimental ones [14].

Our experiments were performed with a 1-kHz 35-fs 4-mJ Ti:sapphire laser system. An acousto-optic programmable dispersive filter (DAZZLER) was used to change the central wavelength between 802.5 and 809.3 nm, while maintaining the spectral width of the amplified pulses approximately equal to 25 nm. High-order harmonics were generated in a pulsed Ar gas cell, filtered using a spatial aperture and a 200-nm thick Al thin film [15], and focused by a toroidal mirror into a vacuum chamber containing an effusive He gas jet. A magnetic bottle electron spectrometer (MBES) allowed us to record and analyze in energy the ejected electrons. Part of the laser field was extracted before the generation of harmonics, and recombined downstream collinearly with the harmonics, after a variable time delay that could be adjusted with sub-100-as precision [12].

A comb of about seven phase-locked harmonic fields [Fig. 1(c)], corresponding in the time domain to a train of attosecond pulses of 260 as duration, was thus sent into the interaction chamber together with the dressing field at frequency ω with an adjustable phase φ (or time $\tau = \varphi/\omega$) delay. In addition, a half-wave plate and polarizer in the dressing IR field arm allowed precise control of the pulse energy and therefore the intensity in the interaction region of the MBES. The detuning was determined from $\delta = 15hc/\lambda_0 - E_{3p}$, where E_{3p} is 23.087 eV and λ_0 is the barycenter of the fundamental frequency spectrum, shifted to the blue by $\delta\lambda \simeq 3.5$ nm to account for the blueshift from free electrons in the generation gas [16,17]. The dressing laser intensity was determined by measuring the energy shifts of the photoelectron peaks of harmonics 17 to 23 in the presence of the laser field, which is simply equal to the ponderomotive energy $U_p \approx 6.0I$ eV where the intensity I is in units of 10^{14} W cm^{-2} for a laser wavelength of 800 nm [18,19].

Figures 2(a) and 2(b) present electron spectra as a function of delay between the harmonics and the dressing field, obtained for two different detunings. Electrons are observed at energies corresponding to one-photon absorption of the harmonics (from the 17th) and at "sideband" energies due to two-photon ionization processes, which we label by the corresponding net number of infrared photons (16, 18, etc.). These sideband peaks strongly oscillate with the delay at a frequency equal to 2ω. The oscillations of sidebands 18, 20, 22, and 24 do not depend on the detuning, while sideband 16 is strongly affected by it. A Fourier transform of the sideband signal over about 10 fs (four cycles) allows us to determine the relative phases of the sideband oscillations with a precision of 0.1 rad. The phases are plotted in Fig. 2(c) for the two cases shown in (a),(b).

The relationship between the R2PI phase and the experimental results in Fig. 2 can be understood within second-order perturbation theory [10,12]. Using the notation from Fig. 1, the photoelectron signal S_{f_1} can be expressed as

$$S_{f_1} = |a_1^a + a_2^e|^2, \tag{1}$$

where a_1^a and a_2^e are the two-photon probability amplitudes with the superscript a or e referring to an absorption or emission of an ω photon and with the subscript 1 or 2 referring to absorption of an ω_1 or ω_2 photon. Introducing φ_1 and φ_2 as the phases of the radiation fields, as well as

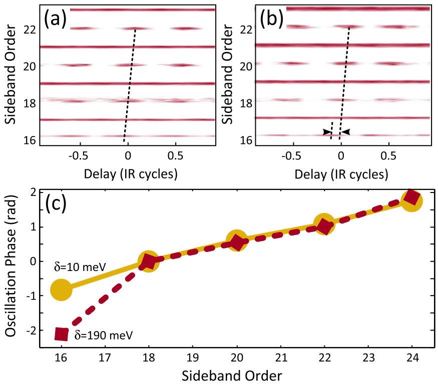

FIG. 2 (color online). Electron spectra as a function of delay for detunings $\delta = 10$ meV (a) and $\delta = 190$ meV (b). The oscillation of the 16th sideband depends on the detuning while the others do not (see dashed line) (c) Phase of the oscillations of the sideband peaks in light orange for (a) and dark red for (b). The two results have been superposed at sideband 18.

φ_1^a and φ_2^e as the phase terms involved in the two-photon transitions, Eq. (1) becomes

$$\begin{aligned} S_{f_1} &= ||a_1^a|e^{i\varphi_1^a+i\varphi_1+i\varphi}+|a_2^e|e^{i\varphi_2^e+i\varphi_2-i\varphi}|^2 \\ &= |a_1^a|^2+|a_2^e|^2+2|a_1^a a_2^e|\cos(\varphi_1^a-\varphi_2^e+2\varphi+\varphi_1-\varphi_2). \end{aligned} \tag{2}$$

The cosine term leads to the modulation of the signal observed in the experiment. In general, the phase terms involved do not depend much on the photon energies. In two-photon ionization via a resonant state, however, the phase (φ_1^a) changes by π across the resonance. The study of the variation of φ_1^a as a function of detuning δ provides interesting information on the two-photon ionization process, e.g., on the relative importance of resonant and nonresonant contributions, ac Stark shift of the resonant state, depending on the spectral characteristics of the XUV and laser fields.

The variation of φ_1^a with the detuning can be experimentally obtained from $S_{f_1}(\varphi)$ provided the other phase terms φ_2^e, φ_1, φ_2 do not depend on δ and provided the phase delay φ is known in absolute value, which is generally not the case. $S_{f_1}(\varphi, \delta)$ is therefore referenced against $S_{f_2}(\varphi)$, assuming that the phase terms involved, φ_2^a and φ_3^e, are independent of the detuning and thus removing the need of knowledge of the absolute φ. When changing δ, the laser intensity used to generate the harmonics varies slightly, leading to a (small) variation of the group delay of the attosecond pulses and thus of $\varphi_1 - \varphi_2$. We take this effect into account by assuming a linear group delay [20], which we experimentally determine using higher-order sidebands. Its contribution is then subtracted from the measured phases and the phase of sideband 18 is set to zero for all detunings. The results are presented in Fig. 3(a). As expected, the phases corresponding to all sidebands except the 16th are almost superposed to each other and show no influence of detuning.

Figure 3(b) shows the variation of the R2PI phase as a function of detuning. We can tune only over half the resonance since for lower (negative detunings) sideband 16 moves progressively below the ionization threshold, thus making our phase measurement inaccurate. We also compare our measurements with the results of two different calculations (solid lines): The dark red line is obtained by a simple perturbative model [21], only considering the resonant state. Gaussian envelopes were used for the ir and XUV pulses with FWHMs of 30 and 10 fs, respectively. The light orange curve shows the result of calculations performed by numerically integrating the TDSE in the single active electron approximation [14] in conditions close to the experiment. We use a He pseudopotential with the energy of the $1s3p$ state equal to 23.039 eV. The result is therefore shifted by 40 meV for comparison with the experiment. The result shown in Fig. 3(b) agrees very well with the experiment, thus confirming our detuning calibration.

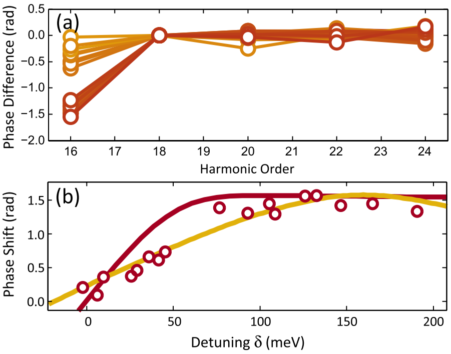

FIG. 3 (color online). (a) Measured sideband phases corrected for the attosecond group delay and normalized at zero for sideband 18. Different detunings are indicated by the color code [going from 11 meV below the resonance (dark red, lower points in order 16) to 190 meV above the resonance (light orange, upper in order 16)]. (b) Measurements (circles) of the R2PI phase as a function of detuning. The dark red line indicates results of a simple perturbative model while the light orange line shows results of simulations based on solving the TDSE.

In order to investigate how the $1s3p$ resonance behaves in a laser field, we measured the dependence of the R2PI phase on the dressing laser intensity. Figure 4(a) shows the R2PI phase determined similarly to Fig. 3(a) but keeping the wavelength constant at 805.5 nm and gradually increasing the dressing intensity. We verified that even at the highest intensity, higher-order multiphoton transitions were still negligible [22], thus not affecting our phase determination. Increasing the intensity from 0.1 to 1.8×10^{12} W/cm^2, the R2PI phase varies from -0.7 to 0.9 radians. Figure 4(b) presents the intensity dependence of all of the measured phases (circles). We find an almost linear increase of the phase with intensity, as indicated by the dark red curve obtained by averaging, with a saturation at around 1.3×10^{12} W/cm^2, due to the suppression of R2PI when part of the two-photon excitation bandwidth moves partly below the ionization threshold. The light orange line obtained by TDSE calculations agrees well with our measurements.

Combining our previous phase measurements as a function of detuning for a fixed (low) intensity and as a function of intensity (for a fixed detuning) allows us to determine the intensity dependence of the $1s^2 \longrightarrow 1s3p$ transition energy. Both experimental (dark red solid) and TDSE (light orange solid) results are shown in Fig. 5(a). The dashed line is equal to $\Delta E_{1s^2} + U_p$, representing the variation of the transition energy if the $1s3p$ state was moving as a high-lying Rydberg state, following U_p [19]. The ac Stark shift of the fundamental state ΔE_{1s^2} is very small, equal to $-0.3I$ eV where the intensity I is in units of 10^{14} W cm^{-2} [23,24] so that $\Delta E_{1s^2} + U_p \approx U_p$. We find that the measured transition energy increases about 40%

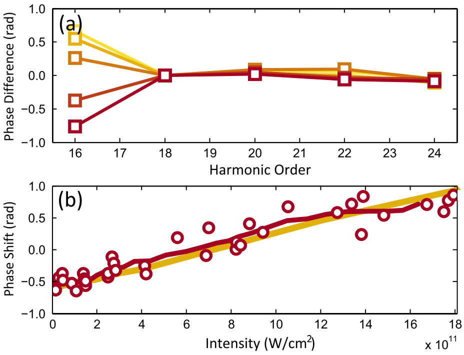

FIG. 4 (color online). Intensity dependence of the R2PI phase. (a) Harmonic phase differences at dressing intensities from 0.1 (dark red) to 2.2×10^{12} W cm^{-2} (light orange), with attosecond chirp correction and normalization at sideband 18. (b) R2PI phase (circles) as a function of intensity, with a six-point moving average (dark red line) and TDSE (light orange).

more rapidly with the laser intensity than U_p, up to the saturation at 1.3×10^{12} W cm^{-2}.

To better understand this faster than ponderomotive shift, we have calculated the XUV absorption cross section for helium in the presence of an 800 nm field by numerically solving the TDSE as a function of both XUV wavelength and laser intensity [Fig. 5(b)]. Using an XUV bandwidth of 50 meV or smaller we find that beyond 1×10^{11} W cm^{-2}, the $3p$ resonance has at least two components the higher of which shifts significantly faster than the ponderomotive energy. With the experimental XUV bandwidth (150 meV), however, the different components cannot be resolved. As a result, we observe shifts exceeding $E_{1s^2} + U_p$. Experimentally, the predicted structure in the $3p$ resonance could be observed using longer fundamental laser pulses, leading to spectrally narrower harmonic peaks.

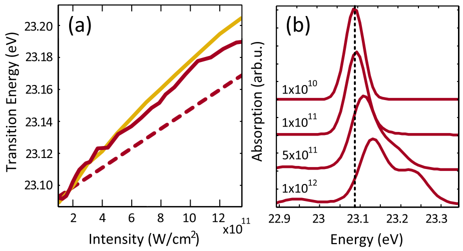

FIG. 5 (color online). (a) Measured transition energy of the $1s3p$ state. Experimental results (solid dark red), compared with $\Delta E_{1s^2} + U_p$ (dashed) and TDSE calculation (solid light orange). (b) TDSE calculation of XUV absorption for three different intensities with 50 meV resolution. The position of the $1s3p$ state is indicated by the dashed line.

In conclusion, we have shown how well-characterized phase-locked high-order harmonics can be used to measure the phase of R2PI and we have applied it to the determination of the ac Stark shift of the $1s3p$ $^1P_1$ state. Although our resolution was unsufficient to detect the splitting of the excited state, we observed a nontrivial, faster than ponderomotive, ac Stark shift. Our method, here demonstrated in He, could be applied to the study of numerous resonant or quasiresonant processes in atoms and molecules.

We thank A. Maquet and R. Taïeb for fruitful suggestions at the beginning of this work. This research was supported by the Marie Curie Intra-European Fellowship ATTOCO, the Marie Curie Early Stage Training Site (MAXLAS), the European Research Council (ALMA), the Knut and Alice Wallenberg Foundation and the Swedish Research Council. Funding at LSU is provided by the National Science Foundation through grant numbers PHY-0449235 and PHY-0701372.

*anne.lhuillier@fysik.lth.se
URL: http://www.atto.fysik.lth.se

[1] A. Osterwalder and F. Merkt, Phys. Rev. Lett. **82**, 1831 (1999).
[2] E. G. Robertson and J. P. Simons, Phys. Chem. Chem. Phys. **3**, 1 (2001).
[3] U. Koster, V. Fedoseyev, and V. Mishin, Spectrochim. Acta, Part B: At. Spectrosc. **58**, 1047 (2003).
[4] M. Ferray *et al.*, J. Phys. B **21**, L31 (1988).
[5] J. L. Krause, K. J. Schafer, and K. C. Kulander, Phys. Rev. Lett. **68**, 3535 (1992).
[6] P. B. Corkum, Phys. Rev. Lett. **71**, 1994 (1993).
[7] F. Brandi, D. Neshev, and W. Ubachs, Phys. Rev. Lett. **91**, 163901 (2003).
[8] P. Ranitovic *et al.*, New J. Phys. **12**, 013008 (2010).
[9] L. H. Haber, B. Doughty, and S. R. Leone, Phys. Rev. A **79**, 031401(R) (2009).
[10] V. Véniard, R. Taïeb, and A. Maquet, Phys. Rev. A **54**, 721 (1996).
[11] P. M. Paul *et al.*, Science **292**, 1689 (2001).
[12] K. Varjú *et al.*, Laser Phys. **15**, 888 (2005).
[13] S. Haessler *et al.*, Phys. Rev. A **80**, 011404(R) (2009).
[14] K. J. Schafer and K. C. Kulander, Phys. Rev. Lett. **78**, 638 (1997).
[15] R. López-Martens *et al.*, Phys. Rev. Lett. **94**, 033001 (2005).
[16] C. G. Wahlström *et al.*, Phys. Rev. A **48**, 4709 (1993).
[17] M. B. Gaarde, M. Murakami, and R. Kienberger, Phys. Rev. A **74**, 053401 (2006).
[18] R. K. Freeman *et al.*, Phys. Rev. Lett. **59**, 1092 (1987).
[19] K. Burnett, V. Reed, and P. Knight, J. Phys. B **26**, 561 (1993).
[20] Y. Mairesse *et al.*, Science **302**, 1540 (2003).
[21] N. Dudovich, D. Oron, and Y. Silberberg, Phys. Rev. Lett. **88**, 123004 (2002).
[22] M. Swoboda *et al.*, Laser Phys. **19**, 1591 (2009).
[23] M. D. Perry, A. Szoke, and K. C. Kulander, Phys. Rev. Lett. **63**, 1058 (1989).
[24] H. Rudolph *et al.*, Phys. Rev. Lett. **66**, 3241 (1991).

PAPER XI

Photoemission-time-delay measurements and calculations close to the 3s-ionization-cross-section minimum in Ar

D. Guénot, K. Klünder, C. L. Arnold, D. Kroon, J. M. Dahlström, M. Miranda, T. Fordell, M. Gisselbrecht, P. Johnsson, J. Mauritsson, E. Lindroth, A. Maquet, R. Taïeb, A. L'Huillier, and A. S. Kheifets.

Phys. Rev. A **85**, 053424 (2012).

PHYSICAL REVIEW A **85**, 053424 (2012)

Photoemission-time-delay measurements and calculations close to the 3*s*-ionization-cross-section minimum in Ar

D. Guénot,[1] K. Klünder,[1] C. L. Arnold,[1] D. Kroon,[1] J. M. Dahlström,[2] M. Miranda,[1] T. Fordell,[1] M. Gisselbrecht,[1]
P. Johnsson,[1] J. Mauritsson,[1] E. Lindroth,[2] A. Maquet,[3] R. Taïeb,[3] A. L'Huillier,[1] and A. S. Kheifets[4]
[1]*Department of Physics, Lund University, P.O. Box 118, 22100 Lund, Sweden*
[2]*Department of Physics, Stockholm University, Sweden*
[3]*Laboratoire de Chimie Physique-Matière et Rayonnement, Université Pierre et Marie Curie, 11, rue Pierre et Marie Curie, 75231 Paris Cedex 5, France*
[4]*Research School of Physical Sciences, The Australian National University, Canberra ACT 0200, Australia*

(Received 2 April 2012; published 31 May 2012)

We present experimental measurements and theoretical calculations of photoionization time delays from the 3s and 3p shells in Ar in the photon energy range of 32–42 eV. The experimental measurements are performed by interferometry using attosecond pulse trains and the infrared laser used for their generation. The theoretical approach includes intershell correlation effects between the 3s and 3p shells within the framework of the random-phase approximation with exchange. The connection between single-photon ionization and the two-color two-photon ionization process used in the measurement is established using the recently developed asymptotic approximation for the complex transition amplitudes of laser-assisted photoionization. We compare and discuss the theoretical and experimental results, especially in the region where strong intershell correlations in the $3s \to kp$ channel lead to an induced "Cooper" minimum in the 3*s* ionization cross section.

DOI: 10.1103/PhysRevA.85.053424 PACS number(s): 32.80.Fb, 32.80.Rm

I. INTRODUCTION

Attosecond pulses created by harmonic generation in gases [1,2] allow us to study fundamental light-matter interaction processes in the time domain. When an ultrashort light pulse impinges on an atom, a coherent ultrabroadband electron wave packet is created. If the frequency of the pulse is high enough, the electronic wave packet escapes by photoionization [3]. As in ultrafast optics, the *group delay* of an outgoing electron wave packet can be defined by the energy derivative of the phase of the complex photoionization matrix element. When photoionization can be reduced to one noninteracting angular channel L, this phase is the same as the scattering phase η_L, which represents the difference between a free continuum wave and that propagating out of the effective atomic potential for the L angular channel. In fact, the concept of time delay was already introduced by Wigner in 1955 to describe s-wave quantum scattering [4]. In collision physics, with both ingoing and outgoing waves the (Wigner) time delay is twice the derivative of the scattering phase.

In general, photoionization may involve several strongly interacting channels. Only in some special cases can the Wigner time delay be conveniently used to characterize delay in photoemission. One such case might be valence-shell photoionization of Ne in the 100-eV range [5,6]. In this case, there is no considerable coupling between the $2s \to \epsilon p$ and $2p \to \epsilon s$ or ϵd channels, and ϵd is strongly dominant over ϵs, following Fano's propensity rule [7]. The case of valence-shell photoionization of Ar in the 40-eV range [8] is more interesting. In this case, the 3s photoionization is radically modified by strong intershell correlation with 3p [9]. As a result, the 3s photoionization cross section goes through a deep "Cooper" minimum at approximately 42-eV photon energy [10]. Such a feature is a signature of intershell correlation and cannot be theoretically described using any independent electron, e.g., Hartree-Fock (HF) model.

Recent experiments [5,8] reported the first measurements of delays between photoemission from different subshells from rare-gas atoms, thus raising considerable interest from the scientific community. Different methods for the measurements of time delays were proposed, depending on whether single attosecond pulses or attosecond pulse trains were used. The streaking technique consists of recording electron spectra following ionization of an atom by a single attosecond pulse in the presence of a relatively intense infrared (IR) pulse, as a function of the delay between the two pulses [11,12]. Temporal information is obtained by comparing streaking traces from different subshells in an atom [5] or from the conduction and valence bands in a solid [13]. On the other hand, the so-called RABBIT (reconstruction of attosecond bursts by interference of two-photon transitions) method consists of recording photoelectron above-threshold-ionization (ATI) spectra following ionization of an atom by a train of attosecond pulses and a weak IR pulse at different delays between the two fields [14]. Temporal information on photoionization is obtained by comparing RABBIT traces from different subshells in an atom [8]. The name of the technique, which we will use throughout, refers to its original use for the measurement of the group delay of attosecond pulses in a train [15].

Both methods involve absorption or stimulated emission of one or several IR photons, and it is important to understand the role of these additional transitions for a correct interpretation of the measured photoemission delays. A temporal delay difference of 21 as was measured for the photoionization from the 2s and 2p shells in neon using single attosecond pulses of 100-eV central energy [5]. Interestingly, the electron issued from the 2p shell was found to be delayed compared to the more bound 2s electron. Similarly, delay differences on the order of ~100 as were measured for the photoionization from the 3s and 3p shells in argon using attosecond pulse trains with central energy around 35 eV. Again, the 3p electron appears to be delayed relative to the 3s electron, with a difference which depends on the excitation energy [8].

These experimental results stimulated several theoretical investigations, ranging from advanced photoionization calculations, including correlations effects [6], to time-dependent numerical approaches [5,16–18] to semianalytical developments aimed at understanding the effect of the IR field on the measured time delays [19–21]. The picture which is emerging from this productive theoretical activity is that when the influence of the IR laser field is correctly accounted for, such time-delay measurements may provide very interesting information on temporal aspects of many-electron dynamics.

The present work reports theoretical and experimental investigation of photoionization in the $3s$ and $3p$ shells in argon in the 32–42-eV photon energy range. Besides providing a more extensive description of the experimental and theoretical methods in [8], we improve the results in three different ways.

(1) We performed more precise measurements using a *stabilized* Mach-Zehnder interferometer [22] for the RABBIT method. The stabilization allows us to take scans during a longer time and thus to extract the phase more precisely. Some differences with the previous measurements are found and discussed.

(2) For the comparison with theory, we determined the phases of the single-photon ionization amplitudes using the random-phase approximation with exchange (RPAE) method, which includes intershell correlation effects [9,23,24]. This represents a clear improvement to the calculations presented in [8], using Hartree-Fock data [25], especially in the region above 40 eV, where photoionization of Ar passes through an interference minimum, owing to $3s$-$3p$ intershell correlation effects.

(3) Finally, we improved our calculation of the phase of a two-photon ionization process, thus making a better connection between the experimental measurements and the single photoionization calculated phases [20].

This paper is organized as follows. Section II presents the experimental setup and results. Section III describes the phase of one- and two-photon ionization processes using perturbation theory in an independent-electron approximation. Section IV includes intershell correlation using the RPAE method. A comparison between theory and experiment is presented in Sec. V.

II. EXPERIMENTAL METHOD AND RESULTS

The experiments were performed with a titanium:sapphire femtosecond laser system delivering pulses of 30-fs (FWHM) duration, centered at 800 nm, with a 1-kHz repetition rate and a pulse energy of ~3 mJ. A beam splitter divides the laser output into the probe and the pump arm of a Mach-Zehnder interferometer (see Fig. 1). The energy of the probe pulses can be adjusted by a $\lambda/2$ plate followed by an ultrathin polarizer. The pump arm is focused by a $f = 50$ cm focusing mirror into a pulsed argon-gas cell, synchronized with the laser repetition rate, in order to generate an attosecond pulse train via high-order harmonic generation. An aluminum filter of 200-nm thickness blocks the fundamental radiation, and subsequently, a chromium filter of the same thickness selects photon energies of about 10-eV bandwidth in the range of harmonics 21 to 27.

The probe and the pump arm of the interferometer are recombined on a curved holey mirror, transmitting the pump attosecond pulse train but reflecting the outer portion of the IR probe beam. The exact position of the recombination mirror with respect to the focal position of the pump arm is essential in order to precisely match the wave fronts of the probe and extreme ultraviolet (XUV) beams. A toroidal mirror ($f = 30$ cm) focuses both beams into the sensitive region of a magnetic-bottle electron spectrometer (MBES), where a diffusive gas jet provides argon as detection gas. The relative timing between the ultrashort IR probe pulses and the attosecond pulse train can be reproducibly adjusted on a subcycle time scale due to an active stabilization of the pump-probe interferometer length [22].

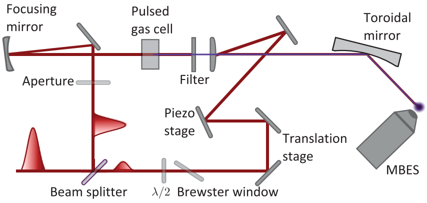

FIG. 1. (Color online) Schematic illustration of our experimental setup.

Figure 2 presents an electron spectrum obtained by ionizing Ar atoms with harmonics selected by both Al and Cr filters, with orders ranging from 21 to 27. We can clearly identify three ionization channels towards the $3s^2p^5$, $3s^1p^6$, and $3s^2\,3p^4n\ell$ ($n\ell = 4p$ or $3d$) continua [26]. The corresponding ionization energies are 15.76, 29.2, and ~37.2 eV. Note that the settings of the MBES were here chosen to optimize the spectral resolution at low energy. The large asymmetric profile obtained at high electron energy can be reduced by optimizing the MBES settings differently. The spectrum due to $3p$ ionization is strongly affected by the behavior of the ionization cross section in this region. The relative intensities of the 21st to the 27th harmonics are approximately 0.2:0.7:1:1.

Figure 3 shows a typical RABBIT spectrogram, i.e., electron spectra as a function of delay between pump and probe

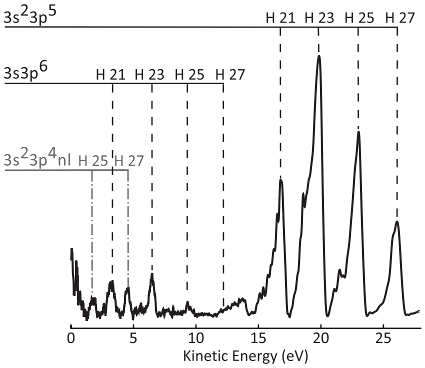

FIG. 2. Electron spectrum obtained by ionizing Ar with four harmonics of orders 21, 23, 25, and 27. The ionization channels are shown on the top.

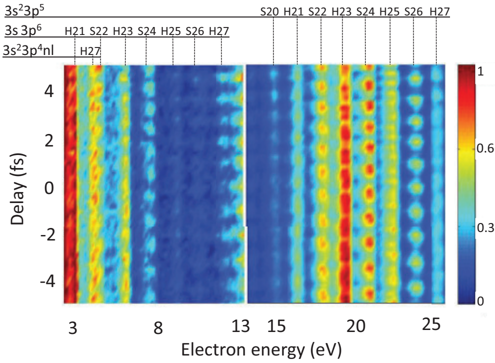

FIG. 3. (Color online) Electron spectrum as a function of time delay between the attosecond pulses and the IR laser. The signal strength is indicated by colors. The spectrum on the right ($3p$) follows that on the left ($3s$) with a factor of 6 reduction in the color code and a slight overlap in energy.

pulses. The electron yield is indicated as colors. Compared to the spectra obtained with the harmonics only, Fig. 3 includes electron peaks at sideband frequencies, including additional absorption or emission of one IR photon (see Fig. 4). The intensity of these sidebands oscillates with a delay at a frequency equal to 2ω, with ω being the IR laser photon energy, according to

$$S_{2q}(\tau) = \alpha + \beta \cos(2\omega\tau - \Delta\phi_{2q} - \Delta\theta_{2q}), \tag{1}$$

where α and β are constant quantities, independent of the delay, and $2q$ represents the total number of IR photons involved, i.e., an odd number to create harmonic $2q-1$ or $2q-1$ plus or minus one IR photon. $\Delta\phi_{2q}$ denotes the phase difference between two harmonics with order $2q+1$ and $2q-1$, while $\Delta\theta_{2q}$ arises from the difference in phase between the amplitudes of the two interfering quantum paths leading to the same final state [Fig. 4(a)]. At high IR intensity, other quantum paths involving more than one IR photon become possible and may change the retrieved RABBIT phase [27]. We kept the IR laser intensity low enough to avoid such higher-order effects, which can be identified through oscillations at higher frequencies. $\tau_A = \Delta\phi_{2q}/2\omega$ can be interpreted as the group delay of the attosecond pulses [15]. We define in a similar way $\tau^{(2)} = \Delta\theta_{2q}/2\omega$ arising from the two-photon ionization process. Since the same harmonic comb is used for ionization in the $3s$ and $3p$ shells, the influence of the attosecond group delay can be subtracted, and the delay difference $\tau^{(2)}(3s) - \tau^{(2)}(3p)$ can be deduced. The results of these measurements are indicated in Table I for sidebands 22, 24, and 26. We also indicate in Table I previous results from [8]. It is quite difficult in such an experiment to estimate the uncertainty of our measurement. The stability of the interferometer is measured to be ~50 as. The relative uncertainty in comparing the phase offsets of different sideband oscillations is estimated to be of the same magnitude or even slightly better.

Our measurements agree well with those of [8] for sideband 24. For sideband 22, the measurements performed in [8] could not resolve the sideband peak from electrons ionized by harmonic 27 towards the continuum $3s^2\,3p^4 n\ell$ (see Fig. 3). A new analysis done by considering only the high-energy part of the sideband peak leads to the number indicated in parentheses in Table I, which is in good agreement with the present measurement. There is, however, a difference for the delay measured at sideband 26. We will comment on this difference in Sec. V.

TABLE I. Time-delay measurements.

	Sideband		
	22	24	26
Photon energy (eV)	34.1	37.2	40.3
$\tau^{(2)}(3s) - \tau^{(2)}(3p)$, this work (as)	−80	−100	10
$\tau^{(2)}(3s) - \tau^{(2)}(3p)$, Ref. [8] (as)	−40 (−90)	−110	−80
$\tau_{cc}(3s) - \tau_{cc}(3p)$ (as)	−150	−70	−40
$\tau^{(1)}(3s) - \tau^{(1)}(3p)$ (as)	70	−30	50

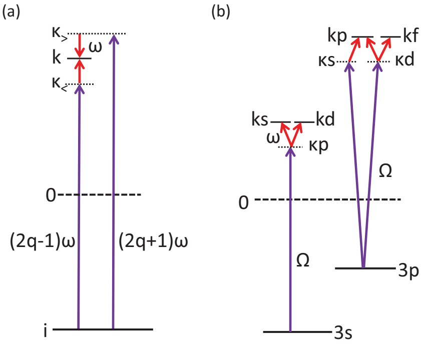

FIG. 4. (Color online) Energy-level scheme of the processes discussed in the present work: (a) RABBIT principle and (b) different channels in two-photon ionization from the $3s$ and $3p$ subshells.

III. THEORY OF ONE- AND TWO-PHOTON IONIZATION

To interpret the results presented above, we relate the one-photon ionization delays to the delays measured in the experiment. Using lowest-order perturbation theory, the transition matrix elements in one- and two-photon ionization are

$$M^{(1)}(\vec{k}) = -iE_\Omega \langle \vec{k}|z|i\rangle, \tag{2}$$

$$M^{(2)}(\vec{k}) = -iE_\omega E_\Omega \lim_{\varepsilon\to 0^+} \sum\!\!\!\!\!\!\int_\nu \frac{\langle \vec{k}|z|\nu\rangle\langle \nu|z|i\rangle}{\epsilon_i + \Omega - \epsilon_\nu + i\varepsilon}. \tag{3}$$

Atomic units are used throughout. We choose the quantization axis (z) to be the (common) polarization vector of the two fields. The complex amplitudes of the laser and harmonic fields are denoted by E_ω and E_Ω, with photon energies ω and Ω, respectively. The initial state is denoted $|i\rangle$ and the final state $|\vec{k}\rangle$. The energies of the initial and intermediate states are denoted ϵ_i and ϵ_ν, respectively. The sum in $M^{(2)}$ is performed over all possible intermediate states $|\nu\rangle$ in the discrete and continuum spectra. The infinitesimal quantity ε is added to ensure the correct boundary condition for the ionization process, so that the matrix element involves an outgoing photoelectron. The magnitude of the final momentum is restricted by energy conservation to $\epsilon = k^2/2 = \Omega + \epsilon_i$ for one-photon absorption and $\epsilon = k^2/2 = \Omega + \omega + \epsilon_i$ for two-photon absorption. The two-photon transition matrix element involving emission of a laser photon can be written in the same way, with ω replaced by $-\omega$ in the energy conservation relation and E_ω replaced by its conjugate.

The next step consists of separating the angular and radial parts of the wave functions. The different angular channels involved are indicated in Fig. 4(b). We split the radial and angular dependence in the initial state as $\langle \boldsymbol{r}|i\rangle = Y_{l_i m_i}(\hat{r}) R_{n_i l_i}(r)$ and use the partial-wave expansion in the final state,

$$\langle \boldsymbol{r}|\vec{k}\rangle = (8\pi)^{\frac{3}{2}} \sum_{L,M} i^L e^{-i\eta_L(k)} Y^*_{LM}(\hat{k}) Y_{LM}(\hat{r}) R_{kL}(r). \tag{4}$$

We perform the spherical integration in Eq. (1) and obtain

$$M^{(1)}(\vec{k}) \propto \sum_{\substack{L=l_i\pm 1\\ M=m_i}} e^{i\eta_L(k)} i^{-L} Y_{LM}(\hat{k}) \times \begin{pmatrix} L & 1 & l_i \\ -M & 0 & m_i \end{pmatrix} T_L^{(1)}(k), \tag{5}$$

where the reduced dipole matrix element is defined as

$$T_L^{(1)}(k) = \hat{L}\hat{l}_i \begin{pmatrix} L & 1 & l_i \\ 0 & 0 & 0 \end{pmatrix} \langle R_{kL}|r|R_{n_i l_i}\rangle \tag{6}$$

using $3j$ symbols and with the notation $\hat{l} = \sqrt{2l+1}$. The reduced matrix element (6) is real. When the dipole transition with the increased momentum $L = l_i + 1$ is dominant, which is often the case [7], the phase of the complex dipole matrix element $M^{(1)}$ is simply equal to

$$\arg[M^{(1)}(k)] = \eta_L(k) - L\pi/2. \tag{7}$$

(There is also a contribution from the fundamental field which we do not write here, as well as trivial phases, e.g., from the spherical harmonic when $M \neq 0$ [20]). Similarly, for two-photon ionization,

$$M^{(2)}(\vec{k}) \propto \sum_{\substack{L=\lambda\pm 1,\lambda=l_i\pm 1\\ M=\mu=m_i}} e^{i\eta_L(k)} i^{-L} Y_{LM}(\hat{k}) \times \begin{pmatrix} L & 1 & \lambda \\ -M & 0 & \mu \end{pmatrix} \begin{pmatrix} \lambda & 1 & l_i \\ -\mu & 0 & m_i \end{pmatrix} T_{L\lambda}^{(2)}(k), \tag{8}$$

where

$$T_{L\lambda}^{(2)}(k) = \hat{L}\hat{\lambda}^2\hat{l}_i \begin{pmatrix} L & 1 & \lambda \\ 0 & 0 & 0 \end{pmatrix} \begin{pmatrix} \lambda & 1 & l_i \\ 0 & 0 & 0 \end{pmatrix} \langle R_{kL}|r|\rho_{\kappa\lambda}\rangle. \tag{9}$$

Here, we have introduced the radial component of the perturbed wave function,

$$|\rho_{\kappa\lambda}\rangle = \lim_{\varepsilon\to 0^+} \sum\!\!\!\!\!\!\!\int_{\nu} \frac{|R_{\nu\lambda}\rangle\langle R_{\nu\lambda}|r|R_{n_i l_i}\rangle}{\epsilon_i + \Omega - \epsilon_\nu + i\varepsilon}, \tag{10}$$

where the sum is performed over the discrete and continuum spectra. κ denotes the momentum corresponding to absorption of one harmonic photon such that the energy denominator goes to zero ($\kappa^2/2 = \epsilon_i + \Omega$). The summation can be decomposed into three terms, the discrete sum over states with negative energy, a Cauchy principal-part integral where the pole has been removed (both these terms are real), and a resonant term which is purely imaginary. The important conclusion is that in contrast to the radial one-photon matrix element, the radial two-photon matrix element is a complex quantity.

To evaluate the phase of this quantity, as explained in more detail in [20], we approximate $R_{kL}(r)$ and $\rho_{\kappa\lambda}(r)$ by their asymptotic values. We have, for example,

$$\rho_{\kappa\lambda}(r) \approx -\sqrt{\frac{2}{\pi\kappa}} \langle R_{\kappa\lambda}|r|R_{n_i l_i}\rangle \times \frac{1}{r} \exp\left\{ i\left[\kappa r + \frac{\ln(2\kappa r)}{\kappa} + \eta_\lambda(\kappa) - \frac{\pi\lambda}{2} \right] \right\}. \tag{11}$$

This allows us to evaluate analytically the integral $\langle R_{kL}|r|\rho_{\kappa\lambda}\rangle$ in Eq. (9). We obtain

$$\arg\left[T_{L\lambda}^{(2)}(k)\right] \approx (L-\lambda)\frac{\pi}{2} + \eta_\lambda(\kappa) - \eta_L(k) + \phi_{cc}(k,\kappa), \tag{12}$$

where $\phi_{cc}(k,\kappa)$ is the phase associated with a continuum-continuum radiative transition resulting from the absorption of IR photons in the presence of the Coulomb potential. It is independent from the characteristics of the initial atomic state, in particular its angular momentum. An important consequence is that, when inserting the asymptotic form (11) in Eq. (8), the scattering phase η_L is canceled out, so that the total phase will not depend on the angular momentum of the final state. In the case of a dominant intermediate channel λ, the phase of the complex two-photon matrix element $M^{(2)}(k)$ is equal to

$$\arg[M^{(2)}(k)] = \eta_\lambda(\kappa) - \lambda\pi/2 + \phi_{cc}(k,\kappa). \tag{13}$$

It is equal to the one-photon ionization phase towards the intermediate state with momentum κ and angular momentum λ plus the additional "continuum-continuum" phase. The difference of phase which is measured in the experiment is therefore given by

$$\Delta\theta_{2q} = \eta_\lambda(\kappa_>) - \eta_\lambda(\kappa_<) + \phi_{cc}(k,\kappa_>) - \phi_{cc}(k,\kappa_<), \tag{14}$$

where $\kappa_>$ and $\kappa_<$ are the momenta corresponding to the highest (lowest) continuum state in Fig. 4(a). Dividing this formula by 2ω, we have

$$\tau^{(2)}(k) = \tau^{(1)}(k) + \tau_{cc}(k), \tag{15}$$

where

$$\tau^{(1)}(k) = \frac{\eta_\lambda(\kappa_>) - \eta_\lambda(\kappa_<)}{2\omega} \tag{16}$$

is a finite difference approximation to the Wigner time delay $d\eta_\lambda/d\epsilon$ and thus reflects the properties of the electronic wave packet ionized by one-photon absorption into the angular channel λ. $\tau^{(2)}$ also includes a contribution from the IR field which is independent of the angular momentum,

$$\tau_{cc}(k) = \frac{\phi_{cc}(k,\kappa_>) - \phi_{cc}(k,\kappa_<)}{2\omega}. \tag{17}$$

We refer the reader to [20] for details about how to calculate τ_{cc}. Figure 5 shows τ_{cc} as a function of photon energy for the two subshells $3s$ and $3p$ and for the IR photon energy

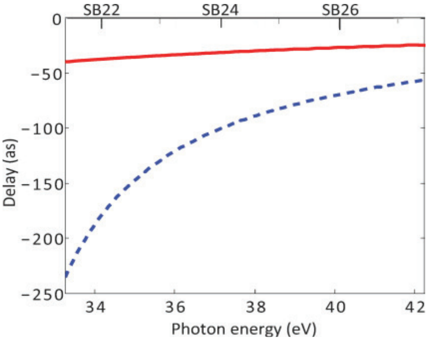

FIG. 5. (Color online) Continuum-continuum delay τ_{cc} as a function of excitation photon energy for subshells $3s$ (red solid line) and $3p$ (blue dashed line) for an IR photon energy of 1.55 eV (800-nm wavelength).

$\omega = 1.55$ eV used in the experiment. The corresponding difference in delays for the $3s$ and $3p$ subshells is only due to the difference in ionization in energy between the two shells (13.5 eV). We also indicate in Table I the measurement-induced delays for the three considered sidebands.

The processes discussed in this section can be represented graphically by the Feynman-Goldstone diagrams displayed in Figs. 6(a) and 6(b). The straight lines with arrows represent electron (arrow pointing up) or hole (arrow pointing down) states. The violet and red wavy lines represent interaction with the XUV and IR fields. We are neglecting here two-photon processes where the IR photon is absorbed first [20].

IV. INTERSHELL CORRELATION EFFECTS

To include intershell correlation effects, we use RPAE [9]. In this approximation, the dipole matrix element of single photoionization is replaced by a "screened" matrix element $\langle k|Z|i\rangle$, which accounts for correlation effects between the $3s$ and $3p$ subshells. These screened matrix elements, represented graphically in Fig. 6(c), are defined by the self-consistent equation

$$\langle\vec{k}|Z|i\rangle = \langle\vec{k}|z|i\rangle + \lim_{\varepsilon\to 0^+} \sum\!\!\!\!\!\!\!\int_{\nu} \left[\frac{\langle\nu|Z|j\rangle\langle j\vec{k}|V|\nu i\rangle}{\Omega-\epsilon_\nu+\epsilon_j+i\varepsilon} - \frac{\langle j|Z|\nu\rangle\langle \nu\vec{k}|V|ji\rangle}{\Omega+\epsilon_\nu-\epsilon_j}\right], \qquad (18)$$

where i and j are $3s$ or $3p$ or vice versa and $V = 1/r_{12}$ is the Coulomb interaction. The sum is performed over the discrete as well as continuum spectra. The Coulomb interaction matrices $\langle j\vec{k}|V|\nu i\rangle$ and $\langle\nu\vec{k}|V|ji\rangle$, represented by dashed lines in Fig. 6(c), describe the so-called time-forward and time-reversed correlation processes. (Note that the time goes upward in the diagrams.) If we replace Z by z in the right term in Eq. (18), we obtain a perturbative expansion to the first order in the Coulomb interaction. More generally, the use of the self-consistent screened matrix elements [Eq. (18)] implies infinite partial sums over two important classes of so-called "bubble" diagrams. Each bubble consists of an electron-hole pair νj, which interacts via $1/r_{12}$ with final electron-hole pair $\vec{k}i$. The energy integration in the time-forward term of Eq. (18) (first line) contains a pole, and the screened matrix element acquires an imaginary part and therefore an extra phase. For a single dominant channel L, the phase of the one-photon matrix element [see Eq.(7)] becomes

$$\arg[M^{(1)}(k)] = \eta_L(k) + \delta_L(k) - L\pi/2, \qquad (19)$$

where $\delta_L(k) = \delta_{i\to kL}$ denotes the additional phase due to the correlations accounted within the RPAE. The photoemission time delay is then determined by the sum of two terms:

$$\tau^{(1)} = \frac{d\eta_L}{d\epsilon} + \frac{d\delta_L}{d\epsilon}. \qquad (20)$$

The first term represents the time delay in the independent electron approximation, equal to the derivative of the photoelectron scattering phase in the combined field of the nucleus and the remaining atomic electrons. The second term is the RPAE correction due to intershell correlation effects.

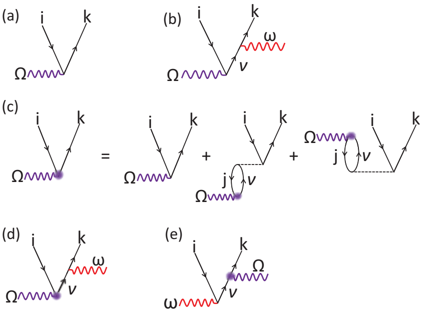

FIG. 6. (Color online) Feynman-Goldstone diagrams representing (a) one-photon and (b) two-photon ionization processes. (c) Diagrammatic representation of the RPAE equations. The second and third diagrams on the right-hand side refer to time forward and time reversed, respectively. (d) Two-photon ionization including intershell correlation effects. (e) Two-photon ionization with the XUV photon absorbed after the IR photon.

We solve the system of integral equations (18) numerically using the computer code developed by Amusia and collaborators [28]. The basis of occupied atomic states (holes) $3s$ and $3p$ is defined by the self-consistent HF method [29]. The excited electron states are calculated within the frozen-core HF approximation [30]. We present some results for one-photon ionization in Fig. 7. In the top panel, we show the partial photoionization cross sections from the $3p$ state calculated using the HF and RPAE approximations (see figure caption). From this plot, we see that the $3p \to kd$ transition is clearly dominant at low photon energies. Intershell correlation effects are more important for the $3p \to ks$ than for the $3p \to kd$ transition. The sum of the two partial cross sections calculated with the RPAE correction (red solid line and green line with circles) is very close to the the experimental data (solid circles) [31]. The middle panel presents the calculated cross section for $3s$ ionization and compares it to the experimental data

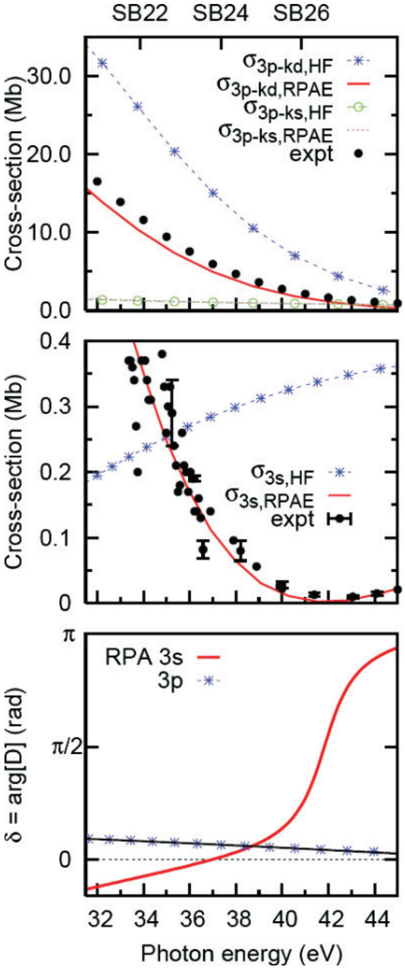

FIG. 7. (Color online) (top) The photoionization cross sections $\sigma_{3p\to kd}$ calculated in the HF (blue dotted line) and RPAE (red solid line) approximations are compared with the $\sigma_{3p\to ks}$ cross sections (HF, green open circles; RPAE, purple dashed line). The experimental data for the σ_{3p} cross section are from Ref. [31]. (middle) Photoionization cross sections σ_{3s} calculated in the HF (blue dotted line) and RPAE (red solid line) approximations are compared with experimental data [10]. (bottom) Correlation-induced phase shifts for the 3s and 3p dipole matrix elements.

from [10]. The RPAE correction is here essential to reproduce the behavior of the cross section, which, in this spectral region, is a rapid decreasing function of photon energy.

The bottom panel shows the correlation-induced phase shifts $\delta_{3s\to kp}$ and $\delta_{3p\to kd}$ from the same RPAE calculation. We observe that the RPAE phase correction $\delta_{3p\to kd}$ is relatively weak. In contrast, $\delta_{3s\to kp}$ varies significantly with energy, especially near the Cooper minimum. This qualitative difference can be explained by a different nature of the correlations in the 3p and 3s shells. In the 3p case, the correlation takes place mainly between the electrons that belong to the same shell with not much influence of the intershell correlation with 3s. We confirmed this conclusion by performing a separate set of RPAE calculations with only the 3p shell included. These calculations lead to essentially the same results for 3p ionization as the complete calculations. In the case of intrashell correlation, the time-forward process [see Fig. 6(c)] is effectively accounted for by calculating the photoelectron wave function in the field of a singly charged ion. It is therefore excluded from Eq. (18) to avoid double count. The remaining time-reversed term [second line in Eq. (18)] does not contain any poles and therefore does not contribute to an additional phase to the corresponding dipole matrix element. The small phase $\delta_{3p\to kd}$ is due to intershell correlation, which is indeed weak. In contrast, 3s ionization is strongly affected by correlation with the 3p shell. Consequently, the RPAE phase correction $\delta_{3s\to kp}$, which comes from the correlation with the 3p shell in the time-forward process, is large and exhibits a rapid variation with energy (a π phase change) in the region where the cross section decreases significantly.

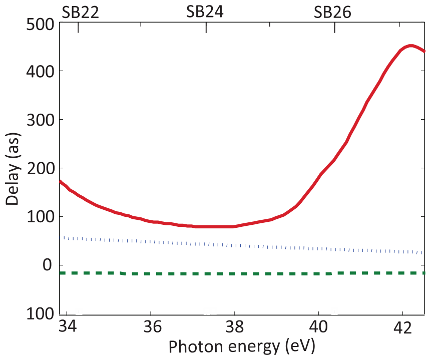

FIG. 8. (Color online) Ionization delay for the three angular channels: $3p \to kd$ (blue dotted line), $3p \to ks$ (green dashed line), and $3s \to kp$ (red solid line).

Finally, we generalize our theoretical derivation of two-photon ionization to including the effect of intershell correlation on the XUV photon absorption. As shown graphically in the diagram in Fig. 6(d), we replace the (real) transition matrix element corresponding to one-XUV photon absorption by a (complex) screened matrix element, with an additional phase term. As a consequence the phase of the two-photon matrix element becomes

$$\arg[M^{(2)}(k)] = \eta_\lambda(\kappa) + \delta_\lambda(\kappa) - \lambda\pi/2 + \phi_{cc}(k,\kappa). \qquad (21)$$

The time delay measured in the experiment is expressed as before as $\tau^{(2)}(k) = \tau^{(1)}(k) + \tau_{cc}(k)$, with $\tau^{(1)}(k)$ modified by intershell correlation:

$$\tau^{(1)}(k) = \frac{\eta_\lambda(\kappa_>) - \eta_\lambda(\kappa_<)}{2\omega} + \frac{\delta_\lambda(\kappa_>) - \delta_\lambda(\kappa_<)}{2\omega}. \qquad (22)$$

Figure 8 presents calculated time delays $\tau^{(1)}$ for the $3s \to kp$, $3p \to ks$, and $3p \to kd$ channels. The ionization delays from the 3p channel do not vary much with photon energy and

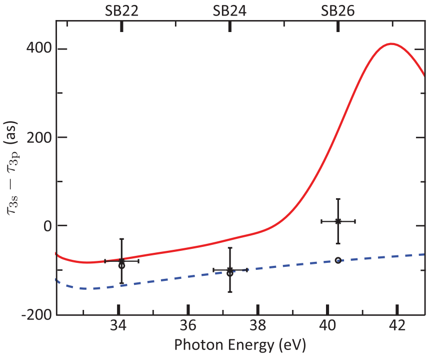

FIG. 9. (Color online) Comparison between our theoretical calculations (dashed blue line, HF; red solid line, RPAE) and experiments (circles, Ref. [8]; crosses, present work)

remain small. The $3p \rightarrow ks$ delay is negligible, while it takes about 70 as more time for the wave packet to escape towards the *d* channel due to the angular momentum barrier. The wave packet emitted from the 3*s* channel takes considerably more time to escape, especially in the region above 40 eV, owing to strong intershell correlation leading to screening by the $3p$ electrons.

V. COMPARISON BETWEEN THEORY AND EXPERIMENT

We present in Fig. 9 a comparison between our experimental results (see Table I) and our calculations. The dashed blue and solid red lines refer to the independent-electron HF and RPAE calculations, respectively. The circles refer to the results of [8], while the other symbols (with error bars both in central energy and delay) are the results obtained in the present work. Regarding the two sets of experimental results, they agree very well, except for that obtained at the highest energy corresponding to the sideband 26. Our interpretation is that we may be approaching the rapidly varying feature due to $3s$-$3p$ intershell correlation. Therefore a small change in the photon energy between the two measurements may lead to an important change in the delay. The experimental and RPAE results agree well for the first sideband but less for the two higher-energy sidebands. Surprisingly and perhaps accidentally, the HF calculation gives there a closer agreement with the experiment.

We now discuss possible reasons for the discrepancy. Our calculation of the influence of the dressing by the IR laser field is approximate. It only uses the asymptotic form of the continuum-wave functions (both in the final and intermediate states), thereby neglecting the effect of the core. This approximation should be tested against theoretical calculations, especially in a region where correlation effects are important. We also neglect the influence of the two-photon processes where the IR photon is absorbed (or emitted) first [32] [see Fig. 6(e)]. The corresponding matrix elements are usually small, except possibly close to a minimum of the cross section, where the other process, usually dominant, is strongly reduced. Interestingly, in such a scenario, the IR radiation would not simply be a probe used for the measurement of the phase of a one-photon process but would modify (control) the dynamics of the photoemission on an attosecond time scale. Finally, in our theoretical calculation, correlation effects are only accounted for in the single ionization process (XUV absorption). Additional correlation effects surrounding the probing, e.g., after the IR photon is absorbed, might play a role.

In conclusion, the results shown above point out the need for explicit time-dependent calculations, which would account for many-electron correlation and include not only one-photon but also two-photon ionization. We also plan to repeat these experimental measurements using attosecond pulses with a large and tunable bandwidth. Our results demonstrate the potential of the experimental tools using single attosecond pulses [5] or attosecond pulse trains [8]. These tools now enable one to measure atomic and molecular transitions, more specifically, quantum phases and phase variation, i.e., group delays, which could not be measured previously.

ACKNOWLEDGMENTS

We thank G. Wendin for useful comments. This research was supported by the Marie Curie program ATTOFEL (ITN), the European Research Council (ALMA), the Joint Research Programme ALADIN of Laserlab-Europe II, the Swedish Foundation for Strategic Research, the Swedish Research Council, the Knut and Alice Wallenberg Foundation, the French ANR-09-BLAN-0031-01 ATTO-WAVE program, and COST Action CM0702 (CUSPFEL).

[1] P. B. Corkum and F. Krausz, Nat. Phys. **3**, 381 (2007).
[2] F. Krausz and M. Ivanov, Rev. Mod. Phys. **81**, 163 (2009).
[3] V. Schmidt, Rep. Prog. Phys. **55**, 1483 (1992).
[4] E. P. Wigner, Phys. Rev. **98**, 145 (1955).
[5] M. Schultze *et al.*, Science **328**, 1658 (2010).
[6] A. S. Kheifets and I. A. Ivanov, Phys. Rev. Lett. **105**, 233002 (2010).
[7] U. Fano, Phys. Rev. A **32**, 617 (1985).
[8] K. Klünder *et al.*, Phys. Rev. Lett. **106**, 143002 (2011).
[9] M. Y. Amusia, V. K. Ivanov, N. A. Cherepkov, and L. V. Chernysheva, Phys. Lett. A **40**, 361 (1972).
[10] B. Möbus, B. Magel, K. H. Schartner, B. Langer, U. Becker, M. Wildberger, and H. Schmoranzer, Phys. Rev. A **47**, 3888 (1993).
[11] E. Goulielmakis *et al.*, Science **305**, 1267 (2004).
[12] G. Sansone *et al.*, Science **314**, 443 (2006).
[13] A. Cavalieri *et al.*, Nature (London) **449**, 1029 (2007).
[14] P. M. Paul, E. S. Toma, P. Breger, G. Mullot, F. Augé, Ph. Balcou, H. G. Muller, and P. Agostini, Science **292**, 1689 (2001).
[15] Y. Mairesse *et al.*, Science **302**, 1540 (2003).
[16] V. S. Yakovlev, J. Gagnon, N. Karpowicz, and F. Krausz, Phys. Rev. Lett. **105**, 073001 (2010).

[17] S. Nagele, R. Pazourek, J. Feist, and J. Burgdorfer, J. Phys. B **44**, 081001 (2011); Phys. Rev. A **85**, 033401 (2012).

[18] L. R. Moore, M. A. Lysaght, J. S. Parker, H. W. vanderHart, and K. T. Taylor, Phys. Rev. A **84**, 061404 (2011).

[19] C.-H. Zhang and U. Thumm, Phys. Rev. A **84**, 033401 (2011).

[20] J. M. Dahlstrom, D. Guénot, K. Klünder, M. Gisselbrecht, J. Mauritsson, A. L'Huillier, A. Maquet, and R. Taïeb, Chem. Phys. (in press, 2012).

[21] M. Ivanov and O. Smirnova, Phys. Rev. Lett. **107**, 213605 (2011).

[22] D. Kroon *et al.* (unpublished).

[23] G. Wendin, J. Phys. B **5**, 110 (1972).

[24] A. L'Huillier, L. Jönsson, and G. Wendin, Phys. Rev. A **33**, 3938 (1986).

[25] D. J. Kennedy and S. T. Manson, Phys. Rev. A **5**, 227 (1972).

[26] A. Kikas *et al.*, J. Electron Spectrosc. Relat. Phenom. **77**, 241 (1996).

[27] M. Swoboda, J. M. Dahlström, T. Ruchon, P. Johnsson, J. Mauritsson, A. L'Huillier, and K. J. Schafer, Laser Phys. **19**, 1591 (2009).

[28] M. Ia. Amusia and L. V. Chernysheva, *Computation of Atomic Processes: A Handbook for the ATOM Programs* (Institute of Physics Pub., Bristol, UK, 1997).

[29] L. V. Chernysheva, N. A. Cherepkov, and V. Radojevic, Comput. Phys. Commun. **11**, 57 (1976).

[30] L. V. Chernysheva, N. A. Cherepkov, and V. Radojevic, Comput. Phys. Commun. **18**, 87 (1979).

[31] J. A. R. Samson and W. C. Stolte, J. Electron Spectrosc. Relat. Phenom. **123**, 265 (2002).

[32] V. Véniard, R. Taïeb, and A. Maquet, Phys. Rev. A **54**, 721 (1996).